A phenomenological model of the neural response to pulsatile electrical stimulation: a novel approach and theoretical considerations

Colin Horne, B.Sc. (Hons)

Thesis submitted to the University of Nottingham
for the degree of Doctor of Philosophy

July 2016

UNITED KINGDOM · CHINA · MALAYSIA

Abstract

Cochlear implants stimulate the spiral ganglion cells (SGCs) with trains of charge-balanced current pulses. How the SGCs respond has often been studied with the leaky integrate-and-fire (LIF) model. However, while the LIF model partially reproduces how SGCs respond to monophasic pulses, which are not charge balanced, it does not reproduce how the opposite-polarity phases of charge-balanced pulses interact to reduce their efficacy, and nor does it reproduce the temporal distributions of the evoked spikes, or how they depend on the strength of the stimulus. To address these limitations, I extended the LIF model by adding an initiation period to spiking, delaying spike emission by a stochastic, stimulus-dependent duration, so that the temporal distribution of the model reproduces that of the SGC. During its initiation, a spike may be cancelled by anodic current, thus allowing opposite-polarity phases to interact, reducing the stimulus's efficacy in a way that reproduces how the thresholds of SGCs depend on the delay between the phases of cathodic-leading biphasic pulses.

A spike may only be cancelled by anodic current after it has been initiated by cathodic current, and thus, cancellation only occurs in response to pulses in which a cathodic phase precedes an anodic phase. Reversing the phase order of a pulse therefore changes how the phases interact. To investigate whether phase order has a similar effect in the real neuron, I analysed the phase plane of a biophysical point-neuron model and found that the qualitative description of excitation depends on phase order in a way that is consistent with the theory of spike cancellation. That the phase order of a biphasic pulse affects how excitation occurs has direct consequences for cochlear implant coding strategies, as it affects whether the interactions between consecutive biphasic pulses are facilitatory or inhibitory.

Publications and communications
arising from the work of this thesis

Journal articles

Horne, C., Sumner, C., and Seeber, B. (2016). A phenomenological model of the electrically stimulated auditory nerve fiber: temporal and biphasic response properties. *Frontiers in Computational Neuroscience,* 10(8).
DOI: 10.3389/fncom.2016.00008.

Invited presentations

Horne, C., Sumner, C., and Seeber, B. (2014). A phenomenological model to reproduce the latency distribution and threshold of the electrically stimulated auditory nerve fibre. *Bernstein Sparks Session, 13th International Conference on Cochlear Implants and other Implantable Auditory Technologies (CI 2014),* Munich.

Published abstracts

Horne, C., Sumner, C., and Seeber, B. (2012). Improving the timing realism of the modelled neural response: an extension to the integrate-and-fire model. *International Journal of Audiology,* 52(4):242-302. Poster.

Horne, C., Sumner, C., and Seeber, B. (2014). Extending the leaky integrate and fire model to reproduce the dependence of biphasic threshold on interphase gap. *International Journal of Audiology,* 53(9):641-696. Presentation.

Conference posters

Horne, C., Sumner, C., and Seeber, B. (2013). A phenomenological model of the auditory nerve fiber response to monophasic and biphasic electrical stimulation. *Conference on Implantable Auditory Prostheses (CIAP 2013),* California.

Horne, C., Sumner, C., and Seeber, B. (2013). A phenomenological model of the electrically stimulated auditory nerve fibre. *Neuroscience@Nottingham Poster & Lecture Day (N@N, December 2013),* Nottingham.

Acknowledgements

I would like to thank my supervisors Chris Sumner, Bernhard Seeber, and Alexander Kalashnikov for their help and support during the PhD, and for being so very patient while I have been writing this thesis! I am particularly grateful to Chris for selflessly adopting me as his student mid-way through the PhD. I would like to thank Mike A and John O'D for all their help and support while I was applying for the PhD. I would like to thank Christian and Thomas for being so kind to me at my first conference and making me feel welcome to the field, long before I was *in* the field. I would like to thank Fletcher for starting maths club at the institute and Rob for sharing his very considerable mathematical knowledge and explaining it in a way that we could understand. I would like to thank Ning for all the interesting conversations and very pleasant times, Steaders for going adventuring with me up cliffs and on bikes, Toby for always waving when walking by my window, Ian and Fletcher for their very sound advice, and David, Hettie, Sonia, and Antje for being so wonderful friends. I would like to thank Jonathan L, Mark W, Ian B, and David O'G for being so kind and supportive of me at CIAP 2013; it was my first time presenting my model to others in the field and I was anxious as to how it would be received. I would also like to thank Ian B and Stefan F at CI 2014 for similar reasons. I would like to thank my family, Elspie, Graeme, Mum, and Dad, for their continued support throughout the last four to twenty seven years, and finally, and most importantly, I would like to thank Claudia for her scientific and emotional support, her friendship and companionship, for making me happy, and for marrying me. It is to her that I dedicate this thesis, as well as my life in general.

Contents

Chapter 1

Introduction

In normal hearing, acoustic signals are transduced to electro-chemical activity by inner hair cells in the cochlea, which are then linked to the brain via the auditory nerve. If the inner hair cells become damaged, then the transduction of acoustic signals to electro-chemical activity cannot occur and deafness results. It is possible to treat this form of deafness by stimulating the auditory nerve with electrical current, bypassing the need for inner hair cells. Cochlear implants are clinical devices that have been used to treat deafness by these means since the 1970s.

Cochlear implants have been remarkably successful in treating profound deafness to the extent that many otherwise deaf individuals are able to understand speech without the use of lipreading or other visual cues. However, despite their success, cochlear implants are not able to transduce the acoustic signal as effectively as the inner hair cells do in normal hearing. Among other limitations, the temporal structure of the acoustic signal is to some extent distorted in the transduction with cochlear implants. This affects how cochlear implant recipients perceive sounds and is detrimental to their ability to understand speech, especially in the presence of background noise or reverberations.

It may be possible to overcome this limitation in cochlear implants by changing how they transduce the acoustic signal to electrical current, so that the auditory nerve's response closer mimics that in normal hearing. To achieve this, we must first understand how the auditory nerve responds to a given electrical stimulus, and then understand how to generate the stimulus that evokes the response we desire. This thesis is concerned with the former of these two problems.

This thesis presents a phenomenological model of how an individual fibre of the auditory nerve responds to stimulation. As a phenomenological model, the statistics

of the fibre's response and how they depend on the electrical stimulus are reproduced without reproducing the underlying biophysics. A primary contribution of the model is in phenomenologically describing how the fibre responds to a biphasic pulse. Additionally, the thesis provides an in-depth analysis of the biophysics behind excitation with biphasic pulses, drawing comparisons to the model and making a contribution to our understanding of how biphasic pulses excite the neuron.

1.1 Physiology of the peripheral auditory system

The peripheral auditory system is responsible for detecting sound and encoding it in a way that can be transmitted to and understood by the auditory cortex, the part of the brain responsible for processing auditory information. The peripheral auditory system consists of the *outer ear*, the *middle ear*, and the *inner ear*. The outer ear collects sound and channels it to the middle ear. It provides a gain in sound intensity by focusing acoustic energy from the larger area of the *pinna* (the visible portion of the ear that is external to the head) to the smaller area of the *tympanic membrane* (a barrier separating the outer ear from the middle ear), similar to how a horn intensifies sound (Stinson, 1985; Rabbitt and Holmes, 1988). The middle ear provides mechanical impedance matching between the low impedance tympanic membrane and the high impedance inner ear (Pickles, 2012; Moore, 2012). The inner ear is a bony labyrinth that forms the *cochlea*, a fluid filled, bone formed, channel that spirals around a central axis, visually resembling the shape of a snail's shell. This channel is divided by *Reissner's membrane* and the *basilar membrane* into three longitudinal chambers, forming the *scala vestibuli*, the *scala media*, and the *scala tympani*.

Conceptually, the cochlea starts at its *base* and concludes at its *apex*, the tip of the conical spiral that it forms. There are two membrane-covered windows at the base of the cochlea, the *oval window*, which opens onto the scala vestibuli, and the *round window*, which opens onto the scala tympani. An opening in the basilar membrane is situated at the apex of the cochlea, allowing fluid to flow between the scala vestibuli and the scala tympani. In this way, a displacement of fluid may be caused by depressing the oval window, causing bulging at the round window to relieve the resulting pressure.

Acoustic vibrations are transmitted to the cochlea via the oval window by the middle ear. The vibrations at the oval window are transmitted to the fluid that fills the scala vestibuli and scala tympani, ultimately causing vibrations in the basilar membrane. Due to longitudinally changing stiffness and mass of the basilar membrane, the frequency at which the basilar membrane most easily vibrates varies along its

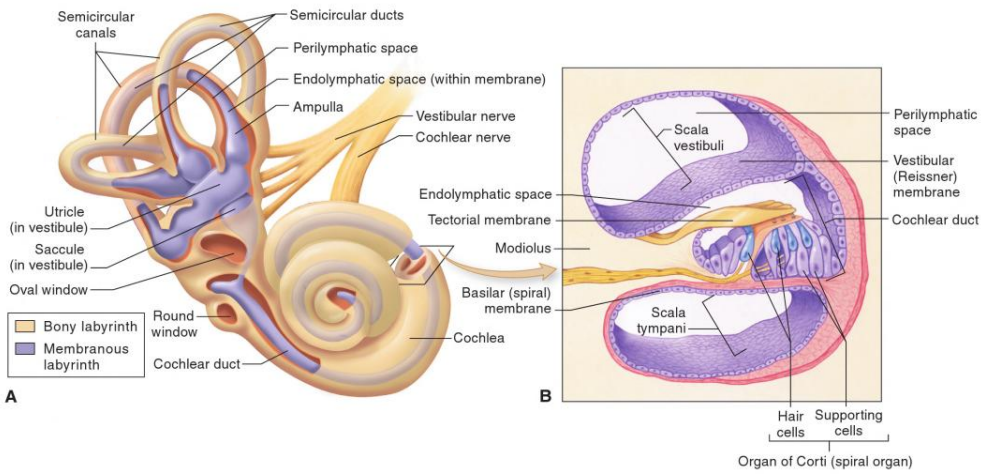

Figure 1.1: Anatomy of the cochlea (**diagram A**), with a cross-section revealing the division of the cochlea into three longitudinal chambers (**diagram B**). Figure reproduced from Patton and Thibodeau (2016) with permission from the publisher.

length, with positions closer to the apex favouring lower frequency vibration. Therefore, the cochlea performs the function of a mechanical spectrum analyser, with the basilar membrane vibrating with greatest amplitude at positions corresponding to the spectral peaks of the acoustic sound. The frequency that causes the greatest amplitude of vibration at a particular position along the basilar membrane is referred to as that position's *characteristic frequency*. The mapping between cochlear position and characteristic frequency is approximately exponential, with linear increases in distance from the apex corresponding to exponential increases in characteristic frequency (Greenwood, 1990; Robles and Ruggero, 2001).

Resting on the basilar membrane—within the scala media—is the *Organ of Corti*, a structure that is populated by receptor cells. These receptor cells may be divided into two groups, *inner hair cells (IHCs)* and *outer hair cells (OHCs)*. The IHCs act to transduce the mechanical vibrations of the cochlea to neural activity in the auditory nerve. The OHCs are believed to act to amplify the response of the basilar membrane to quiet sounds and to enhance its frequency selectivity (Moore, 2012; Pickles, 2012; Moore, 2014), although the biophysics underlying how they perform these roles is still a subject of debate (Ashmore, 2008; Hudspeth, 2008). Both the IHCs and the OHCs are evenly distributed along the length of the cochlea, from base to apex.

The IHCs and OHCs communicate auditory information to the cochlear nucleus

of the brainstem via the *spiral ganglion cells (SGCs)*, neurons that are either *afferent*, transmitting information *to* the brain, or *efferent*, transmitting information *from* the brain. In humans, ∼30,000 of the SGCs are *afferent* (Moore, 2012; Harrison and Howe, 1974) and ∼1,600 are *efferent* (Gelfand, 2009). Each afferent SGC may be classified as being either *type I*, innervating a single IHC (Fuchs et al., 2003), or *type II*, innervating several OHCs (Pickles, 2012). The vast majority—90 to 95%—are type I (Spoendlin, 1985; Gelfand, 2009).

The human cochlea has ∼3,500 IHCs (Wright et al., 1986), each of which forms a synapse to ∼10 type I SGCs (Spoendlin, 1970), providing redundancy that facilitates reliable transmission of information from the IHC to the cochlear nucleus (Faisal et al., 2008). From the cochlear nucleus, the auditory information is distributed to the higher levels of the auditory system.

A SGC consists of a *cell body*, *dendrite*, and *axon*. The dendrite and axon form cable-like protrusions from the cell body. The cell body is located in the *modulus*—the central axis of the cochlea—close to the IHC that it innervates by its dendrite. The axon follows the modulus out of the cochlea, where it and the other SGC axons collectively form the auditory nerve. As it is the type I SGCs that convey auditory information to the brain (Moore, 2014), all subsequent references to SGCs will implicitly refer to the type I SGCs.

1.2 The neural coding of sound

Neurons communicate by means of *action potentials*, brief spikes of electrical activity that are conducted by the axon. An individual neuron has an electrical potential that may vary along its length. The electrical potential of the neuron may be affected by synaptic or electric stimulation. An action potential is evoked if this potential is driven sufficiently high. The action potential does not in itself encode any information: once initiated, its amplitude and duration do not depend on the stimulus by which it was evoked. As such, neural activity may be abstracted to a sequence of discrete dimensionless *spikes* occurring in time. After a neuron fires (i.e., emits a spike), it cannot fire again for some fixed period of time (the *absolute refractory period*), after which firing may resume, but with increased threshold (the *relative refractory period*). Greater detail on the biophysics of the neuron and the electrochemical basis of the action potential will be given in section 2.1.

A SGC is synaptically stimulated by the IHC that it innervates, which in turn is stimulated by local displacements of the basilar membrane. Hence, each SGC is

associated with a particular frequency due to the frequency discrimination properties of the cochlea. This is known as *place coding*, and is one way in which frequency information is conveyed to the brain.

When continuously stimulated, a SGC will elicit a series of spikes. The spiking output of a neuron is quantified by is *firing rate*, the number of spikes it elicits per second. The firing rate of a SGC is related to the intensity of the acoustic stimulus. Within a SGC's *dynamic range*, increasing the stimulus level increases the firing rate, until the stimulus level increases beyond the dynamic range, after which the firing rate saturates at its asymptote. As the stimulus level decreases below the dynamic range, the SGC continues to fire sporadically at its *spontaneous rate*. The dynamic range of a SGC is centred around its *threshold*, which I[1] define as the stimulus level at which the firing rate is halfway between its minimum and maximum asymptotes.

Threshold varies between SGCs, with thresholds occupying a range of ∼60 dB. Each individual SGC has a dynamic range of about ∼25 dB. The wide range of thresholds allows a population of SGCs to encode the intensity of sounds over a much larger range than is possible by any cell individually.

When stimulated with a sinusoidal acoustic stimulus at frequencies of up to ∼5,000 Hz, it has been found that the spiking activity of the SGCs correlates with the positive phase of the stimulus. This is known as *phase locking*. An individual SGC may not necessarily elicit a spike to every positive phase of the stimulus. Instead, spiking to every phase is achieved because of the large number of responding neurons.

Phase locking is unable to occur at frequencies above ∼3,500 Hz in guinea pigs (Palmer and Russell, 1986) and ∼5,000 Hz in cats (Johnson, 1980); data from humans is not available, although it is commonly assumed to occur up to ∼5,000 Hz (Joris and Verschooten, 2013). The inability of the auditory nerve to produce phase locking at higher frequencies is not due to the saturation of the firing rates of the individual SGCs, as might be presumed, but is due to the temporal variability of the individual spikes (Anderson et al., 1971) and the time it takes the IHCs to return to baseline activity following stimulation by the excitatory phase of the stimulus (Palmer and Russell, 1986; Grothe et al., 2010). At low frequencies (i.e., frequencies below the cutoff above which phase locking does not occur), phase locking plays an important role in the perception of sound, influencing the perception of pitch and providing temporal cues that allow for sound localisation.

Pitch is a perceived attribute of a sound that allows sounds to be rated on a scale

[1]Individual researchers use different definitions; I use this definition as it is more consistent with the definition of threshold normally used in electrophysiology.

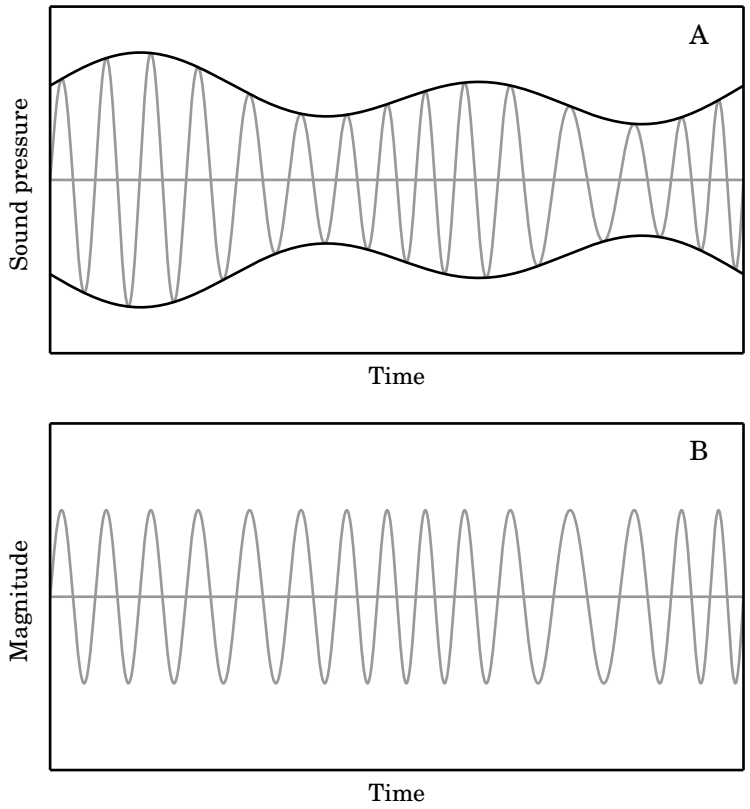

Figure 1.2: Depiction of the decomposition of a narrow-band signal $x(t)$ (**plot A**, **grey line**) into its upper and lower envelopes (**plot A**, **black lines**), and its TFS (**plot B**). If the upper envelope is denoted $x_{\text{env}}(t)$ and the TFS is denoted $x_{\text{TFS}}(t)$, then $x(t) = x_{\text{env}}(t)\, x_{\text{TFS}}(t)$.

from low to high, unrelated to their perceived loudness (Plack and Oxenham, 2005a). Pitch is closely related to the frequency of a sound, although—especially for sounds with complex waveforms—the two are not equivalent. Phase locking is hypothesised to contribute to our perception of pitch by producing spiking activity whereby the intervals between spikes are distributed around integer multiples of the period of the stimulus (Plack and Oxenham, 2005b).

Sound localisation occurs by various means (for reviews, see Fay and Popper, 2005; Moore, 2014). A key cue in localising broad-spectrum sounds (including speech; Smith et al., 2002; Wightman and Kistler, 1992) is the *interaural time difference* (Wightman and Kistler, 1992), which is the difference in the time it takes the sound to arrive at the two ears. A narrow-band signal may be viewed as a rapidly-oscillating carrier (known

as the *temporal fine structure*, or TFS) that is modulated by a slow-varying *envelope*, as depicted in Figure 1.2. At a given position along the length of the cochlea, the local vibrations of the basilar membrane form a narrow-band signal, and, at low frequencies (frequencies less that ∼1500 Hz; Zwislocki and Feldman, 1956), the central auditory system derives the interaural time difference (ITD) on the basis of the TFS of these vibrations (although how it does this in humans is disputed; Grothe et al., 2010; Joris and Yin, 2007; Ashida and Carr, 2011; McAlpine and Grothe, 2003).

1.3 Cochlear implants

Pathology of the inner hair cells prevents vibrations in the cochlea from being transduced into neuronal activity in the auditory nerve, resulting in hearing loss or profound deafness. Such *sensorineural hearing loss* may be treated by a cochlear implant. A cochlear implant is an electronic device that works by stimulating the auditory nerve with electrical currents delivered by electrodes inserted within the cochlea. The auditory nerve responds to the electrical stimulation with action potentials, and so the cochlear implant is able to perform the role of the inner hair cells in transducing acoustic vibrations to neuronal activity.

A cochlear implant consists of three main components: an external unit housing a *speech processor*, batteries and microphone, an implanted *electrode array*, and a *transcutaneous link*. The speech processor transduces acoustic sound received by the microphone to electrical stimulation delivered by the electrode array. The transcutaneous link uses electromagnetic induction so that the speech processor may power and communicate with the electrode array.

The electrode array is a long, thin tube that houses between 8 and 22 (depending on the device) electrodes that are equally spaced longitudinally. It is surgically implanted into the scala tympani of the cochlea by threading it through the round window or a cochleostomy (Wysocki and Skarzyński, 1997; Briggs et al., 2005). By using an array of spatially separated electrodes, the electrical stimulation may be delivered to spatially targeted groups of nerve fibres, allowing the cochlear implant to make use of the place coding that is present in normal hearing.

1.4 Stimulation strategy

The algorithm used by the cochlear implant's speech processor to map an acoustic signal to an electrical current signal is referred to as the *stimulation strategy* (or

the *coding strategy*). For the recipient of a cochlear implant to be able to perceive sound, the stimulation strategy must evoke spiking activity in the auditory nerve that somehow encodes the information present in the acoustic waveform, normally by mimicking the activity that would have been evoked in normal hearing.

The earliest commercially successful cochlear implants were developed in the 1970s and stimulated the auditory nerve by means of a single electrode implanted within the cochlea (Loizou, 1998; Rubinstein, 2004). The two most widely used single-channel implants were the House/3M device and the Vienna/3M device. The House/3M device band-pass filtered the acoustic signal to preserve frequencies in the 340-2700 Hz range, and used this band-passed signal to amplitude-modulate a 16 kHz sinusoid. The modulated signal was amplified and delivered to the electrode (Fretz and Fravel, 1985). While patients reported a perception of sound, they had very little perception of temporal information, perceiving only the envelope of the acoustic waveform (Loizou, 1998). Further, sounds at levels greater than ∼70 dB SPL were distorted due to them saturating the gain of the amplifier, resulting in amplitude clipping. To address these shortcomings, the Vienna/3M device used automatic gain control to prevent amplitude clipping, and delivered the signal unmodulated to prevent loss of temporal information. Further, it applied *frequency equalisation* to maintain equal loudness across frequencies. Without such equalisation, high frequency sounds would be less perceivable than low frequency sounds due to high frequency electrical stimulation being less efficient at evoking spiking activity in the nerve (Shannon, 1993, 1983).

Despite the Vienna/3M device stimulating with only a single channel and therefore not utilising the place cues that are present in normal hearing, recipients of the device were able to achieve moderate speech understanding without the aid of lip reading, scoring as high as 86% in word recognition tests (Tyler, 1988). This suggests that some temporal information is available to the recipient by means of rate encoding (Rosen, 1992), as has been verified by various studies investigating the effect of pulse rate on perceived pitch (Townshend et al., 1987; Tong and Clark, 1985; Macherey et al., 2011; Kong et al., 2009; Kong and Carlyon, 2010; Fearn and Wolfe, 2000). However, while these studies have found that pitch is related to pulse rate, increasing the pulse rate was only found to produce higher pitches within a very narrow range of rates (between ∼100 and ∼300 pulses per second), limiting the extent of pitch information that may be conveyed by the pulse rate. To provide greater pitch information, cochlear implants were engineered to convey pitch by means of place cues, instead of relying solely on rate cues. The electrode array of a multi-electrode cochlear implant provides

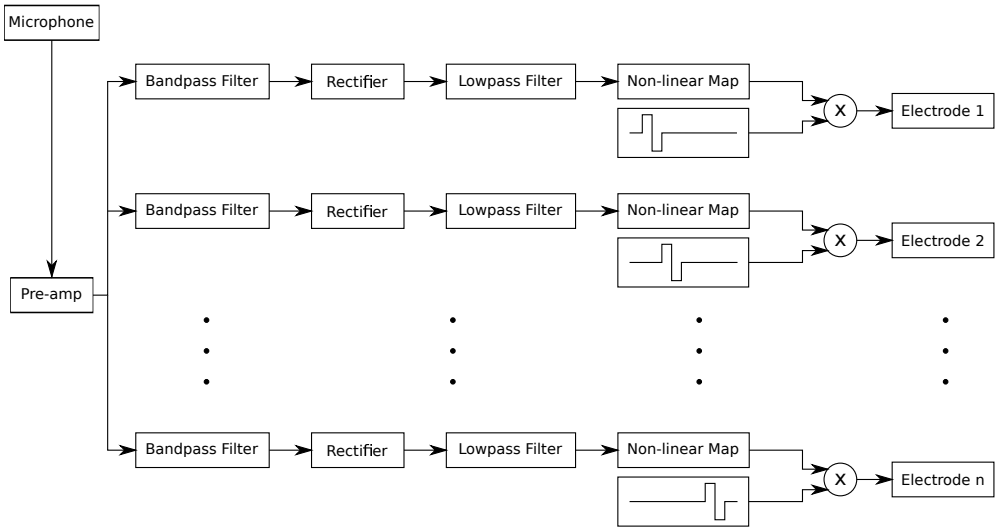

Figure 1.3: Block diagram representation of the CIS stimulation strategy. The input from the microphone is first amplified, and then processed by a collection of parallel pathways. Each pathway band-pass filters the signal, extracts the envelope (by means of first half-wave rectifying and then low-pass filtering the signal; see Rangayyan, 2015), compresses the amplitude (via a non-linear map), modulates by a periodic pulse-train waveform, and then delivers the resulting signal to an individual electrode. The pass-bands of the filters are consecutive across pathways so that the centre-band frequency decreases with advancing electrode position, and the modulating waveforms are identical, but phase-offset so that no two are non-zero at the same time. Diagram derived from the description of the CIS strategy in Wilson et al. (1991).

the means to deliver electrical stimulation to a specific site along the length of the cochlea, thus predominantly evoking activity in the SGCs innervating that location.

Early multi-electrode cochlear implants delivered continuous analogue signals to each electrode independently. This had the problem that the electromagnetic fields generated by the multiple electrodes would interact with one another (i.e., by summation of the individual fields; see White et al., 1984) in a way that was detrimental to sound perception (Favre and Pelizzone, 1993). This problem was addressed by the *CIS* strategy (Wilson et al., 1991), which rapidly interleaves the delivery of current between electrodes so that no two electrodes are ever simultaneously active. A block diagram of the CIS strategy is shown in Figure 1.3. The acoustic signal is decomposed into n spectrally-adjacent channels by means of a bank of band-pass filters. Each channel is associated with an individual electrode so that higher channels are perceived to have

higher pitches (normally by associating higher channels with more basal electrodes). The envelopes of each channel are extracted, compressed, and modulated by periodic biphasic pulse trains. The resulting amplitude-modulated pulse trains are then delivered to the electrodes. By taking the envelope of each channel, the strategy tracks the intensity of each channel through time. Compressing the envelope (by means of a non-linear map) matches the dynamic range of the microphone to the dynamic range of the auditory nerve, ensuring that quiet sounds are audible and that loud sounds are not overstimulating. By making the modulating pulse trains mutually out of phase, the strategy ensures that no two electrodes are simultaneously active, thereby avoiding the aforementioned problems of interacting electromagnetic fields.

The development of the CIS strategy dramatically improved the speech understanding ability of cochlear implant recipients (Wilson et al., 1991, 1992; Wilson, 2013, 2015). However, despite its success, the strategy has a substantial limitation: the TFS of the acoustic waveform is not encoded in the pulse train stimulus, and so the only temporal information provided by the strategy arises from the fluctuating amplitude of the envelope. ITD cues derived from the TFS are very important in spatial hearing (Dietz et al., 2013; Drennan et al., 2007; Majdak et al., 2006; Smith et al., 2002; Wightman and Kistler, 1992) and for understanding speech in noise (Nie et al., 2005; Zeng et al., 2005), and so bilaterally-implanted cochlear implant recipients are disadvantaged in not having these cues available. It has been shown that cochlear implants recipients are able to localise sounds when provided with the TFS at pulse rates of up to 800 pps (Majdak et al., 2006; Laback et al., 2005), and it is widely anticipated that bilateral cochlear implant recipients would benefit if stimulation strategies were to encode the TFS in the stimulating pulse train (e.g., Drennan et al., 2007; Majdak et al., 2006; Litvak et al., 2003a).

1.5 Computational modelling

While designing a stimulation strategy, it is necessary to consider whether the information encoded by the pulse train will survive the transduction of the electrode-neural interface and continue to be encoded by the spiking activity of the auditory nerve. To do this requires recording from a large number of the individual fibres of the auditory nerve during electrical stimulation. Recording from individual fibres is an invasive procedure that cannot be done in human cochlear implant recipients. While it is possible to record from individual fibres in animal models, there are many difficulties that make it infeasible to record from a large number of fibres. Therefore, computational

models provide an attractive alternative as recordings may be taken at a scale and level of automation that is not achievable in animal models.

Broadly speaking, there are two methods by which to computationally model how electrical stimulation elicits spiking activity in an auditory nerve fibre. One method is to describe mathematically the biophysical processes of the fibre and how they are affected by the application of electrical current, resulting in a *biophysical model*. The other method is to view the fibre as a system that transforms an input (a current signal) to an output (a spike train), and to derive a system of equations that is able to mimic how the output of the fibre relates to its input, resulting in a *phenomenological model*.

Both biophysical and phenomenological approaches have been used extensively in the context of cochlear implants. Since the publication of the Hodgkin-Huxley (HH) model of the electrically-stimulated neural membrane in 1952, biophysical models have been able to reproduce many aspects of how neurons respond to electrical currents. However, biophysical models are computationally demanding and have many parameters. Phenomenological models, by contrast, tend to be less computationally demanding and have fewer parameters. While simulating an individual nerve fibre with a biophysical model requires only modest computational demands by today's standards, simulating a whole population of fibres remains a huge computational undertaking. Further, there has been no methodology published by which to systematically derive the parameters of a biophysical model so as to reproduce electrophysiological data. This is especially troublesome when deriving the parameters for a population of fibres so as to reproduce the variability in behaviour that is observed empirically (Miller et al., 1999c) across fibres. There is therefore a strong motivation to develop phenomenological models that are less computationally demanding and easier to parametrise en masse. Developing such a phenomenological model has been a large focus in this PhD.

The model presented in this thesis (Chapter 5) has been developed specifically to reproduce the temporal stochasticity of the auditory nerve fibre while responding realistically to not only monophasic pulses, but also biphasic pulses, while still being computationally efficient to parametrise. Given that the model is intended to be used in the development of TFS-encoding stimulation strategies, it is necessary that the model reproduces the temporal properties of the auditory nerve fibre's response. In particular, when an auditory nerve fibre is stimulated into evoking an action potential, the action potential does not occur immediately, but occurs with a certain degree of

temporal variability (Shepherd and Javel, 1999; Miller et al., 1999b). If this variability is not reproduced by the model, then simulations of a strategy may either over- or under- estimate the ability of the nerve to encode temporal information in its spiking activity. Further, some degree of temporal variability may in fact be beneficial to the encoding of information in the nerve by mutually desynchronising the individual fibres from which the nerve is comprised. This is as desynchronised fibres are thought to better transmit information about the stimulus (Rubinstein et al., 1999; Litvak et al., 2003c; Stocks et al., 2002; Morse and Evans, 1996). Recent studies have attempted to facilitate and exploit this (Rubinstein et al., 1999; Litvak et al., 2003c,a,b; Litvak, 2002; Hong et al., 2003), and so if the model is to be useful in simulating the nerve's response to such strategies, it must clearly reproduce the temporal variability on which the strategies rely. As well as reproducing the temporal variability of the fibre's response, it is necessary to reproduce how the fibre responds to the biphasic pulses used by the majority of cochlear implants. Responding to biphasic pulses realistically complicates the design of phenomenological models, and so many previous studies (e.g., Bruce et al., 1999b,a; Hamacher, 2004; Fredelake and Hohmann, 2012) have chosen to approximate biphasic pulses by simpler monophasic pulses. However, while making such an approximation may be reasonable in some circumstances (such as when responding to pulses in isolation or in low-rate trains, where temporally-neighbouring pulses do not interact), failing to reproduce the interactions that underpin how the nerve fibre responds to biphasic pulses limits the applicability of the model in other circumstances (such as when responding to trains of alternating-polarity monophasic pulses, where inter-pulse interactions make the sequence of alternating-polarity monophasic pulses indistinguishable from a sequence of biphasic pulses). By reproducing the temporal variability with which auditory nerve fibres respond to electrical stimulation while simultaneously reproducing the inter-pulse interactions that occur during biphasic stimulation and complex monophasic stimulation, the model presented in this thesis contributes a useful tool for developing novel stimulation strategies to better encode temporal information in the nerve's spiking activity.

1.6 Thesis overview

The novel results of this thesis are described in chapters 3, 4, 5, and 6. Chapter 2 provides an introduction to, and literature review on, the concepts that are relevant to the remainder of the thesis. It introduces the neuron, the biophysical basis of the action potential, how the neuron responds to electrical stimulation, and how the

neuron is modelled, both biophysically and phenomenologically.

Chapter 3 qualitatively describes how stimulation with monophasic and biphasic pulses evoke excitation in a simplified (*reduced*) biophysical model of the membrane. Understanding at a qualitative level how different pulse shapes evoke excitation in a biophysical model may provide us with a better understanding of how excitation should be modelled phenomenologically. The descriptions of the chapter are derived by analysing the phase plane of the simplified biophysical model, and investigating how stimulation by different pulse shapes gives rise to different phase paths. Chapter 4 investigates how the previous analysis is affected by the stochasticity that is present in the real neuron. It further quantifies how stochasticity differently affects the responses to different pulse shapes by means of a novel analysis.

Chapter 5 describes the phenomenological model that I developed as part of the PhD. It is split into three sections, each describing a self-contained model that is iteratively improved across sections.

Chapter 6 investigates a theme that has been recurrent throughout the thesis, which is that the nature of excitation under biphasic stimulation seems to depend upon the order in which the opposite-polarity phases of the stimulus are delivered, both in the phenomenological model of Chapter 5, and in the analyses of Chapters 3 and 4. In the chapter, it is shown that when the cathodic phase leads, thresholds may be predicted on the basis of "spike cancellation", and when the anodic phase leads, thresholds may be predicted on the basis of leaky integration and accommodation. The chapter also considers the implications of these different modes of excitation in the context of pulse trains, showing that the phase order of the pulses affects how consecutive pulses interact.

Chapter 7 discusses the main results of this thesis and compares them and the methodology to those of previous studies, while also discussing the limitations of point models and suggesting how they might be overcome. Finally, it describes the next steps that should be undertaken in order to extend the phenomenological model of Chapter 5 so as to be able to simulate the responses of the SGCs under cochlear implant stimulation.

Chapter 2

Background

In order to develop the phenomenological model of chapter 5, I found it necessary to first obtain an understanding of the electrical properties of the neuron. This chapter provides an overview of the electrical properties of the neuron, describing their biophysical underpinnings and how they give rise to the excitability of the neural membrane. Further, it describes how extracellular currents affect the neuron, and how the response of the neuron depends on the stimulus in pulsatile stimulation. These factors will be referred back to throughout the thesis and play an important role in the context of cochlear implants, which stimulate the SGCs with interleaved pulses delivered by extracellular electrodes. Finally, this chapter provides an overview of previous phenomenological models of electrical stimulation, with a particular focus on those that have previously been used in the context of cochlear implants.

2.1 Biophysics of the neuron

The neuron is an excitable cell, which is to say that it may be stimulated into emitting action potentials. The space inside the neuron, the *intracellular space*, is separated from its surrounding environment, the *extracellular space*, by the *cell membrane*. Across the membrane is an electrical potential difference, the *membrane potential*. This potential difference arises due to differing ionic concentrations in the solutions that occupy the intra- and extracellular spaces. Perforating the membrane are pores through which ions may flow. These *ion channels* are selective, giving passage to only specific ionic species. There are many different families of ion channel, characterised by which ionic species they allow passage. Those most relevant to the shape of the action potential are the *sodium* and *potassium* families.

Due to diffusion, individual ions from a given species tend to move from regions where they exist in high concentration to regions where they exist in lower concentrations. That is, ionic species tend to move down their concentration gradient, as described by Fick's first law (see, e.g., Cotterill, 2003, chapter 5). As ions possess electrical charge, a net flux of ions corresponds to a flow of electrical charge, i.e., *current*, and so an ionic concentration gradient leads to an electromotive force.

2.1.1 The membrane as an electrical circuit

The electrical properties of a patch of neural membrane may be well approximated by an electrical circuit. The electrical properties of any given family of ion-channel are equivalent to those of a voltage source in series with a resistor. The conductivity of the resistor is related to the permeability of the membrane to the admitted ionic species, and the electromotive force of the voltage source is equal to the *Nernst potential* of the species, which is related to the concentration gradient of the species by

$$E \propto \frac{1}{q} \log \frac{[\text{extracellular concentration}]}{[\text{intracellular concentration}]},$$

where q is the valence of the species (see, e.g., Hille and Catterall, 2012; Aidley, 1998). The membrane is a separator of electrical charge, and so also has the electrical properties of a capacitor. Combined, the electrical properties of the membrane may be well-represented by a series of resistor-batter pathways in parallel with a capacitor, as shown by the circuit diagram in Figure 2.1. The circuit is that famously proposed to describe the membrane of the squid giant axon by Hodgkin and Huxley (1952). It includes pathways representing the sodium and potassium families of ion channel, as well as a third, *leakage*, pathway that approximates the permeability of the membrane to all other ionic species (later shown to be largely due to chloride ions; see Schiff, 2012, and Sterratt et al., 2011). The leakage pathway has a constant conductance g_{L}, where-as the sodium and potassium pathways have variable conductances given by

$$g_{\mathrm{Na}} = \bar{g}_{\mathrm{Na}} m^3 h$$

and

$$g_{\mathrm{K}} = \bar{g}_{\mathrm{K}} n^4$$

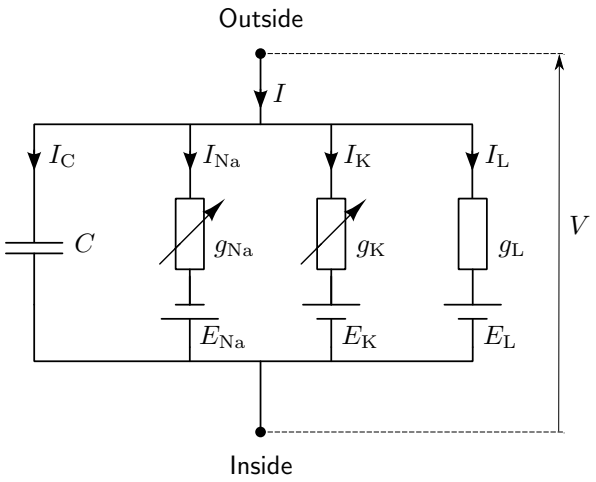

Figure 2.1: The equivalent electrical circuit of the Hodgkin-Huxley model of a patch of membrane.

respectively, where $\bar{g}_{\mathrm{Na}}$ and $\bar{g}_{\mathrm{K}}$ are constants,

$$\frac{\mathrm{d}x}{\mathrm{d}t} = \alpha_x(V(t)) \cdot (1 - x) - \beta_x(V(t)) \cdot x \tag{2.1}$$

for each $x \in \{m, n, h\}$, and V is the time-varying membrane potential, given by the potential difference across the capacitor. The variables m, n, and h are *gating variables* (also known as *activation variables* in the case of m and n, and *inactivation variables* in the case of h); they describe the states of individual *subunits* of the sodium and potassium ion channels. Each subunit may either be *open* or *closed*, independent to the state of other subunits. The probability of a given subunit being open is given by its respective gating variable. A sodium ion channel consists of four subunits. It is itself open only if its three *activation* subunits—each governed by the gating variable m—and its single *deactivation* subunit—governed by the gating variable h—are all open. It thus has probability m^3h of being open. The potassium ion channel has four subunits—each governed by the gating variable n—that must all be open for the channel to be open. It thus has probability n^4 of being open.

The gating variable of subunit type x is due to the rate at which closed subunits become open (given by α_x), and the rate at which open subunits become closed (given by β_x):

$$\text{closed} \underset{\beta_x}{\overset{\alpha_x}{\rightleftharpoons}} \text{open}.$$

The *transition rates* α_x and β_x depend on the membrane potential so that if the membrane potential is held fixed at some arbitrary value $V = v$, then the gating

x	E_x (mV)	$\bar{g}_x$ (mS $\cdot$ cm^{-2})
K	-12	36
Na	115	120
L	10.6	0.3

x	$\alpha_x(v)$	$\beta_x(v)$
n	$\frac{0.01(10-v)}{\exp([10-v]/10)-1}$	$0.125\exp(-v/80)$
m	$\frac{0.1(25-v)}{\exp([25-v]/10)-1}$	$4\exp(-v/18)$
h	$0.07\exp(-v/20)$	$\frac{1}{\exp([30-v]/10)+1}$

C	1 uF $\cdot$ cm^2

Table 2.1: Parameters of the Hodgkin and Huxley (1952) model. The voltages have been shifted relative to their physiological values by a constant amount so that the model has a resting potential of 0 mV. The Nernst potentials of the individual ionic species (E_x) are thus relative to the resting potential.

variable x will approach a steady state $x_\infty(v)$ with time constant $\tau_x(v)$, where

$$x_\infty(v) = \frac{\alpha_x(v)}{\alpha_x(v) + \beta_x(v)}$$

and

$$\tau_x(v) = \frac{1}{\alpha_x(v) + \beta_x(v)}.$$

With these definitions, (2.1) may be rewritten as

$$\frac{\mathrm{d}x}{\mathrm{d}t} = \frac{x_\infty(v) - x}{\tau_x(v)}. \tag{2.2}$$

This latter definition tends to offer a more intuitive understanding of how the gating variables develop over time.

The total current flowing inwards through the membrane is denoted by I. By Kirchhoff's current law, this must equal the sum of the inwards currents of the individual pathways, I_C, I_Na, I_K, and I_L, so that

$$I = I_\mathrm{C} + I_\mathrm{Na} + I_\mathrm{K} + I_\mathrm{L}. \tag{2.3}$$

From Ohm's law, we have $I_x = g_x(V - E_x)$ for each $x \in \{\mathrm{Na}, \mathrm{K}, \mathrm{L}\}$, where E_x is the Nernst potential of the given ionic species. Further, from the current-voltage law of

capacitors, we have $I_{\mathrm{C}} = C\frac{\mathrm{d}V}{\mathrm{d}t}$, where C is the membrane capacitance. Rearranging and expanding (2.3) gives

$$C\frac{\mathrm{d}V}{\mathrm{d}t} = I - \bar{g}_{\mathrm{Na}}m^3h(V - E_{\mathrm{Na}}) - \bar{g}_{\mathrm{K}}n^4(V - E_{\mathrm{K}}) - g_{\mathrm{L}}(V - E_{\mathrm{L}}), \tag{2.4}$$

which describes the time course of the membrane potential $V(t)$ in relation to an applied current $I(t)$, thus completing the description of the Hodgkin-Huxley (HH) model. A full list of parameters, including the equations that govern the transition rates, is given in Table 2.1.

2.1.2 Membrane stochasticity

The dynamics of the HH model are deterministic, which is to say that the dynamics of the model at a given moment in time are entirely determinable from the model's parameters and the state of the model at that moment (i.e., as given by the values of V, m, h, and n at that moment). Consequently, the model responds identically across multiple trials to the same stimulus, provided that the model variables are identically initiated in each trial: if excitation occurs, it will occur in all trials, with exactly the same latency in each. This is in contrast to in the real neuron, where multiple trials of the same stimulus will not necessarily result in consistent excitation, and when excitation does occur, it will occur with different latencies across different trials (as will be discussed in section 2.3).

The stochasticity of the real neuron arises due to the compounded effects of many sources of noise. The most significant sources of noise arise from synaptic processes (known as *synaptic noise*; Calvin and Stevens, 1968) and from stochastic opening and closing of individual ion channels (known as *channel noise*; White et al., 1998). As the SGCs of a deaf cochlea tend not to receive synaptic input, channel noise has been theorised to be the dominant source of noise in the SGCs of cochlear implant recipients (Bruce, 2009; Matsuoka et al., 2001; Rubinstein et al., 1999), and so it has become standard practice for computer models of the electrically stimulated auditory nerve to assume a complete absence of synaptic activity, with stochasticity arising only by means of channel noise (e.g., Imennov and Rubinstein, 2009; Mino et al., 2004; Mino and Rubinstein, 2006; Woo et al., 2009, 2010).

Various methods have been proposed for introducing channel noise to the HH model. The simplest has been to add *current noise* to the membrane equation, so

that (2.4) becomes

$$C\frac{\mathrm{d}V}{\mathrm{d}t} = I - \bar{g}_{\mathrm{Na}}m^3h(V - E_{\mathrm{Na}}) - \bar{g}_{\mathrm{K}}n^4(V - E_{\mathrm{K}}) - g_{\mathrm{L}}(V - E_{\mathrm{L}}) + \xi_V(t), \qquad (2.5)$$

where ξ_V is a Gaussian white noise process (Finke et al., 2008; Goldwyn and Shea-Brown, 2011). Models that utilise current noise are empirically, rather than theoretically, motivated: they do not represent mathematical formulations of our understanding of ion channel kinetics, but for many practical purposes, they produce similar behaviour to models that do (Finke et al., 2008; Huber and Braun, 2007; Rowat, 2007). To implement channel noise with a biophysical level of detail, we should reproduce how the stochastic openings and closings of individual ion channels result in *conductance noise*—that is, stochastic fluctuations in the conductance of the membrane. To produce conductance noise, we may model each individual ion channel as a continuous-time Markov process that transitions between states at rates derived from the gating variables of the HH model (e.g., see Clay and DeFelice, 1983; DeFelice and Isaac, 1993; Mino et al., 2002, 2004). Each state of a given channel may be interpreted as representing a particular configuration of the channel's subunits, with one state representing the channel when it is open, and the others representing the various configurations in which the channel is closed.[1] If we write m_xh_y to denote the state of a sodium ion channel that has x open m-class subunits and y open h-class subunits, then m_3h_1 denotes the open state of a sodium ion channel, and the kinetic scheme is given by

$$\begin{array}{ccccccc}
[m_0h_1] & \underset{\beta_m}{\overset{3\alpha_m}{\rightleftharpoons}} & [m_1h_1] & \underset{2\beta_m}{\overset{2\alpha_m}{\rightleftharpoons}} & [m_2h_1] & \underset{3\beta_m}{\overset{\alpha_m}{\rightleftharpoons}} & [m_3h_1] \\
\alpha_h \uparrow\downarrow \beta_h & & \alpha_h \uparrow\downarrow \beta_h & & \alpha_h \uparrow\downarrow \beta_h & & \alpha_h \uparrow\downarrow \beta_h \\
[m_0h_0] & \underset{\beta_m}{\overset{3\alpha_m}{\rightleftharpoons}} & [m_1h_0] & \underset{2\beta_m}{\overset{2\alpha_m}{\rightleftharpoons}} & [m_2h_0] & \underset{3\beta_m}{\overset{\alpha_m}{\rightleftharpoons}} & [m_3h_0]
\end{array} .$$

Similarly, if we write n_x to denote the state of a potassium ion channel that has x open subunits, then n_4 denotes the open state of a potassium ion channel, and the

[1] When enumerating the states of a given channel, it is convenient (although not necessary) to collapse all identical states to a single state. Two states are identical if they only differ in *which* subunits within each class are open/closed. For example, a sodium channel has three m-class subunits and one h-class subunit, and thus there are three ways in which a single m-class subunit could be open while the h-class subunit is closed. These three ways may be encapsulated by a single state, in which case the in-going and out-going transition rates of should both be multiplied by three. In the case of the sodium ion channel, there are 8 states, consisting of one open state (representing the case when all subunits are open) and 7 closed states (representing the various configurations where any individual subunit is close). Similarly, in the case of the potassium ion channel, there are 4 states, consisting of one open state and 3 closed states.

kinetic scheme is given by

$$[n_0] \underset{\beta_n}{\overset{4\alpha_n}{\rightleftharpoons}} [n_1] \underset{2\beta_n}{\overset{3\alpha_n}{\rightleftharpoons}} [n_2] \underset{3\beta_n}{\overset{2\alpha_n}{\rightleftharpoons}} [n_3] \underset{4\beta_n}{\overset{\alpha_n}{\rightleftharpoons}} [n_4] \ .$$

When an ion channel assumes any given state, the delay before it transitions to its next state has an exponential distribution with rate constant given by the sum of the out-going transition rates. The conductance of the membrane at a given moment in time is given by the sum of the conductances of the open channels[2], and so (2.4) becomes

$$C\frac{\mathrm{d}V}{\mathrm{d}t} = I - \gamma_{\mathrm{Na}} N_{\mathrm{Na}}(t)(V - E_{\mathrm{Na}}) - \gamma_{\mathrm{K}} N_{\mathrm{K}}(t)(V - E_{\mathrm{K}}) - g_{\mathrm{L}}(V - E_{\mathrm{L}}), \tag{2.6}$$

where γ_{Na} is the conductance of a single open sodium ion channel, $N_{\mathrm{Na}}(t)$ is the number of open sodium ion channels at time t, and γ_{K} and $N_{\mathrm{K}}(t)$ are similarly defined for the potassium ion channels. As the number of modelled ion channels tends to infinity, $\gamma_{\mathrm{Na}} N_{\mathrm{Na}}(t)$ tends to $\bar{g}_{\mathrm{Na}} m^3 h$ and $\gamma_{\mathrm{K}} N_{\mathrm{K}}(t)$ tends to $\bar{g}_{\mathrm{K}} n^4$, and so the original HH equations emerge. In the most straightforward implementation, every individual ion channel in the modelled patch of membrane is simulated by a dedicated Markov process, and $N_x(t)$ simply counts the number of x-family ion channels that are open at time t (for $x \in \{\mathrm{Na}, \mathrm{K}\}$). Such an implementation is exceedingly computationally demanding, however, and so various methods have been proposed to make channel noise models more efficient. Some of these methods are exact algorithms for implementing the Markov scheme without the need for individually simulating each ion channel (e.g., Chow and White, 1996; Faisal and Laughlin, 2007; Skaugen and Walløe, 1979), while others are approximations that are more computationally efficient, but are not mathematically equivalent to the original Markov scheme (e.g., Fox, 1997; Fox and Lu, 1994).

A common method of efficiently approximating the Markov scheme, first described by Fox and Lu (1994), is to introduce stochasticity to the individual gating variables, replacing (2.1) with

$$\frac{\mathrm{d}x}{\mathrm{d}t} = \alpha_x(V(t)) \cdot (1 - x) - \beta_x(V(t)) \cdot x + \xi_x(t), \tag{2.7}$$

[2]It is generally assumed that the leakage channels are always open and do not have gating kinetics, and that channels in a closed state are non-conducting.

for $x \in \{m, n, h\}$, where $\xi_x(t)$ is a Gaussian process with

$$\mathrm{E}\left[\xi_x(t)\right] = 0$$

and

$$\mathrm{E}\left[\xi_x(t)\xi_x(t')\right] = \frac{\alpha_x(1-x) + \beta_x x}{\bar{N}_X}\delta(t-t'),$$

where X is Na when $x \in \{m, h\}$, or K when $x \in \{n\}$, and $\bar{N}_X$ is the total number of X-family ion channels. In the original paper by Fox and Lu, the dynamics of V are then described by the the membrane equation of the HH model (Equation 2.4). More recently, other investigators (e.g., Mino et al., 2002; Bruce, 2007; Huang et al., 2013) have chosen to instead describe the dynamics of V by means of (2.6), using m, n, and h to estimate $N_{\mathrm{Na}}(t)$ and $N_{\mathrm{K}}(t)$, with

$$N_{\mathrm{Na}}(t) = \mathrm{rnd}(\bar{N}_{\mathrm{Na}} m^3 h)$$

and

$$N_{\mathrm{K}}(t) = \mathrm{rnd}(\bar{N}_{\mathrm{K}} n^4),$$

where $\mathrm{rnd}(z)$ rounds z, either downwards (as in Mino et al., 2002), or towards the nearest integer (as first advocated by Bruce, 2007, and later expanded on by Huang et al., 2013). The purpose of the rounding is to better reproduced how changes in conductance occur at discrete steps due to the opening and closing of individual channels, noting that without rounding, the conductance would fluctuate smoothly.

2.1.3 The action potential

The dynamics of the gating variables depend upon the membrane potential, as shown in Figure 2.2, which plots the steady state x_∞ and time constant τ_x of each gating variable $x \in \{n, m, h\}$ as a function of membrane potential V. Coupled with knowledge of the Nernst potentials of each ionic species (given in Table 2.1), a qualitative understanding of the action potential may be obtained. At rest ($V = 0$ mV), almost all of the sodium ion channels are closed (see curve for m_∞^3 near $V = 0$ mV), and most of the potassium ion channels are closed (see curve for n_∞^4 near V_0 mV). As V is raised, m reacts quickly (much quicker than the other gating variables due to its much smaller time constant), resulting in inwards current through the sodium pathway. Inwards current leads to an increase in V, which in turn leads to more sodium current; this positive feedback is responsible for the formation of the action potential. Over

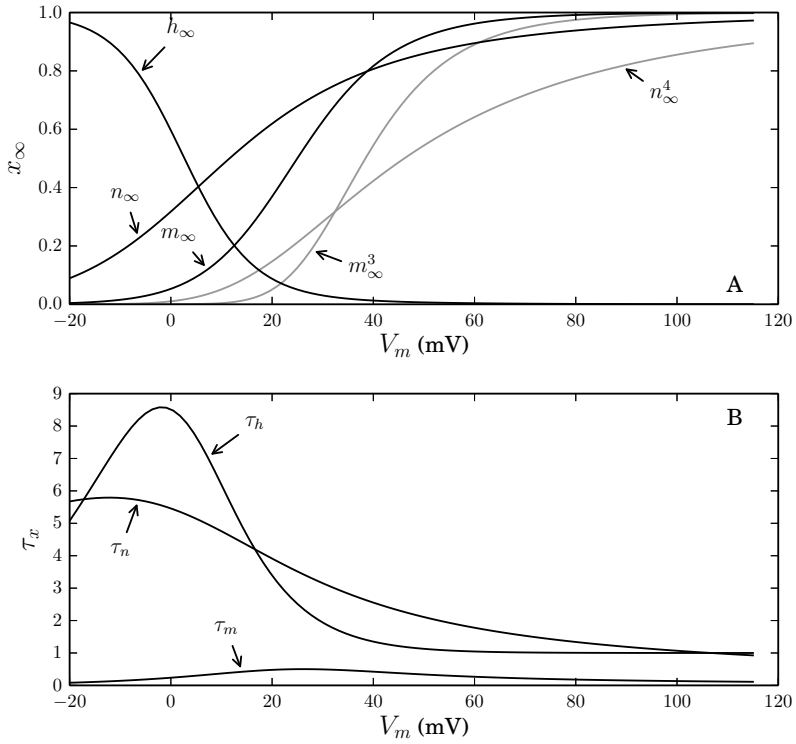

Figure 2.2: Asymptotic values (**plot A**) and time constants (**plot B**; ordinate units in ms) of the gating variables of the Hodgkin and Huxley model. The model is parametrised such that the resting potential is 0 mV (see table 2.1).

a short period of time, the sodium current will drive V towards E_{Na} (115 mV above resting potential). This increase in V slowly leads to an increase in n and a decrease in h (slowly because of the much longer time constants of n and h compared to m). A decrease in h biophysically corresponds to the inactivation of the sodium ion channels, which eventually abolishes the inwards sodium current. An increase in n leads to an outwards flow of potassium current, which drives V towards E_{K} (12 mV below resting potential). During this time, all the gating variables (n, m, and h) are driven towards (or slightly beyond) their resting values by V, and the system eventually returns to its resting equilibrium.

To summarise, the initial rise in membrane potential during an action potential is due to the rapidly responding sodium ion channels (m). The duration of the action potential is made finite by the inactivation of the sodium ion channels (h). The membrane potential is then driven slightly below its resting value by the slow responding potassium ion channels (n).

2.1.4 The neuron as an electrical circuit

The HH equations describe the time course of the potential difference across a patch of membrane that is at equipotential. However, the electrical potential of the neuron varies not only with time, but also with space, with potential gradients existing along the neuron's length. To reproduce the effects of space, a *multicompartment model* discretises the neuron along its length, producing multiple segments (or *compartments*), each of which is assumed to be at equipotential. Neighbouring compartments are connected at their intracellular nodes (i.e., the node labelled "Inside" in Figure 2.1) with a resistance that represents the longitudinal resistance of the intracellular medium. Each compartment may have different dynamics and parametrisations, reflecting the different behaviours of the dendrites, the axon, and the soma.

A multicompartment model of a morphologically-simplified SGC is depicted in Figure 2.3. Parts of the cell are covered by myelin, an electrical insulator. These parts are normally assumed to be passive, having only a leak resistance and no active (i.e., voltage-dependent) dynamics. The axon is mostly myelinated, but spatially distributed *nodes of Ranvier* are unmyelinated, having active dynamics, and are responsible for maintaining the amplitude of the action potential as it propagates along the length of the axon. In some species (e.g., cat), the soma is myelinated, while in others (e.g., man), it is not. The model discretises the neuron into multiple segments, each representing either the soma, a node of Ranvier, or a myelinated internodal seg-

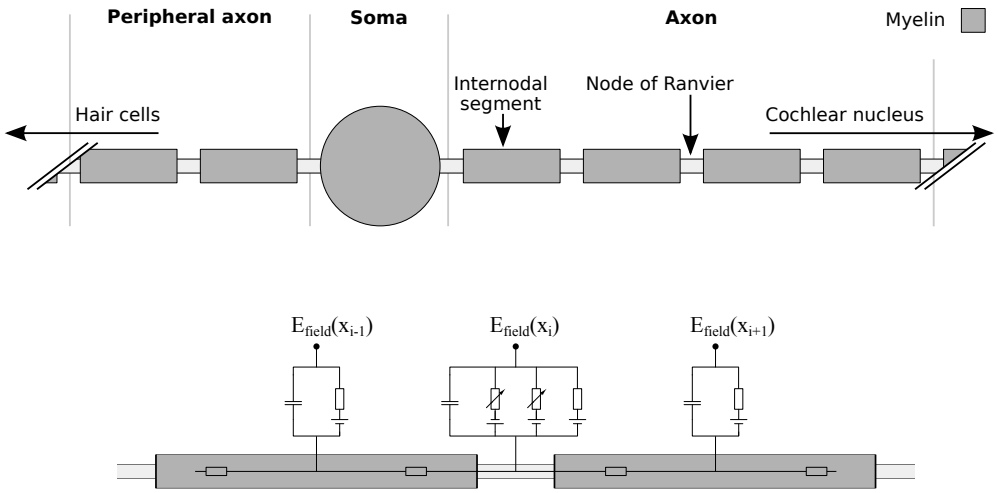

Figure 2.3: Simplified morphology of a spiral ganglion cell (top diagram) with corresponding electrical circuits (bottom diagram) that form the basis of a multicompartment model. Myelinated internodal segments are modelled with passive circuits and the nodes of Ranvier are modelled with Hodgkin and Huxley equations. An electrical field model (not depicted) provides the extracellular potentials labelled $E_{\text{field}}(x_i)$. Whether or not the soma is myelinated, and the number of peripheral nodes, depends on species. Based on diagrams and descriptions from Imennov and Rubinstein (2009) and Brown and Hamann (2014).

ment. Each segment is typically assumed to be at equipotential, and thus, is modelled as a single compartment (Rattay et al., 2001b).

2.1.5 The membrane in different species

Since Hodgkin and Huxley published their equations of the squid giant axon membrane, other investigators have used similar methodologies to find equations that describe the membranes of other nerves in other species. Most notably, Frankenhaeuser and Huxley (1964) published a model of toad *Xenopus laevis* nerve membrane (the *Frankenhaeuser-Huxley (FH)* equations), Chiu et al. (1979) published a model for rabbit sciatic nerve membrane (the *Chiu-Ritchie-Rogart-Stagg-Sweeney (CRRSS)* equations), and Schwarz and Eikhof (1987) published a model for rat myelinated membrane (the *Schwarz-Eikhof (SE)* equations). They have all been used extensively to model the mammalian SGC in the context of cochlear implants. Various studies have found the HH equations favourable for this purpose (Motz and Rattay, 1986; Rattay and Aberham, 1993; Rattay, 1990; Rattay et al., 2001b; Smit et al., 2008; Cartee, 2000), despite them not exhibiting the adaptation and long-term accommodation phenomena that occur in the SGC (Negm and Bruce, 2008). As these phenomena are not investigated in this thesis,[3] the HH equations will be used in later chapters to model the SGC membrane.

2.2 Electrical stimulation of the neuron

In order to develop a phenomenological model of electrical stimulation, it is useful to first have a qualitative understanding of how stimulation affects the neuron. The previous chapter described the *active* dynamics of the membrane; that is, the voltage-dependence of the ion channels. These active dynamics are intuitively difficult to understand. While the membrane potential is sufficiently close to its resting value, these dynamics are sluggish, and so, for short time-durations, the ion channels may be considered *passive*.

2.2.1 Passive behaviour of the membrane

While the membrane is passive, the gating variables m, n, and h do not deviate from their resting values. The ordinary differential equation (ODE) governing the

[3] Chapter 6 does investigate how accommodation affects the membrane's response to biphasic current pulses, however this is over very short durations and is distinct to the long-term accommodation mentioned above.

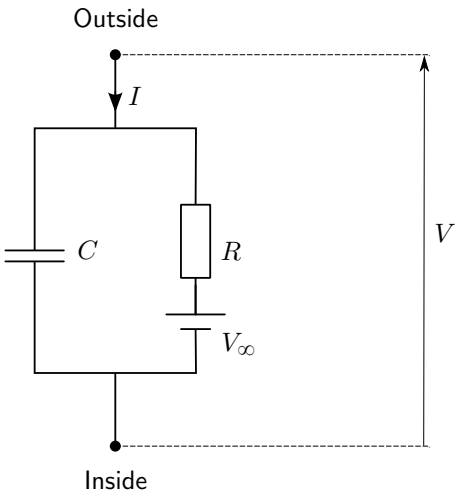

Figure 2.4: The equivalent electrical circuit of a patch of passive membrane. The three resistor-battery pathways of the HH model (see Figure 2.1) have been collapsed to a single pathway with resistance R and electromotive force V_∞ by assuming that the conductances of the HH resistors are constant.

membrane potential in the HH model (2.4) may then be rewritten as

$$C\frac{\mathrm{d}V}{\mathrm{d}t} = I + \frac{1}{R}(V_\infty - V), \tag{2.8}$$

where

$$R = \frac{1}{g_{\mathrm{Na}}m^3h + g_{\mathrm{K}}n^4 + g_{\mathrm{L}}}$$

gives the membrane resistance at rest and

$$V_\infty = R(g_{\mathrm{Na}}m^3hE_{\mathrm{Na}} + g_{\mathrm{K}}n^4E_{\mathrm{K}} + g_{\mathrm{L}}E_{\mathrm{L}})$$

gives the membrane potential at rest. The equivalent electrical circuit of a patch of passive membrane is shown in Figure 2.4; its single resistor-battery pathway is equivalent to the three resistor-battery pathways of the HH model when their conductances are held constant. It is convenient to rewrite (2.8) in terms of $\tau = RC$, referred to as the *membrane time constant*, so that

$$\tau\frac{\mathrm{d}V}{\mathrm{d}t} = RI + V_\infty - V. \tag{2.9}$$

The passive membrane may thus be considered a linear time-invariant filter with time constant τ. The linearity of (2.9) allows for easy analysis; if I is time-variant, then

$$V(t) = \frac{1}{C}\int_0^t I(s)\exp(-\frac{t-s}{\tau})\,\mathrm{d}s + V_\infty + (V(0) - V_\infty)e^{-t/\tau}, \tag{2.10}$$

and if I is time-invariant, then this reduces to

$$V(t) = RI(1 - e^{-t/\tau}) + V_\infty + (V(0) - V_\infty)e^{-t/\tau}. \tag{2.11}$$

It has widely been assumed that the membrane is passive until a discrete moment of excitation (see, e.g., Levitan et al., 2015; Dayan and Abbott, 2001; Reilly et al., 1985). Under this assumption, the previous equations describe the time-course of the membrane potential up until the moment of excitation, thus providing a very convenient framework under which to analyse how the membrane responds to simple electrical stimulation. This framework forms the basis for many phenomenological models, including the novel model presented in the next chapter.

2.2.2 Excitation of the membrane

The electrical stimulation of the membrane produces a driving force on the membrane potential, with cathodic current driving the potential to higher values (*depolarising* the membrane) and anodic current driving the potential to lower values (*hyperpolarising* the membrane). It is common to take the simplified view that the membrane produces an action potential when its potential exceeds a *threshold potential* (e.g., see Reilly et al., 1985). However, even under this simplification, the threshold potential is non-linearly affected by changes in membrane potential. Following a depolarisation, the threshold potential is increased, while following a hyperpolarisation, it is decreased. This phenomenon is known as *accommodation* and occurs due to voltage-induced changes in the activation of the potassium ion channels and the inactivation of the sodium ion channels (Fitzhugh, 1961; Frankenhaeuser and Vallbo, 1965; Noble and Stein, 1966; Vallbo, 1964; Bergman and Stampfli, 1966).

A model of accommodation

A simplified but influential model of excitation and accommodation was proposed by Hill (1936a), who assumed that the membrane will always "accommodate" with time constant λ to changes in potential so that the threshold potential will always be some fixed amount above the membrane potential as the membrane becomes fully accom-

modated (i.e., as the threshold potential reaches an asymptote after the membrane potential has been held fixed for an arbitrarily long period of time). Formally, he proposed that the threshold potential U is related to the membrane potential V by the differential equation

$$\lambda \frac{\mathrm{d}U}{\mathrm{d}t} = V - V_\infty + U_\infty - U,$$

where V_∞ and U_∞ represent the resting values of the membrane and threshold potentials, respectively[4]. Under Hill's theory, excitation occurs if the membrane potential and threshold potential ever intersect. He notes that the time constant λ of accommodation is considerably larger (10 to 200 times) than the membrane time constant τ, and so the membrane potential reacts to stimulation much faster than the threshold potential reacts to deviations in membrane potential. While Hill's theory does not describe the biophysical processes underpinning accommodation, it provides a useful and intuitive description of accommodation, and describes how the threshold potential is intrinsically related to the membrane potential. Hill's model has been used as a basis for modern phenomenological models of electrical stimulation that exhibit accommodative behaviour (see, for example, Mihalas and Niebur, 2009; Dodla et al., 2006).

2.2.3 Extracellular stimulation of the neuron

In the extracellular stimulation of a neuron, the stimulus affects the neuron by creating an extracellular potential gradient that drives longitudinal intracellular currents (Ranck Jr, 1975). Current flows in through the membrane at nodes with higher extracellular potentials and out through nodes with lower extracellular potentials, depolarising the membrane at the points of inwards flow and hyperpolarising it at the points of outwards flow. Therefore, a stimulus of given polarity simultaneously depolarises and hyperpolarises the neuron at different points along the neuron's length. The direction and magnitude of the membrane current at a given point in an unmyelinated neuron has been related to the second spatial derivative of the extracellular potential by Rattay (1986, 1987, 1989). Rattay (1986) defined the *activating function* as

$$f_{\mathrm{unmyl}} = \frac{\mathrm{d}^2 V_e}{\mathrm{d}x^2},$$

[4]In Hill's paper, the terms $V - V_\infty$ and $U_\infty - U$ contribute with different time constants so that $\mathrm{d}U/\mathrm{d}t = (V - V_\infty)/\beta + (U_\infty - U)/\lambda$, but the paper then assumes that $\beta = \lambda$. If $\beta/\lambda \neq 1$, then the change in membrane potential required for excitation when the membrane is fully accommodated is different to the change in membrane potential required when the membrane is at rest.

where $V_e(x)$ is the extracellular potential at point x along the length of the neuron. Rattay theorised that the neuron will be depolarised where the activating function is positive, and hyperpolarised where it is negative. In the case of a myelinated neuron, the activating function is defined as the difference quotient

$$f_{\text{myl}} = \frac{\Delta^2 V_e}{\Delta x^2},$$

where Δx is segment length of the axon (i.e., the combined length of an internode and node; Rattay, 1986). The myelinated activating function converges towards the unmyelinated function as the distance between the stimulating electrode and the neuron is increased, with close convergence occurring at distances above Δx (Rattay, 1986).

Figure 2.5 plots the activating functions of idealised (straight, infinitely long, and morphologically uniform) myelinated and unmyelinated axons stimulated by an extracellular electrode under idealised conditions (infinite, isotropic, and homogeneous extracellular space). In both the myelinated and unmyelinated axons, cathodic current depolarises the axon at regions proximal to the electrode, while simultaneously hyperpolarising the axon at regions distal to the electrode. The depolarised region experiences greater driving force than the flanking hyperpolarised regions, and so the action potential is expected to be initiated at the point (unmyelinated axon) or node of Ranvier (myelinated axon) that is closest to the stimulating electrode. Inverting the polarity of the delivered current inverts the sign of the activating function, and so under anodic current hyperpolarises the axon at regions proximal to the electrode while depolarising the axon at regions distal to the electrode.

It is tempting to use the activating function to predict the magnitude of depolarisation or hyperpolarisation at a given node of Ranvier, and it has been used for this purpose in various studies of extracellular stimulation (Altman and Plonsey, 1990; Ferguson et al., 1987; Rattay, 1988, 1989, 1990; Meier et al., 1992). However, one must exercise caution in doing so, for the activating function comes with a caveat: beyond the insulating effects of the myelin, it does not take into account the electrical properties of the neuron itself, or how they change during stimulation. This caveat becomes particularly important near the soma, as it has a much larger capacitance than the nodes of Ranvier due to its much larger diameter. Given its high capacitance, the soma is less affected by a given amount of charge flowing through its membrane than a node of Ranvier would be, and thus, even when the activating function has a large magnitude near the soma, the soma may be less affected by the extracellular field

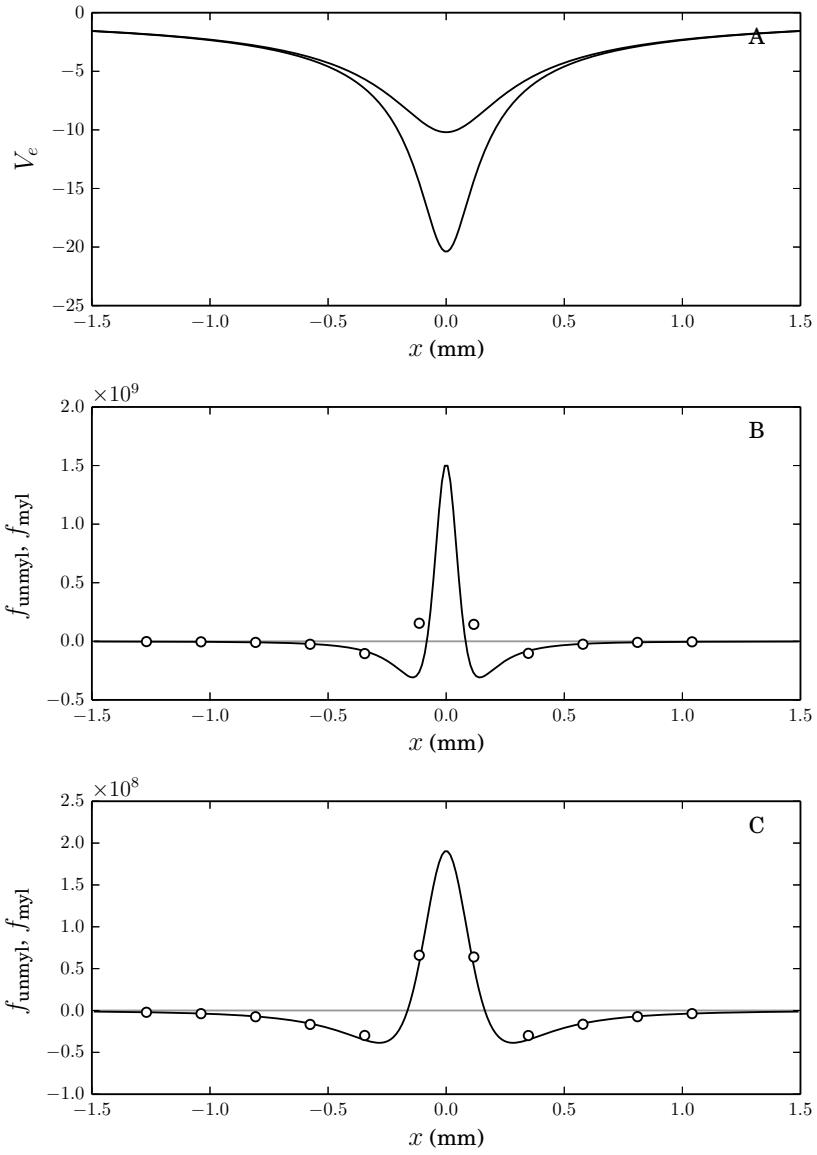

Figure 2.5: The extracellular potential distribution (**plot A**) and activating function (**plots B and C**) of unmyelinated (**solid lines**, **plots B and C**) and myelinated (**open circles**, **plots B and C**) axons stimulated by cathodic current at two different electrode-axon distances (**plot A**, **bottom line**, and **plot B**: 115 µm; **plot A**, **top line**, and **plot C**: 231 µm). In the case of the myelinated axon, the activating function is only defined at the nodes of Ranvier (indicated by the open circles), which are spaced at 231 µm intervals (values for a cat SGC; Imennov and Rubinstein, 2009). In all conditions, the axon lies straight in the extracellular medium, which is assumed to be infinite, isotropic and homogeneous. Moving the axon further from the stimulating electrode widens the region of depolarisation (inferred from where the activating function is positive).

than nodes of Ranvier at locations with lower magnitude (Rattay et al., 2001b). This effect of the soma's large capacitance extends to the nodes close to it (Rattay, 1998, 1999; Rattay et al., 2001b). Rattay (1998) extended the activating function to account for the varying morphology along the neuron's length, giving rise to the generalised definition

$$f_{\text{gen}}(n) = \left[\frac{V_{e,n-1} - V_{e,n}}{R_{n-1}/2 + R_n/2} + \frac{V_{e,n+1} - V_{e,n}}{R_{n+1}/2 + R_n/2} + ... \right] / C_{m,n},$$

where $V_{e,n}$ is the extracellular potential at the n-th compartment and R_n and $C_{m,n}$ are the resistance and capacitance of the membrane of the n-th compartment (i.e., node of Ranvier or soma), respectively. This generalised definition, however, only partially addresses the complexities of the varying membrane capacitance along the neuron. While the generalised activating function at compartment n is normalised by the capacitance of compartment n, it does not take into account the capacitances of neighbouring compartments. This leads to sharp spikes in the activating function near the soma that do not reflect the membrane potentials observed during stimulation (Rattay, 1998, 1999).

To address the limitations of the activating function, Warman et al. (1992) developed the related *total equivalent driving function*, which takes into account the passive electrical properties of the neuron and provides a more accurate estimate of how extracellular stimulation affects the membrane potential at different points along the neuron's length. Warman et al. (1992) proposed that two factors affect the membrane potential of the neuron at a given point: the flow of current through the membrane, and also the flow of current along the axon, representing a redistribution of charge. The latter factor has an increased influence with increasing stimulation duration (Warman et al., 1991, 1992).

The longitudinal currents factored by the total equivalent driving function are a consequence of a non-uniform distribution of charge along the length of the axon, and as such, they do not occur when the membrane is at equipotential, as is assumed to be the case in point-neuron models (such as the HH equations or the resistor-capacitor (RC) circuit model). The redistribution of charge results in membrane currents during and immediately following stimulation (see, for example, McNeal, 1976) that would not occur in space-clamped stimulation. These currents effectively decrease the time constant of the membrane compared to its physiologically-derived value (i.e., as the product of the membrane's resistance and capacitance; Rattay et al., 2012). The effects of the longitudinal currents do, however, decrease as the distance between the

stimulating electrode and the neuron increases (Rattay et al., 2012). Therefore, point-neuron models may still be used to model the electrical properties of the membrane at a particular node of Ranvier, but only with caution and with the assumption of a suitably large electrode-neuron distance. Further, the time constant that best represents the electrical properties of the membrane in a point model may be smaller than the physiologically-derived time constant, and so point-model results should not be used to infer physiological parameters, and vice versa. Nevertheless, many studies have found that point-neuron models are useful in interpreting electrophysiological data in extracellular stimulation (Butikofer and Lawrence, 1978; Dean and Lawrence, 1985).

Modes of excitation

Inwards current depolarises the membrane, causing excitation by driving the membrane potential above the threshold potential. Excitation by this means is referred to as *make excitation* (e.g., see Matthews, 1978), and is either initiated by cathodic current depolarising the axon proximal to the electrode (*cathodic make excitation*), or by anodic current depolarising the axon distal to the electrode (*anodic make excitation*). Excitation may also occur after the cessation of outwards current, which hyperpolarises the membrane. The membrane accommodates to the hyperpolarisation with a reduction in the threshold potential. After the cessation of the stimulus, the recovery of the membrane potential occurs faster than the recovery of the threshold potential, and so, if the membrane was sufficiently hyperpolarised before the stimulus's cessation, then the membrane potential will cross the threshold potential as both recover to their resting values (Hill, 1936a). Excitation by this means is referred to as *break excitation* (e.g., see Matthews, 1978), and requires current levels considerably greater than for make excitation (Ooyama and Wright, 1961).

2.3 Response properties of the auditory nerve fibres

Cochlear implants stimulate the SGCs with trains of discrete current pulses. Each individual pulse has the potential to evoke an action potential, or to interact with temporally neighbouring pulses, either increasing or decreasing their efficacy. This section introduces the *response properties* of individual pulses; that is, how the variables of an individual pulse (amplitude, duration, and so forth) affect the pulse's efficacy in evoking an action potential, and the temporal distribution of the action potential if evoked.

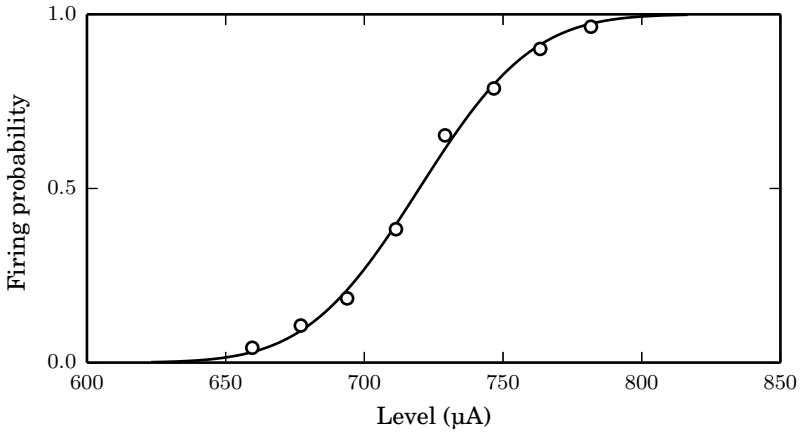

Figure 2.6: The input-output function of a cat SGC (**open circles**; data from Miller et al., 1999b). Also plotted is a Gaussian CDF that has been fitted to the data (**solid line**).

2.3.1 Monophasic stimulation

The simplest current pulse is the *monophasic pulse*, which delivers some amount of charge Q over some duration d by delivering a constant current Q/d over the entirety of its duration.

The input-output function

The input-output function of a neuron relates the level of a stimulus pulse to its *firing efficiency*, the probability of it evoking an action potential in the neuron. It has been found that the input-output functions of nerves (including the SGCs; Dynes, 1996) stimulated by monophasic current pulses are well approximated by the cumulative distribution function (CDF) of the Gaussian distribution (Verveen, 1960, 1961), so that firing efficiency FE is related to current level l by the equation

$$\mathrm{FE}(l) = \Phi\left(\frac{l-m}{s}\right), \tag{2.12}$$

where Φ is the Gaussian CDF and m and s are the mean and standard deviation of the input-output function, respectively. The *threshold level* of a pulse is defined as the current level at which it evokes an action potential with probability 0.5, and is thus given by the parameter m of the Gaussian-fitted input-output function. The *dynamic range* is a measure of the range of current levels that cause an increase in

firing efficiency. It is convenient to quantify the dynamic range as the ratio of the standard deviation and the mean (Verveen, 1961), giving *relative spread (RS)*,

$$\mathrm{RS} = \frac{s}{m}.$$

The input-output function of a cat SGC is plotted in Figure 2.6, using data from Miller et al. (1999b).

The strength-duration function

The threshold level of a monophasic pulse depends on its duration, with greater durations incurring lower thresholds. The strength-duration function relates stimulus duration to threshold level and is often summarised by two measures: rheobase and chronaxie. As the stimulus duration increases, the threshold level reaches an asymptotic value—the rheobase. The stimulus duration that has a threshold level of twice the rheobase is the chronaxie. Measures of the chronaxies and strength-duration functions of cat SGCs were made by van den Honert and Stypulkowski (1984). They found that the threshold level I_{thr}, when measured in amperes, was well predicted by the equation

$$I_{\mathrm{thr}} = \frac{I_{\mathrm{thr}}^{\infty}}{1 - \exp\left(-kd\right)}, \tag{2.13}$$

where d is the pulse duration in seconds, $I_{\mathrm{thr}}^{\infty}$ is the rheobase in amperes, and $\log(2)/k$ is the chronaxie. The mean chronaxie was found to be 247 µs (44 µs standard deviation). Equation 2.13 was first proposed by Lapicque (1907) and has since been found to accurately fit strength-duration data from a wide variety of neurons (e.g., Lapicque, 1907; Hill, 1936b; Dean and Lawrence, 1985; Panizza et al., 1994; Mogyoros et al., 1996). The strength-duration function of a cat SGC, and its fit by (2.13), is plotted in Figure 2.7, using data from van den Honert and Stypulkowski (1984).

The strength-duration function and chronaxie are affected by the longitudinal redistribution of charge that occurs during point stimulation of the axon (see section 2.2.3), with the resulting longitudinal currents tending to decrease the chronaxie (Rattay et al., 2012; Rubinstein and Spelman, 1988; Jack et al., 1975; Cooley and Dodge Jr, 1966; Noble and Stein, 1966). The distance of the stimulating electrode from the neuron thus also affects the chronaxie (i.e., because the longitudinal currents are less pronounced at larger electrode-neuron distances), with smaller electrode-neuron distances resulting in shorter chronaxies (Rattay et al., 2012).

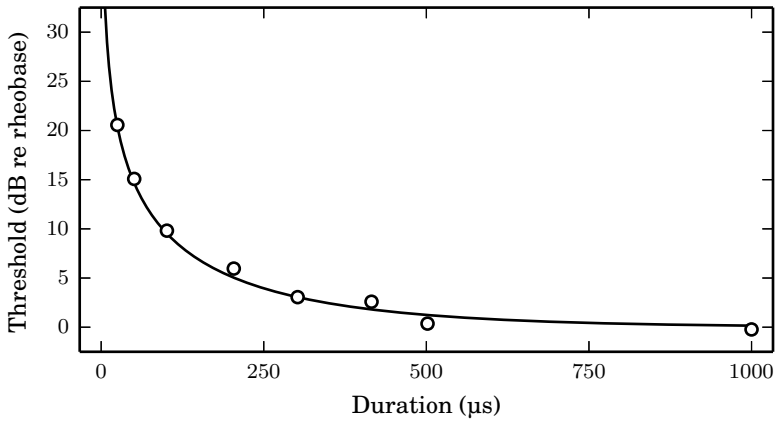

Figure 2.7: The strength-duration function of a cat SGC (**open circles**; data from van den Honert and Stypulkowski, 1984). Also plotted is a line of best fit having the form of equation 2.13 (**solid line**).

Threshold during the refractory period

The delivery of a *suprathreshold pulse* (i.e., a pulse that evokes an action potential) affects how the neuron responds to subsequent pulses. This suprathreshold *interpulse interaction* may be investigated via a *conditioner-probe paradigm*, whereby the neuron is stimulated by a suprathreshold *conditioner pulse*, and then, following a controlled delay, the threshold of a subsequent *probe pulse* is measured (Miller et al., 2001a). After the action potential evoked by the conditioner, the threshold of the probe pulse follows a predictable time-course. For the duration of the absolute refractory period, t_{abs}, the neuron cannot emit another action potential, and so the probe's threshold may considered to be ∞. From time $t = t_{\text{abs}}$ and onwards, the threshold decays back to its resting value. When both the conditioner and the probe are cathodic, the time-course of the probe's threshold I_{thr} (measured in amperes) in cat SGCs has been described by Miller et al. (2001a) by

$$I_{\text{thr}}(t) = \begin{cases} \infty & \text{if } t < t_{\text{abs}} \\ \dfrac{I_{\text{thr}}^{\infty}}{1 - \exp\left(-(t - t_{\text{abs}})/\tau_{\text{thr}}\right)} & \text{otherwise,} \end{cases} \tag{2.14}$$

where t is the time of the probe pulse's delivery relative to the time of the spike evoked by the conditioner, τ_{thr} is a parameter, and I_{thr}^{∞} is the threshold of the probe in the absence of the conditioner. The average duration of the absolute refractory period t_{abs} was found to be 332 µs (97.9 µs standard deviation), and the average time constant

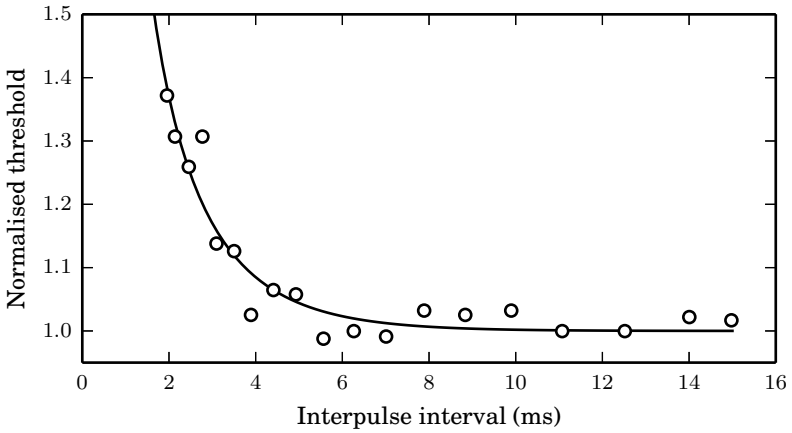

Figure 2.8: Threshold during the refractory period in a SGC of an adult cat (**open circles**; data from Dynes, 1996). A cathodic probe pulse (100 µs duration) was delivered at varying intervals following a supra-threshold cathodic conditioner pulse (100 µs duration). Thresholds are normalised with respect to the resting threshold. Also plotted is the line of best fit having the form of equation 2.14 (**solid line**).

τ_{thr} was found to be 411 µs (226 µs standard deviation). The dependence of threshold on time during the refractory period of a cat SGC, and its fit by (2.14), is plotted in figure 2.8.

Subthreshold stimulation and temporal integration

While the delivery of a suprathreshold pulse affects how the neuron responds to subsequent pulses, so too does the delivery of a *subthreshold pulse* (i.e., a pulse that does not evoke an action potential). The conditioner-probe paradigm may be re-applied to investigate *subthreshold interpulse interactions* by reducing the amplitude of the conditioner pulse to some arbitrary subthreshold level and ignoring any trials wherein a spike is evoked before the delivery of the probe pulse. Under this paradigm, Dynes (1996) found that a cathodic conditioner (100 µs duration) initially reduces the threshold of a cathodic probe (100 µs duration) in cat SGCs by ∼8 dB, but, after the delay between the conditioner and probe increases beyond 0.5 ms, the threshold of the probe becomes *increased*, peaking at ∼0.8 dB above the resting threshold at a delay of ∼2 ms (Figure 2.9). The increase in threshold is presumably due to the threshold potential of the membrane increasing as it accommodates to the depolarisation incurred by the conditioner (see section 2.2.2). In a related study, Cartee et al. (2000) investigated how

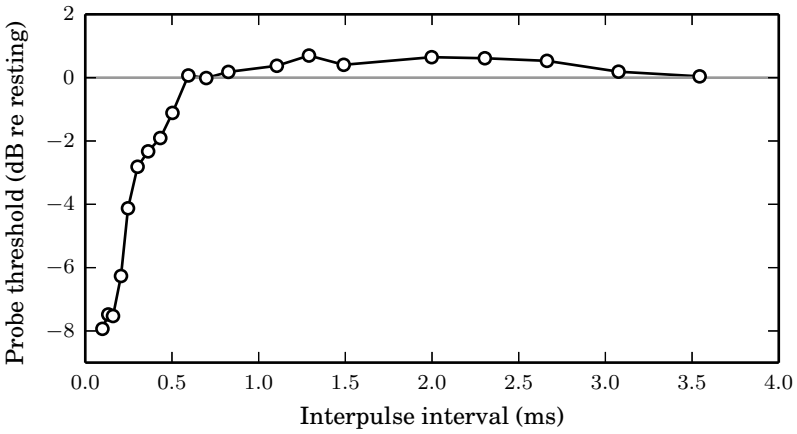

Figure 2.9: Effect of a cathodic subthreshold conditioner (100 µs duration, 2 dB below threshold) on a following cathodic probe's threshold (100 µs) in a cat SGC (empirical data from Dynes, 1996). When the probe immediately follows after the conditioner, its threshold is reduced. However, at delays between ∼0.5 and ∼3.5 ms, the probe's threshold is increased.

the threshold of two consecutively-delivered cathodic pulses depends on their temporal separation. In this study, the threshold level denotes the amplitude that both pulses must take for an action potential to be evoked with 0.5 probability. Their results for a single cat SGC are plotted in figure 2.10. It was found that the threshold levels of cat SGCs were initially halved at no separation, and that they increased with increasing separation. The time-course of the threshold I_{thr} of a given SGC were fit by

$$I_{\text{thr}}(t) = I_{\text{thr}}^{\infty}(1 - \frac{1}{2}\exp(-t/\tau_{\text{sum}})), \tag{2.15}$$

where t is the separation of the pulses in seconds, I_{thr}^{∞} is the threshold of an individual pulse delivered in isolation, and $\tau_{\text{sum}} = 147$ µs is a parameter.

Spike latency

The latency of a SGC's response to a stimulus pulse is defined as the delay between the onset of the pulse and the observation of the action potential by the recording electrode. It is stimulus-dependent and stochastic in nature. The jitter of the response is defined as the standard deviation of the latency. Miller et al. (1999b) recorded the mean latency and jitter of spikes evoked by monophasic stimulation of a cat SGC (Figure 2.11). The stimulus, a cathodic monophasic pulse of 40 µs duration, was delivered at

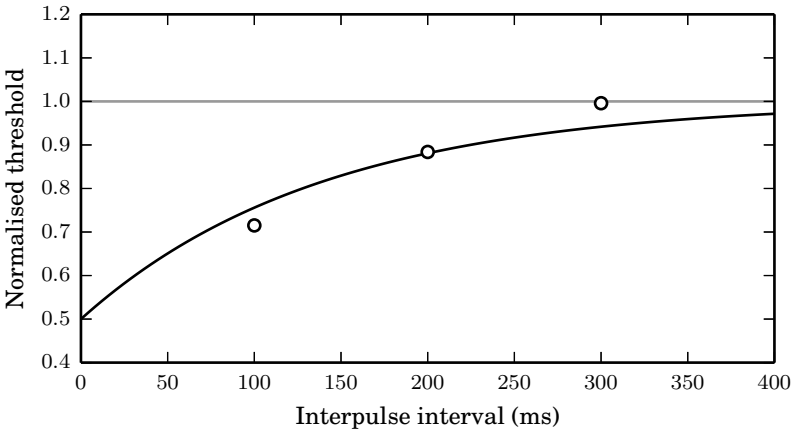

Figure 2.10: Summation thresholds for a single cat SGC (**open circles**; data from Cartee et al., 2000). Also plotted is the line resulting from fitting equation 2.15 to the data (**solid line**).

varying current levels across the dynamic range of the neuron. Both the mean latency and jitter decreased with increasing stimulus level. The mean latency fell from 794 µs, when delivered at a level sufficient to evoke spiking ∼5% of the time, to 356 µs (a reduction of 55%), when delivered at a level sufficient to evoke spiking ∼95% of the time. The jitter fell from 135 µs to 40 µs (across the same range of stimulus levels), a reduction of 70%. Neither the mean latency nor the jitter show signs of having reached their asymptotic minimum values at the highest current level tested, and so increasing current levels beyond the dynamic range presumably continues to drive forward the time of spiking while simultaneously decreasing the spike's temporal variability.

As presently defined, the latency includes not just the time it takes the action potential to be generated, but also the time it takes to be conducted to a more central location. This is the most clinically relevant definition of latency as the action potential must be conducted to the brainstem in cochlear implant recipients. However, it is nevertheless useful to study the latency and jitter under space-clamped conditions (in which the intracellular space is kept at equipotential by shorting it with an uninsulated wire), where only the time for the action potential to be generated contributes to the latency. In space-clamped conditions, both the latency and the jitter values are smaller (Mino et al., 2004), though they are both similarly affected by stimulus current, with greater current levels decreasing both latency and jitter (Rubinstein, 1995;

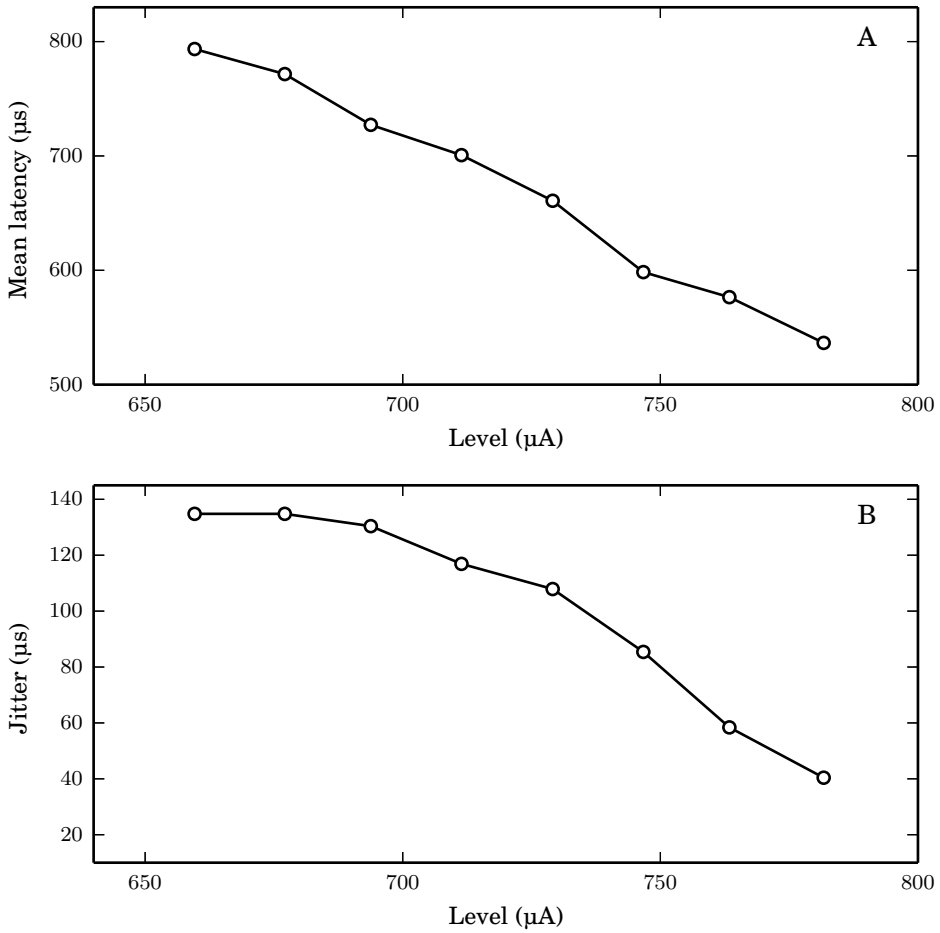

Figure 2.11: The dependency of mean latency (**plot A**) and jitter (**plot B**) on the level of a cathodic pulse (40 µs duration). Increasing the stimulus level decreases both the latency and the temporal variability of the action potential. Data are from a single cat SGC (Miller et al., 1999b).

Mino et al., 2002)[5]. The temporal distribution of spiking in space-clamped conditions resembles a slightly skewed Gamma distribution (e.g., see distributions in Rubinstein, 1995; van den Honert and Stypulkowski, 1987). The temporal distribution from in-vivo preparations have similar shapes in some units (e.g., see Javel and Shepherd, 2000), while other units show bimodal distributions due to the site of action potential initiation alternating between pre- and post-somatic locations (Miller et al., 1999b; Woo et al., 2010; Rattay et al., 2001b; Javel and Shepherd, 2000).

Pulse polarity in monophasic stimulation

Both cathodic and anodic monophasic pulses are able to evoke spiking in the SGCs under monopolar electrode configurations (Miller et al., 1998; Undurraga et al., 2013). Surprisingly, however, cathodic pulses do not necessarily have lower thresholds. The cathodic/anodic threshold ratio varies with species, subject, electrode configuration, and pulse duration (Hanekom, 2001; Reilly et al., 1985; Rattay et al., 2001a; Miller et al., 1998; Rubinstein, 1993). In general, cathodic pulses have lower threshold in cats (Miller et al., 1998), whereas anodic pulses have lower thresholds in humans (Macherey et al., 2008; Undurraga et al., 2013) and guinea pigs (Miller et al., 1998). Various studies have sought to explain the cause of this discrepancy between species (Undurraga et al., 2013; Bahmer and Baumann, 2013; Potrusil et al., 2012; Rattay et al., 2001a). Rattay et al. (2001b,a) has been able to reproduce the polarity preferences of cat and man in a computer model by taking into account the differences between species in myelination and nodal/somatic location; it was found that degeneration of the peripheral processes that occurs in humans plays a role for the human preference of anodic stimulation. This study also predicts that, regardless of polarity, monophasic pulses of clinically-relevant durations (i.e., short durations up to $\sim$100 µs) evoke spiking in the SGCs by means of *make* excitation (i.e., either cathodic make or anodic make), and not *break* excitation (inferred from Rattay et al., 2001a, as excitation occurs during, not after, stimulation).

2.3.2 Biphasic stimulation

A biphasic pulse is comprised from two opposite-polarity monophasic pulses of a given *phase duration* that are separated in time by a delay, the *interphase gap (IPG)*. The *phase order* (or *polarity order*) of a biphasic pulse refers to the order in which its

[5]Both the cited studies used computer models of space-clamped conditions; I was unable to find any suitable studies that used in-vivo preparations.

opposite-polarity phases are delivered. A pulse in which the leading phase is cathodic is referred to as a cathodic-leading biphasic pulse (CL-BP), and a pulse in which the leading phase is anodic is referred to as an *anodic-leading biphasic pulse (AL-BP)*. A pulse is *charge balanced* if its phase cancel one another so that the total charge delivered by the pulse is zero. Cochlear implants use trains of charge-balanced pulses (with biphasic pulses being used most commonly) to avoid delivering a net flow of current, which would result in harmful chemical reactions occurring at the surfaces of the electrodes (Brummer and Turner, 1977). Other than where explicitly described, all the biphasic pulses considered in this thesis are charge balanced.

It is common to compare the response properties of a biphasic pulse against those of an *equivalent monophasic pulse*; that is, a monophasic pulse that has a duration equal to the individual phases of the given biphasic pulse. In this thesis, the equivalent monophasic pulse is always assumed to be cathodic, regardless of the polarity order of the biphasic pulse.

Threshold and relative spread

The threshold of a biphasic pulse is higher than that of an equivalent monophasic pulse (Gorman and Mortimer, 1983; Miller et al., 2001b; Shepherd and Javel, 1999; van den Honert and Mortimer, 1979). The RS of a CL-BP[6] is similar (mean biphasic RS=0.0405; mean monophasic RS=0.0480, n=22), though slightly less ($t(21) = 2.41$, $p = 0.025$; paired-comparison t-test), to that of a monophasic pulse (Miller et al., 2001b).

Effect of phase duration

The strength-duration function of a biphasic pulse relates threshold to phase duration. It has been theorised by Reilly et al. (1985) that the biphasic strength-duration function shall approximate the monophasic strength-duration function at large durations (relative to the membrane time constant), and that at short durations, biphasic thresholds shall be higher due to the loss in efficiency incurred by charge reversal. Using a biophysically-detailed computer model, they predicted that a cathodic-leading biphasic shall be most efficient at evoking excitation at 100 µs/phase, theorising that longer durations will be inefficient due to the leaky properties of the membrane, and

[6]To the best of my knowledge, no published studies have compared the RSs of an AL-BPs to that of a monophasic pulse. Various studies (e.g., Shepherd and Javel, 1999; Shepherd et al., 2001; Javel et al., 1987; Javel and Shepherd, 2000) have reported the RS of biphasic pulses of both polarity orders when delivered by bipolar electrodes, but bipolar stimulation incurs confounding effects that are beyond the scope of this thesis.

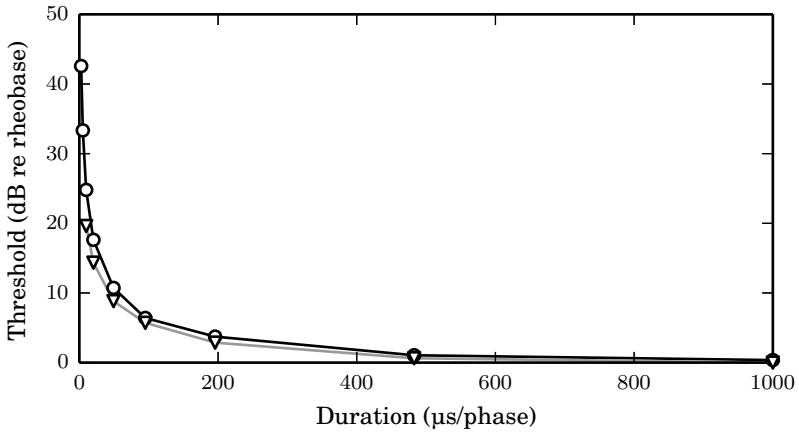

Figure 2.12: Comparison of monophasic (**open triangles**) and biphasic (cathodic-phase leading; **open circles**) strength-duration functions, both obtained from a biophysically-detailed computational model by Reilly et al. (1985). At long durations, the biphasic strength-duration function approximates its monophasic counterpart. At short durations (relative to the membrane time constant), the biphasic function is elevated.

shorter durations will be inefficient due to the reversal of charge. These predictions were consistent with data obtained from the SGC of a squirrel monkey by Parkins and Colombo (1987), who found that biphasic stimulation to be most efficient at 100 µs/phase. Figure 2.12 compares the monophasic and biphasic strength-duration functions obtained by Reilly et al. (1985). Psychophysical results[7] suggest that the dependence of threshold on phase duration is similar, regardless of phase order (Coste and Pfingst, 1996).

Effect of interphase gap

The elevation in the threshold of a biphasic pulse relative to that of a monophasic pulse may be reduced by increasing the IPG of the biphasic pulse (Butikofer and Lawrence, 1978; van den Honert and Mortimer, 1979; Gorman and Mortimer, 1983; Shepherd and Javel, 1999; McKay and Henshall, 2003; Carlyon et al., 2005; Prado-

[7]To the best of my knowledge, there has been no published study that compares the strength-duration functions of cathodic-leading and anodic-leading biphasic pulses delivered via a monopolar electrode. This is despite the large number of studies investigating biphasic strength-duration functions (e.g., Smith and Finley, 1997; Miller et al., 1999a; Moon et al., 1993; Abbas and Brown, 1991; Shepherd et al., 2001; Pfingst et al., 1991; Coste and Pfingst, 1996), all of which either use bipolar electrode configurations, or do not investigate the effect of phase order, either only investigating the strength-duration function when the anodic phase leads (as reported in the main text), or compounding together the results of both phase orders.

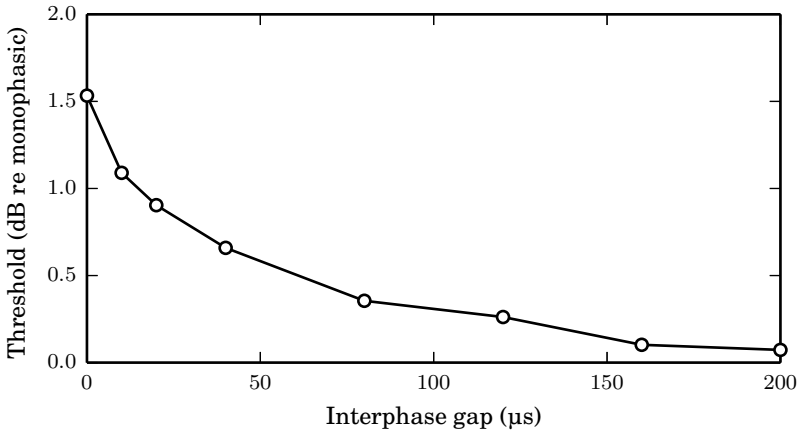

Figure 2.13: The dependence of threshold on IPG in cathodic-leading biphasic stimulation (100 µs/phase) of a single cat SGC. Increasing the IPG decreases the threshold, with the threshold reaching a steady state after an IPG of ∼200 µs. Data taken from Shepherd and Javel (1999).

Guitierrez et al., 2006; Cappaert et al., 2013; Ramekers et al., 2014; Weitz et al., 2011, 2014), as shown in Figure 2.13. As the IPG is increased beyond ∼100 to ∼200 µs, the threshold becomes approximately equal to the (cathodic) monophasic threshold. The effect of the IPG on the threshold is empirically similar, regardless of which order the opposite-polarity phases of the pulse are delivered (Shepherd and Javel, 1999).

Effect of phase order

Whether the phase order of a biphasic pulse affects how it excites the neuron has been investigated in a number of studies (e.g., Coste and Pfingst, 1996; Miller et al., 1997; Shepherd and Javel, 1999; Game et al., 1989; Ramekers et al., 2014). In most studies of extracellular stimulation, the phase order has been found to have only a small (<∼2 dB) to negligible effect on the threshold of a biphasic pulse (Girvin et al., 1982; Coste and Pfingst, 1996; Shepherd and Javel, 1999), especially at longer phase durations (Colombo and Parkins, 1987). In order to ascertain which phase is responsible for excitation, the timing of the action potential has been correlated to the timing of each phase's delivery. Shepherd and Javel (1999) stimulated the SGCs of deafened cats with AL-BPs and found that the latencies of the evoked action potentials were affected by IPG, with increases in IPG corresponding to approximately equal increases in latency. The correlation in the time of trailing-phase delivery and evoked

spiking was hypothesised to imply that the trailing (cathodic) phase was responsible for evoking the spikes. Ramekers et al. (2014) applied a similar methodology to deafened guinea pigs using CL-BPs. In this study, IPG was found to have negligible effect on the time of spiking (as measured by the latency of the electrically-evoked compound action potential (ECAP)). It was therefore hypothesised that the leading, temporally-stationary cathodic phase was responsible for evoking spiking. From these studies (and others, e.g., Grumet, 1999; Game et al., 1989; Hartmann et al., 1984), it would appear that the cathodic phase is responsible for evoking spiking in biphasic stimulation, regardless of the phase order. However, the polarity of the evoking phase has been found to change due to hearing status (i.e., deafened/undeafened), presumably due to a change in the site of action potential initiation (Ramekers et al., 2014).

Effects of cathodic-phase amplitude (cathodic-leading stimulation)

When the cathodic phase leads in a biphasic pulse, increasing its amplitude increases the likeliness of the pulse exciting the membrane. This increased excitability may be countered by increasing the amplitude of the opposing, anodic phase. This has been quantified by van den Honert and Mortimer (1979), who measured for various *cathodic levels*, the anodic level (or *anodic threshold*) required to reduce to 0.5 the probability of a CL-BP evoking excitation. Their results, reproduced in Figure 2.14, show that linear increases in cathodic level require exponential increases in anodic level to maintain the 0.5 firing probability of the stimulus.

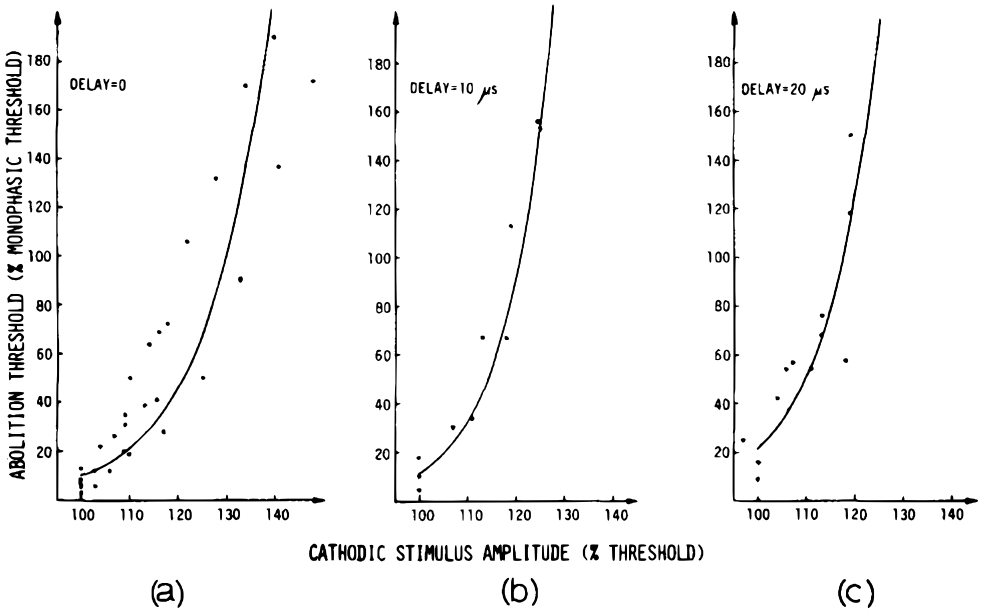

Figure 2.14: Plots showing the relationship between *abolition threshold* and *cathodic level* under cathodic-leading biphasic stimulation of isolated nodes of Ranvier from the Xenopus Laevis sciatic nerve at various IPGs. In all cases, a 50 µs/phase duration was used. The ordinate and abscissa magnitudes are given in percentages of the threshold of a 50 µs cathodic monophasic pulse. *A linear increase in the amplitude of the leading, cathodic phase of a CL-BP requires an exponential increase in the amplitude of the trailing, anodic phase in order to maintain threshold level.* Figure reproduced from van den Honert and Mortimer (1979) with permission from the publisher.

2.4 Phenomenological models of electrical stimulation

Phenomenological models aim to have a reduced parameter-space and computational demand compared to biophysical models while simultaneously reproducing the response properties of the neuron. Many methodologies have been applied in an effort to achieve this. One approach that is common in a large number of these is to model a single patch of membrane (or a single node of Ranvier) instead of modelling the entire neuron. Such a model, referred to as a *point-neuron model*, is implicitly grounded on the assumption that a single node is responsible for the initiation of all action potentials. It has already been shown when discussing the activating function that the driving force of electrical stimulation is greatest (under simplifying conditions) at the node closest to the electrode, and so the assumption has some degree of biophysical grounding and eliminates the need for morphological parameters while reducing computational demand by limiting the scope of the simulation. Another common approach is to assume that the membrane is passive until a discrete moment of spiking, allowing the non-linear equations of, e.g., the HH model to be replaced with the much simpler equations of the passive membrane. This approach essentially defines the *leaky integrate-and-fire (LIF) neuron*, discussed next, which has long provided a de facto standard against which other phenomenological models are compared.

2.4.1 The leaky integrate-and-fire neuron

The LIF neuron, first introduced by Lapicque (1907), has a single dimension, the time-variant membrane potential V, which is related to a stimulus signal I by the linear differential equation

$$\tau \frac{\mathrm{d}V}{\mathrm{d}t} = RI(t) - V_\infty - V, \tag{2.16}$$

where τ, R, and V_∞ are parameters. The model *spikes* when the membrane potential crosses a threshold potential θ from below, an event that will subsequently be referred to as *threshold crossing*. Following spiking, the membrane potential is reset to some predefined value, V_{reset}, and the process continues.

The equation governing V in the LIF neuron is equal to (2.9), which describes the time-course of the membrane potential in the passive neuron. The LIF neuron is therefore implicitly assuming that the neural membrane is passive until a discrete moment of spiking. The five parameters (τ, R, V_∞, θ, and V_{reset}) of the LIF neuron may be reduced to only three (τ, θ, and V_{reset}) without loss of generality by arbitrarily

setting R to 1 Ω and V_∞ to 0 V. It is common to add a noise signal to the stimulus signal I so as to reproduce the stochastic properties of the neuron (see, e.g., Plesser and Gerstner, 2000).

The LIF neuron has been used extensively to model how the SGCs respond to electrical stimulation by cochlear implants (see, e.g., Stocks et al., 2002; Chen and Zhang, 2006, 2007; Fredelake and Hohmann, 2012; Hamacher, 2004; Macherey et al., 2007). Despite its simplicity, it is able to reproduce both the input-output and strength-duration functions of arbitrary neurons (details given in next chapter). As such, it provides a convenient framework upon which to ground more complex models.

2.4.2 The spike response model

The LIF neuron is commonly extended so as to reproduce the refractoriness that follows spiking. One such extension is the *spike response model (SRM)*, first introduced by Gerstner (1991, 1995) and Gerstner and van Hemmen (1992). Like the LIF neuron, the SRM has a variable representing the time-course of the membrane potential, defined as

$$V_{\kappa\eta}(t; S, I) = \int_0^t \eta(s)S(t-s)\,\mathrm{d}s + \int_0^t \kappa(s)I(t-s)\,\mathrm{d}s + V_\infty,$$

where S is the train of previous spikes (defined as $S(t) = \sum_s \delta(t-s)$, where each s is a time of previous spiking and δ is the Dirac delta function), I is the stimulus current signal, and κ and η are parameters; κ is a kernel function that represents the response of the membrane to instantaneous stimulation, and η is a kernel function that represents the shape of the action potential. Like the LIF neuron, spiking occurs in the SRM model when the membrane potential exceeds a threshold potential θ. However, in the SRM model, the threshold potential is time-variant, depending on spiking history, with

$$\theta_\vartheta(t; S) = \theta_0 + \int_0^t \vartheta(s)S(t-s)\,\mathrm{d}s,$$

where ϑ is a kernel function that describes how spiking affects threshold. Refractoriness is implemented by selecting ϑ so as to increase the threshold after spiking. Adaptation may occur due to the cumulative effects of ϑ on the threshold after a series of spikes.

The LIF neuron is a special case of the SRM, with

$$\eta(s) = V_{\text{reset}} \exp(-s/\tau) H(s)$$
$$\vartheta(s) = 0$$
$$\kappa(s) = \frac{1}{C} \exp(-s/\tau),$$

where H is the Heaviside step function (defined as $H(s) = 1$ if $s > 0$, and otherwise $H(s) = 0$), and C and τ are equal to their definitions in the LIF neuron (Kistler et al., 1997). Parametrisations that outperform the LIF neuron may be found via numerical optimisation, requiring only a current signal I and corresponding spike train S as input (Kistler et al., 1997; Jolivet et al., 2006).

2.4.3 Generalised linear models

The SRM improves the LIF neuron by the allowing adaptive and refractory properties of the neuron to be reproduced. However, like the LIF neuron, it is a deterministic model and does not reproduce the stochasticity of the real neuron. To introduce stochasticity to the SRM, it is useful to turn to the statistical framework of *generalised linear models*. In a generalised linear model (GLM), a response variable is fitted by an arbitrary *link function* applied to a linear combination of a set of predictor variables (Nelder and Wedderburn, 1972). Expressing a model as a GLM is useful because standardised mechanisms have been developed by which to fit a GLM to a given set of data by means of maximum likelihood estimation (Nelder and Wedderburn, 1972; McCullagh and Nelder, 1989). For this reason, GLMs have found much popularity in the context of phenomenological modelling of neurons (e.g., Truccolo et al., 2005; Gerstner et al., 2014; Naud and Gerstner, 2012; Koyama and Kass, 2008; Koyama et al., 2010; Paninski et al., 2004; Mensi et al., 2011; Gerwinn et al., 2010; Goldwyn et al., 2012; Jolivet et al., 2004).

A GLM is characterised by its *conditional intensity function*, $\lambda(t|S, I)$, which relates to the instantaneous probability of the model spiking given the stimulus signal I and spiking history S. The instantaneous intensity function of a GLM must be defined in terms of the link function applied to a linear combination of discrete samples of I and S. For instance, to formulate the SRM as a GLM, we define the conditional intensity function as

$$\lambda_{\kappa\eta\vartheta}(t; S, I) = f(V_{\kappa\eta}(t|S, I) - \theta_{\vartheta}(t; S)),$$

noting that the link function f may be non-linear and that both $V_{\kappa\eta}$ and θ_ϑ are linear functions with respect to I and S, which are both discretised so as to produce a finite parameter-space. The link function determines the stochastic nature of the threshold. It has been found that using $f(u) = \alpha \exp(\beta u)$, where α and β are parameters, provides a good fit to neural data (Paninski et al., 2004; Gerstner et al., 2014).

The model is readily fitted to the training data $\{S, I\}$ (where S in this case is the spike train response of a target neuron to the stimulus signal I, rather than the previous spiking of the GLM) by choosing kernels κ, η, and θ so as to maximise

$$\log L_{\kappa\eta\vartheta}(\{S, I\}) = -\int_0^T \lambda_{\kappa\eta\vartheta}(s|S, I)\, ds + \sum_{i=1}^{n} \log \lambda_{\kappa\eta\vartheta}(t_i|S, I),$$

where $t_{1..n}$ are the times of the spikes in S and $[0, T]$ is the interval over which the target neuron's spiking activity was observed. The function $L_{\kappa\eta\vartheta}$ is the model's *likelihood function*; it describes the probability of observing the spike train S in response to the stimulus I given the parameters $\{\kappa, \eta, \vartheta\}$. Providing that the link function satisfies some convexity constraints, convergence to an optimal parametrisation is ensured when using the method of maximum likelihood (Paninski et al., 2004).

Unfortunately, not all spiking models may be formulated in the framework of GLMs. The adaptive exponential integrate-and-fire neuron, for instance, has non-linear membrane dynamics, and so the conditional intensity function cannot be represented as a linear combination of predictor variables. However, the model can nevertheless be well-approximated by a GLM (Mensi et al., 2011). In some specific cases where a model cannot be formulated as a GLM, it may instead be formulated as a *generalised additive model (GAM)*. GAMs are related to GLMs, but allow the predictor variables to be individually transformed by a non-linear function, providing the function satisfies various smoothness constraints. As with GLMs, standard numerical methods exist for optimising the parameters of a GAM (Hastie and Tibshirani, 1987, 1990). GAMs have been applied to spiking models by Koyama et al. (2010).

2.4.4 Point process models

A *point process model* is a stochastic model that is entirely defined by a conditional intensity function (Daley and Vere-Jones, 2003). The GLM discussed previously is, in fact, just a point process model with constraints placed on its conditional intensity function. In a point process model, the probability that the model will spike in the interval $[t,\, t + \Delta_t]$, $\Delta_t \to 0$, may be expressed in terms of its conditional intensity

function $\lambda(t|S,I)$ as $\Delta_t\lambda(t|S,I)$. The probability that the model will emit a spike in the arbitrary interval $[t_1,t_2]$ is given by its lifetime distribution function

$$L(t_1,t_2|S,I) = 1 - \exp(-\Lambda(t_1,t_2|S,I)),$$

where Λ is the integrated intensity function,

$$\Lambda(t_1,t_2|S,I) = \int_{t_1}^{t_2} \lambda(s|S,I)\mathrm{d}s.$$

These three functions, the conditional intensity function, the lifetime distribution function, and the integrated intensity function, may be used to analyse the response properties of a point process model. Goldwyn et al. (2012) have shown that it is possible to define the conditional intensity function in such a way that the parameters of the model conveniently cancel when analysing particular response properties, leaving only a single free parameter that directly controls the given property. This elegant formulation forgoes the need for the numerical techniques of the GLMs, as the parameters of the model may be derived analytically from the response properties that should be reproduced.

The conditional intensity function of Goldwyn's model is defined as

$$\lambda(t|S,I) = [J * f(\kappa_S^+ * I^+ + \kappa_S^- * I^-)](t),$$

where I^+ is I when I is positive and 0 otherwise, I^- is I when I is negative and 0 otherwise, J is a constant kernel function, and f, κ^+, and κ^- are kernel functions that non-linearly depend on the time of the most recent spike. Both κ^+ and κ^- are exponential decays of equal time constants, but κ^- may be scaled so as to vary the contribution of the negative charge delivered by the stimulus. The expression $\kappa_S^+ * I^+ + \kappa_S^- * I^-$ may be interpreted as a membrane potential. The non-linear function f transforms the membrane potential to a time-varying spiking rate and is defined as $f(x) = x^\alpha$ if $x > 0$ and 0 otherwise, where α is a parameter. The kernel function J is an exponential decay of parametrisable time constant that temporally smears the intensity function without changing its integral (i.e., so that the total probability of spiking over all time is unaffected by convolution with J); it thereby acts to introduce temporal stochasticity to spiking without affecting the non-temporal response properties of the model.

While Goldwyn's model is related to previous point process models of spiking

activity (e.g., Miller and Mark, 1992; Litvak et al., 2003b; Plourde et al., 2011; Truccolo et al., 2005), it differs in how it is parametrised. Goldwyn's model may be uniquely parametrised to reproduce a given jitter, threshold, RS, chronaxie, and summation time constant (the latter of which relates how a threshold of a pulse is affected by a preceding pulse; Cartee et al., 2006). Further, the model may be parametrised to reproduce how the threshold and relative spread change following spiking. Given that the model may be parametrised to reproduce such a rich set of response properties, it is remarkable that each parameter may be fitted either analytically or via numerical optimisation in a single dimension.

2.4.5 Models of extracellular stimulation

The models discussed above have not included any parameters describing the morphology of the neuron or the interactions between consecutive nodes of Ranvier. This is despite both having the potential to affect how the neuron responds to stimulation (see section 2.2.3). The limitations of not including such parameters may depend on the distance of the stimulating electrode from the neuron being modelled (i.e., the *electrode-neuron distance*). It has been found that at large electrode-neuron distances, the strength-duration function of a biophysical multi-compartment model is well approximated by that of the LIF neuron, but that this breaks down at smaller electrode-neuron distances (Reilly et al., 1985). In an effort to avoid the need for a full multi-compartment model in order to predict the time-course of the membrane potential, Robert (2006) proposed a modified single compartment model that approximates the neighbouring compartments by voltage sources. The driving forces of the neighbouring compartments are approximated as a fraction of the intracellular potential of the modelled compartment. This fraction is a model parameter, empirically derived from the steady state solution of a multi-compartment model, and does not change throughout the simulation. Robert found that using this first-order approximation of the effects of neighbouring compartments resulted in better predictions than simply reducing the number of compartments in a multi-compartment model. Other investigators have taken different approaches in solving the same problem. McNeal (1976) proposed the use of a morphologically-detailed model of the axon, but limits the computationally-expensive non-linear descriptions of the membrane dynamics to the single node closest to the stimulating electrode, with the dynamics of all other nodes being approximated by more tractable linear equations. Plonsey and Barr (Plonsey and Barr, 1995,2000; Barr and Plonsey, 1995) found that the entire axon may be

considered passive (i.e., approximated with linear equations) for much of the duration ($\sim 0.2\,\tau$, where τ is the membrane time constant) of a stimulus without adversely affecting the time-course of the membrane potential along the axon's length. Their model allows for the possibility of selectively employing the more computationally-demanding non-linear equations only when it is known that they are needed, and otherwise employing the much less demanding linear equations.

Chapter 3

Qualitative descriptions of excitation by pulsatile stimulation

The novel phenomenological model that will be presented in Chapter 5 was designed to reproduce how the threshold of a cathodic pulse is increased by the addition of a trailing anodic pulse. This chapter analyses excitation under various pulse shapes, providing a biophysical basis on which to interpret the phenomenological model. Excitation is analysed from the point of view of a reduced variant of the Hodgkin-Huxley (HH) model by means of *phase plane analysis* (described later; for more details, see, e.g., Izhikevich, 2007). The choice of the HH model was motivated by its simplicity and its well-accepted track record in reproducing how spiral ganglion cells (SGCs) respond to electrical stimulation (see section 2.1.5).

3.1 Background

3.1.1 The time-scaled Hodgkin-Huxley model

The parameters of the HH model that were given in table 2.1 were fitted to data from a squid giant axon stimulated at room temperature. This preparation has slower dynamics than a SGC stimulated in vivo, and so the parameters of the model must be *temperature adjusted*. This is generally done by applying a constant coefficient k to the right hand side of (2.1) (Sterratt et al., 2011), with $k = 12$ having been used

to reproduce data from mammalian SGCs stimulated in vivo (Rattay et al., 2001b). However, while this parametrisation produced realistic thresholds and latencies for monophasic and biphasic stimulation, it produced an unrealistic chronaxie of 752 µs, which is considerably larger than the 247 µs (44 µs standard deviation) that is typical of a SGC (van den Honert and Stypulkowski, 1984). To address this, a time-scaling methodology was used instead, where a constant coefficient $k = 1/9.05$ was applied to the left hand side of (2.4), producing realistic thresholds and latencies under monophasic and biphasic stimulation, as well as a realistic chronaxie of 195 µs. The practice of scaling time to make a biophysical model behave like a SGC has previously been published by O'Gorman et al. (2009, 2013).

3.1.2 The reduced HH model

The HH model is a system of ordinary differential equations (ODEs). The system has four dimensions, corresponding to the variables V, m, h, and n. The state of the system at any point in time is therefore given by the values of these four variables. During the initiation of an action potential, the variables V and m change rapidly with time, while the variables h and n do not change appreciably until after the action potential has developed to such an extent that it cannot possibly be averted. Thus, during an action potential's formation, the h and n variables may be held fixed without affecting the model's dynamics. Reformulating the HH model with h and n held at their resting values results in the (V, m)-*reduced HH model* (henceforth referred to as the *reduced HH model*). This model has only two dimensions, compared to the four of the HH model, yet will respond similarly to a brief stimulus, up until the point at which the action potential becomes well developed (i.e., after which excitation is inevitable). The reduced HH model was pioneered by Fitzhugh (1960, 1961) as a method of understanding the processes behind excitation in the neuron.

3.1.3 Phase plane analysis

The state of the reduced HH model at any moment in time may be represented as a point (the *phase point*) in a two-dimensional space (the *phase plane*). In the absence of externally applied current, the phase point of the model will follow a trajectory (the *phase path*) determined by its governing system of ODEs. Externally applied currents affect the phase path by acting on the V dimension, as determined by equation (2.4).

Associated with each variable of the model is a *nullcline*. The x-nullcline is a manifold containing all the points that satisfy the equation $\frac{\mathrm{d}x}{\mathrm{d}t} = 0$. The nullclines

intersect at points of equilibrium, or *nodes*. The V and m nullclines of the reduced HH model intersect to give three nodes: the resting node, the saddle node, and the excited node. The resting and excited nodes are stable, which is to say that the phase point is attracted to them while in their vicinity. The saddle node is unstable, which is to say that the phase point is repelled from it. The resting and excited nodes have associated with them stable manifolds. The *stable manifold* of a node is a set of points that will converge in forward time to it. The saddle node has not only a stable manifold, but also an *unstable manifold*, which is a set of points that will converge in negative time to it.

A *separatrix*, defined as the stable manifold of the saddle node, divides the phase plane of the reduced HH model into two domains, the *subthreshold domain*, which contains the resting node, and the *subthreshold domain*, which contains the excited node. In the absence of externally applied current, the phase point will converge to the stable node of its containing domain, and thus, the firing outcome of a stimulus may be predicted on the basis of which domain contains the phase point at the moment of the stimulus's cessation. Regardless of which node (resting or excited) the phase point converges to, it will approach it via the node's stable manifold. The stable manifolds of the resting and excited nodes thus help us understand the dynamics of the system, as all phase paths will eventually converge upon them during their trajectory towards equilibrium.

The phase plane of the reduced HH model is shown in figures 3.1A and 3.1B. In both figures, a solid black line denotes the stable manifolds of the resting and excited nodes, a bold dashed line denotes the separatrix, dotted lines the V and m manifolds, and filled circles denote the resting (**a**), saddle (**b**), and excited nodes (**c**). Figure 3.1B shows the detail of the phase plane around the separatrix. Example phase trajectories are plotted (grey lines) to show the dynamics of the system in the absence of externally-applied current.

All the phase paths that approach the resting node **a** of the reduced HH model via the proximity of the saddle node **b** pass through a region enclosed by the V and m nullclines. Once the phase point enters this region, or *well*, it cannot escape, other than by external application of current. The well of the reduced HH model is very narrow, and so the phase point, once in the well, is never far from the V and m nullclines. While the phase point is close (in the x dimension) to the x-nullcline, its dynamics are slow in the x dimension. Thus, once the phase point enters the narrow well of the reduced HH model, its dynamics shall tend to be slow compared to prior

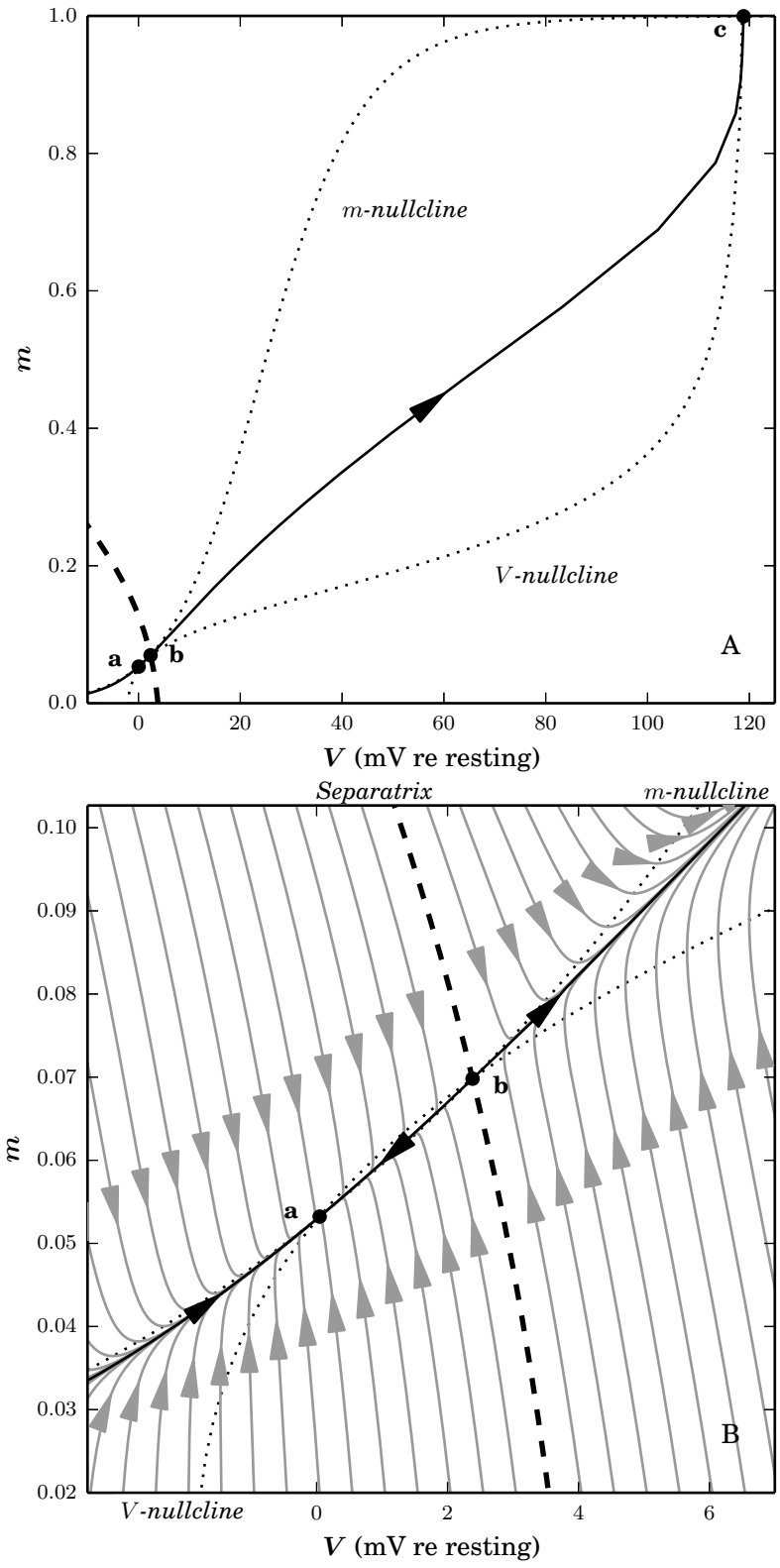

Figure 3.1: The phase plane of the (V, m)-reduced HH model (h and n held at resting values). **Plot A** shows the resting (**a**) and excited (**c**) nodes; **plot B** shows the detail at the bifurcation. The separatrix (**bold dashed line**) divides the phase plane into subthreshold (containing point **a**) and suprathreshold (containing point **c**) domains. Note that the nodes (points of equilibrium, **filled circles**) are located at the points the nullclines (**dotted lines**) intersect, and that all example phase paths (**grey lines**) are repelled by the separatrix as they approach the saddle node (**b**), converging upon a stable node via its stable manifold (**solid black line**).

of entering.

3.1.4 Short duration current pulses

A current pulse may be quantified by its duration and charge. Because the membrane is leaky, increasing the duration of a pulse reduces its efficacy in depolarising the membrane, and so to achieve the same depolarisation, a long-duration pulse must deliver more charge. This may be seen by plotting the charge-duration function, which relates the duration of a pulse to the amount of charge that it must deliver in order to just cause excitation (i.e., the *threshold charge*). Figure 3.2 (black line) plots the charge-duration curve of the reduced HH model. While the duration is small in relation to the time-constant τ of the model ($\tau = RC = 162$ µs, where R is the resting membrane resistance, see 2.2.1), there is no appreciable change in threshold charge. At durations above $\sim \tau$, the threshold charge increases with increasing duration. For comparison, the charge-duration curves of the full HH equations (grey line), the leaky integrate-and-fire (LIF) neuron (grey dashed line), and a perfect-integrator neuron (i.e., the LIF neuron with an infinite time-constant; black dashed line) are also plotted; these curves will be further commented on in Section 3.3.1.

Because the threshold charge does not depend on the duration of the pulse at the short durations that are relevant to cochlear implants, a current pulse may be well-approximated by an instantaneous injection of charge. Such an approximation has a simplifying effect on the qualitative analysis of excitation, as an instantaneous current pulse manifests as a horizontal displacement in the (V, m) phase-plane, with the magnitude of the displacement dependent only on the charge delivered by the pulse, and not the location of the phase point at the time of the pulse's delivery. Therefore, throughout the reminder of this chapter (and, when convenient, throughout the remainder of this thesis), monophasic pulses have been approximated by instantaneous injections of charge, and biphasic pulses have been approximated by two instantaneous injections of opposite-polarity charge, separated in time by a delay that represents the interphase gap (IPG).

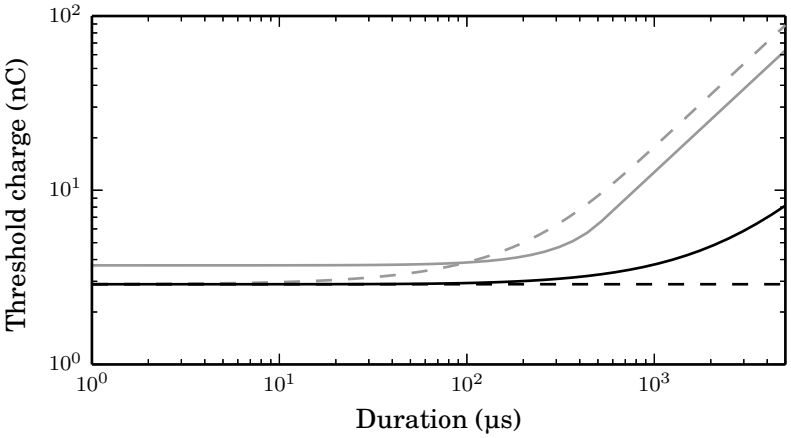

Figure 3.2: Charge-duration functions of the reduced HH model (**black line**), the HH model (**grey line**), the LIF neuron (parametrised to have the same threshold charge at instantaneous durations as the reduced HH model; **grey dashed line**), and the perfect-integrator neuron (i.e., the LIF neuron with an infinite time-constant; **black dashed line**). The LIF neuron has been parametrised to have the same time-constant $\tau = 162$ µs as the reduced and full HH models (their time constants taken as $\tau = RC$, where R is their membrane resistances at rest). In all models, the threshold-charge (i.e., the minimum amount of charge needed for a cathodic pulse of the given duration to evoke excitation) does not depend on duration when the duration is small relative to the time-constant τ. At durations around and above τ, increasing the duration increases the threshold charge in all models other than in the perfect integrator neuron (for which $\tau = \infty$). In the perfect integrator neuron, the threshold charge is constant throughout all durations. *At short durations relative to the membrane time-constant τ, a pulse of given charge may be approximated by an instantaneous injection of equal charge.*

3.2 Phase plane portraits of excitation

3.2.1 Excitation by a cathodic pulse

A cathodic pulse provides the most direct way to excite the membrane. The delivery of a cathodic pulse drives the phase point to higher values in the V dimension of the reduced HH model. If the pulse is delivered at a level above threshold, then the phase point will be driven across the separatrix and into the suprathreshold domain, resulting in eventual excitation. Figure 3.3 plots the phase paths taken by the reduced HH model when stimulated by an instantaneous cathodic injection of charge. Because the stimulus is of instantaneous duration, its delivery causes a horizontal displacement of the phase point, moving it from the resting node (point **a**) towards (and possibly beyond) the separatrix. Subsequently, the phase point traverses a trajectory that is approximately parallel to the separatrix, until approaching the unstable manifold of the saddle node (solid lines, arrows pointing towards **b**), at which point it is repelled from the saddle node (point **b**) towards either the resting node or the excited node (point **c**, not shown; see Figure 3.1A). Regardless of which node the phase point converges upon, it reaches it via the unstable manifold of the saddle node.

A cathodic injection of threshold charge will move the phase point so that it lies upon the separatrix at point **d**. In this case (and this case only), the system will reach an unstable equilibrium at the saddle node, leaving the system poised between returning to rest and reaching excitation. Any lesser charge would have cause the phase point to return to the resting node, and any greater charge would have displaced it across the separatrix, causing it to converge upon the excited node. This mode of excitation, whereby the membrane is excited by means of a depolarisation, is referred to as *make excitation* (see Section 2.2.3).

3.2.2 Excitation by an anodic pulse

An anodic pulse excites the membrane in a way that is very different to a cathodic pulse. As shown in the previous section, a cathodic pulse evokes excitation by moving the phase point to higher values in the V dimension so that it crosses the separatrix into the suprathreshold domain. An anodic pulse, however, moves the phase point to lower values in the V dimension, moving it *further* from the separatrix, apparently reducing the excitability of the system. Indeed, in the reduced HH model, an anodic pulse is incapable of evoking excitation, and the system will return to resting after the pulse's cessation. However, in the original equations, where the n and h variables are

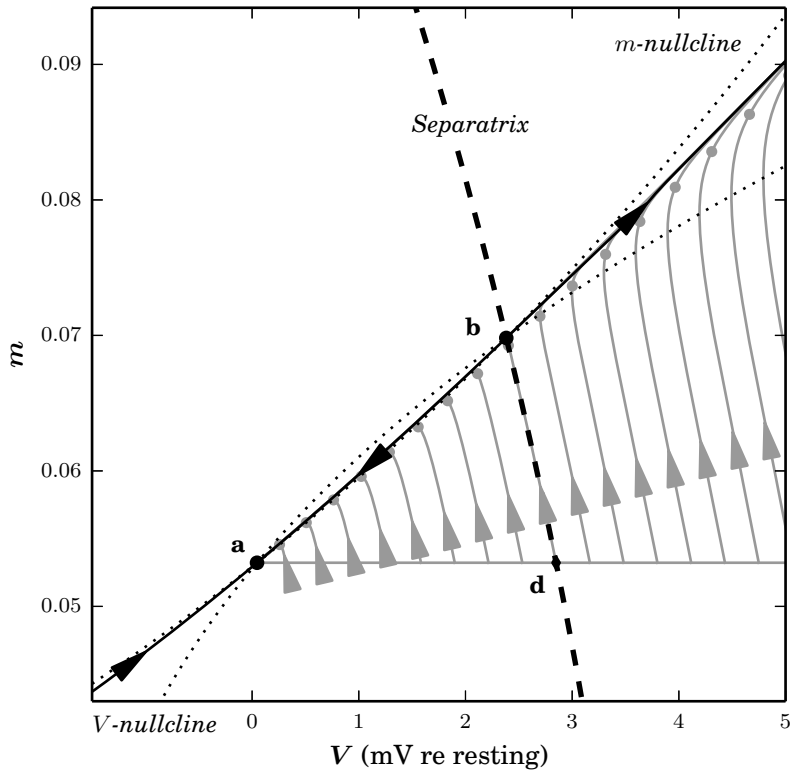

Figure 3.3: Phase paths of the reduced HH model stimulated by instantaneous cathodic injections of charge at various levels (**grey lines**). **Grey arrows** mark the position and trajectory of the phase point 10 µs after the charge injection; **small grey circles** mark the position 80 µs after. **Solid lines** denote the stable manifold of the resting node (point **a**; manifold arrows point towards **a**) and the unstable manifold of the saddle node (point **b**; manifold arrows point away from **b**). Note that the unstable manifold of the saddle node partially overlaps with the stable manifold of the resting node (segment **ab**). The charge injection moves the phase point from the resting node towards (and possibly beyond) the separatrix. All phase paths that do not cross the separatrix (i.e., resulting from a subthreshold injection of charge) converge upon the resting node. Phase paths that do cross the separatrix (i.e., resulting from a suprathreshold injection of charge) converge upon the excited node (not shown, see Figure 3.1A). The rate at which the phase point advances its trajectory is seen to increase with increasing initial displacement (compare grey arrow positions).

not held fixed, an anodic pulse is able to evoke excitation by affecting the V-nullcline so that it no longer intersects with the m-nullcline, thus removing the resting and saddle equilibria, leaving the excited node as the sole attractor of the system. This behaviour is shown in Figure 3.4, which plots the V and m dimensions of the phase path of the HH model stimulated by an instantaneous anodic pulse. To show the effect of the evolving values of n and h on the model's dynamics, the V-nullcline has been plotted with respect to the values of n and h at times $t = 0$, 50, and 100 µs.[1] As time increases, the V-nullcline moves downwards and rightwards, initially moving the resting and saddle nodes towards one another at very small values of t ($t \lesssim 8$ µs), until at $t \approx 8$ µs, the m and V nullclines cease intersecting, at which point the resting and saddle nodes—as well as the nullcline—vanish, and the phase point is attracted towards the remaining stable node, the excited node (not shown; see node **c** in Figure 3.1A). It should be mentioned as a footnote that, as the system is governed by the full HH equations and not their (V, m)-reduced form, the phase point does not reach equilibrium at the excited node, but instead returns to rest via a large upwards loop that represents the action potential; the downwards sweep of this loop is partially visible in the figure, although the simulation ends before it converges upon the resting node.

In excitation by means of an anodic pulse, the driving (hyperpolarising) force of the applied anodic current tends to overpower the dynamics of the phase point, so that excitation only occurs after the current's cessation. Presumably for this reason, this mode of excitation is referred to as *break excitation* (see Section 2.2.3).

3.2.3 Excitation by a cathodic-leading biphasic pulse

When the reduced HH model is stimulated with a CL-BP, the cathodic phase initially drives the phase point to higher values in the V dimension, and then, after the delay of the IPG, the anodic phase drives the phase point back towards lower values of V. If the pulse is charge balanced and each phase is of vanishingly-small duration, then both phases shall have an equal but opposite effect in the V dimension. Thus, if the phases are delivered one immediately after the other (i.e., with zero IPG), then they should exactly cancel and excitation should not occur. However, if a delay—the IPG—separates the two phases, then the neuron has time to react to the cathodic phase, moving the phase point before the onset of the anodic phase. If the cathodic phase delivered sufficient charge to drive the phase point beyond the separatrix, then

[1] Formally, I define the V-nullcline at time $t = s$ as the set of points $\{(V, m) \mid V, m \in \mathbb{R},\ f(V, m, n(t), h(t)) = 0\}$, where $\frac{\mathrm{d}V}{\mathrm{d}t} = f(V, m, n, h)$.

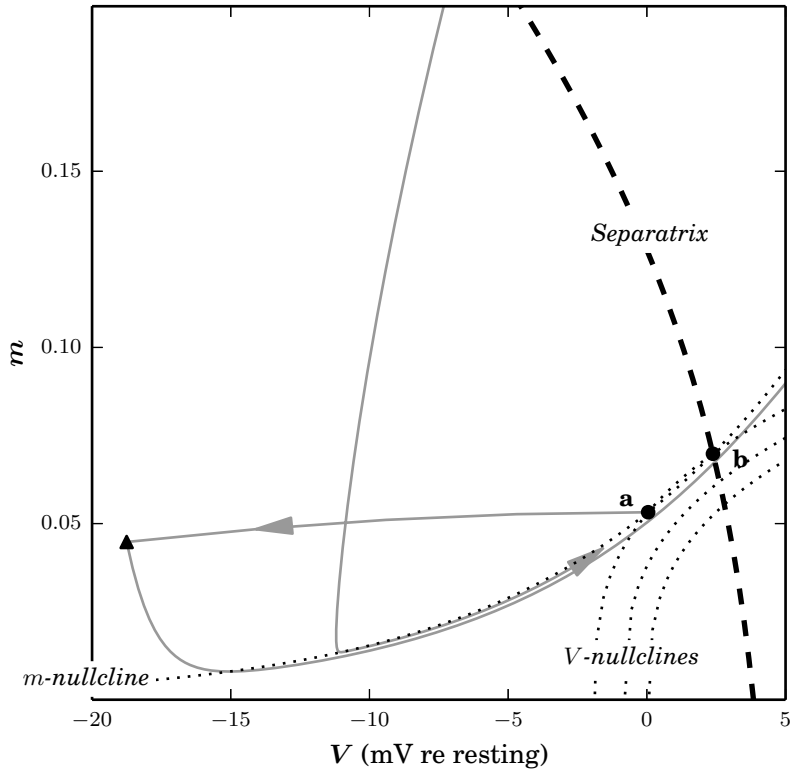

Figure 3.4: Plot showing the (V, m)-projection of the phase path of the HH model stimulated by an anodic pulse of near-instantaneous duration (**solid grey line**). Also plotted is the separatrix with respect to the values of n and h at rest (**thick dashed lines**), and V-nullclines (**dotted lines**) projected to the (V, m)-space with respect to the values of n and h at times t = 0, 50, and 100 µs. Each 50 µs increase in time resulted in a rightwards-downwards shift in the nullcline. *Excitation occurs by the vanishing of the separatrix and saddle node after a short delay (< 50* µs*) due to the changing values of the n and h variables.*

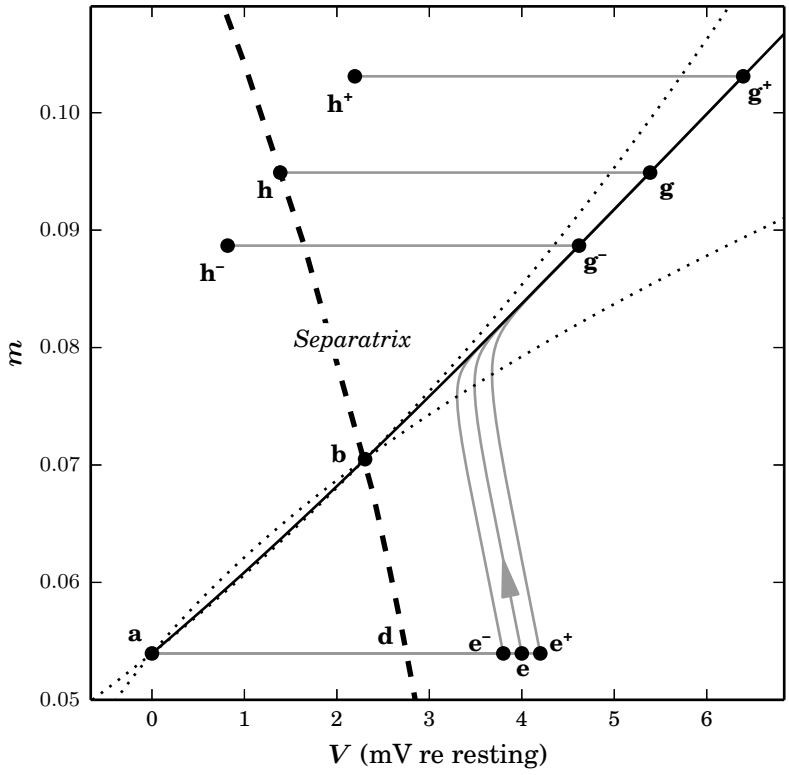

Figure 3.5: The phase plane of the (V, m)-reduced HH model stimulated by a CL-BP. Each phase is of instantaneous duration and the IPG is arbitrarily set to 300 µs, with similar qualitative trends occurring at all IPGs. Three trajectories are plotted (solid grey lines), corresponding to levels of 95%, 100%, and 105% threshold. Even though the 95%-level will not cause excitation, it drives the phase point into the suprathreshold domain briefly, before returning it to the subthreshold domain. *The neuron may briefly become suprathreshold when responding to a subthreshold CL-BP.*

the phase point will begin the trajectory towards excitation during the IPG, moving it away from the separatrix. At the end of the IPG, the anodic phase will drive the phase point back in the direction of the separatrix. If the IPG was made long enough, then the phase point will have advanced too far for the anodic phase to drive it back across the separatrix, and the phase point will instead remain within the suprathreshold domain and excitation will thus occur. Conversely, if the IPG was made short enough, then the phase point will be sufficiently close to the separatrix at the time of anodic-phase onset that it will be driven back across the separatrix and into the subthreshold domain, and thus, excitation will not occur.

The discussed behaviour is demonstrated in Figure 3.5, which plots the phase paths of the reduced HH model's response to a charge balanced CL-BP of 300 µs IPG and vanishingly small phase duration. If the stimulus is delivered at threshold level, then the phase point follows the path **aegh**, with the phase point moving from the resting node to the suprathreshold domain during the cathodic phase (**ae**), and then following a trajectory towards excitation during the interphase gap (**eg**), and then moving back towards the separatrix during the anodic phase (**gh**). At the moment of stimulus cessation, the phase point lies on the separatrix, at **h**. As such, the system will reach an unstable equilibrium at the saddle node (**b**).

Delivered at levels just above (1.05x) and just below (0.95x) threshold, the same stimulus will result in the phase paths $\mathbf{a^-e^-g^-h^-}$ and $\mathbf{a^+e^+g^+h^+}$. Both phase paths are similar to **aegh**, though the location of the phase point at stimulus cessation differs, lying either within the subthreshold domain (path $\mathbf{a^-e^-g^-h^-}$), or within the suprathreshold domain (path $\mathbf{a^+e^+g^+h^+}$). All three phase paths converge upon a common trajectory during the IPG: they all follow the unstable manifold of the saddle node towards the excited node. However, by the time of the onset of the anodic phase, the phase paths corresponding to higher stimulus levels have traversed further along this trajectory (e.g., comparing $\mathbf{g^+}$ to $\mathbf{g^-}$), and as such, are further from the separatrix and require more anodic charge to return them to the subthreshold domain. It is due to the difference in the speed at which the phase points advance during the IPG that causes the phase path $\mathbf{a^+e^+g^+h^+}$ to be suprathreshold while the phase path $\mathbf{a^-e^-g^-h^-}$ is subthreshold.

3.2.4 Excitation by an anodic-leading biphasic pulse

When the reduced HH model is stimulated with an anodic-leading biphasic pulse (AL-BP), the anodic phase initially drives the phase point to lower values in the V

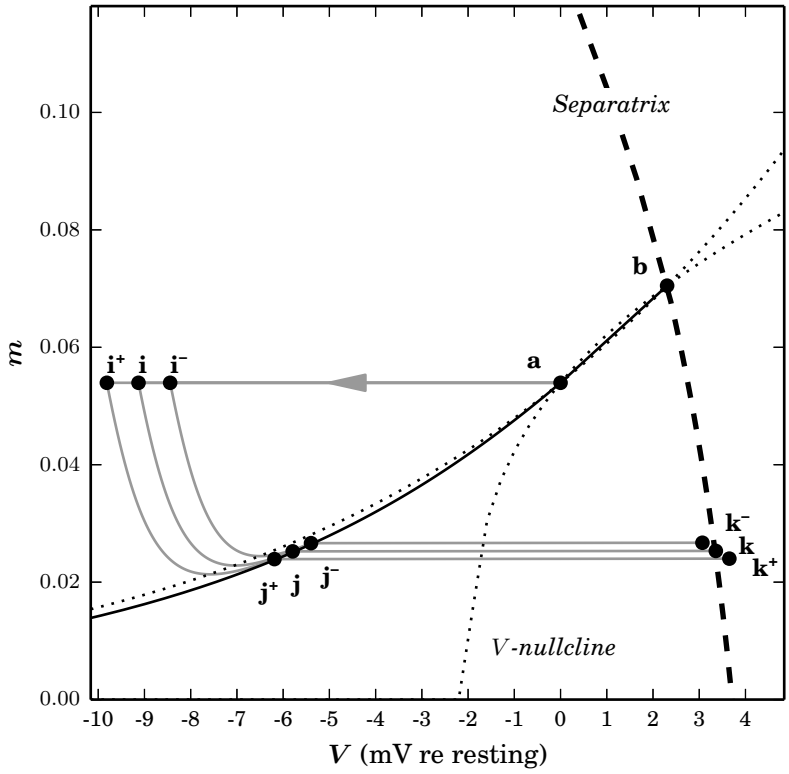

Figure 3.6: The phase plane of the (V, m)-reduced HH model stimulated by a AL-BP. Each phase is of instantaneous duration and the IPG is arbitrarily set to 100 µs, with similar qualitative trends occurring at all IPGs. Three trajectories are plotted (solid grey lines), corresponding to levels of 95%, 100%, and 105% threshold. *The phase point does not cross the separatrix into the suprathreshold domain, other than when the stimulus is suprathreshold.*

dimension, and then, after the delay of the IPG, the cathodic phase drives the phase point back towards higher values of V. As in the case of a CL-BP, if the pulse is charge balanced and each phase is of vanishingly-small duration, then both phases shall have equal and opposite effect in the V dimension, exactly cancelling one another if not separated by a delay. It is therefore how the system reacts during this delay—the IPG—that allows the pulse to evoke excitation. At all stimulus levels, the phase point is attracted to the resting node (via its stable manifold) during the IPG. At higher stimulus levels, this attraction is stronger (i.e., the phase node traverses its given trajectory faster), and so, upon the end of the IPG, this brings the phase point closer to the resting node (and thus, the separatrix) relative to its initial displacement.

Figure 3.6 plots the phase paths of the reduced HH model when stimulated by an AL-BP of 100 µs IPG and instantaneous phase duration. Three phase paths are plotted ($\mathbf{ai^-j^-k^-}$, **aijk**, and $\mathbf{ai^+j^+k^+}$), each corresponding to a different stimulus level (0.95x threshold, 1x, and 1.05x, respectively). At all stimulus levels, the phase point is displaced to lower values of V during the anodic phase of the stimulus (path **ai**), and is then attracted to the stable manifold of **a** during the IPG (path **ij**), and is finally displaced to higher values of V by the cathodic phase (path **jk**). At exactly threshold level, the phase point lies on the separatrix at the end of the stimulus (point **k**). At higher levels, it lies in the suprathreshold domain upon stimulus cessation (e.g., point $\mathbf{k^+}$), and at lower levers, it lies in the subthreshold domain (e.g., point $\mathbf{k^-}$).

The phase path resulting from stimulation by an AL-BP only crosses the separatrix if the stimulus is suprathreshold. This is in stark contrast to the case of stimulation by a CL-BP, wherein subthreshold stimuli may cause the phase point to briefly occupy the suprathreshold domain.

3.3 Analysis

3.3.1 Relation to the LIF neuron

An analysis of the phase plane of the reduced HH model is able to contribute to our understanding of the LIF neuron. The phase space of the LIF neuron has a single dimension, V, the dynamics of which are equivalent to those of the V dimension of the HH model when the m, h, and n variables of the latter are held at their resting values and V is less than the threshold potential θ of the former (see Section 2.4.1). The phase point of the reduced HH model thus behaves identically in the V dimension to that of the LIF neuron when $m = m_\infty$ and $V < \theta$, where m_∞ is the resting value of m. With this in mind, we may "lift" the phase space of the LIF neuron on to the (V, m) phase plane of the reduced HH model, as shown in Figure 3.7. The resting nodes of both models overlap (at **a**) and the lifted phase space crosses the separatrix of the reduced HH model at $V = \theta$. While the phase points of both models occupy a common position close to the LIF neuron's phase space, their dynamics are similar in the V dimension. However, we may see from the example phase trajectories (grey lines) of the Figure that the phase point of the reduced HH model will rapidly move away from the LIF neuron's phase space. This has two effects: it affects the dynamics of the phase point in the V dimension, and it affects the distance of the phase point from the separatrix.

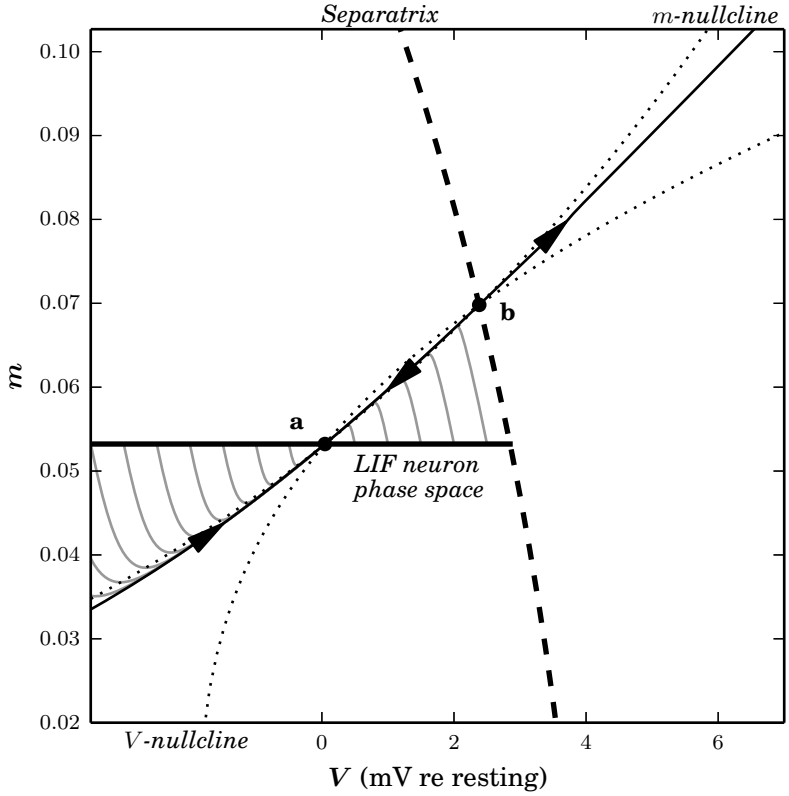

Figure 3.7: The phase space of the LIF neuron (horizontal **bold black line** passing through **a**) "lifted" to the (V, m) phase plane of the reduced HH model. The phase point of the LIF neuron may not leave the lifted phase space and is attracted directly towards the resting node (point **a**). The phase point of the reduced HH model, by contrast, diverges from the lifted phase space, as demonstrated by example phase paths (**grey lines**). Also plotted are the separatrix of the reduced HH model (**dashed line**), the V and m nullclines (**dotted lines**), and the stable manifolds (**black lines**) of the resting and excited nodes.

As the phase point of either model moves closer to the V-nullcline, the V dimension becomes less attracted to the resting node (point **a** in the figure). In the LIF neuron, this occurs only as the phase point moves horizontally towards **a**. However, in the reduced HH model, this occurs in two dimensions simultaneously, and further, we may see that it occurs more rapidly in the m dimension than in the V dimension, given that the phase paths go upwards/downwards towards the V-nullcline more than they move leftwards/rightwards towards **a**. Therefore, after an instantaneous departure from resting, the phase point will return to its resting value in the V dimension considerably faster in the LIF neuron than in the reduced HH model.

After an instantaneous subthreshold departure from resting, the phase point of the reduced HH model follows a trajectory towards the stable manifold of the resting node. Until adjoining the stable manifold, this trajectory is approximately parallel to the separatrix (compare the grey lines in the Figure to the dashed line of the separatrix). While the trajectory is parallel to the separatrix, the amount of charge needed for an instantaneous cathodic pulse to move the phase point beyond the separatrix does not change (recalling that instantaneous charge injections cause horizontal displacements of magnitude proportional to the charge and invariant to the location of the phase point). Therefore, following a just-below threshold depolarisation, the reduced HH model will remain just-below threshold for the duration of time it takes the phase point to approach the stable manifold. After this time, the phase point is very close to both the V and m nullclines, and so while the phase point now moves away from the separatrix, it does so very slowly. This is compared to the phase point of the LIF neuron, which directly returns to resting following a subthreshold depolarisation, immediately following a trajectory that moves it away from the separatrix.

This qualitative analysis of the phase spaces of the reduced HH model and the LIF neuron has shown that the reduced HH model (and by extension, the HH model and the real neuron) will remain just-below threshold for considerably longer than the LIF neuron, following a depolarising pulse. To demonstrate that this is true, Figure 3.8 plots the time-course of V following an instantaneous subthreshold depolarisation in both the reduced HH model and the LIF neuron (black lines). Consistent with the analysis, both models react similarly immediately after the depolarisation, for $\sim$20 µs while their phase points are still close together in the phase plane, but beyond $\sim$20 µs the curves of the two models diverge, with that of the LIF neuron returning to rest at a much faster rate than that of the reduced HH model. The Figure also plots the thresholds of the two models, defined as the difference in the V dimension between the

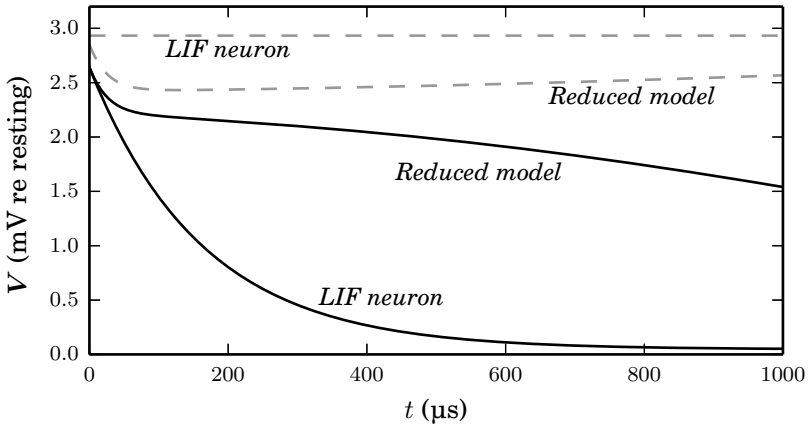

Figure 3.8: Time-course of V (**black lines**) after an instantaneous depolarisation in the reduced HH model and the LIF neuron. The stimulus level is 0.9x threshold in both models. The curves of both models follow similar trajectories during the first ∼20 µs, after which they diverge, with the reduced HH model returning to the resting potential much slower than the LIF neuron. Also plotted are the threshold potentials of both models (**grey dashed lines**), defined as the difference in the V dimension between the phase point and the separatrix. The threshold of the LIF neuron does not vary with time, whereas the threshold of the reduced HH model initially follows a trajectory roughly parallel to that of V, and then slowly begins to diverge at ∼400 µs. *The reduced HH model continues to be near-threshold for the duration of the plot, being at 0.6*x *threshold after 1* ms*, whereas the LIF neuron rapidly diverges from threshold, reaching 0.6*x *threshold after only 67* µs*.*

phase point and the separatrix (grey dashed lines). Consistent with the analysis, the threshold of the reduced HH model follows a trajectory that is approximately parallel to that of the V curve, diverging slowly after ∼400 µs. The reduced HH model continues to be near threshold for the duration of the plot, being at 0.6x threshold after 1 ms. The LIF neuron, however, rapidly diverges from threshold, reaching 0.6x threshold after only 67 µs. Subthreshold facilitation is thus predicted to occur for much longer durations in the reduced HH model than in the LIF neuron.

3.3.2 Effect of the h and n dimensions

The qualitative descriptions of excitation given in this section have been written from the point of view of the reduced HH model, with the working hypothesis that they will also apply to the full HH model. However, the dynamics of the HH model are affected by the h and n dimensions in a way that is not reproduced by the reduced HH model. The saddle node of the HH model, projected to the (V, m) plane, is affected by a constant rightwards-upwards drift while the membrane is depolarised, and a leftwards-downwards drift while it is hyperpolarised (in both cases, moving along the path of the m-nullcline). These movements of the saddle node are responsible for the accommodation phenomenon discussed in section 2.2.2. The dynamics of the phase point are relatively unaffected while the phase point is not in the saddle node's vicinity. However, as the phase point approaches the saddle node, its behaviour becomes complex as it is repelled by a continually moving point. The phase point's trajectory may be abruptly reversed if the saddle node passes it while traversing a similar trajectory. This occurs during just-subthreshold cathodic stimulation as the trajectory of the saddle node (i.e., the m-nullcline) is initially very similar to the trajectory of the phase path; see Figure 3.9 and its caption.

In the qualitative descriptions given in this chapter, I did not attempted to include the complex effects of the saddle node's dynamics, for doing so would have made them prohibitively complicated, defying the aim of providing intuitive descriptions of excitation. Instead, I believe it is most useful to form hypotheses in the intuitively-understandable context of the reduced HH model, and then verify that they continue to apply in the context of the full HH model. In some cases (as was seen in the description of excitation by an anodic pulse), the differing behaviour of the full model entirely changes the qualitative description of excitation. However, in other cases (as was seen in the case of an AL-BP), moving to the full model only adds an additional process to the qualitative description. Curiously, the description of excitation by means of a

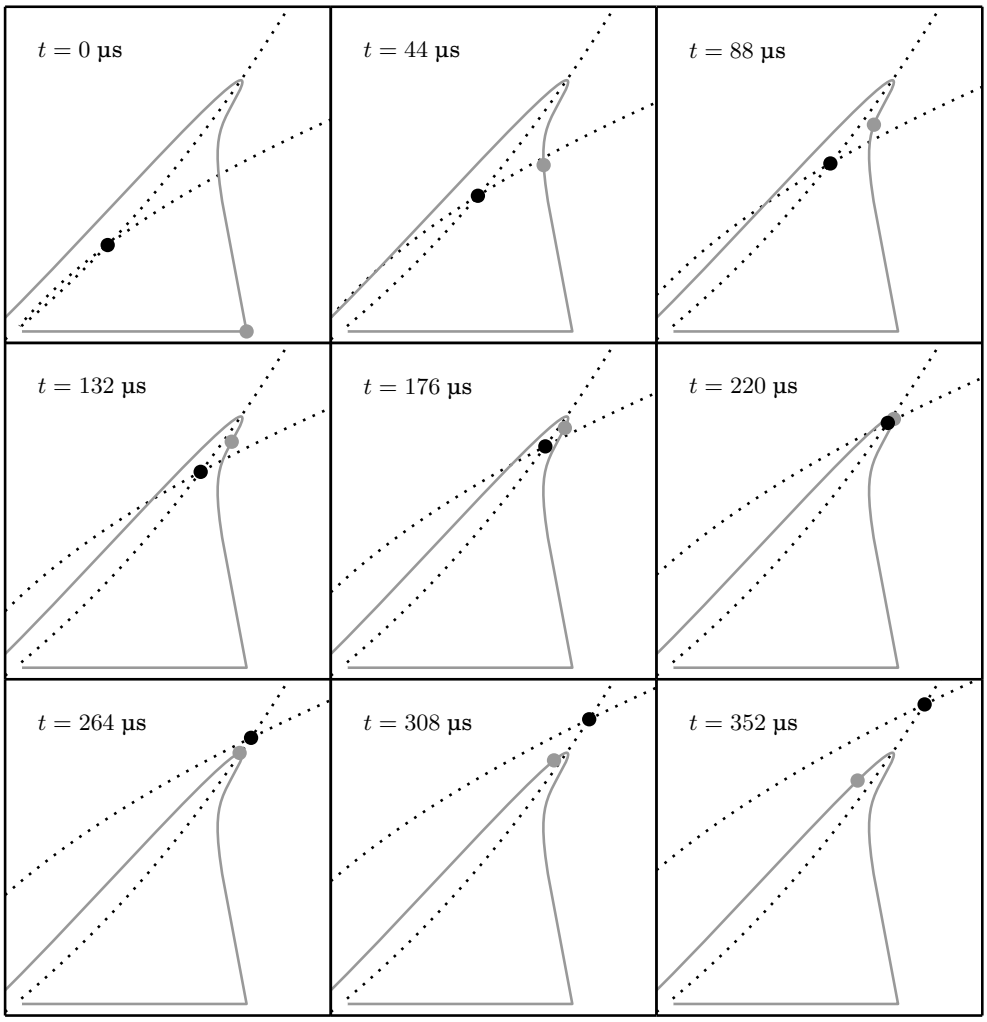

Figure 3.9: Development of the (V, m)-projected phase path (**grey line**) of the HH model stimulated by a just-subthreshold (0.95x threshold) cathodic pulse of instantaneous duration. A snapshot of the (V, m)-projected phase plane is plotted in different panes at 44 µs time increments, from 0 to 352 µs. The V-nullcline is plotted (**mobile dashed line**) at each time step (see footnote 1) and the point at which it intersects with the m-nullcline (**static dashed line**) to form the saddle node is marked (**black filled circle**). The position of the phase point at each time step is also marked (**filled grey circle**). Until $t \approx 220$ µs, it appears as though the stimulus is suprathreshold, with the phase point being repelled by the saddle node towards higher values in the V and m dimensions. However, the saddle node is itself continually drifting towards higher values in the V and m dimensions due to the changing values of the n and h variables, and at $t \approx 220$ it overtakes the phase point, causing an abrupt reversal of the phase point's trajectory. With the n and h dimensions held constant (as is the case in the reduced HH model), the same stimulus would have resulted in excitation.

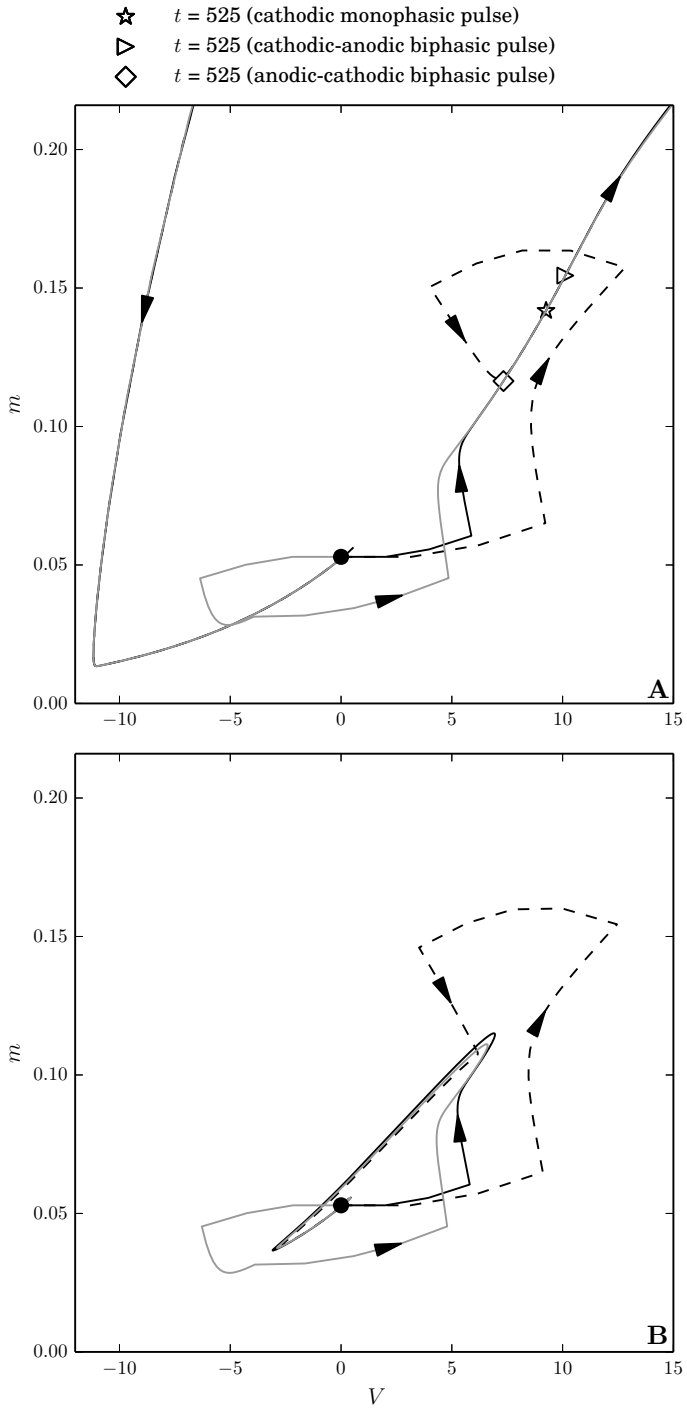

Figure 3.10: Suprathreshold (**plot A**; 1.01x threshold) and subthreshold (**plot B**; 0.9x threshold) (V, m)-projected phase paths of the full HH model stimulated with a cathodic pulse (**black lines**), a CL-BP (**dashed lines**), and an AL-BP (**grey lines**). In all cases, the initial position of the phase point is set to the resting node of the HH model (**black filled circle**). To allow a comparison of the rates at which the different phase paths are traversed, the positions of the phase point at time $t = 525$ µs are marked (see legend; plot A only). To understand how the phase paths of the reduced HH model compare against those of the full HH model, these phase paths may be compared against those from figures 3.3, 3.4, and 3.5. *In all cases, the phase paths of the reduced HH model are qualitatively similar to those of the HH model.* (See main text for discussion of minor differences.)

CL-BP, which is perhaps the most complex of the four descriptions, is the description that is *least* affected by moving from the reduced HH model to the full HH model. This is because the phase path resulting from delivery of a CL-BP does not ever approach the vicinity of the saddle node (other than in the case of large IPGs, or when delivered at *precisely* threshold level), and so it is relatively insensitive to the saddle node's dynamics. For reference, I provide Figure 3.10, which plots the (V, m)-projected phase paths of the full HH model stimulated with a cathodic pulse, a CL-BP, and an AL-BP. For each pulse shape, a phase path has been plotted for when the pulse is delivered at a suprathreshold level (plot A), and for when it is delivered at a subthreshold level (plot B). Comparing these phase paths with their counterparts in the reduced HH model, we see that they are qualitatively similar in the case of suprathreshold delivery. In the case of subthreshold deliver, the phase paths resulting from cathodic stimulation and anodic-leading biphasic stimulation both briefly sway towards excitation before returning to the resting node. This only occurs in the full equations and is due to the dynamics of the saddle node previously discussed. The subthreshold phase paths resulting from cathodic-leading biphasic stimulation are qualitatively similar in both models. In all phase paths, however, their are quantitative differences: the phase paths of the full equations stretch to greater values in the V dimension. This is due to threshold differences due to the saddle node dynamics rendering excitation harder. To demonstrate that these quantitative differences do not affect the phenomenological trends of how the threshold depends on the stimulus, I have compared the threshold-IPG curves resulting from cathodic-leading and anodic-leading biphasic stimulation in the full and reduced equations (Figure 3.11). While the curves are offset between models by ~ 1 to ~ 4 dB, both models show similar trends in threshold with respect to IPG under both polarity orders, with thresholds monotonically decreasing from $\sim$22 dB ($\pm$5 dB) to $\sim$0 dB ($\pm$3 dB). Given the similarity of the curves, holding the n and h dimensions of the HH model at their resting values does not prevent the reduced HH model from providing a useful platform for analysing excitation by means of biphasic stimulation.

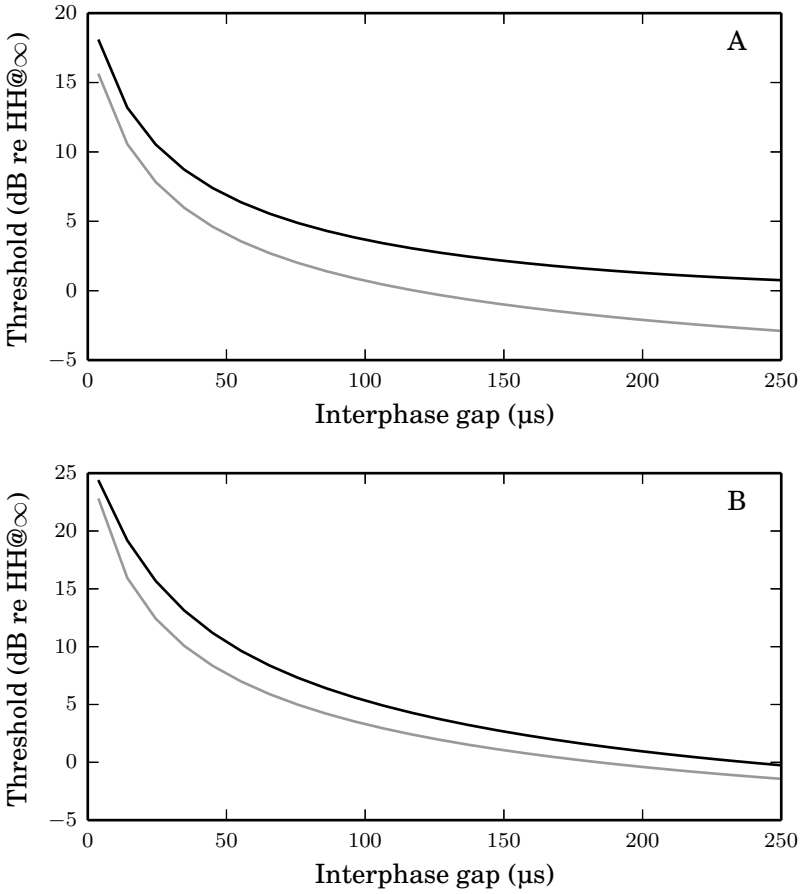

Figure 3.11: Threshold-IPG curves of the reduced HH model (**grey lines**) and the HH model (**black lines**) under cathodic-leading (**plot A**) and anodic-leading (**plot B**) biphasic stimulation. Thresholds are given in dB relative to the monophasic threshold of the HH model. The phase durations are instantaneous in both polarity orders. *The threshold-IPG curves of the reduced HH model are qualitatively similar to those of the full HH model for stimulation with both polarity orders at IPGs less than 250* µs.

Chapter 4

Stochasticity and excitation

The dynamics of the phase point in the reduced HH model are deterministic. This chapter uses the model of Fox and Lu (1994) to explore how the stochasticity that is present in the real neuron affects the qualitative descriptions of excitation that were given in the previous chapter.

4.1 Background

4.1.1 Stochastic model

The implementation of the Fox and Lu model used throughout this chapter, henceforth referred to as *the stochastic HH model*[1], is due to Goldwyn and Shea-Brown (2011). It uses the Euler-Maruyama method (described in Higham, 2001) coupled with the forward Euler method (described in Ascher and Petzold, 1998) to numerically simulate (2.7) and (2.4), respectively, using a 1 µs time step. The values of m, n, and h are not rounded as described in Section 2.1.2, but are reset to 0 or 1 if they diffuse outside the $[0, 1]$ interval. The model uses channel densities of 60 µm^{-2} and 18 µm^{-2} for the sodium and potassium families, respectively, with the number of channels determined by a free variable A that describes the area of the patch of membrane under study (i.e., so that $\bar{N}_X = Ad_X$, where $\bar{N}_X$ is the number of X-family channels and d_X is the channel density of the X-family). The area was chosen so that the relative spread (monophasic cathodic probe pulse, 39 µs duration) of the model was ∼0.08, similar to that of a typical SGC (Miller et al., 1999c). The time-scaling scheme described in Section 3.1.1 was applied.

[1] Available via ModelDB (http://senselab.med.yale.edu/modeldb) under accession number 138950.

4.1.2 Validation of stochastic model

While the Fox and Lu model has been used extensively as a biophysical model of the stochastic membrane (e.g., De Vries and Sherman, 2000; Schmid et al., 2001; Shuai and Jung, 2002; Casado, 2003; Rowat and Elson, 2004; Wang et al., 2004; Ozer and Ekmekci, 2005; Saarinen et al., 2008; Finke et al., 2008; Cudmore et al., 2010; Sato et al., 2010), it is nevertheless prudent to show that it responds to the cathodic-leading biphasic pulses that are of most interest to this thesis similarly to the real neuron. With that in mind, this section reproduces the methodology of van den Honert and Mortimer (1979), described previously in section 2.3.2, and compares the results of the stochastic HH model against those of the original study.

Figure 4.1 plots the voltage time-courses of a single node of Ranvier's response to stimulation by various pulse shapes. Plot A shows the responses of the membrane to a single cathodic pulse delivered at various amplitudes. It shows that when delivered above a threshold amplitude, excitation is reliably achieved. Plot B shows the responses of the membrane to an above-threshold cathodic pulse followed immediately by an anodic pulse. As the leading cathodic pulse is above threshold, an action potential would reliably occur in the absence of the anodic pulse. However, when the anodic pulse is delivered at a sufficiently large amplitude, excitation is averted. Plot C shows that if delivery of the anodic pulse is sufficiently delayed, then excitation may again be achieved. Figure 4.2 shows the results of an identical methodology when applied to the stochastic HH model. All of the discussed trends are qualitatively reproduced by the stochastic model.

Van den Honert and Mortimer quantified the ability for an anodic pulse to abolish an action potential by measuring the *abolition threshold*, the level with which the anodic pulse must be delivered for an action potential to be just averted. The abolition threshold depends on the *cathodic level*, the level at which the leading cathodic pulse is delivered. This is shown in Figure 4.3A, which plots how the abolition threshold depends on cathodic level for various delays between the cathodic and anodic pulses. It shows that a linear increase in cathodic level results in an exponential increase in abolition threshold. Figure 4.3B summarises this by showing how the thresholds of the stimulus depend on the delay between the two pulses (the IPG) when the stimulus is symmetric (charge balanced). It shows that an increasing in delay leads to a decrease in threshold. Figure 4.4 shows that the stochastic model reproduces both the exponential dependence of abolition threshold on cathodic level, and the decrease in symmetric biphasic threshold with increasing IPG.

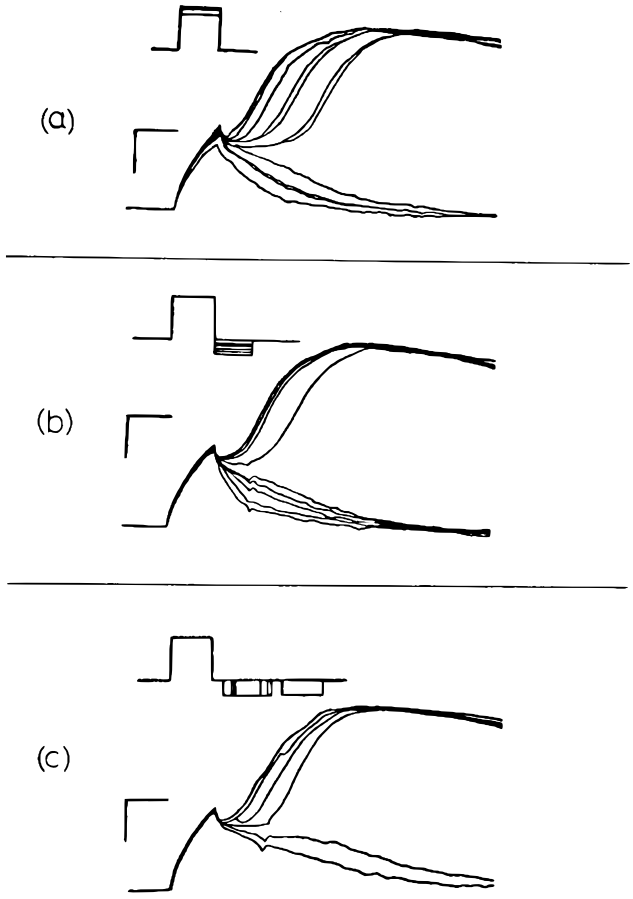

Figure 4.1: Voltage time-courses of a single node of Ranvier's response to stimulation by various pulse shapes. **Plot a**: responses to a cathodic monophasic pulse of 50 µs duration delivered at various levels. **Plot b**: responses to an above-threshold cathodic pulse (50 µs duration) immediately followed by an anodic pulse of varying level (50 µs duration). **Plot c**: responses to an above-threshold cathodic pulse (50 µs duration) followed at various intervals by a fixed-amplitude anodic pulse (50 µs duration). Figure reproduced from van den Honert and Mortimer (1979) with permission from the publisher.

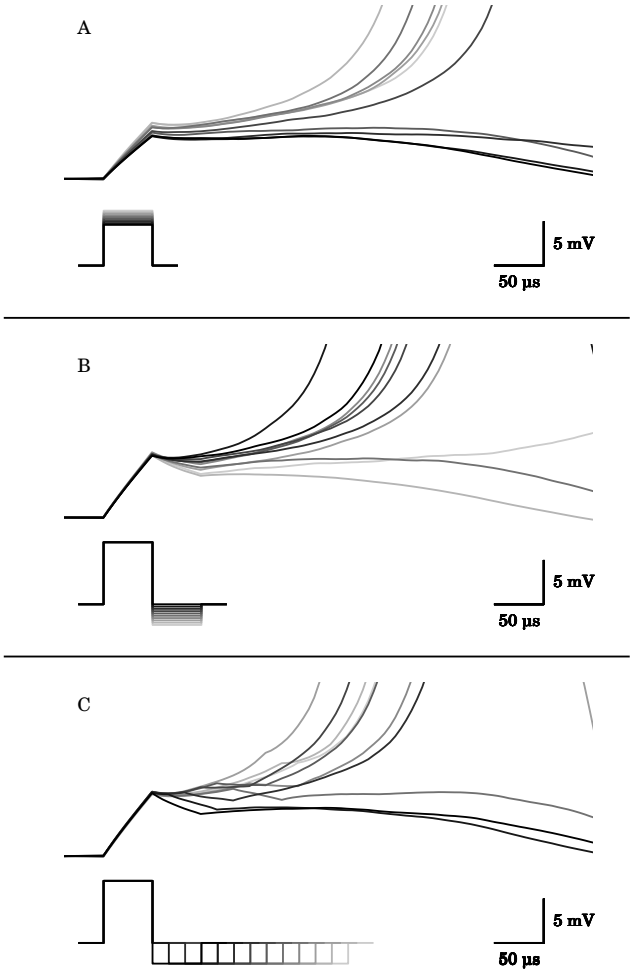

Figure 4.2: Demonstration that the stochastic HH model reproduces the trends of the membrane shown in Figure 4.1. **Plot A**: responses of the stochastic HH model to a cathodic monophasic pulse of 50 µs duration delivered at various levels. **Plot B**: responses of the stochastic HH model to an above-threshold cathodic pulse (50 µs duration) immediately followed by an anodic pulse of varying level (50 µs duration). **Plot C**: responses of the stochastic HH model to an above-threshold cathodic pulse (50 µs duration) followed at various intervals by a fixed-amplitude anodic pulse (50 µs duration). *For all paradigms, the traits exhibited by the stochastic HH model reproduce those empirically observed by van den Honert and Mortimer (1979).*

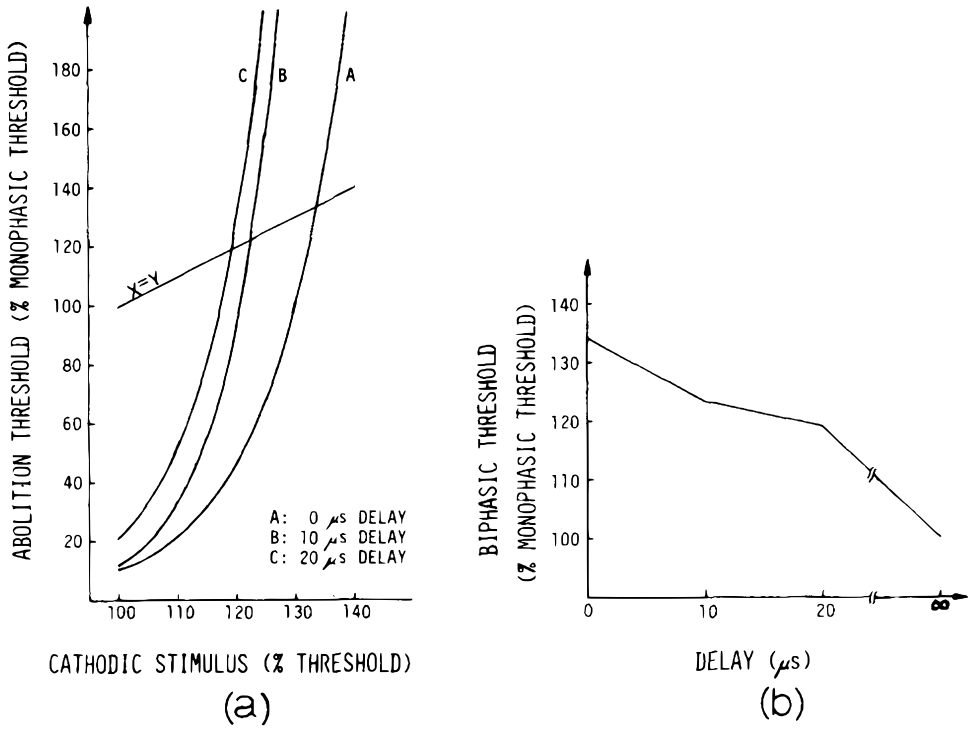

Figure 4.3: The relationship between *abolition threshold* and *cathodic level* under cathodic-leading biphasic stimulation at various IPGs (**plot A**). The data from which the curves A, B, and C were fit were shown earlier in Figure 2.14. The intersections of the line $X{=}Y$ and the curves A, B, and C mark the points at which the stimulus is symmetric and charge balanced. The stimulus levels at these points are plotted against their respective IPGs in **plot B** (where an infinite IPG corresponds to a cathodic monophasic pulse). Note that all curves in plot A *should* have an abolition threshold of 0% at a cathodic level of 100%, by definition (as when the cathodic level is 100% of the threshold, the stimulus is *already* at threshold in the absence of subsequent anodic stimulation). The considerable deviation from this in curve C is possibly due to deterioration of the units with time, noting that very few units survived long enough to contribute to curve C (van den Honert and Mortimer, 1979). Figure reproduced from van den Honert and Mortimer (1979) with permission from the publisher.

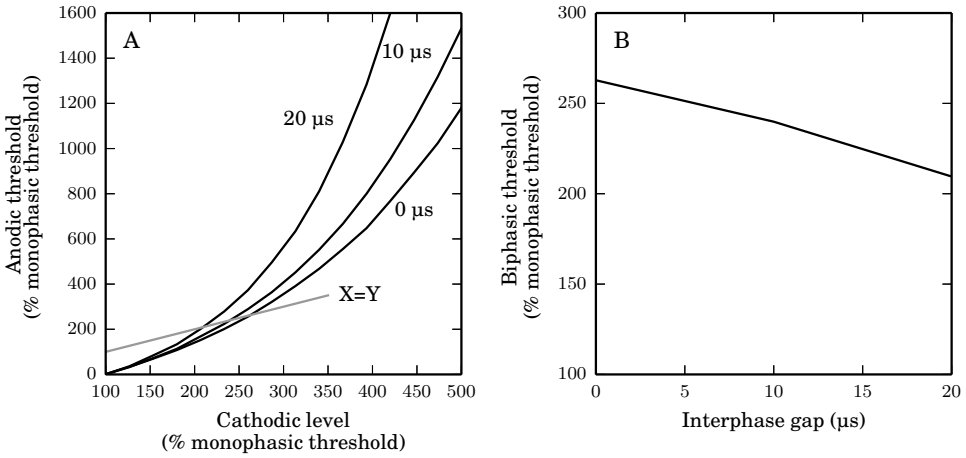

Figure 4.4: Demonstration that the stochastic HH model reproduces the trends of the membrane shown in Figure 4.3. **Plot A**: The dependence of anodic threshold on cathodic level in cathodic-leading biphasic stimulation (50 µs/phase duration) at three IPGs. Each curve corresponds to a different IPG, as labelled. The intersections of the line $X{=}Y$ and the curves mark the points at which the stimulus is symmetric and charge balanced. The stimulus levels at these points are plotted against their respective IPGs in **plot B**. *In both plots, the trends empirically observed by van den Honert and Mortimer are reproduced by the stochastic HH model.*

4.1.3 Phase paths of the stochastic HH model

As in the original, *deterministic*, HH model, the phase paths of the stochastic HH model may be projected to the (V, m) space. Unlike the HH model, the trajectory of the stochastic HH model is not deterministic, and so repeated executions (or *trials*) of the model will produce different phase paths, even if the initial states are identical. To qualitatively understand the behaviour of the stochastic HH model, the phase paths of a large number of trials may be projected, providing an estimate of the distribution of phase paths. The model is most likely to behave as in a phase path from the centre of the distribution, but in some trials, it will behave differently, taking on the behaviour of an outlier phase path. As an example, see Figure 4.5, which shows the (V, m)-projections of the phase paths resulting from 1000 trials of stimulating the model with a cathodic pulse; also plotted is the deterministic phase path.

As in the HH model, the phase point of the stochastic HH model is attracted to the resting node. However, unlike in the HH model, the phase point of the stochastic HH model does not converge upon it, for when the phase point is in the proximity of a stable node, the non-deterministic term of (2.7) dominates its dynamics, preventing convergence. Therefore, the "resting state" of the stochastic HH model is a random variable that is centred on the resting node of the HH model. While this stochasticity of the resting state affects the phase path of any given trial of the stochastic HH model, it does so in a way that can be equally reproduced in the HH model by initiating the system to the same random variable, and as such, it does not alter the way by which excitation is achieved compared to how it is achieved in the HH model. Therefore, throughout this chapter, the phase point of the stochastic HH model is explicitly set to the resting node of the HH model so that only the phenomena that is unique to the stochastic HH model are investigated. Analysing the effect of the stochastic resting state is then akin to analysing the behaviour of the non-resting deterministic model (e.g., as occurs following conditioning stimulation), which I did not investigate in this thesis.

4.2 Phase plane portraits of excitation

4.2.1 Excitation by a cathodic pulse

The (V, m)-projected phase paths resulting from repeated trials of delivery of a cathodic pulse (threshold level, 20 µs duration) to the stochastic HH model (initial state at pulse onset set to resting state of the HH model) are shown in Figure 4.5. Plot A

shows those phase paths that resulted in excitation (the *excited phase paths*) and plot B shows those that did not (the *unexcited phase paths*). For comparison, the deterministic phase paths of the HH model responding to the same stimulus (delivered at levels just-above and just-below threshold) are also shown (black line and dashed line, respectively). The Figure only shows the phase paths in the vicinity of the bifurcation between the excited and unexcited phase paths; for reference, Figure 4.6 re-plots the phase paths to show the full upwards-sweep of the action potential in the case of excitation.

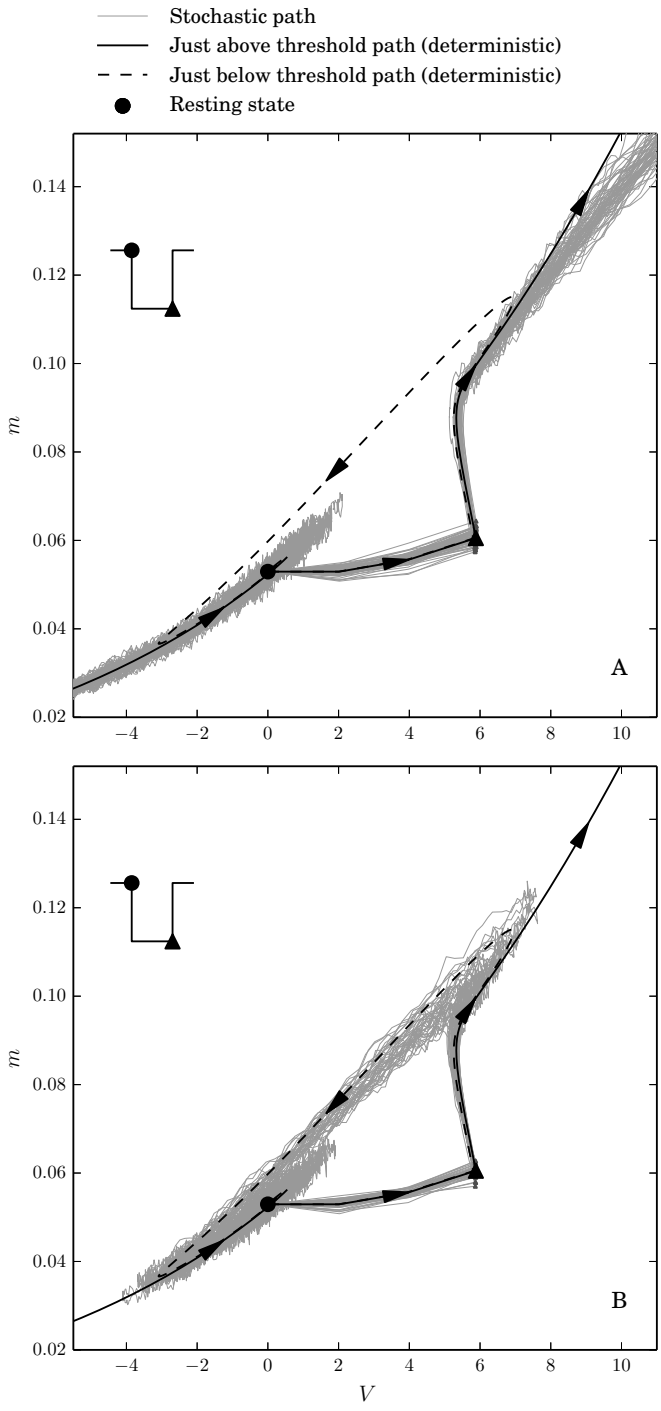

Figure 4.5: The (V, m)-projected phase paths of the stochastic HH model resulting from 100 trials of stimulation by a cathodic monophasic pulse (20 µs duration) delivered at threshold level (**grey lines**). Upon the onset of the stimulus, the phase point is positioned at the resting node of the HH model (**black circle**). For reference, trajectories of the HH model are plotted when stimulated at levels just-above- (1.05x; **solid black line**) and just-below- (0.95x; **dashed black line**) threshold. **Plot A**: Just the trials in which an action potential occurred (manifesting as an upwards loop in the phase path); **plot B**: just the trials in which an action potential did not occur. Arrows mark the forward progression of time.

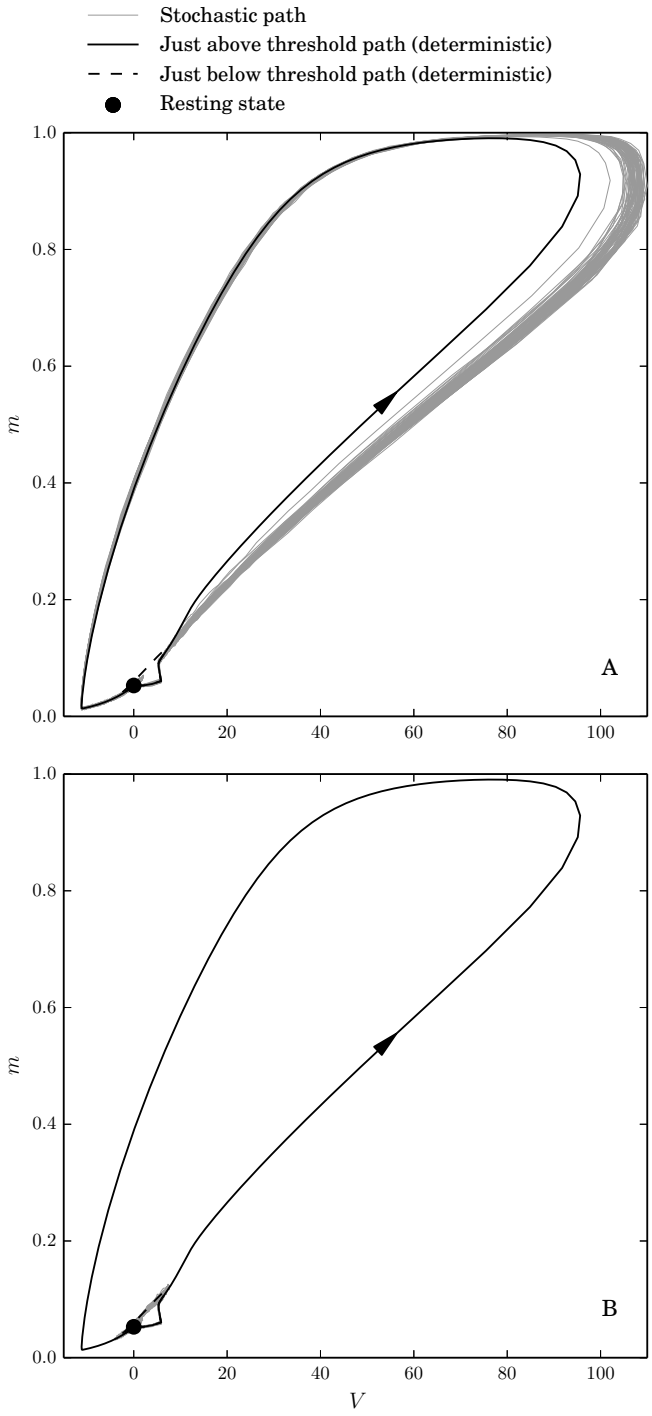

Figure 4.6: As in Figure 4.5, with the same phase paths plotted on a different scale so as to show the full upwards loop of the action potential.

The phase paths of the stochastic HH model are both qualitatively and quantitatively similar to those of the HH model. Qualitatively, the phase point is displaced to higher values in the V dimension by the pulse's delivery (remaining relatively static in the m dimension). Following the pulse's cessation, the phase point traverses a trajectory approximately parallel to the separatrix of the reduced HH model (not shown; see Figure 3.3) until approaching the location of the saddle node in the reduced HH model (not shown; see Figure 3.3), at which point it is repelled and follows an upwards-rightwards trajectory. During this trajectory, bifurcation occurs in the deterministic equations due to the saddle node overtaking the slower phase point of the subthreshold path while being outpaced by the faster phase point of the suprathreshold path (see Section 3.3.2). In the excited paths (plot A), the phase point continues the upwards-rightwards trajectory of the action potential and excitation occurs. In the unexcited paths (plot B), the phase point's trajectory is reversed and it returns to the vicinity of the resting node. Quantitatively, the phase paths do not diverge widely from the their equivalent deterministic phase path, and the divergence that does occur occurs around and after the point of bifurcation, considerably after the pulse's cessation.

4.2.2 Excitation by an anodic pulse

The (V, m)-projected phase paths resulting from repeated trials of delivery of an anodic pulse (threshold level, 20 µs duration) to the stochastic HH model (initial state at pulse onset set to resting state of the HH model) are shown in Figure 4.7. The phase paths are qualitatively similar to their deterministic counterparts: the pulse's delivery displaces the phase point to lower values in the V dimension without a large immediate effect in the m dimension. Following the pulse's cessation, all phase points follow a common trajectory towards excitation as both the resting and saddle nodes disappear (not shown; see Section 3.3.2). Both nodes re-appear behind (i.e., at lower values in the V and m dimensions) the phase point after ∼830 µs and the saddle node advances on the phase point, following the trajectory of the m-nullcline. The rate at which the phase point advances towards excitation varies between trials due to stochasticity; bifurcation occurs in those trials where the saddle node outpaces (and overtakes) the phase point, resulting in the phase point abruptly changing its trajectory and returning to rest.

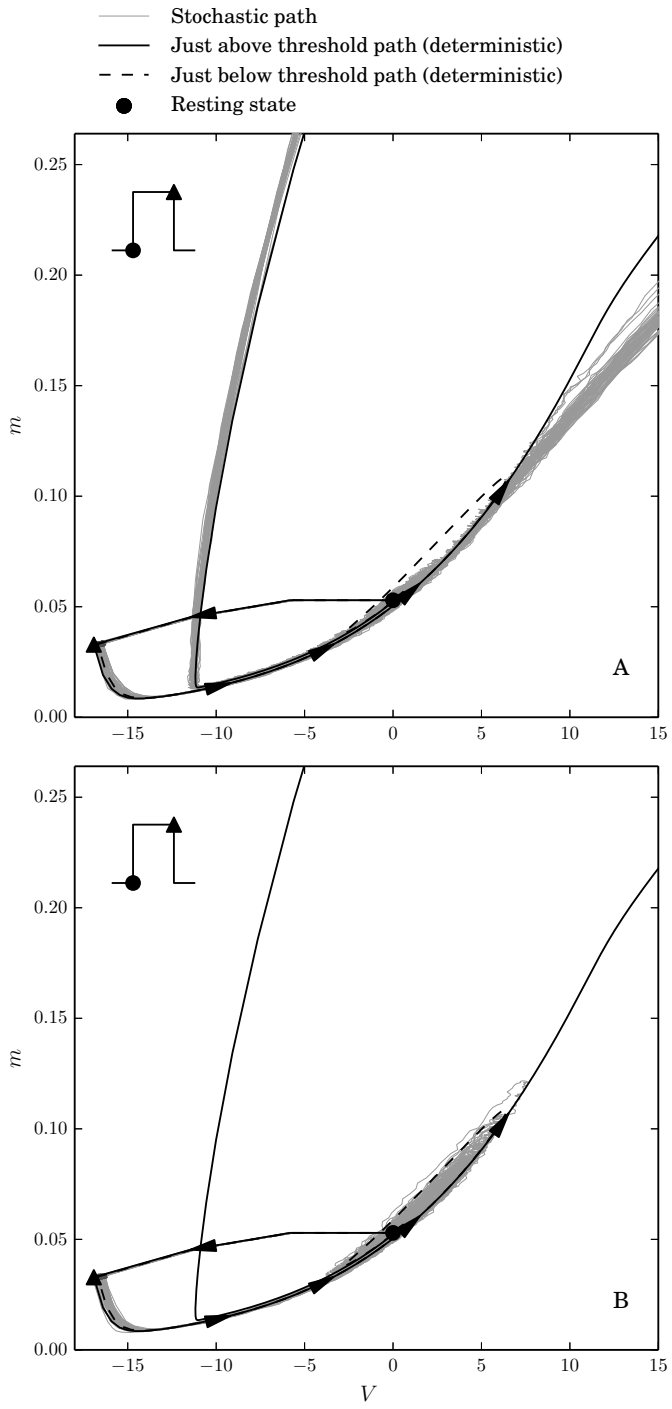

Figure 4.7: The (V, m)-projected phase paths of the stochastic HH model resulting from 100 trials of stimulation by an anodic pulse (20 µs duration) delivered at threshold level (**grey lines**). Upon the onset of the stimulus, the phase point is positioned at the resting node of the HH model (**black circle**). For reference, trajectories of the HH model are plotted when stimulated at levels just-above- (1.05x; **solid black line**) and just-below- (0.95x; **dashed black line**) threshold. **Plot A**: Just the trials in which an action potential occurred (manifesting as an upwards loop in the phase path); **plot B**: just the trials in which an action potential did not occur. Arrows mark the forward progression of time.

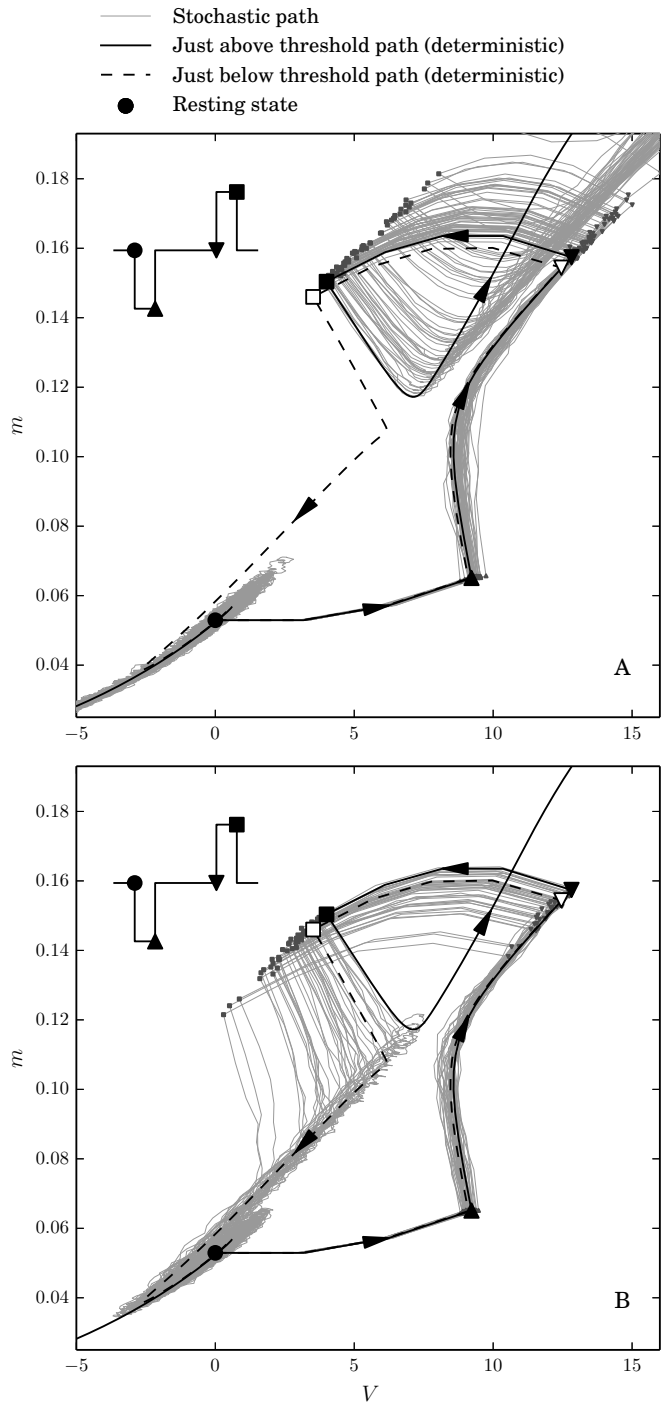

Figure 4.8: The (V, m)-projected phase paths of the stochastic HH model resulting from 100 trials of stimulation by a CL-BP (20 µs/phase duration; 100 µs IPG) delivered at threshold level (**grey lines**). Upon the onset of the stimulus, the phase point is positioned at the resting node of the HH model (**black circle**). For reference, trajectories of the HH model are plotted when stimulated at levels just-above- (1.05x; **solid black line**) and just-below- (0.95x; **dashed black line**) threshold. **Plot A**: Just the trials in which an action potential occurred (manifesting as an upwards loop in the phase path); **plot B**: just the trials in which an action potential did not occur. Arrows mark the forward progression of time.

4.2.3 Excitation by a cathodic-leading biphasic pulse

The (V, m)-projected phase paths resulting from repeated trials of delivery of a CL-BP (threshold level, 20 µs/phase duration, 100 µs IPG) to the stochastic HH model (initial state at pulse onset set to resting state of the HH model) are shown in Figure 4.8. The phase paths are qualitatively similar to their deterministic counterparts: the cathodic phase of the pulse displaces the phase point to higher values in the V dimension without a large immediate effect in the m dimension, and then during the delay of the IPG, the phase point follows a trajectory as though towards excitation, and then the delivery of the anodic phase displaces the phase point to lower values in the V dimension without having a large immediate effect in the m dimension. Following the pulse's cessation, the phase point approaches the dynamic saddle node (not shown) via a trajectory approximately parallel to the separatrix (not shown), and is then repelled from the saddle node towards either the resting node or the excited node.

In all trials, the phase point follows a common trajectory (approximately the unstable manifold of the saddle node) towards excitation, up until the onset of the anodic phase. Prior to the anodic phase, there is very little across-trial variability in the phase paths—they all overlap closely to form a tight bundle. However, at the moment of anodic-phase onset, the phase points of different trials occupy different positions along the length of the bundle (small grey squares), indicating that some phase points traversed the common trajectory faster than others, and so the stochasticity of the system manifests in stochasticity in traversal speed. The delivery of the anodic phase shifts all the phase points towards lower values in the V dimension, resulting in a final spread of phase points, centred on the separatrix (not shown), with the main axis of the spread approximately perpendicular to the separatrix. Only the very few phase points near the centre of the spread are close to the separatrix upon the pulse's cessation, and it is only these few that have the potential to diffuse (i.e., due to stochasticity) across the separatrix, changing the firing outcome of the trial. For the majority of the trials, the phase point is so far from the separatrix upon the pulse's cessation that the probability of the phase point crossing the separatrix is vanishingly small. As such, we may expect the stochasticity of the system to only affect the firing outcome following delivery of a CL-BP *during* the pulse's delivery, and not after.

4.2.4 Excitation by an anodic-leading biphasic pulse

The (V, m)-projected phase paths resulting from repeated trials of delivery of a AL-BP (threshold level, 20 µs/phase duration, 100 µs IPG) to the stochastic HH model

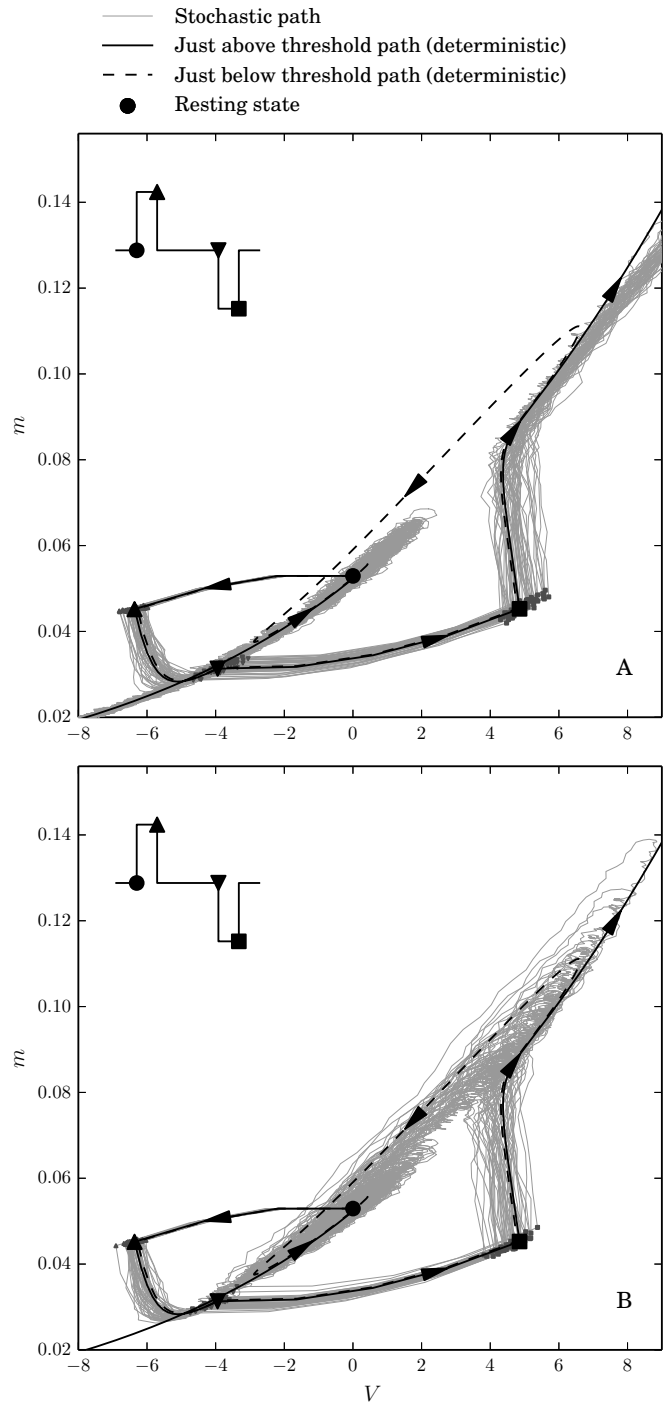

Figure 4.9: The (V, m)-projected phase paths of the stochastic HH model resulting from 100 trials of stimulation by an AL-BP (20 µs/phase duration; 100 µs IPG) delivered at threshold level (**grey lines**). Upon the onset of the stimulus, the phase point is positioned at the resting node of the HH model (**black circle**). For reference, trajectories of the HH model are plotted when stimulated at levels just-above- (1.05x; **solid black line**) and just-below- (0.95x; **dashed black line**) threshold. **Plot A**: Just the trials in which an action potential occurred (manifesting as an upwards loop in the phase path); **plot B**: just the trials in which an action potential did not occur. Arrows mark the forward progression of time.

(initial state at pulse onset set to resting state of the HH model) are shown in Figure 4.9. The phase paths are qualitatively similar to their deterministic counterparts. The delivery of the initial anodic phase moves the phase point to lower values in the V dimension without a large immediate effect in the m dimension. During the IPG, the phase point traverses a trajectory towards the resting node until being displaced towards higher values in the V dimension by the delivery of the cathodic phase. In all trials, the delivery of the cathodic phase moves the phase point well beyond the separatrix of the reduced HH model (not shown), so that the phase point follows a trajectory towards excitation. However, the saddle node does not remain static and advances along a similar trajectory (see Section 3.3.2), in some cases outpacing and overtaking the phase point. In these cases, excitation does not occur.

During the pulse's delivery, the phase points of the different trials follow qualitatively similar trajectories. However, the rates at which they traverse their trajectories varies between trials due to stochasticity. This results in considerable spatial variability of the phase points in the (V, m) plane upon the pulse's cessation, with some phase points positioned close to the separatrix of the reduced HH model. As the separatrix advances in time as the membrane is depolarised, it seems possible that some phase points may reside within the subthreshold side of the moving-separatrix by the time the phase point approaches the saddle node. If this were to occur, it would change the qualitative nature of excitation: the "race" between the saddle node and the phase point would not occur. To this end, I analysed to which side of the saddle node the phase points lay upon advancing beyond the saddle node in the m dimension. I found that in all trials, the phase point did advance beyond the saddle node in the m dimension, and that in all cases, it did so from higher values in the V dimension. Thus, the "race" between the saddle node and the phase point occurs in all 100 cases analysed.

The response of the stochastic HH model to a AL-BP is qualitatively similar to the response to a cathodic pulse. The longer duration of the AL-BP means that the position of the phase point upon pulse cessation has greater variability in the biphasic pulse compared to the monophasic pulse, but, as shown in the previous paragraph, this variability does not qualitatively affect how the model responds. We may thus hypothesise that the interactions between neighbouring AL-BPs will be similar to the interactions between neighbouring cathodic pulses, and in particular, we may expect to see the same temporal facilitation that occurs in monophasic stimulation. This will be investigated in the next chapter.

4.3 Analysis

4.3.1 Quantifying the effect of stochasticity

One motivation in investigating the responses of the stochastic HH model was to support my view that the phase order of a biphasic pulse fundamentally changes how the pulse excites the membrane. The stochastic model can support this view if how its responses differ from those of the HH model depends on phase order.

Suppose that part-way through a simulation with the stochastic HH model, one replaces the stochastic equations of the stochastic HH model with the deterministic equations of the original HH model.[2] Continuing the simulation with the original equations may then be used to predict whether or not excitation would have occurred under the stochastic equations. The accuracy of such a prediction depends on the time at which the equations were switched (which I shall refer to as the *time at which the prediction was made*). The earlier the prediction was made, the more likely it was that the phase path of the stochastic HH model would have diverged from that of the deterministic HH model, leading to an erroneous prediction. A particular epoch of importance is the moment of stimulus cessation. If stochasticity only affects the response of the stochastic HH model *during* a given pulse, then we would expect the firing outcome to be predictable at the time of the pulse's cessation. Alternatively, if stochasticity continues to affect how the response of the stochastic model *after* the pulse's delivery, then we would expect the firing outcome of the model to be unpredictable (or poorly predictable) at the time of the pulse's cessation. If different pulse shapes evoke excitation in a similar way, then we would expect predictions made upon stimulus cessation to be similar regardless of pulse shape. With this in mind, the firing outcomes across 1000 trials of the stochastic HH model were predicted at the moment of stimulus cessation when stimulated by monophasic and biphasic pulses. For each stimulus, the number n_{TP} of correct predictions of excitation (*true positives*), the number n_{TN} of correct predictions of non-excitation (*true negatives*), the number n_{FP} of incorrect predictions of excitation (*false positives*), and the number n_{FN} of incorrect predictions of non-excitation (*false negatives*), were recorded, and from these, the prediction accuracy

$$A = \frac{n_{\mathrm{TP}} + n_{\mathrm{TN}}}{n_{\mathrm{TP}} + n_{\mathrm{TN}} + n_{\mathrm{FP}} + n_{\mathrm{FN}}}$$

[2] In other words, taking a snapshot of the position of the (V, m, n, h)-projected phase point of the stochastic model at the given moment t in time, and placing the phase point of the HH model at this position and stimulating the latter with the remaining stimulus signal from time t onwards.

was derived (Table 4.1). In the case of cathodic-leading biphasic stimulation, stochasticity had almost no effect on firing outcome after the pulse's delivery. In the cases of both anodic-leading stimulation and cathodic monophasic stimulation, stochasticity had an effect both during and after the pulse's delivery. In the case of anodic monophasic stimulation, stochasticity had almost no effect after the pulse's delivery. These results suggest that an AL-BP evokes excitation similarly to a cathodic monophasic pulse in the stochastic model, and that this is different to how a CL-BP evokes excitation, consistent with the hypothesis of this thesis that phase order of a biphasic pulse changes how the pulse excites the membrane.

4.3.2 Firing outcome to a cathodic-leading biphasic pulse may be predicted at pulse cessation

When the neuron is stimulated with a monophasic pulse, stochasticity continues to affect whether excitation occurs after the pulse's cessation. To determine whether the same is true when the neuron is stimulated with a CL-BP, the firing outcome of the stochastic HH model was predicted, across multiple trials, at the moment of a CL-BP's cessation. From these predictions, an input-output function was derived (the *predicted input-output function*) and compared against an input-output function derived from the actual firing outcomes (the *actual input-output function*). If stochasticity continues to affect excitation for some time after the cessation of the stimulus, then the relative spread (RS) of the actual input-output function should be greater than that of the predicted input-output function. If it does not, then the two input-output functions should precisely overlap. The difference in the RSs of the two input-output functions may thus be used to quantify the extent that stochasticity affects excitation following stimulus cessation.

The firing outcome was predicted based on the location of the phase point at the moment of the stimulus's cessation (in the example phase paths shown in Figure 3.5, this corresponds to the points $\mathbf{h}^{-}$, $\mathbf{h}$, and $\mathbf{h}^{+}$). Excitation was predicted to occur if—and only if—the phase point exceeded threshold values in both the V and m dimensions. These threshold values were derived from the location that the phase point would occupy at the moment of stimulus cessation if stochasticity were removed from the model and the CL-BP were delivered at threshold level. This point is shown in Figure 4.8, plots A and B, as a filled black square (the phase path on which the square lies resulted from stimulation with CL-BP delivered at a level infinitesimally above threshold level; the square marks the phase point at the moment of stimulus

Stimulus	n_{TP}	n_{TN}	n_{FP}	n_{FN}	n_{E}	Accuracy
A-MP	0	514	0	486	486	0.514
*A-MP	0	514	0	486	486	0.514
C-MP	244	370	123	263	386	0.614
AC-BP	284	408	96	212	308	0.692
*C-MP	439	436	57	68	125	0.875
CA-BP	486	484	9	21	30	0.97

Table 4.1: Quantifying how the effect of stochasticity depends on the stimulus in the stochastic HH model. Four pulse shapes were investigated, a cathodic monophasic pulse (abbreviated C-MP; 20 µs duration), an anodic monophasic pulse (abbreviated A-MP; 20 µs duration), a CL-BP (20 µs/phase duration, 100 µs IPG), and an AL-BP (20 µs/phase duration, 100 µs IPG). For a given stimulus, the firing outcome of the stochastic model was predicted at the moment of the stimulus's cessation across 1000 trials to the stimulus. For each pulse shape, the prediction accuracy was obtained from the number of true positives (n_{TP}), true negatives (n_{TN}), false positives (n_{FP}), and false negatives (n_{FN}); see main text for formula. An extra column reports $n_{\mathrm{E}} = n_{\mathrm{FP}} + n_{\mathrm{FN}}$, the total number of erroneous predictions. As the time of stimulus cessation is earlier for the monophasic pulses, second predictions were made for them (rows marked by an asterisk) at the time $t = 140$ µs, equal to the time of stimulus cessation in the biphasic pulses. *In the case of the CL-BP, stochasticity had almost no effect on firing outcome after the pulse's delivery. In the cases of the AL-BP and the C-MP, stochasticity had an effect both during and after the pulse's delivery. In the case of the A-MP, stochasticity had almost no effect after the pulse's delivery.* Note that an accuracy of 0.5 implies that the firing outcome of the stochastic model cannot be predicted from the firing outcome of the HH model. An accuracy below 0.5 would imply an inverse correlation, which is not expected.

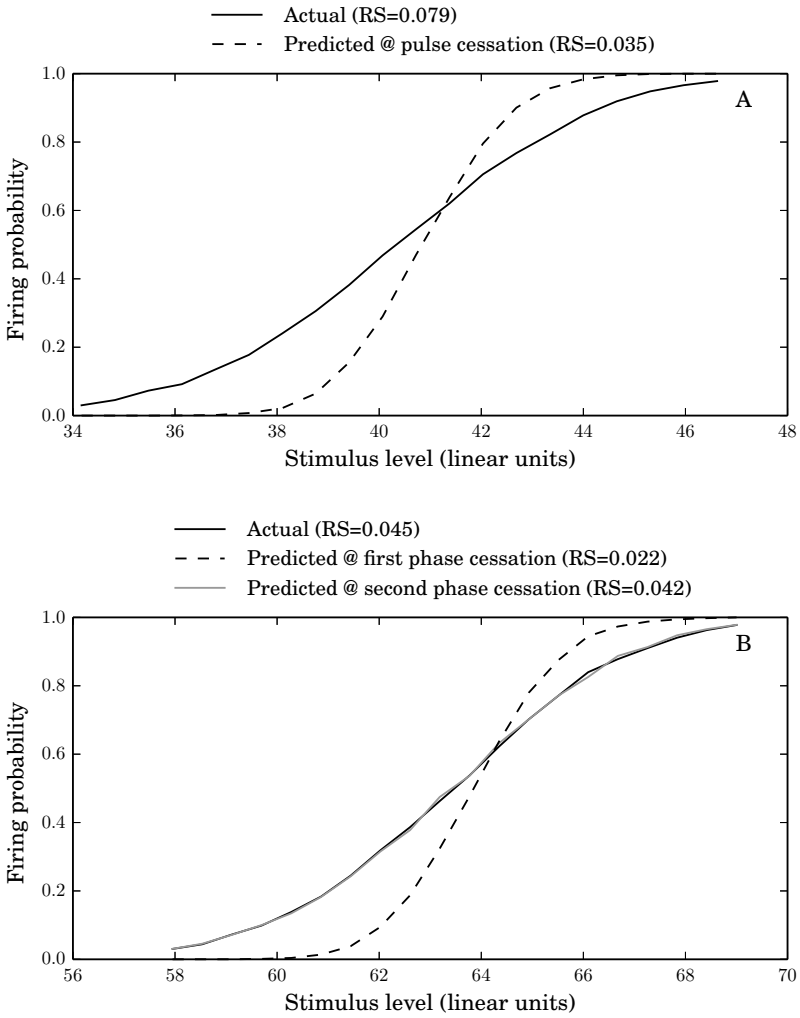

Figure 4.10: Plot A: stimulus is a cathodic monophasic pulse (20µs duration). Plot B: stimulus is a CL-BP (20µs/phase duration, 100 µs IPG).

cessation).

The stochastic HH model was stimulated with a CL-BP of 20 µs/phase duration and 100 µs IPG. The stimulus was delivered at 20 levels, spanning the model's dynamic range. At each level, 7,500 trials were performed. For each trial, the predicted and actual firing outcomes were noted and used to infer the predicted and actual input-output functions, respectively, which are plotted in Figure 4.10, plot B. They overlap almost precisely, having RSs of 0.042 and 0.045, respectively, and thus, excitation can be accurately predicted immediately upon the cessation of the CL-BP. This is in stark contrast to the case of stimulation by a monophasic pulse. To illustrate this, the same methodology was carried out using a cathodic pulse, making predictions at the moment of the pulse's cessation and deriving input-output functions from the predictions and the actual firing outcomes. These are plotted in Figure 4.10, plot A. Here, the RS of the actual input-output function is over twice that of the predicted input-output function (0.079 vs 0.035).

To summarise, when the stochastic HH model is stimulated with a monophasic pulse, stochasticity continues to affect the firing outcome of the model for some time after the pulse's cessation. However, when stimulated with a CL-BP, the firing outcome is already determined by the time of the pulse's cessation.

4.3.3 Related work

As it has thus far been described, whether excitation occurs depends only on whether the stimulus drives the phase point beyond the separatrix and into the suprathreshold domain of the phase plane. Unless driven by externally applied current, the phase point will never cross the separatrix. In the presence of stochasticity, however, Brownian motion in the V and m dimensions can cause the phase point to straddle the separatrix until the saddle node is approached, at which point the phase point is repelled towards either rest or excitation. Figure 4.5 plots the (V, m)-projected phase paths of trials in which the stochastic HH model is stimulated with a 20 µs cathodic pulse. Clear from the Figure is that the phase plane of the stochastic HH model cannot be divided into subthreshold and suprathreshold domains, as was done in the reduced HH model. If one were to attempt to do so, one would find that the phase point drifts between domains due to stochasticity. This is quantified in Figure 4.10, plot A, which plots the input-output function of the stochastic HH model and the input-output function that would be expected if excitation could be predicted from the phase point's location at the moment of stimulus cessation (see Figure caption for methodology). The RS

of the actual input-output function is over twice that predicted, indicating that the predictions underestimate the of stochasticity of the response. The reason that the predictions have a non-zero RS is that the phase point is affected by stochasticity during the pulse's delivery (recalling that the predictions were based on the location of the phase point at the moment of pulse cessation).

Figure 4.10 shows that the predictions of excitation in the stochastic HH model become more reliable as the stimulus level moves further away from the threshold level (either by increasing or decreasing the stimulus level). This is because the probability of the phase point crossing the separatrix due to random perturbation decreases as its distance from the separatrix increases. It would be useful to formalise this by deriving the probability of excitation occurring, given the location of the phase point at a given moment in time. With this in mind, Lecar and Nossal (1971), analysed linearised the HH equations.

A system of nonlinear ODEs, such as is the HH model, can be linearised around a point, $\boldsymbol{x}$, on the phase plane. While the phase point is close to $\boldsymbol{x}$, the linearised system behaves like the original. The motivation for performing such a transformation is that the linear system can be solved analytically (i.e., without numerical integration). Lecar and Nossal linearised the (V, m)-reduced HH model around the saddle point. By doing so, they were able to analytically describe the effect of the Brownian motion in the V and m dimensions. From this, they were able to derive a probability density function (PDF) of the phase point's location after some elapsed period of time. By taking the PDF of the phase point's location an infinite time after stimulus cessation, they were able to determine the probability of excitation. Their analysis provided an important mathematical link between the biophysical variables of the HH model and the input-output function.

Chapter 5

A novel phenomenological model of electrical stimulation

When stimulated with an electrical current pulse, the SGC may elicit an action potential after a stochastic delay. The shape of the stimulating pulse affects the probability of the SGC eliciting an action potential in response to it, and the temporal distribution of the action potential, if elicited. Further, temporally-separated pulses may interact within short time windows, blurring the distinction between individual pulses. To be useful, a model of the electrically stimulated SGC must thus be capable of realistically responding to a stimulus pulse of complex and arbitrary shape. One method by which to achieve this is to directly model the biophysics of the neuron. Biophysical models have been developed which are successful in reproducing the response characteristics of the ANF (e.g., Cartee, 2000; Negm and Bruce, 2008; Rattay et al., 2001a; Rubinstein, 1995; Woo et al., 2010). However, while these models have previously been used to study the responses of large populations of SGCs (e.g., Imennov and Rubinstein, 2009), they are difficult to use: the parameter-space of a biophysical model is vast and the individual parameters affect the response of the neuron in complex ways. There has been no procedure published for systematically parametrisation a biophysical model to reproduce a desired set of response statistics.

Phenomenological models provide an alternative to biophysical models. Phenomenological models reproduce only the statistics of the response, without explicitly modelling the biophysics of the SGC. By doing so, the parameter-space is reduced and it is possible to directly and independently control individual response characteristics via the model parameters. Phenomenological models have previously been used to model

the electrically stimulated SGC (e.g., Carlyon et al., 2005; Chen and Zhang, 2007; Chen, 2012; Cohen, 2009a,b,c,d,e; Goldwyn et al., 2012; Hamacher, 2004; Macherey et al., 2007). However, none have simultaneously reproduced how the shape of a stimulus pulse affects both the probability of it evoking an action potential and the temporal distribution that the action potential takes if evoked.

A key focus of my PhD has been to develop a model capable of reproducing the statistics of the SGC's response to both monophasic and CL-BPs. The model that I developed, presented in this chapter, is the first phenomenological model that has been shown to reproduce the effect on threshold of the trailing anodic phase of a CL-BP. The standard phenomenological model, the stochastic leaky integrate-and-fire (SLIF) neuron, discretises the action potential as a single moment of spiking. In my model, the membrane potential of the SGC is modelled by processing the stimulus current with a leaky integrator. As in the SLIF neuron, excitation occurs when the membrane potential exceeds a stochastic threshold. Unlike the SLIF neuron, there exists a delay between the moment at which the membrane potential exceeds the threshold and the moment at which the resulting spike is emitted. This emulates the delay in the generation of the action potential that is present in the SGC. Further, inspired by empirical observations, the spike is allowed to be cancelled if sufficient anodic stimulation occurs before the spike is emitted. By doing so, the model is able to reproduce the effect of the interphase gap on the probability of a CL-BP evoking an action potential in the SGC. The description of the model is split into three sections. First, I introduce the existing SLIF neuron, describing its parametrisation and summarising its capabilities and limitations (section 5.1). I then extend the SLIF neuron to introduce a delay between the moment at which the membrane potential exceeds the threshold and the moment at which the resulting spike is elicited. This forms a self-contained model in itself, reproducing temporal properties of the SGC's response to a monophasic stimulus (Section 5.2). Finally, I further extend the model so that a spiking may be cancelled by anodic current, comparing its results against those from cat SGCs (section 5.3).

5.1 The stochastic leaky integrate and fire neuron

The stochastic leaky integrate-and-fire (SLIF) neuron provides a simple model of the electrically stimulated neuron. The model is identical to the LIF model, other than that the threshold potential $\boldsymbol{\theta}$ is a normally-distributed random variable instead of a constant.

5.1.1 Model description

The stimulus signal $I(t)$ is processed by a leaky integrator to give $V(t)$, which may be interpreted as the membrane potential of the model neuron at time t (Abbott and Kepler, 1990; Gerstner, 1995). The stimulus signal and the membrane potential are related by the ordinary differential equation

$$\tau \frac{\mathrm{d}V}{\mathrm{d}t} = -RI - V, \tag{5.1}$$

where τ is the time constant of the neural membrane and R is its resistance, arbitrarily assumed to be 1 Ω. A spike is generated at the moment $V(t)$ first exceeds a threshold value $\boldsymbol{\theta}$, an event that referred to as *threshold crossing*. Throughout this section, I use t_0 to denote the time of threshold crossing. In order to reproduce the stochastic properties of excitation, $\boldsymbol{\theta}$ is a normally-distributed random variable with mean μ and standard deviation σ. The outcome of $\boldsymbol{\theta}$ is time-invariant and does not change other when explicitly reset (i.e., so that $\boldsymbol{\theta}$ is a single, scalar value, rather than a time-varying signal).

5.1.2 Model response properties

The SLIF neuron has three parameters: μ, σ, and τ. This section shows how these can be uniquely determined so that the model reproduces data from cat SGCs.

Excitation

To be consistent with extracellular stimulation, V is defined in (5.1) so that cathodic current (corresponding to negative values of I) is depolarising, driving V towards or above threshold. The SLIF neuron does not model the depolarising effects of anodic current on the nodes with negative activating function values, and thus, anodic current can not cause excitation in the SLIF neuron.

Input-output function

The probability of a stimulus evoking a spiking in the SLIF neuron is given by the probability of V exceeding $\boldsymbol{\theta}$. Let $v(t)$ equal the value of V at time t in the case of $I = -1$ A. Because (5.1) is linear, $Lv(t)$ is then the value of V at time t in the case of $I = -L$ A. Solving (5.1) for V with $I = -1$ A and $R = 1$ Ω, we have

$$v(t) = 1 - e^{-\varphi/\tau}.$$

We may now express the probability $\Pr(\text{spiking}|L,\varphi)$ of a cathodic, monophasic stimulus of level L and duration φ evoking a spiking in the SLIF neuron as

$$\begin{aligned}\Pr(\text{spiking}|L,\varphi) &= \Pr(V \text{ exceeds } \boldsymbol{\theta}) \\ &= \Pr(Lv(\varphi) > \boldsymbol{\theta}) \qquad\qquad \text{as } \boldsymbol{\theta} \text{ is time-invariant} \\ &= F_{\boldsymbol{\theta}}(Lv(\varphi)), \end{aligned} \tag{5.2}$$

where $F_{\boldsymbol{\theta}}$ is the cumulative distribution function of $\boldsymbol{\theta}$. As $\boldsymbol{\theta}$ is normally-distributed with mean μ and standard deviation σ, we have

$$F_{\boldsymbol{\theta}}(x) = \Phi\left(\frac{x-\mu}{\sigma}\right),$$

and so

$$\Pr(\text{spiking}|L,\varphi) = \Phi\left(\frac{Lv(\varphi)-\mu}{\sigma}\right), \tag{5.3}$$

which may be re-arranged to have the same as (2.12), which described the input-output functions of cat SGCs (Section 2.3.1). Collating the two, we have

$$\Phi\left(\frac{L-m}{s}\right) = \Phi\left(\frac{L-\mu/v(\varphi)}{\sigma/v(\varphi)}\right),$$

and thus,

$$m = \frac{\mu}{v(\varphi)} \tag{5.4}$$

and

$$s = \frac{\sigma}{v(\varphi)}, \tag{5.5}$$

where m and s are as defined in section 2.3.1. Inverting (5.4) and (5.5) gives the model parameters μ and σ in terms of the empirically-derived values m and s.

To summarise, the input-output function of the SLIF neuron has the form of the cumulative distribution function (CDF) of the Gaussian distribution, which has previously been shown to describe the input-output functions of SGCs (see Section 2.3.1). The SLIF neuron may thus be parametrised to reproduce a given SGC's input-output function. Given the mean and standard deviation of this function (or equivalently, the threshold level and RS), the model parameters that will reproduce it may be derived analytically.

Strength-duration function

The strength-duration function relates pulse duration to threshold level. The threshold level is defined as the stimulus level that evokes spiking with probability 0.5. Thus, if L is the threshold level of a monophasic pulse of duration φ, then from (5.3) we have

$$\Pr(\text{spiking}|L,\varphi) = 0.5 = \Phi\left(\frac{Lv(\varphi)-\mu}{\sigma}\right),$$

from which we obtain

$$Lv(\varphi) = \mu.$$

Rearranging and expanding $v(\varphi)$, we have

$$L = \frac{\mu}{1-\exp(-\varphi/\tau)}, \tag{5.6}$$

which is of the same form as (2.13), which describes the strength-duration functions of cat SGCs (see section 2.3.1).[1] Collating the two equations, (5.6) and (2.13), gives

$$\frac{\mu}{1-\exp(-\varphi/\tau)} = \frac{I_{\text{thr}}^{\infty}}{1-\exp\left(k\varphi\right)},$$

and so we find that $\mu = I_{\text{thr}}^{\infty}$ and $1/\tau = k$, giving an alternative parametrisation of model parameter μ in terms of the empirically-observed rheobase, and giving model parameter τ in terms of the empirical parameter k. Recalling from Section 2.3.1 that the empirically observed chronaxie is given by chronaxie $= \log(2)/k$, we have

$$\tau = \frac{\text{chronaxie}}{\log(2)}.$$

To summarise, the strength-duration function of the SLIF neuron has the same form as those of SGCs, and further, the model parameter τ may be derived analytically from the chronaxie of a given SGC so that the model reproduces the SGC's input-output function.

Temporal response properties

Figure 5.1 plots mean latency and jitter of a cat SGC's response to a brief (40 µs) monophasic stimulus (Miller et al., 1999b). Increasing stimulus level reduces both the mean latency and the jitter of the response. Also plotted is the mean latency and jitter

[1] The derivation of the strength-duration function of the passive membrane has previously been given (via different means) in chapter 3 of Tuckwell (1988).

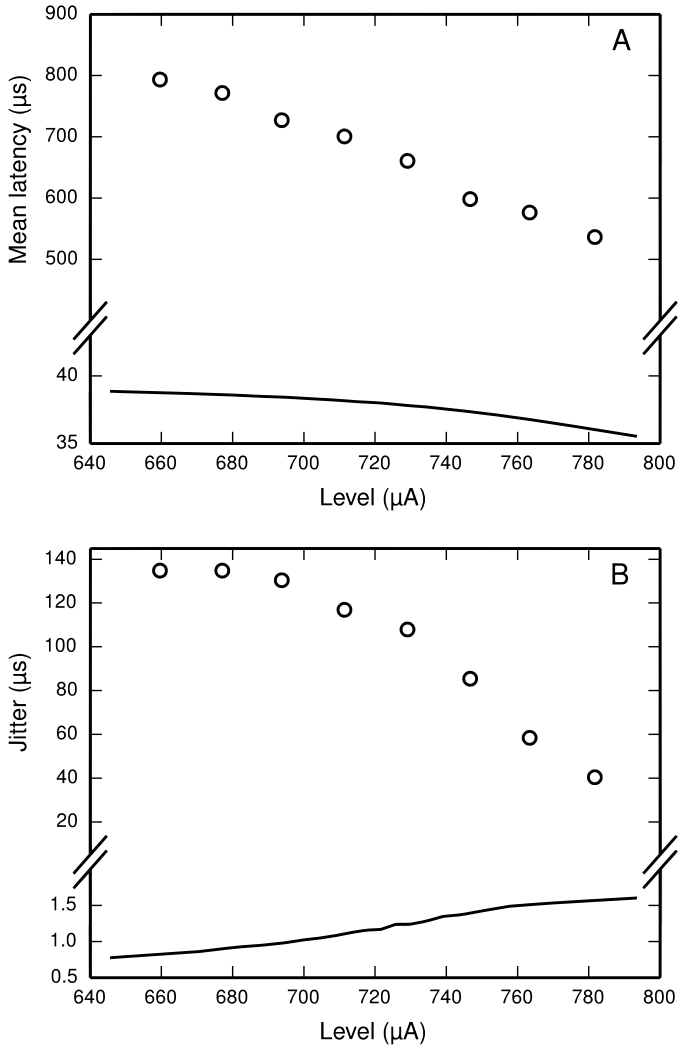

Figure 5.1: The SLIF neuron does not reproduce the temporal response statistics of the ANF or their dependence on stimulus level. Plotted are the mean latency (**plot A**) and jitter (**plot B**) of the responses to a monophasic stimulus (40 µs duration) for the SLIF neuron (**solid lines**) and a cat ANF (Miller et al. 1999; **open circles**). The stimulus levels span the dynamic range of the ANF. Note the change in ordinate scale.

of the SLIF neuron under identical conditions. The SLIF neuron lacks the extent of temporal stochasticity that is observed in the SGC (jitter at threshold level is 1 µs for the model and 112 µs for the SGC). Further, the mean latency is under-predicted by the SLIF neuron (latency at threshold level is 38 µs for the model and 681 µs for the SGC) and does not show the dependence on stimulus level that is seen in the SGC. It is not possible to parametrise the SLIF neuron to reproduce these temporal response properties whilst simultaneously maintaining the input-output and strength-duration functions that have already been fitted to data from cat SGCs. These failings of the SLIF neuron have been noted previously (Fredelake and Hohmann, 2012; Goldwyn et al., 2012; Hamacher, 2004) and are addressed by my extension to the SLIF neuron in section 5.2.

Biphasic response properties

The threshold level of a cathodic pulse is elevated by the inclusion of a trailing anodic phase, transforming it into a CL-BP (Gorman and Mortimer, 1983; Miller et al., 2001b; Shepherd and Javel, 1999). As the IPG is increased, the threshold level tends towards that of the cathodic phase alone, reaching its asymptote after ∼250 µs (Shepherd and Javel, 1999). The SLIF neuron is fundamentally unable to reproduce this increase in threshold level associated with cathodic-leading biphasic stimulation. A threshold crossing, if one occurs, will always occur during the excitatory, cathodic current. If the threshold crossing occurs, then it cannot be undone by the trailing, anodic phase. If a threshold crossing does not occur during the leading cathodic phase, then it cannot occur during the trailing anodic phase. Thus, any trailing, anodic current present in a stimulus has no effect on the threshold level of that stimulus in the SLIF neuron.

Summary

This section has introduced the SLIF neuron and shown that it may be analytically parametrised to reproduce the strength-duration and input-output functions of an arbitrary SGC's response to a monophasic stimulus. The ease with which these important response statistics may be fitted to data makes the SLIF neuron an attractive candidate for modelling the response of the electrically stimulated SGC. However, this section has also shown that the latency distribution of the SLIF neuron does not reproduce that of the SGC and that the SLIF neuron is unable to respond to a CL-BP in a way that mimics the SGC.

5.2 The temporal leaky integrate-and-fire neuron

In this section, the SLIF neuron is extended to reproduce the temporal properties of the SGC's response to a monophasic stimulus. This is done by introducing a stochastic delay between the time of threshold crossing and the time of spiking. The delay has no effect on the probability of the neuron responding to a stimulus, which is unchanged from that of the SLIF neuron. As such, the input-output and strength-duration functions of the SLIF neuron are preserved. I refer to the resulting model as the *temporal leaky integrate-and-fire (TLIF) neuron.*

5.2.1 Model assumptions

The TLIF neuron makes a number of assumptions regarding how the SGC responds to the stimulus. These are discussed here, prior to providing a description of the model.

Predicting the latency distribution from the firing probability

The TLIF neuron assumes that the latency distribution of the ANF's response to a stimulus is well predicted by the probability of the stimulus evoking a spike. The latency distribution of the spike, if evoked, is assumed to be well approximated by a Gaussian distribution.

The action potential initiation period

When a neuron is depolarised sufficiently to evoke an action potential, a delay occurs between the membrane being depolarised by the stimulus and the action potential being generated. During this delay, further stimulation can continue to affect the time at which the action potential is generated (Miller et al., 2001b; van den Honert and Mortimer, 1979). I refer to this delay as the action potential initiation period and assume that its duration is stochastic and stimulus-dependent, with its variability equal to the variability of the spike timing that is observed by the recording electrode.

Previous threshold crossings

As in the SLIF neuron, the time of threshold crossing in the temporal leaky integrate-and-fire (TLIF) neuron is given by t_0. It is assumed that t_0 is the earliest threshold crossing, and so there exists no $s < t_0$ for which $V(s) > \boldsymbol{\theta}$. This assumption does not prevent the model from being able to recover following a threshold crossing, see section 5.5.5.

5.2.2 Model description

Biophysically, the generation of an action potential is a continuous process occurring over a time course of hundreds of microseconds. Stimulation occurring during this time can continue to affect the latency distribution of the response (van den Honert and Mortimer, 1979). In the SLIF neuron, however, the action potential is considered a discrete moment of threshold crossing after which further stimulation has no effect. To allow the stimulus to continue to affect the latency distribution of the response after a threshold crossing, the action potential is discretised into three epochs. The first epoch, modelled by the variable t_0 (defined previously), is the moment at which the stimulus depolarises the ANF sufficiently for an action potential to be generated in the absence of further stimulation. It signifies the start of the action potential initiation period. The second epoch, modelled by the variable t_1, is the moment at which the action potential is irrevocably generated and cannot be influenced by further stimulation. It signifies the end of the action potential initiation period, which is thus modelled by the interval $[t_0, t_1]$. After its initial generation, the action potential is conducted centrally by the axon until it is observed by the recording electrode, an event I refer to as *action potential observation*. The third epoch, modelled by the variable t_{spk}, is the moment of action potential observation.

As defined in Section 5.1.1, the variable t_0 is the time at which a threshold crossing occurs. Upon a threshold crossing occurring in the TLIF neuron, a value is generated for the variable t_1 such that the duration of the delay between t_0 and t_1 is exponentially distributed with a stimulus-dependent variance. A value is then generated for the variable t_{spk} so that the duration of the delay between t_0 and t_{spk} has a normal distribution with a stimulus-dependent mean and variance. The variance is the same as for t_1, though the mean is considerably larger so as to emulate the effects of axonal conductance on latency.

The dependence of the delays $t_1 - t_0$ and $t_{\text{spk}} - t_0$ on the stimulus are achieved by use of two empirically-derived functions: *lat* and *jit*, both of which are plotted in Figure 5.2. The function $lat(p)$ predicts the mean delay between the start of the action potential initiation period and the moment of action potential observation in the ANF stimulated so as to evoke an action potential with probability p. The function $jit(p)$ is similar, but predicts the standard deviation of the action potential initiation period. Both functions are empirically derived. The probability p on which both functions depend is the a-priori probability of V exceeding $\boldsymbol{\theta}$ during the associated action potential initiation period, $[t_0, t_1]$. In this way, continued stimulation during

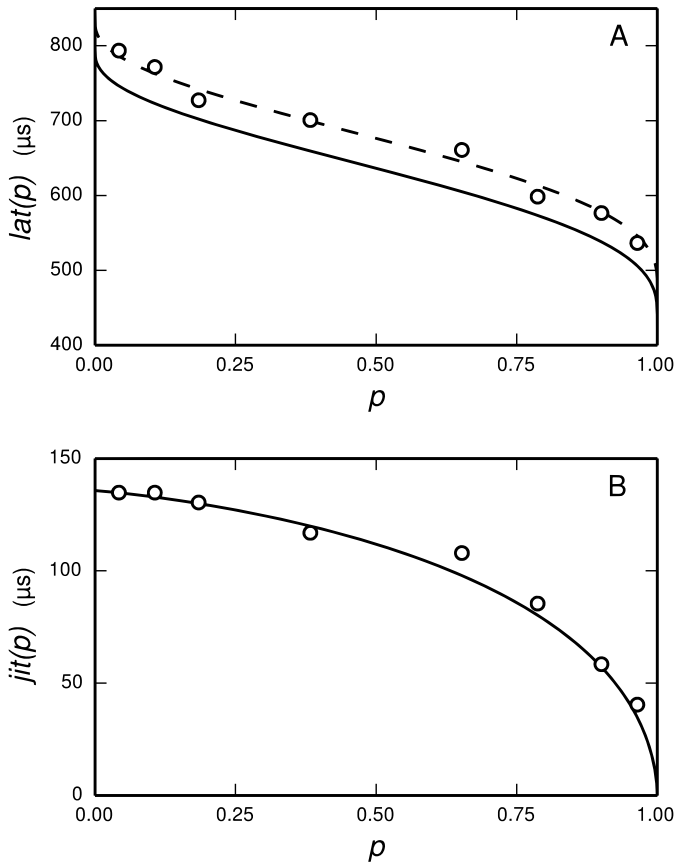

Figure 5.2: Parametrisation of the *lat* and *jit* functions (see text) from empirical data. The *lat* function (**plat A, solid line**) is parametrised to the mean latency of an ANF's response to a 40 µs monophasic pulse (**plot A, open circles**; Miller et al., 1999b). The *jit* function (**plot B, solid line**) is parametrised to the jitter of the same responses (**plot B, open circles**). The action potential initiation period is assumed to begin at the time of stimulus cessation, and so *lat* is chosen to under-predict the data by 40 µs. To better show the fit to data, *lat*+40 µs (**dashed line, plot A**) is also plotted.

the action potential initiation period may shorten it, bringing forward the time of spiking. The next section will show how p is derived.

Probability of V exceeding $\boldsymbol{\theta}$ during the interval $[t_0, t_1]$

The a-priori probability of V exceeding $\boldsymbol{\theta}$ during the associated action potential initiation period $[t_0, t_1]$ is given by $\Pr(V(t) > \boldsymbol{\theta})$, where t is the time at which V is maximal within $[t_0, t_1]$. Because the lower bound of this interval, t_0, is the time of threshold crossing, it must be the case that $t \geqslant t_0$ (otherwise a threshold crossing would have already occurred before time t_0, contradicting the assumption of the model that t_0 is the earliest threshold crossing). Therefore, the lower bound of the interval $[t_0, t_1]$ is redundant and the a-priori probability of V exceeding $\boldsymbol{\theta}$ during $[t_0, t_1]$ is equal to the a-priori probability of it exceeding $\boldsymbol{\theta}$ during $[0, t_1]$. With this in mind, the a-priori probability of V exceeding $\boldsymbol{\theta}$ during the action potential initiation period $[t_0, t_1]$ will henceforth be denoted by $P_{\text{TLIF}}(t_1)$, with

$$P_{\text{TLIF}}(t) = \Phi\left(\frac{V(s) - \mu}{\sigma}\right),$$

where

$$s = \underset{x \in [0,t]}{\arg\max}\,[V(x)]$$

and Φ is the CDF of the Gaussian distribution.

Generation of t_1

The variable t_1 models the time at which the action potential initiation period ends. Here it is described how the TLIF neuron generates a value for t_1 such that the delay between t_0 and t_1 has an exponential distribution with a standard deviation that approximates the jitter of the ANF's response to the same stimulus. The algorithm maintains causality so that at simulation time t, the model only has access to the membrane potential up until time t.

From the time of threshold crossing onwards, the TLIF neuron generates time-varying estimates of t_1. Let Y be an exponentially-distributed (unit rate constant) random variable. The estimate of t_1 made at simulation time t is referred to as $\hat{t_1}(t)$ and is given by

$$\hat{t_1}(t) = t_0 + Y\, jit(P_{\text{TLIF}}(t)). \tag{5.7}$$

The final value for t_1 is the time at which t first reaches or exceeds $\hat{t_1}$, at which point

the action potential initiation period has already come to an end and so its end time is no longer in flux. The time t_1 is thus a fixed point of $\hat{t_1}$; that is,

$$\hat{t_1}(t_1) = t_1. \tag{5.8}$$

Because $jit(P_{\text{TLIF}}(t))$ is non-negative and increases monotonically with t, the function $\hat{t_1}$ has a single, unique, fixed point that may be found by finding the root of

$$g(x) = \hat{t_1}(x) - x.$$

Given that both jit and Y are non-negative, $\hat{t_1}(x)$ must be greater or equal to t_0, and so $g(t_0)$ must be greater or equal to 0. Further, given that jit is always finite, there must exist some finite $x \gg t_0$ for which $g(x) < 0$. We may efficiently find such an x by iterating through successive values of $i \in \mathbb{Z}^+$ until we find an i for which $g(t_0^i) < 0$. We thus have an interval $[t_0, t_0^i]$ whereat opposite ends g has opposite signs, and so, by Bolzano's theorem (Estep, 2006, chapter 32), the interval must contain the root of g, and thus, the fixed point of $\hat{t_1}$. The bisection method (see, for example, Quarteroni et al., 2010, chapter 6) may then be used to find this root, providing the value for t_1.

The definition of $\hat{t_1}$ and the significance of its fixed point may be more readily explained by means of a diagram. We first note that the term $Y\, jit(P_{\text{TLIF}}(t))$ from (5.7) results in an exponentially-distributed random variable with rate constant $\lambda = jit^{-1}(P_{\text{TLIF}}(t))$, and that this may be equivalently expressed as

$$Y\, jit(P_{\text{TLIF}}(t)) = F^{-1}(Y'; jit^{-1}(P_{\text{TLIF}}(t))),$$

where Y' is a uniformly distributed random variable in the interval $(0, 1)$, and

$$F^{-1}(p; \lambda) = -\lambda^{-1} \log(1 - p)$$

is the quantile function[2] of the exponential distribution with rate constant λ. We may then rewrite (5.7) as

$$\hat{t_1}(t) = t_0 + F^{-1}(Y';\ jit^{-1}(P_{\text{TLIF}}(t))),$$

and so

$$Y' = F(\hat{t_1}(t) - t_0;\ jit^{-1}(P_{\text{TLIF}}(t))), \tag{5.9}$$

[2]The quantile function is the inverse of the cumulative distribution function, so that if $p = F(x; \lambda)$, then $x = F^{-1}(p; \lambda)$.

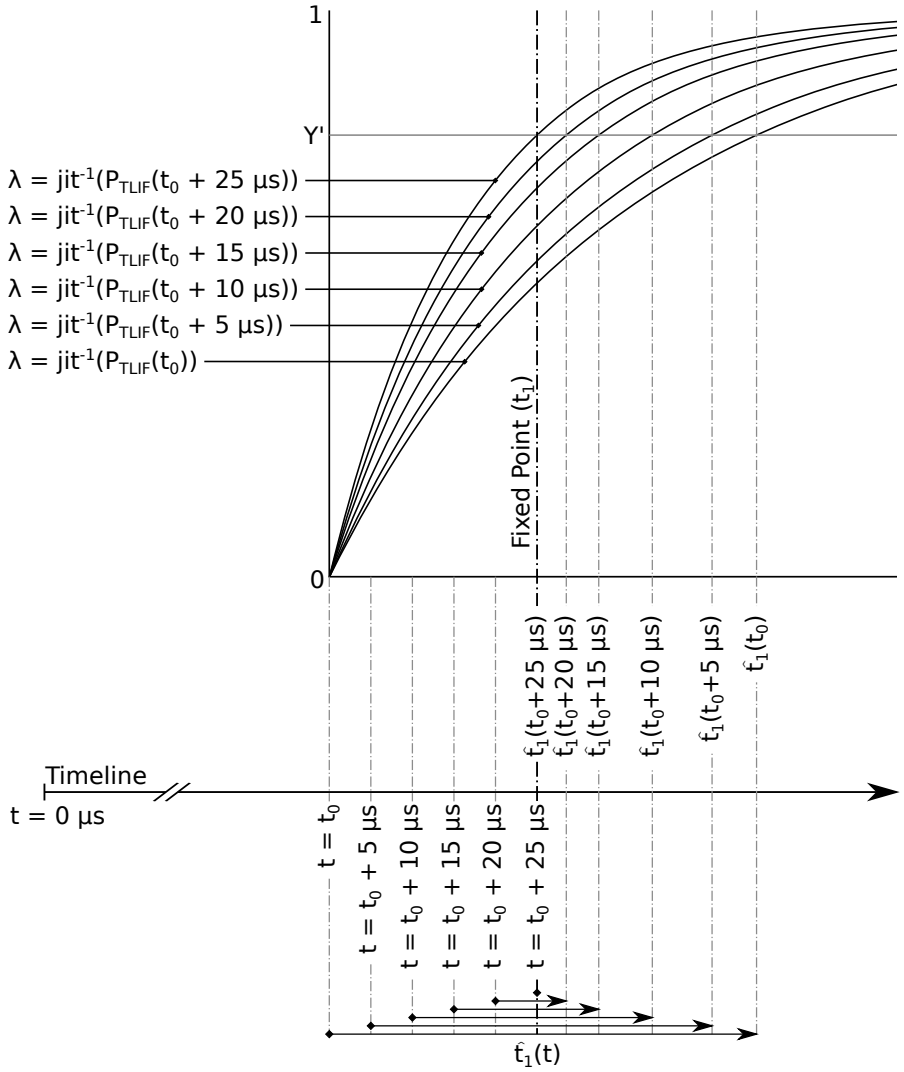

Figure 5.3: Visualising the generation of t_1. A timeline shows the progression of time, with epochs marked in 5 µs increments from time t_0 to time $t_0 + 25$ µs. Overlaid above the timeline is a plot that has its abscissa calibrated with the timeline, so that the plot's origin corresponds to the time t_0. Each curve in the plot is a CDF related to an epoch from the timeline, as described by equation 5.9, so that the epoch with time t has a curve corresponding to the CDF of the exponential distribution with rate constant $\lambda = jit^{-1}(P_{\text{TLIF}}(t))$. A horizontal grey line indicates an example outcome of Y'. For a given epoch of time t, the point (projected to the timeline) at which the grey line intersects the epoch's CDF gives $\hat{t_1}(t)$. This relationship between epoch, point of intersection, and $\hat{t_1}$ is made explicit by arrows at the bottom of the figure, each of which points from a time t to the time $\hat{t_1}(t)$. The arrows corresponding to the five earliest epochs all point rightwards, to the future. The arrow of the sixth epoch points unto itself, marking the fixed point of $\hat{t_1}$, and thus t_1.

where $F(x;\lambda) = 1 - e^{-\lambda x}$ is the cumulative distribution function (CDF) of the exponential distribution with rate constant λ. When expressed in this form, we may visualise $\hat{t_1}(t)$ as the abscissa of the point at which the rightwards-shifted CDF of an exponential distribution of rate constant $\lambda = jit^{-1}(P_{\text{TLIF}}(t))$ is equal to Y', as illustrated in figure 5.3. As time t increases, the rate constant of the exponential distribution may change while the outcome of Y' remains constant, and so the changing rate constant has the effect of horizontally sliding the point at which the CDF equals Y'. Initially (i.e., at the moment t_0 of threshold crossing), this point of intersection is in the future (i.e., $\hat{t_1}(t) > t$, where $t = t_0$). However, as time advances, t shall eventually overtake $\hat{t_1}(t)$, either by the forward-progression of t, or by the backwards-sliding of the point of intersection. The moment at which this happens is a fixed point of $\hat{t_1}$, and is thus, by (5.8), the moment t_1 at which the action potential initiation period ends.

Empirically, when responding to a single, brief ($<\sim$100 ms) stimulus delivered at a level sufficient to evoke a response with probability p, the TLIF neuron generates values of t_1 with a standard deviation close to $jit(p)$, while also ensuring that any stimulus current occurring after t_1 has no effect on the value of t_1.

Generation of t_{spk}

After the action potential initiation period ends at time t_1, the TLIF neuron generates t_{spk}, modelling the time of action potential observation, taking into account the delay associated with axonal conductance. The time t_{spk} is generated so that, across repeated trials to the same stimulus, the delay between t_0 and t_{spk} is normally distributed with mean and standard deviation given by $lat(p)$ and $jit(p)$, respectively, where p is the probability that the membrane potential exceeds threshold during the interval $[t_0, t_1]$. Formally,

$$t_{\text{spk}} = t_0 + X\, jit(p) + lat(p), \tag{5.10}$$

where $p = P_{\text{TLIF}}(t_1)$ and X is a standard normal random variable.

Relationships between model variables

To summarise the flow of information in the TLIF neuron, Figure 5.4 shows how the different model parameters, variables, and functions are related to one another. The input to the model is the current signal I and the final output is the time of action

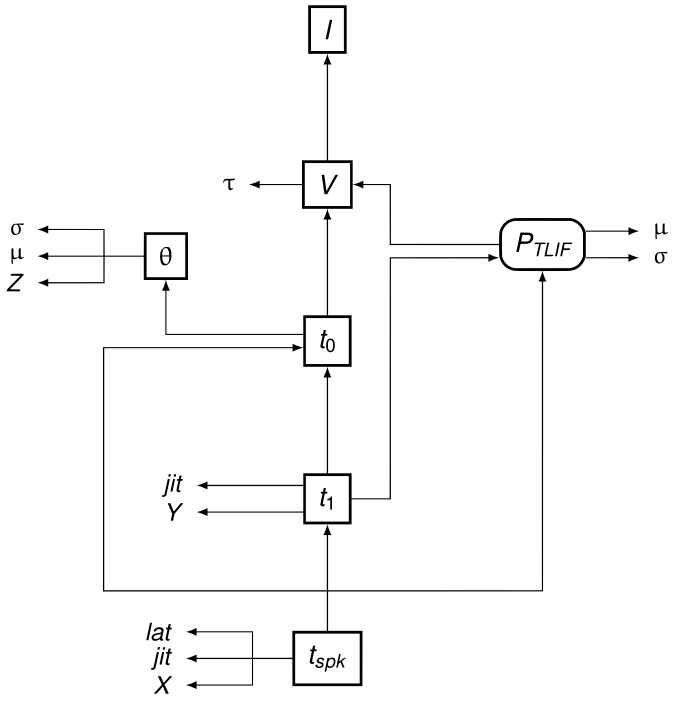

Figure 5.4: Data dependency in the TLIF neuron. The entities are the functions, variables, and parameters of the model. Each entity points to those on which its value depends. Boxed entities with sharp edges are model variables and boxed entities with rounded edges are functions. The unboxed entities X, Y, and Z are random variables. The other unboxed entities are model parameters. The random variables X and Z have standard normal distributions. The random variable Y has an exponential distribution.

potential observation, t_{spk}.

Model response properties

The TLIF neuron responds to a stimulus with the same probability as the SLIF neuron: upon a threshold crossing, both models are guaranteed to emit a spike. Thus, the input-output and strength-duration functions of the SLIF neuron are preserved in the TLIF neuron, without the need to change any of the SLIF neuron's parameters. However, the time t_{spk} of the spiking in the TLIF neuron is changed so as to better reflect the latencies observed empirically in the ANF.

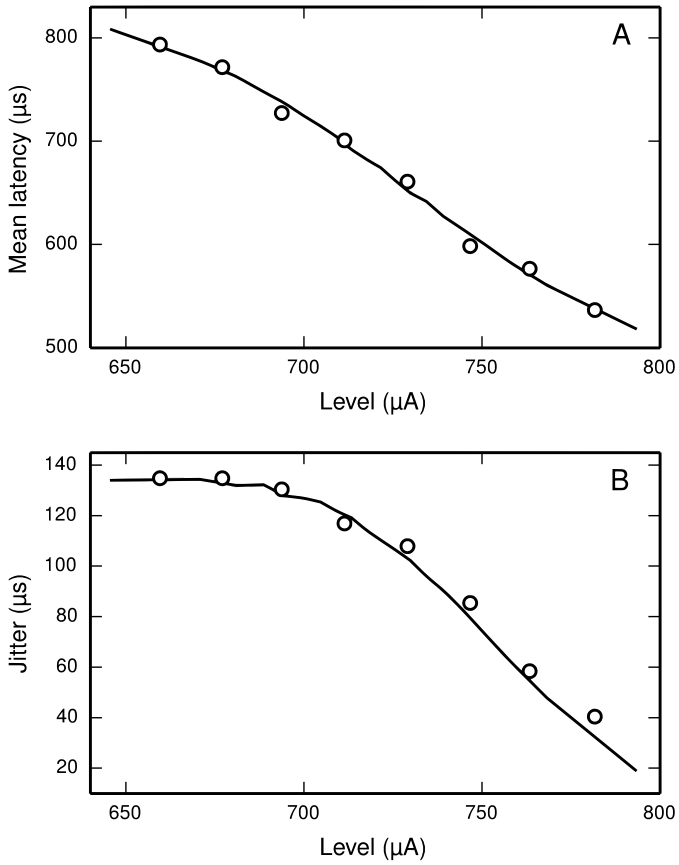

Figure 5.5: The TLIF neuron reproduces the temporal response statistics of the ANF and their dependence on stimulus level. Plotted are the mean latency (**solid line, plot A**) and jitter (**solid line, plot B**) of the TLIF neuron's responses to a monophasic stimulus (40 µs duration) delivered at levels spanning the neuron's dynamic range. The mean latency and jitter data used in Figure 5.1 are also plotted (**open circles**; Miller et al., 1999b).

Miller et al. (1999b) recorded the mean latency and jitter of the responses of an ANF to a monophasic stimulus presented at a range of stimulus levels spanning the dynamic range of the ANF. Their results are plotted in Figure 5.5, along with the corresponding results from the TLIF neuron. The TLIF neuron is able to quantitatively reproduce the mean latency and jitter of the ANF at all stimulus levels. Regardless of stimulus level, the latency distribution of the TLIF neuron is well approximated by a Gaussian distribution, a close approximation to that of the cat ANF (Javel and Shepherd, 2000).

5.2.3 Summary

This section has described how I extended the SLIF neuron so as to model the action potential initiation period of the ANF, resulting in the TLIF neuron. Stimulus current occurring during the action potential initiation period continues to affect the latency of the spike, although the spike's probability is unaffected. The TLIF neuron predicts the latency distribution with which the ANF would have responded to the stimulus by using the probability that the membrane potential exceeds threshold during the action potential initiation period. By doing so, the TLIF neuron is able to quantitatively reproduce the mean and standard deviation of the latency of the ANF's response to a monophasic stimulus, and the dependence of both on stimulus level.

5.3 Biphasic leaky integrate-and-fire neuron

A subthreshold CL-BP may produce an almost arbitrarily-large transient depolarisation of the membrane that does not result in spiking, despite the depolarisation exceeding the threshold above which excitation would have occurred in monophasic stimulation (Dean and Lawrence, 1983; Reilly et al., 1985). If the membrane is modelled by the SLIF neuron, then this transient depolarisation shall immediately cause a threshold crossing, and thus a spike shall be emitted before the anodic phase may have any effect. For this reason, the SLIF neuron is unable to reproduce how the thresholds of CL-BPs are increased relative to monophasic thresholds, or how the magnitude of the threshold increase depends on the IPG of the stimulus. In the TLIF neuron, a delay occurs between threshold crossing and spiking, modelling the action potential initiation period of the membrane. During this delay, continued stimulation may affect the timing of the spike, but not the probability that the spike will eventual occur, and so the TLIF neuron suffers the same shortcoming in responding to a CL-BP as the

SLIF neuron. In this section, the model is further extended so as to reproduce the effect of the anodic current on the probability of a spike being generated. By doing so, the model is able to reproduce the statistics of the SGC's response to a CL-BP, without affecting how it responds to monophasic stimuli. I will refer to the final model as the *biphasic leaky integrate-and-fire (BLIF) neuron.*

5.3.1 Model assumptions

The biphasic leaky integrate-and-fire (BLIF) neuron makes the same assumptions as those made by the TLIF neuron. Further, the BLIF neuron is grounded on the assumption that spiking may be cancelled by anodic current at any time during the action potential initiation period, defined by the interval $[t_0, t_1]$. The ability for anodic currents to abolish an action potential that would have otherwise been generated has been observed experimentally in animal preparations (Tasaki, 1956; van den Honert and Mortimer, 1979; Weitz et al., 2011).

5.3.2 Model description

The BLIF neuron is similar to the TLIF neuron: the time course of the action potential is modelled by the same three variables: t_0, t_1, and t_{spk}. The equations used to generate the values of t_1 and t_{spk} are parallels to those used by the TLIF neuron. The BLIF neuron differs from the TLIF neuron in that a spike may be cancelled after a threshold crossing occurs. A spike is cancelled if sufficient anodic charge is delivered during its associated action potential initiation period.

Generation of t_1

The method by which the BLIF neuron generates the time t_1 is similar to that of the TLIF neuron. However, in the BLIF neuron, it becomes useful to set a minimum possible duration for the action potential initiation period. To do so, a new model parameter is introduced: φ. The time t_1 is now given by

$$t_1 = \max(\varphi, t), \tag{5.11}$$

where t is such that $\hat{t_1}(t) = t$ and $\hat{t_1}$ is as defined previous. Increasing has the effect of decreasing the probability of a CL-BP evoking a spike.

Spike cancellation

Given that a threshold crossing occurred at time t_0 and the corresponding action potential initiation period ends at time t_1, the impending spike is cancelled if

$$\int_{t_0}^{t} I(s)\ \mathrm{d}s > 0, \text{ for any } t \in [t_0, t_1].$$

That is, a spike is cancelled if the total charge delivered during the action potential initiation period ever becomes positive (anodic). In the event of spike cancellation, the model terminates as though no threshold crossing occurred (recovery following spike cancellation is discussed in section 5.5.5).

Probability of spiking in the BLIF neuron

As in the TLIF neuron, the BLIF neuron must predict the probability of the stimulus evoking an action potential in the real ANF to infer the latency distribution with which to respond. In the BLIF neuron, this is given by $P_{\text{BLIF}}(t_1)$, the probability that the membrane potential exceeds threshold during the interval $[t_0, t_1]$ and that the resulting spike is not subsequently cancelled.

Let $T_{Q_0}(t)$ denote the time at which the charge delivered by the stimulus since time t first becomes positive (anodic), defined as the smallest value of s for which $\int_t^s I(u)\ \mathrm{d}u < 0$, or ∞ if no such value for s exists. Given that a threshold crossing occurs at time t_0, the associated spike will be cancelled if $T_{Q_0}(t_0) < t_1$. If $P_{t_1}(t; t_0)$ denotes the probability that t_1 occurs before time t, given the time of threshold crossing t_0, then the probability of spike survival (i.e., no cancellation) is given by $P_{t_1}(T_{Q_0}(t_0); t_0)$. In a single simulation, t_0 has a fixed value. However, across repeated simulations to the same stimulus, t_0 has a degree of variability which affects the probability of spike cancellation. Therefore, the probability derived by P_{t_1} must be integrated across time to account for the variability of t_0. Formally,

$$P_{\text{BLIF}}(t) = \int_0^t P'_{\text{TLIF}}(s) P_{t_1}(T_{Q_0}(s); s)\ \mathrm{d}s, \tag{5.12}$$

where P'_{TLIF} denotes the derivative of P_{TLIF}. The general definition of P_{t_1} is given by

$$P_{t_1}(t; t_0) = \int_{t_0}^{t} \lambda(s) \exp((t_0 - s)\lambda(s))\ \mathrm{d}s + \int_{t_0}^{t} \lambda'(s)(s - t_0) \exp((t_0 - s)\lambda(s))\ \mathrm{d}s,$$

where $\lambda(s) = 1/jit(s)$ and λ' is the derivative of λ. For computational efficiency, it is beneficial to find a closed form expression for P_{t_1}. This is made possible by noting that

λ is monotonically increasing, which allows for the simpler, computationally efficient formulation,

$$P_{t_1}(t;s) = \begin{cases} 1 - \exp\left(-\dfrac{t-s-\varphi}{jit(P_{\text{TLIF}}(t))}\right), & t \geqslant s+\varphi \\ 0, & t < s+\varphi. \end{cases}$$

Generation of t_{spk}

The time t_{spk} at which the spike is observed by the recording electrode in the BLIF neuron is given by

$$t_{\text{spk}} = t_0 + X\, jit(p) + lat(p), \tag{5.13}$$

where $p = P_{\text{BLIF}}(t_1)$ and X is a random variable with a standard (unit variance, zero mean) normal distribution. The definition of t_{spk} given by (5.13) is identical to the corresponding equation (5.10) in the TLIF neuron, but with the function P_{TLIF} replaced by the function P_{BLIF}.

Relationships between model variables

Figure 5.6 summarises the flow of information in the BLIF neuron. As in the TLIF neuron, the input to the model is the current signal I. However, unlike the TLIF neuron, the BLIF neuron has two outputs: the decision as to whether or not cancellation occurs and the time of action potential observation, t_{spk}. In the case of cancellation, no value is generated for t_{spk}.

The relationship between $V(t)$ and the stimulus current signal $I(t)$, the random variable $\boldsymbol{\theta}$, the time t_0 of threshold crossing, the time $T_{Q_0}(t_0)$ at which the charge injected since t_0 first becomes negative, and spike cancellation, is visualised in Figure 5.7. The figure shows how there exists an interval, $[t_0, T_{Q_0}(t_0)]$, during which t_1 must lie if the spike resulting from a threshold crossing at time t_0 is not to be cancelled, and that the duration of this interval depends on the stimulus signal $I(t)$.

5.3.3 Model response properties

In the absence of anodic current, the probability of a stimulus evoking a spike in the BLIF neuron is unchanged from that in the TLIF neuron (without any anodic current, there is no possibility of a spike being cancelled). Similarly, the latency distribution of the BLIF neuron's response to a monophasic stimulus is negligibly different to that of the TLIF neuron's. Therefore, with the exception of φ, which is specific to the BLIF

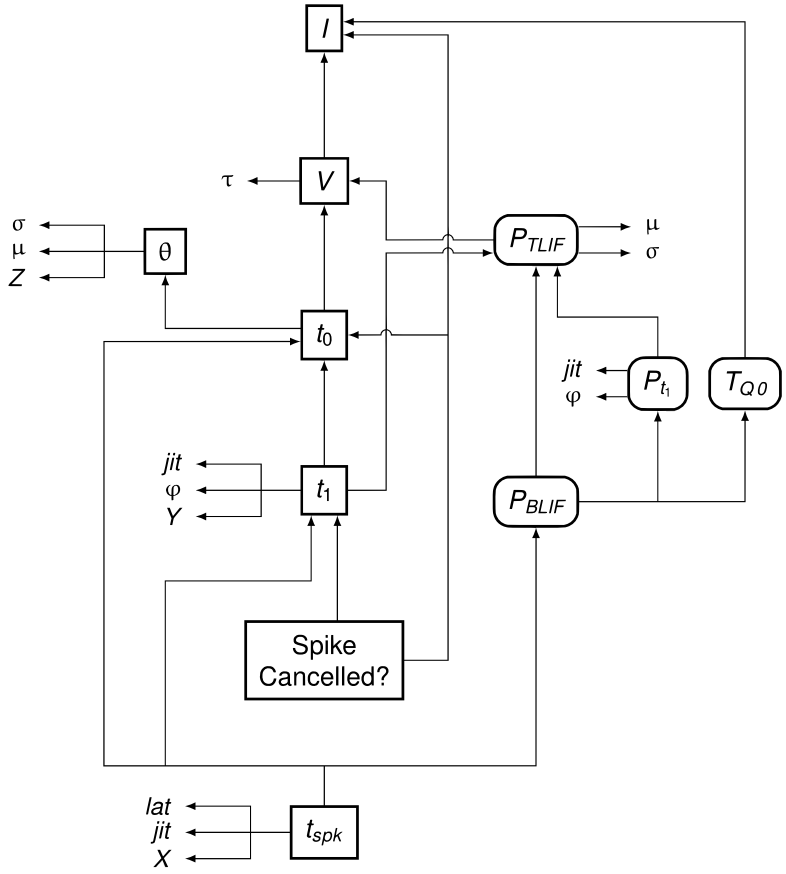

Figure 5.6: Data dependency in the BLIF neuron. The notation is as in Figure 5.4. Entities which are present in the BLIF neuron but not the TLIF neuron are shaded grey. If the impending spike is to be cancelled, then no value is generated for t_{spk}. Comparing this diagram of the BLIF neuron against that of the TLIF neuron in Figure 5.4 demonstrates the similarities between the two models.

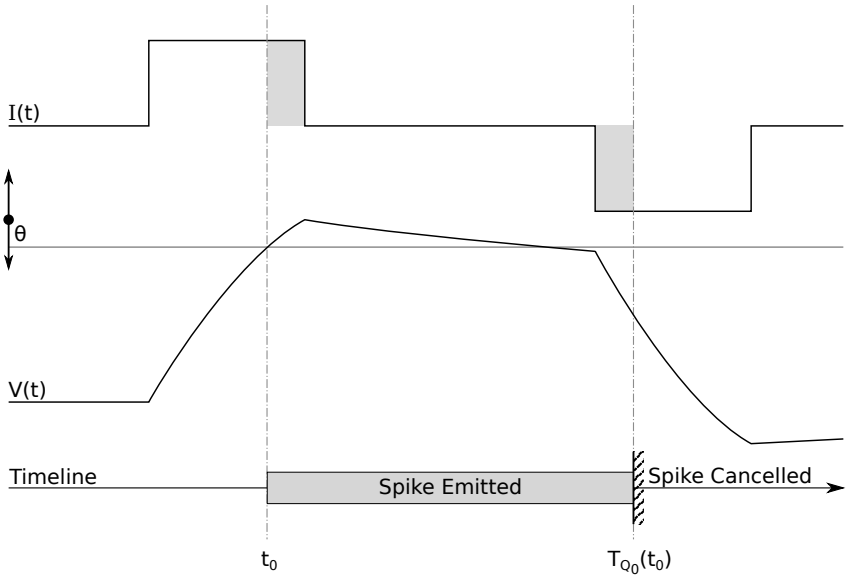

Figure 5.7: Visualising the relationship between threshold crossing, charge injection, and spike cancellation in the BLIF neuron. The BLIF neuron is stimulated by a stimulus signal $I(t)$ and the resulting time-course of $V(t)$ is plotted. The distribution of the random variable $\boldsymbol{\theta}$ is shown (opposing vertical arrows labelled $\boldsymbol{\theta}$), and an example outcome is shown (horizontal grey line). The point t_0 of threshold crossing is indicated (leftmost vertical dash-dotted line), as is the point $T_{Q_0}(t_0)$ at which the stimulus charge delivered since t_0 first falls below zero (rightmost vertical dash-dotted line). If t_1 lies within the shaded box on the timeline (labelled "Spike Emitted"), then a spike shall be emitted. However, if t_1 lies at some point later, then the impending spike shall be cancelled (i.e., not emitted). The shaded regions in the stimulus waveform indicated areas of equal but opposite charge.

neuron, the parametrisation of the BLIF neuron remains as it was in the TLIF neuron and the BLIF neuron preserves the fitting of the input-output, strength-duration, latency-level, and jitter-level functions, in all cases reproducing empirically-derived data from cat SGCs.

Monophasic response latency

If the stimulus signal I contains only excitatory, cathodic current and $\varphi = 0$, then the equations defining t_1 and t_{spk} in the BLIF neuron become equivalent to those in the TLIF neuron. In the case of t_1, this is a trivial consequence of (5.11). In the case of t_{spk}, the definitions in the TLIF and BLIF neurons—given by (5.10) and (5.13), respectively—are equivalent if $P_{\text{BLIF}} = P_{\text{TLIF}}$. If I is a monophasic stimulus, then $T_{Q_0}(t) = \infty$ for all t, and so $P_{t_1}(T_{Q_0}(t); t) = 1$ for all t. Equation (5.12) thus becomes

$$P_{\text{BLIF}}(t) = \int_0^t P'_{\text{TLIF}}(s)\, \mathrm{d}s = P_{\text{TLIF}}(t),$$

and so the definitions of t_{spk} in the TLIF and BLIF neurons are equivalent if I is a monophasic stimulus.

Effect of φ on the latency distribution of the response to a monophasic stimulus

This section demonstrates that even when $\varphi > 0$, its effect on the final latency distribution (i.e., the distribution of t_{spk}) is negligible. The latency of the response of the BLIF neuron to a monophasic stimulus of 40 µs duration was compared across two values of φ, one arbitrarily small ($\varphi = 1$ µs, resulting in a monophasic/biphasic threshold difference of 0.95 dB) and one arbitrarily large ($\varphi = 60$ µs, resulting in a monophasic/biphasic threshold difference of 11.7 dB). For both values of φ, the mean latency and jitter were recorded across 5 stimulus levels, evoking spikes with probabilities between 0.05 and 0.95. The differences in mean latency and jitter across values of φ were noted for each stimulus level. The maximum difference in mean latency was 3.3 µs (2.6 x standard error) and the maximum difference in jitter was 1.5 µs (1.4 x standard error). It may therefore be concluded that the effect of φ on the latency distribution of the response is negligible for values of φ within the range tested. Values beyond this range result in unrealistic monophasic/biphasic threshold differences, and so need not be considered.

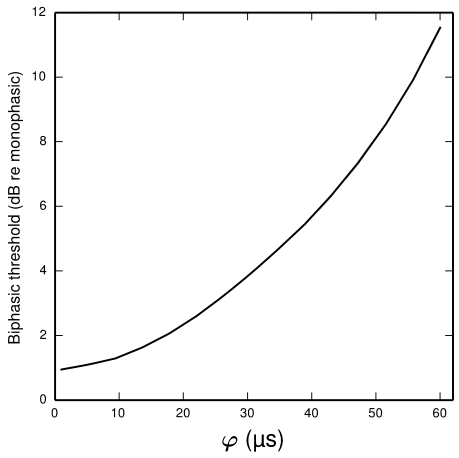

Figure 5.8: Plot showing how the threshold of a CL-BP depends on the model parameter φ in the BLIF neuron. The ordinate is given in dB relative to the threshold of a monophasic stimulus of 40 µs duration. The curve is generated for a biphasic stimulus of 40 µs/phase duration and 0 µs IPG.

Effect of φ on biphasic threshold

In the ANF, the threshold of a CL-BP is elevated relative to that of an equivalent monophasic stimulus (Miller et al., 2001b; Shepherd and Javel, 1999). Increasing the φ parameter of the BLIF neuron increases the thresholds of CL-BPs, while leaving the thresholds of monophasic pulses unchanged. Figure 5.8 quantifies the effect of φ on the biphasic/monophasic threshold difference. To understand why φ affects the threshold of a biphasic stimulus, note that a spike is cancelled if $t_1 > T_{Q_0}(t_0)$. The effect of φ is to ensure that t_1 is greater than $t_0 + \varphi$, and so increasing φ increases the probability that $t_1 > T_{Q_0}(t_0)$, thus increasing the probability of spike cancellation.

Biphasic input-output function

Figure 5.9 plots input-output functions of the BLIF neuron and a cat ANF (Shepherd and Javel, 1999) in response to a CL-BP presented at various IPGs. In both the model and the ANF, increasing the IPG of the stimulus has the effect of shifting the entire curve towards lower thresholds. The model parameter φ was chosen so as to make the curves of the model and the data overlap at their means when the IPG is 0.

The input-output functions shown in Figure 5.9 are summarised in Figure 5.10 by plotting the threshold (Figure 5.10A) and RS (Figure 5.10B) with respect to IPG. The

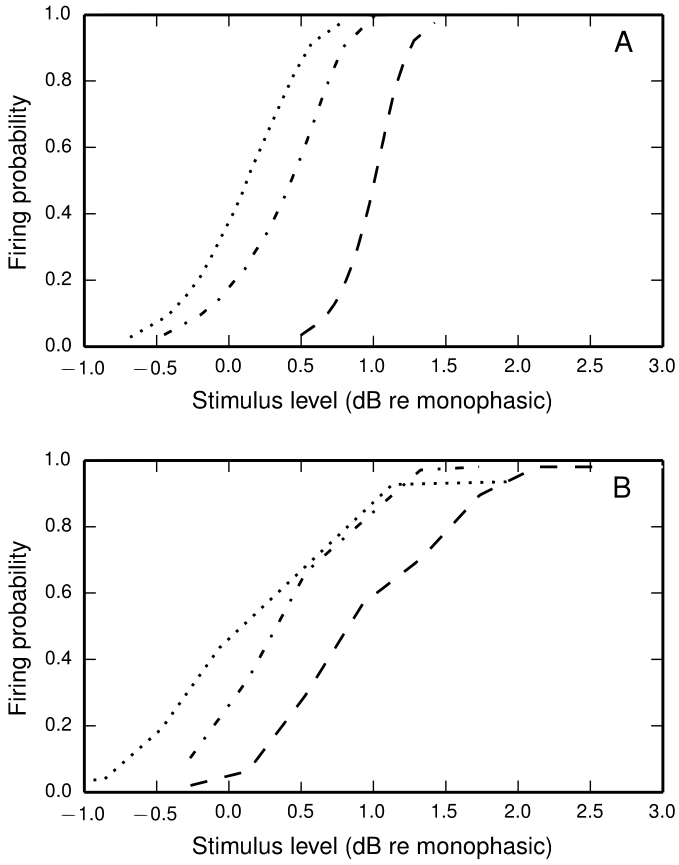

Figure 5.9: Input-output functions for the BLIF neuron (**plot A**) and a cat ANF (**plot B**; Shepherd and Javel, 1999), both stimulated with a CL-BP of 100 µs/phase duration at various IPGs (**dotted line**: 200 µs; **dash-dotted line**: 80 µs; **dashed line**: 20 µs; **solid line**: 0 µs). The means of the input-output functions of the cat ANF are well predicted by the BLIF neuron (see Figure 5.10A), although the slopes are steeper in the BLIF neuron than in the cat ANF (see Figure 5.10B). Stimulus levels are given in dB relative to the threshold of a 100 µs duration monophasic stimulus (the threshold for the ANF is projected from the available data; see Figure 5.10A).

thresholds of the ANF are quantitatively predicted by the model at all IPGs. The RS of the model approaches its monophasic value of 5% as the IPG increases beyond ∼100 µs. However, the ANF has an average RS of 7%, with no apparent dependence on IPG. This is in part because the monophasic RS of the model was chosen to reproduce data from a different neuron to that being compared presently (to the best of my knowledge, no study has been published that contains all the data necessary to parametrise the model using results from only a single neuron). To show that the BLIF neuron can exhibit larger values of RS, it was re-parametrised (by changing σ) to respond to a monophasic stimulus with a RS of 7%. The biphasic input-output functions resulting from this new parametrisation are summarised by the dashed lines figures 5.10A and 5.10B. Changing σ did not affect the monophasic strength-duration function of the model, or the mean latency or jitter of the model's response to a monophasic stimulus. Regardless of the monophasic RS, the model shows a dip in RS at short IPGs ($< \sim$100 µs), a trend that is not present in the ANF. At its peak deviation, the RS of the model is 4/10-ths that of the mean RS of the data.

A caveat in using the data from Shepherd and Javel (1999) is that they were obtained with a bipolar electrode, and thus, there is no clear definition as to which polarity of current is anodic and which is cathodic. The model presented here is a point-neuron model that is excited only by cathodic current. The present data was used due to lack of availability of other monopolar ANF data investigating the effect of the IPG on the threshold of a CL-BP. To justify my use of the bipolar data by noting that Shepherd and Javel report that both polarity orders produced similar results with negligible (0.2 dB) changes in threshold. Further, the trends in the data are comparable to those from other studies of single neurons (from animal preparations and computer models) that used monopolar cathodic-leading biphasic stimulation (Gorman and Mortimer, 1983; Hofmann et al., 2011; van den Honert and Mortimer, 1979; Weitz et al., 2011, 2014).

Pseudo-monophasic threshold

The opposite-polarity phases of a biphasic pulse need not have equal duration for the pulse to be charge balanced. A pseudo-monophasic stimulus has been proposed for use by cochlear implants (e.g., Van Wieringen et al., 2008), where the duration of one phase, typically the second, is extended relative to that of the other. The amplitude of the extended phase is reduced to maintain charge balance. Figure 5.11A plots the threshold of the BLIF neuron in response to a cathodic-leading pseudo-monophasic

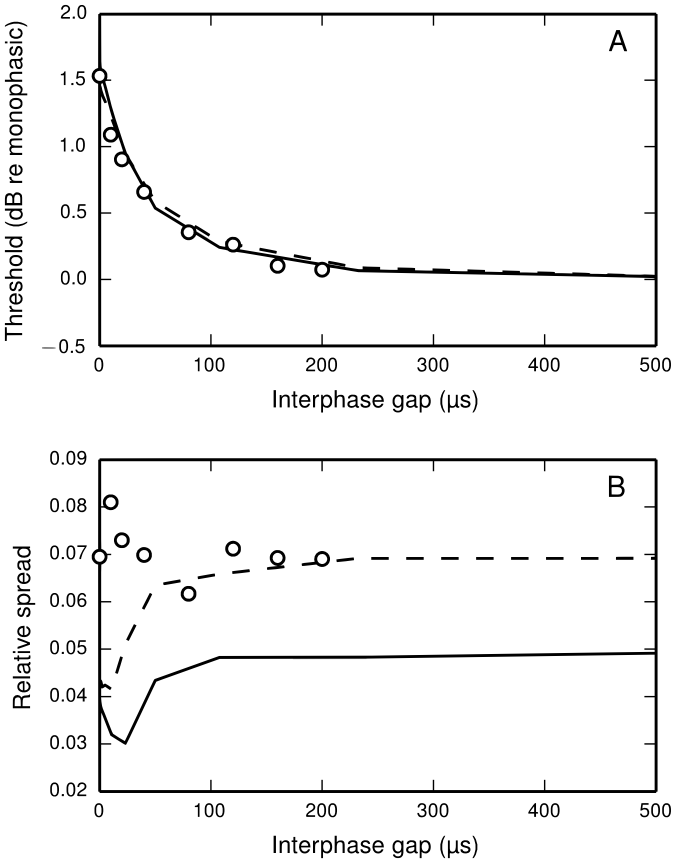

Figure 5.10: Plots showing how the threshold (**plot A**) and RS (**plot B**) of the BLIF neuron (**solid lines**) and a cat ANF (**open circles**; Shepherd and Javel, 1999) depend on the IPG of a CL-BP (100 µs/phase duration). Also plotted are the results after re-parametrising the model to have a monophasic RS of 7% (**dashed line**) by using $\sigma =$ 7.315 µV. Note that the cat ANF is stimulated with a bipolar electrode configuration (see text for discussion).

stimulus of varying anodic-phase duration (APD, varying from 40 to 500 µs). The BLIF neuron quantitatively predicts data from a cat ANF (Miller et al., 2001b) at short APDs. However, as the APD increases beyond ∼200 µs, the BLIF neuron over-predicts threshold by a maximum of 0.47 dB (APD=748 µs). This over-prediction is small when compared to the 5 dB range in the threshold data. The threshold of the BLIF neuron also returns to its monophasic value, however the convergence becomes much slower than in the ANF once the APD exceeds ∼200 µs. At an APD of 5 ms, the BLIF neuron's threshold is 0.24 dB from its monophasic value.

Biphasic strength-duration function

The threshold of a biphasic stimulus also depends upon its overall duration; increasing its duration—by equally increasing the duration of both its phases—decreases its threshold. Figure 5.11B plots the strength-duration functions of the BLIF neuron and a cat ANF (Shepherd et al., 2001), each using a CL-BP as the stimulus. The BLIF neuron predicts the trend that increasing the phase duration decreases the threshold, although it does not quantitatively predict the data, differing with a root-mean-square deviation of 2.5 dB. This value is small in comparison to the range in the threshold data (21.5 dB).

Temporal response statistics

The latency distribution of the ANF's response to a biphasic stimulus depends on stimulus level, with higher levels incurring less jitter (Javel and Shepherd, 2000). An underlying assumption of the TLIF neuron is that the latency distribution of the response is well predicted by the firing probability alone, regardless of the shape of the current pulse waveform. Figure 5.12 shows that the temporal statistics (mean latency, Figure 5.12A, and jitter, Figure 5.12B) of the BLIF neuron's response to a monophasic stimulus and CL-BPs of arbitrary shape are well predicted by firing probability, consistent with the assumption of the TLIF neuron.

5.3.4 Summary

The BLIF neuron responds to a CL-BP with an increased threshold relative to that of a monophasic pulse. The extent of this increase in threshold can be controlled by setting the φ parameter of the model. The effect of φ on the monophasic response statistics is negligible. The BLIF neuron quantitatively predicts the thresholds of a cat ANF responding to a biphasic stimulus across a range of IPGs between 0 and 200

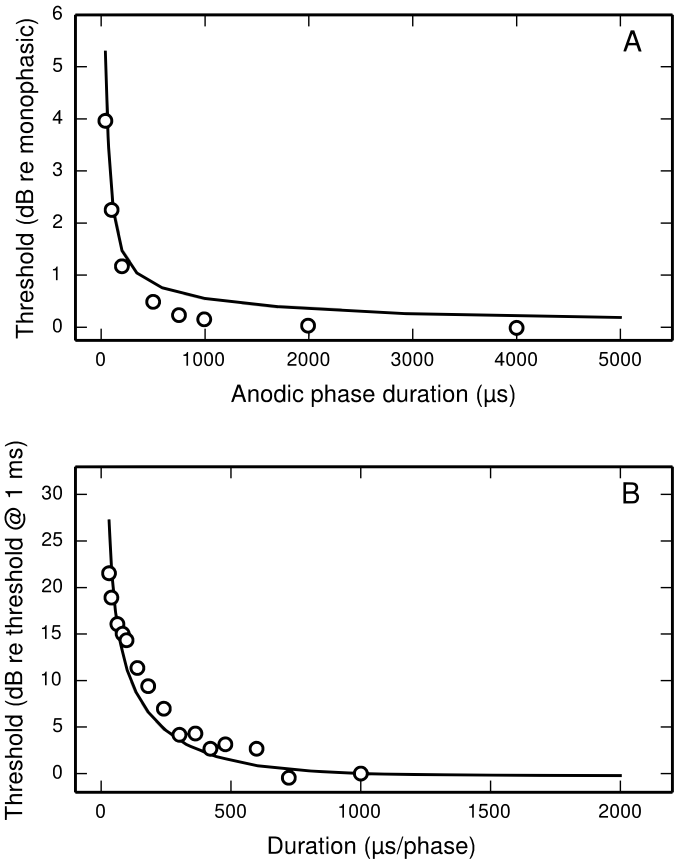

Figure 5.11: The dependence of threshold on phase duration under cathodic-leading biphasic stimulation. **Plot A**: the effect on threshold of increasing the anodic-phase duration in the BLIF neuron (**solid line**) and an ANF (**open circles**; Miller et al., 2001b). The stimulus is an asymmetric, CL-BP (40 µs leading-phase duration) of varying anodic-phase duration. The amplitude of the anodic phase is adjusted to maintain charge balance. **Plot B**: strength-duration functions of the BLIF neuron (**solid line**) and a cat ANF (**open circles**; Shepherd et al., 2001) when stimulated with a symmetric CL-BP (0 s IPG).

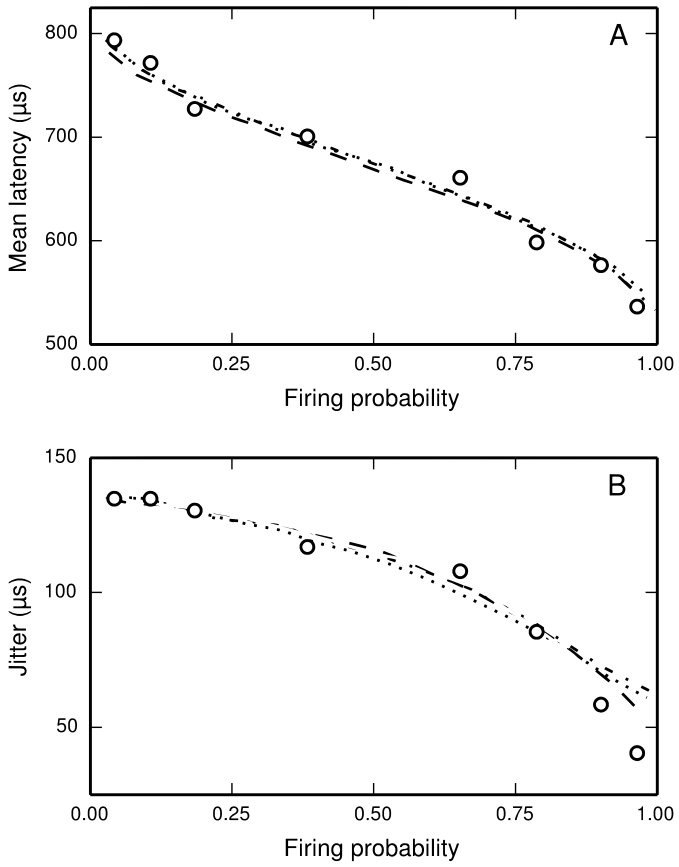

Figure 5.12: The temporal response statistics of the BLIF neuron are well predicted by firing probability, regardless of the stimulus pulse shape. Plotted are the mean latency (**plot A**) and jitter (**plot B**) of the BLIF neuron's response to a CL-BP of various configurations (**solid lines**: 40 µs/phase duration, 0 µs IPG; **dashed lines**: 20 µs/phase duration, 50 µs IPG; **dash-dotted lines**: 80 µs/phase duration, 40 µs IPG) and a monophasic stimulus (40 µs duration; **dotted lines**). Also plotted are the monophasic data (40 µs pulse duration) with which the model was parametrised (**open circles**; Miller et al., 1999b).

µs. The BLIF neuron correctly predicts that the threshold approaches its asymptote as the IPG extends beyond ∼200 µs. Also predicted is the effect on threshold of increasing the duration of both phases of a CL-BP. Further, the effect on threshold of increasing the duration of only the second phase (while adjusting its amplitude to maintain charge balance) is also predicted at durations below ∼200 µs.

Consistent with the assumptions of the TLIF neuron, the latency distribution of the BLIF neuron's response to a stimulus is well predicted by the probability of the stimulus evoking a spike, regardless of its shape. If the stimulus is monophasic, then the BLIF neuron maintains the input-output and strength-duration functions of the SLIF neuron.

5.4 Summary of model parameters and variables

The parametrisation of the SLIF, TLIF, and BLIF neurons is summarised in the tables below. Other than as specified in Figure 5.10, the given values were used to generate all the figures in this paper. The variables of the models are also summarised.

Parameters common to all models

Parameter	Value	Notes
μ	104.5 µV	Mean of $\boldsymbol{\theta}$. Parametrised to reproduce cat ANF data from Miller et al. (1999b).
σ	4.595 µV	Stardand deviation of $\boldsymbol{\theta}$. Parametrised to reproduce cat ANF data from Miller et al. (1999b).
τ	248.4 µs	Membrane time constant. Parametrised to reproduce cat ANF data from van den Honert and Stypulkowski (1984).

Parameters common to the TLIF and BLIF neurons

Parameter	Value	Notes
lat	$\alpha_1 = 109$ µV $\alpha_2 = 5.14$ µV $\alpha_3 = 368$ µs $\alpha_4 = 472$ µs	Mean delay between the start of the action potential initiation period and spike observation, predicted from firing probability p as $lat(p) = \frac{\alpha_3}{1 + \exp(\alpha_2^{-1}(\mu + \sigma\Phi^{-1}(p) - \alpha_1))} + \alpha_4,$ where Φ^{-1} is the quantile function of the standard normal distribution (see Figure 5.2A). Parametrised to reproduced cat ANF data from Miller et al. (1999b).
jit	$\alpha_1 = 109$ µV $\alpha_2 = 3.24$ µV $\alpha_3 = 136$ µs	Standard deviation of the duration of the action potential initiation period, predicted from firing probability p as $jit(p) = \frac{\alpha_3}{1 + \exp(\alpha_2^{-1}(\mu + \sigma\Phi^{-1}(p) - \alpha_1))}$ where Φ^{-1} is the quantile function of the standard normal distribution (see Figure 5.2B. Parametrised to reproduced cat ANF data from Miller et al. (1999b).

Parameters unique to the BLIF neuron

Parameter	Value	Notes
φ	37.81 µs	The minimum delay between t_0 and t_1. Parametrised to reproduce cat ANF data from Shepherd and Javel (1999).

Variables

Variable	Notes
V	Membrane potential.
$\boldsymbol{\theta}$	Normally-distributed threshold potential against which V is compared.
t_0	Time of threshold crossing. The time at which the action potential initiation period begins.
t_1	The time at which the action potential initiation period ends.
t_{spk}	The time of action potential observation.

5.5 Discussion

In this chapter, I have described two novel models, the TLIF and BLIF neurons, both of which extend the SLIF neuron. The TLIF neuron extends the SLIF neuron to reproduce the temporal statistics of the ANF's response to a monophasic stimulus. The BLIF neuron extends the TLIF neuron to realistically reproduce how the threshold of its response to a monophasic stimulus is affected by the introduction of a trailing, anodic phase. An important property of both the TLIF and the BLIF neurons is that they do not affect the already-fitted response statistics of the models that they extend. Thus, the TLIF neuron maintains the input-output and strength duration functions of the SLIF neuron, and the BLIF neuron responds to a monophasic stimulus with the same latency distribution and firing probability as the TLIF neuron. Further, the response of the BLIF neuron to a biphasic stimulus has the same latency distribution as that of the TLIF neuron's response to a monophasic stimulus of equal firing probability. These properties of the TLIF and BLIF neurons makes them simple to parametrise so as to reproduce ANF data.

5.5.1 Relating the BLIF neuron to the (V, m)-reduced HH model

The spike cancellation of the BLIF neuron can be compared against the behaviour of the (V, m)-reduced HH model (henceforth referred to as the *reduced HH model* for brevity). The analysis in Section 3.3.1 showed that, after an instantaneous depolari-

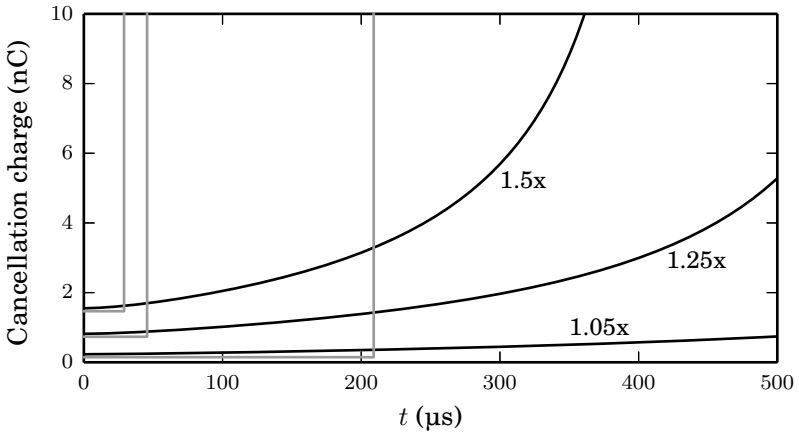

Figure 5.13: The time-course of the cancellation charge Q_{cncl} following an instantaneous injection of cathodic charge that moves the phase point of the reduced HH model from the resting node to beyond the separatrix. Curves for three different charge levels (1.05x, 1.25x, and 1.5x threshold charge) are plotted (**black lines**). Also plotted (**grey lines**) are the time-courses of the cancellation charge in the BLIF neuron under identical conditions. The point at which the cancellation charge becomes infinite in the BLIF neuron is stochastic; mean values are used. The BLIF neuron is parametrised so as to produce similar mean latencies to those of the reduced HH model.

sation, the distance of the phase point from the separatrix in the reduced HH model remains approximately constant for an extended period of time. The analysis focused on the case where the instantaneous depolarisation was subthreshold, so that it could be compared against a similar analysis of the LIF neuron. However, the same qualitative behaviour also occurs following suprathreshold depolarisations: regardless of whether the phase point is subthreshold or suprathreshold following an instantaneous depolarisation, the phase point follows a trajectory approximately parallel to the separatrix until reaching the vicinity of the V and m nullclines (see Figure 3.1), and thus the phase point stays close to the separatrix for a prolonged time following the charge injection. To formalise this, let us refer to the amount of anodic charge that will move the phase point from the suprathreshold region back to the separatrix as the *cancellation charge*, or Q_{cncl} (we shall assume that the charge is delivered in a short enough period of time to be considered instantaneous), and let us suppose that an instantaneous cathodic injection of Q_{thr} charge is needed to move the phase point from resting to the separatrix. Then, immediately following an instantaneous injection of Q_{stim} cathodic charge, we have

$$Q_{\text{cncl}} = Q_{\text{stim}} - Q_{\text{thr}}. \tag{5.14}$$

As time progresses, the cancellation charge Q_{cncl} increases, as shown in Figure 5.13 (black lines), however, as predicted, this increase in Q_{cncl} occurs slowly, taking 197, 249, and 314 µs to double in value after an instantaneous injection of 1.05x, 1.25x, and 1.5x threshold charge, respectively.

The BLIF neuron also has a cancellation charge. In the BLIF neuron, a spike is cancelled if the charge injected since threshold crossing falls below zero before the end of the action potential initiation period at time t_1. Therefore, the cancellation charge of the BLIF neuron is as in (5.14). Unlike in the reduced HH model, the cancellation charge of the BLIF neuron does not vary with time, but cancellation can only occur during the action potential initiation period. This may equivalently be understood to mean that after the end of the action potential initiation period, the cancellation charge of the BLIF neuron becomes infinite. The BLIF neuron is thus approximating the cancellation-charge curve of the reduced HH model (black lines in Figure 5.13) with two straight-line segments (grey lines).

The slow growth of the cancellation charge in the reduced HH model leaves it vulnerable during the early stages of excitation, with anodic stimulation easily able to abolish the excitation process. This initial vulnerability in excitation has previ-

ously been observed in real neurons by van den Honert and Mortimer (1979), who described a *"vulnerable period"* of approximately 100 µs during which an impending action potential could be abolished prior to its occurrence by anodic stimulation. The vulnerable period has since been used in other electrophysiological studies to explain why biphasic pulses are less efficient in exciting the neuron compared to monophasic pulses (Shepherd and Javel, 1999; Middlebrooks, 2004; Rubinstein et al., 2001; McKay and Henshall, 2003).

5.5.2 Latency distribution's dependence on firing probability

The assumption underlying both the TLIF and BLIF neurons is that the mean latency distribution of the response to a stimulus is well predicted by probability of that stimulus evoking an action potential. If this assumption is correct, then the latency and jitter of the responses to two distinct stimuli should be the same, provided the stimuli are all presented at threshold level. To assess the validity of this assumption, I compared the mean latency and jitter of cat ANF responses Miller et al. (2001b) to a monophasic and a cathodic-leading biphasic stimulus. The across-fibre average of the mean latency of the response to the biphasic stimulus was 88% that of the response to the monophasic stimulus; that the biphasic stimulus evoked shorter latencies than the monophasic stimulus was statistically significant ($p < 0.05$). The was no statistically significant difference in the jitter of the monophasic and biphasic responses. The difference in threshold of the monophasic stimulus and the biphasic stimulus was 4 dB, or 3.5 times the monophasic dynamic range (measured as the increase in stimulus level required to increase the probability of firing from 10% to 90%).

From this analysis, the assumption that the latency distribution depends only on the firing probability of a stimulus, and not its shape, is only partially valid. While the variance of the distribution appears unaffected by pulse shape, its mean is shifted when moving from a monophasic stimulus to a biphasic stimulus. However, the extent of the shift, while statistically significant, is small enough for the assumption to be a useful approximation of reality.

5.5.3 Comparison to previous models

The TLIF and BLIF neurons are extensions to the well-studied leaky integrate and fire (LIF) neuron, which has formed the basis of many models of the electrically stimulated ANF (e.g., Chen and Zhang, 2007; Chen, 2012; Goldwyn et al., 2012; Hamacher, 2004; Stocks et al., 2002). Of these models, only the Hamacher model reproduces both the

mean latency and jitter of the ANF's response, and their dependence on stimulus level. However, in the Hamacher model, the stimulus is half-wave rectified (Fredelake and Hohmann, 2012), and thus, the model cannot reproduce the effect of the anodic phase on the threshold of a CL-BP.

The TLIF neuron bears similarities to the Hamacher model. Both models use the probability of a spike being emitted to derive a latency distribution with which to respond. However, the TLIF neuron and the Hamacher model differ in how they predict that probability. The TLIF neuron uses the probability of the membrane potential exceeding threshold at any time during the action potential initiation period. The Hamacher model, however, uses the membrane potential at the single, discrete moment of pulse cessation. This is problem if a pulse is delivered in the time between threshold crossing and spike emission (i.e., during what I refer to as "the action potential initiation period" in my model), as the time of spike emission will not be affected by this further stimulation. For this reason, I was motivated to develop a model which would allow the timing of a spike to be continuously affected by stimulation, up until the moment it is emitted.

The Goldwyn model (already discussed in section 2.4.4) may be parametrised to quantitatively reproduce the response statistics of a biphasic stimulus of arbitrary shape. However, from empirical analysis, I found that once the model has been parametrised so as to reproduce the threshold of a given CL-BP, changing the IPG of the pulse has little effect on its threshold, other than at very short values ($<\sim$30 µs). This is in contrast to the ANF, which is sensitive to changes in IPG up to $\sim$250 µs—a trend that the BLIF neuron is able to reproduce.

5.5.4 Current integration

The BLIF neuron is based on the assumption that a delay exists between the initial depolarisation of the ANF and the moment at which the action potential is generated. During this delay, it is assumed that the action potential may be cancelled by anodic current. By this means, the biphasic threshold is increased relative to the monophasic threshold. This assumption is consistent with a study by van den Honert and Mortimer (1979), who propose that there exists a delay, the *vulnerable period*, between the depolarisation of the neural membrane and the opening of the sodium ion channels. During the vulnerable period, the activation of the sodium ion channels may be prevented by anodic current, resulting in the abolishment of the action potential. This view has been reaffirmed with reference to the cat ANF by Miller et al. (2001b), who

propose that the continued integration of the current during the vulnerable period results in the increased threshold of biphasic stimuli. This is consistent with the BLIF neuron integrating the stimulus current during the action potential initiation period and cancelling the spike if the net charge is negative.

5.5.5 Recovery after spiking and cancellation

In this chapter, I have only considered the response of the neuron to a single, brief, stimulus pulse. However, for the presented models to be useful, they must be capable of responding to trains of pulses, such as those generated by cochlear implants. In this section, I very briefly sketch how both the TLIF and BLIF neurons might be reformulated so as to recover after threshold crossing or spike cancellation. However, a full implementation of recovery has been beyond the scope of my PhD.

Recovery after a spiking at time t may be implemented by terminating the existing simulation and initiating a new simulation with a truncated stimulus signal, I', where

$$I'(s) = \begin{cases} I(s) & \text{if } s \geqslant t \\ 0 & \text{if } s < t. \end{cases}$$

To implement refractoriness, the threshold potential $\boldsymbol{\theta}$ of the model may be scaled by a function of the time since last spiking, as previously described by Goldwyn et al. (2012) and Hamacher (2004).

Truncating the stimulus signal may also be used to recover from spike cancellation, so that upon cancellation, the model is re-run with the truncated and modified signal I', where

$$I'(s) = \begin{cases} I(s) + C(\theta - V)\delta(s - t) & \text{if } s \geqslant t \\ 0 & \text{if } s < t, \end{cases}$$

where δ is the Dirac delta function and θ is the new (i.e., after the re-run) realisation of the threshold potential $\boldsymbol{\theta}$. The extra term added to the original stimulus signal I causes V to be exactly equal to θ at the moment after spike cancellation. This term is added under the assumption that it requires only an infinitely small amount of cathodic current to initiate an action potential immediately after cancellation.

Chapter 6

Effects of phase order in biphasic stimulation

Chapters 3 and 4 analysed how different pulse shapes in monophasic and biphasic stimulation affect the excitation process in the HH model and its stochastic and reduced derivatives. It was found that the phase order of a biphasic stimulus affected the qualitative description of excitation arising from analysis of the (V, m) phase paths in these models. This result motivated further investigation into the effect of phase order. This chapter presents two distinct theories of how excitation occurs under biphasic stimulation, each theory relating to stimulation by a single phase order. These theories are then tested in their ability to predict excitation in the context of the HH model and its stochastic derivative. The chapter closes by showing that phase order affects the interactions between consecutive biphasic in pulse train stimulation. This has direct relevance to cochlear implants, the vast majority of which use trains of biphasic pulses to stimulate the SGCs.

6.1 Threshold and accommodation

To investigate whether the threshold level of a biphasic pulse is affected by the phase order of the pulse, the HH model was stimulated with individual biphasic pulses of both polarity orders at various IPGs. The *threshold-IPG* curves of anodic- and cathodic-leading biphasic stimulation are plotted in figures 6.1A and 6.1B, respectively (solid lines). Both curves are qualitatively similar at low IPGs, where the threshold is initially elevated by about 10 dB relative to its monophasic value when the IPG is 0 µs, and

decays approximately exponentially thereafter with increasing IPG. In the case of cathodic-leading stimulation, the threshold decays to its monophasic value, reaching a steady state as the IPG increases beyond ∼350 µs. In the case of anodic-leading stimulation, however, the threshold falls below its monophasic value at an IPG of ∼200 µs, reaching a minimum value of 3 dB below its monophasic value at 500 µs (the greatest IPG for which thresholds were measured).

That the threshold level of an AL-BP may fall below the monophasic threshold seems surprising, given that the two phases act against one another in their effect on the membrane potential. I hypothesised that this occurs due to the accommodative behaviour of the membrane, which is due to the h and n variables in the HH model (see Section 2.2.2). This is as the threshold potential of the membrane is affected by the membrane's potential, with hyperpolarisations acting to reduce it, and so the leading, hyperpolarising phase of an AL-BP may therefore be expected to reduce the membrane's threshold potential prior to the onset of the cathodic phase, which then has to depolarise the membrane less in order to evoke excitation. To test this hypothesis, the threshold-IPG curves of anodic- and cathodic-leading biphasic stimulation in the (V, m)-reduced HH model (section 3.1.2) were obtained (dashed lines, figures 6.1A and 6.1B, respectively) and compared against those of the HH model. As the reduced HH model holds the h and n variables fixed, it may be used to explore excitation in the absence of accommodation. Consistent with the hypothesis, the (anodic-leading) thresholds of the reduced HH model do not fall below the model's monophasic threshold.

Accommodation has a different effect when the cathodic phase leads. When accommodation is present, the decay of the threshold to its monophasic value with increasing IPG occurs at a faster rate than when accommodation is removed. This is because accommodation brings forward the time of the action potential, even in the simplest case of an instantaneous delivery of cathodic charge. When instantaneously depolarised, the membrane continues to 'accommodate' to the depolarisation, even while the depolarisation becomes self-sustaining, potentially undoing what would have otherwise resulted in an action potential (this may be viewed in terms of the dynamic saddle node, discussed in section 3.3.2). For a given stimulus to overcome these effects of accommodation, it must be delivered at a higher level than would be required in the absence of accommodation. By delivering a stimulus at a higher level, the rate at which sodium activation occurs is increased, and so the action potential is brought forward in time. In the case of a CL-BP, this means that the state of sodium ac-

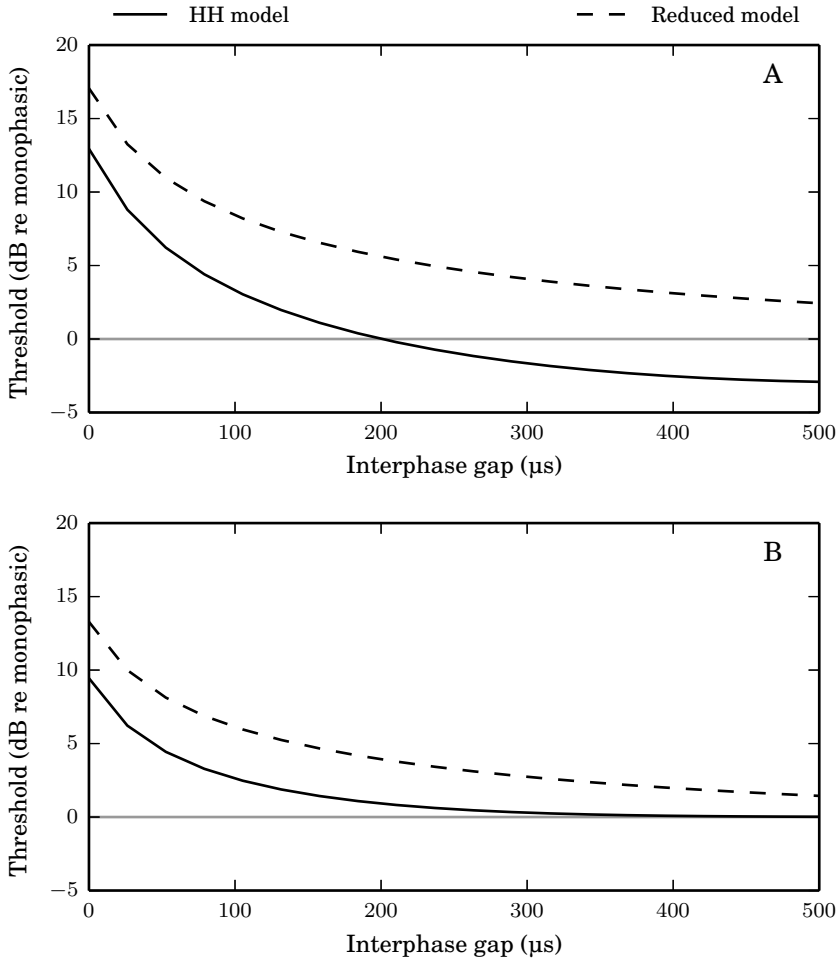

Figure 6.1: Biphasic threshold-IPG curves of the HH model (**solid lines**) and the reduced HH model (**dashed lines**) when the anodic phase is leading (**plot A**) and when the cathodic phase is leading (**plot B**). In all cases, the phase duration of the stimulus is 40 µs/phase. The ordinate units of a given curve are decibels relative to the monophasic threshold (cathodic current, 40 µs pulse duration) of the model from which the curve was obtained. At all IPGs, the threshold of a CL-BP is greater than that of an equivalent monophasic pulse. At IPGs below ∼200 µs, the threshold of an AL-BP is also greater than that of an equivalent monophasic pulse, although at IPGs above ∼200 µs, it is less, *but only in the HH model*, consistent with the hypothesis that the reduction of threshold below the monophasic value is due to the accommodative behaviour that occurs in the HH model but not in the reduced HH model.

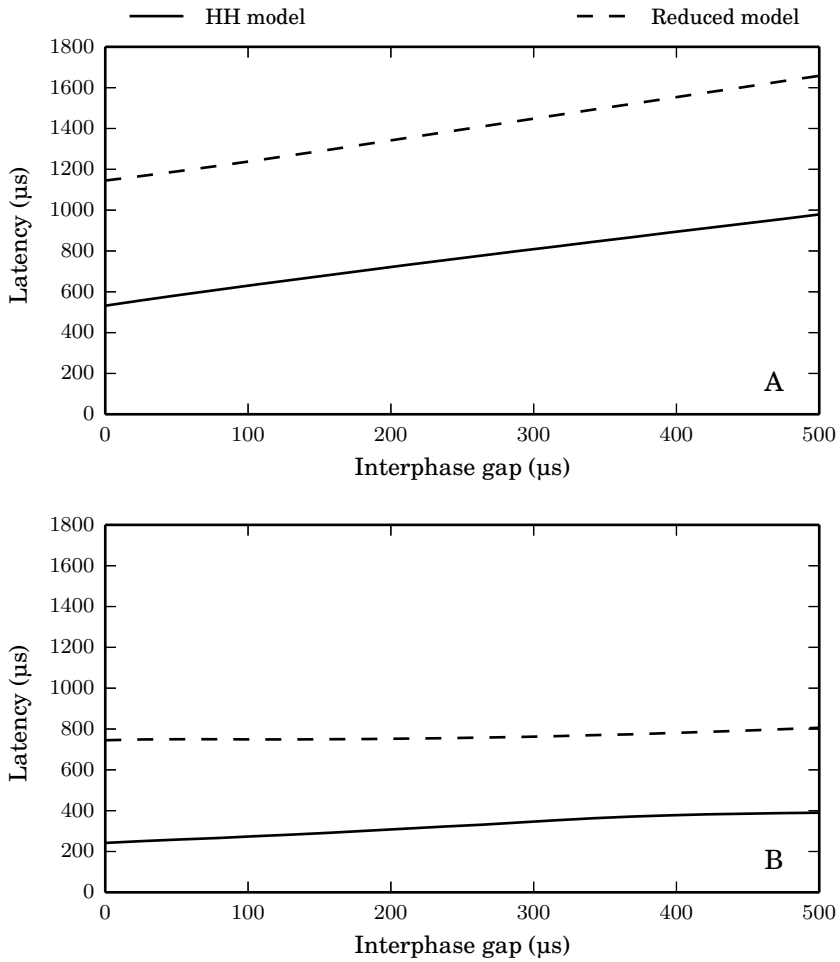

Figure 6.2: Biphasic latency-IPG curves of the HH model (**solid lines**) and the reduced HH model (**dashed lines**) when the anodic phase is leading (**plot A**) and when the cathodic phase is leading (**plot B**). In all cases, the phase duration of the stimulus is 40 µs/phase. The latency is defined as the time since stimulus onset at which the m variable of the model exceeded 0.5 (arbitrarily chosen as a value exceeded in both models only during excitation). *Regardless of phase order, the latency of a given pulse is lower in the HH model, consistent with the hypothesis that accommodation lowers latency.*

tivation is more developed at the time of the trailing anodic phase's delivery when the pulse is delivered at threshold level in the presence of accommodation, compared to when delivered at threshold level in the absence of accommodation. As the previous section demonstrated, bringing forward the time of sodium activation is the mechanism by which increasing the level of a CL-BP increases its ability to evoke excitation. Therefore, since accommodation has the same effect (i.e., in bringing forward the time of sodium activation), the level of a given pulse may be reduced while still being sufficient to evoke excitation, if accommodation is present. To demonstrate that accommodation brings forward the time of the action potential, the latencies of just-above threshold pulses in the HH and reduced HH models are plotted in figures 6.2A and 6.2B, respectively. In both cases, the latency of the reduced HH model is ∼400 to ∼600 µs greater than the latency of the HH model for IPGs in the range of 0 to 500 µs. To demonstrate that accommodation increases the threshold of short-duration monophasic pulses, Figure 6.3 plots the thresholds of monophasic pulses in the HH and reduced HH models. It also re-plots the threshold-IPG curves of figures 6.1A and 6.1B, expressing the thresholds of both models as decibels relative to the monophasic threshold of the HH model (noting that previously the thresholds of each model were plotted in decibels relative to the respective model's own monophasic threshold). It shows that in all cases, the threshold of a given pulse is higher in the HH model than in the reduced HH model.

6.1.1 Leaky integration with an accommodation process qualitatively reproduces trends in threshold under anodic-leading biphasic stimulation

The previous section revealed an interesting phenomenon in the HH model: for a range of IPGs (starting at 200 µs; the upper limit was not investigated), the threshold of an AL-BP is lower than the threshold of an equivalent[1] cathodic monophasic pulse. This phenomenon is not reproduced by the LIF or BLIF neurons, nor is it reproduced by other notable phenomenological models, including those of Bruce et al. (1999b), Hamacher (2004), and Goldwyn et al. (2012). This section investigates whether adding a simple accommodative process to the LIF neuron renders it capable of producing the same phenomenon of the threshold of an AL-BP falling below the monophasic threshold at an IPG of ∼200 µs.

[1]That is, so that the duration of the cathodic monophasic pulse is equal to the duration of the cathodic phase of the AL-BP.

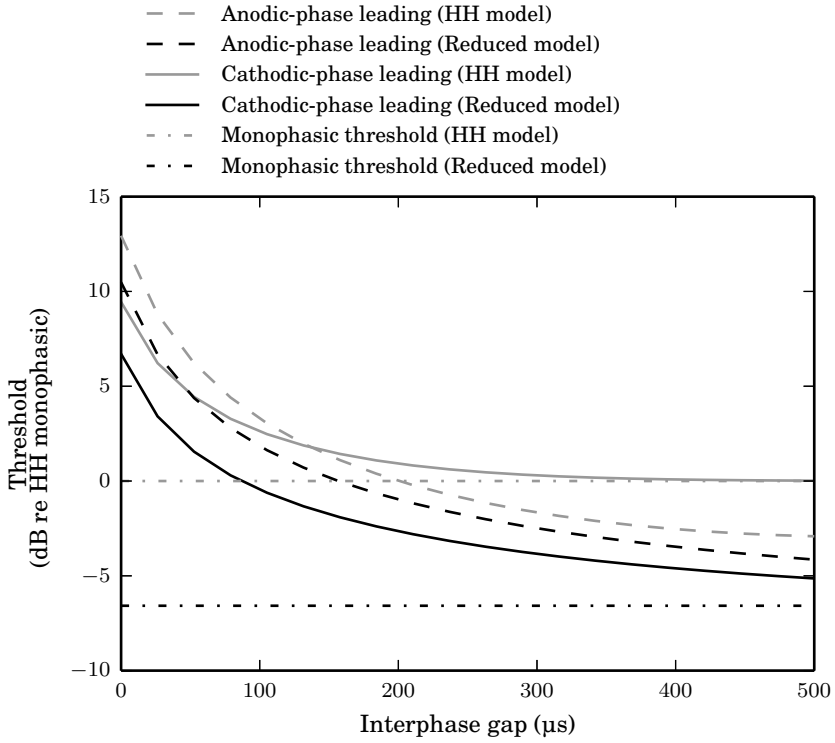

Figure 6.3: Biphasic threshold-IPG curves (40 µs/phase) of the HH model (**grey coloured lines**) and the reduced HH model (**black line coloured lines**) when the anodic phase is leading (**dash styled lines**) and when the cathodic phase is leading (**solid styled lines**). Data is re-plotted from 6.1, but with different ordinate units (decibels relative to the threshold of a 40 µs cathodic pulse in the HH model). Monophasic thresholds (40 µs duration, cathodic current) of both models are also plotted (**dash-dotted lines**). *For any given pulse, the threshold is higher in the HH model than in the reduced HH model.*

The Hill model is equivalent to a LIF neuron with a dynamic, accommodating threshold. It represents perhaps the simplest accommodating spiking-neuron model, and the dynamics of its dynamic threshold may be incorporated into other more complex models, including the BLIF neuron. The model itself is described fully in Section 2.2.2. To test whether the Hill model reproduces the reduced-threshold phenomenon observed in the HH model, the anodic-leading threshold-IPG curves of the two models were compared. Further, to investigate how the simplified spiking dynamics of the LIF neuron affects how it responds to AL-BPs, its threshold-IPG curves were compared against those of the (V, m)-reduced HH model (section 3.1.2; for brevity, henceforth referred to as the *reduced model*). The reduced model does not accommodate to depolarisations, and so if the thresholds of the LIF neuron differ from those of the reduced model, then it is due to the LIF neuron's simplified spiking dynamics rather than due to its lack of an accommodative process.

The results are shown in Figures 6.4A and 6.4B (plots A and B are identical other than for the stimulus having different phase durations; see caption). The Hill model qualitatively reproduced the curves of the HH model at both phase durations, with the curves of both models following an exponential-like decay of threshold with increasing IPG up to values of ∼500 µs, each crossing below the monophasic threshold at similar IPGs (∼200 µs for a phase duration of 40 µs; ∼125 µs for a phase duration of 100 µs). The thresholds of the Hill model (measured in dB relative to the monophasic threshold) are all within 27% of those of the HH model, and, for each phase duration, the IPG at which the threshold first becomes less than the monophasic threshold is within 20 µs of that of the HH model. The curves of the LIF neuron qualitatively reproduced the curves of the reduced model, reproducing the exponential-like decay of the threshold to its monophasic value with increasing IPG. However, the curves of the LIF neuron approach the monophasic threshold faster, reaching a steady state at an IPG of ∼500 µs for both phase durations, whereat the thresholds of the reduced model were still ∼2.5 dB above the monophasic value at an IPG of 500 µs, reduced from ∼17 dB (40 µs/phase duration) and ∼12 dB (100 µs/phase duration) at an IPG of 0 µs. This disparity occurs because hyperpolarisations in the reduced HH model act to decrease m, leading to less depolarising sodium current and a slightly increased membrane time constant, which together amplify and prolong the effect of the leading phase of the AL-BP. These effects are not encapsulated or approximated by the dynamic threshold of the Hill model, and so the use of the dynamic threshold is very much empirically motivated rather than theoretically driven.

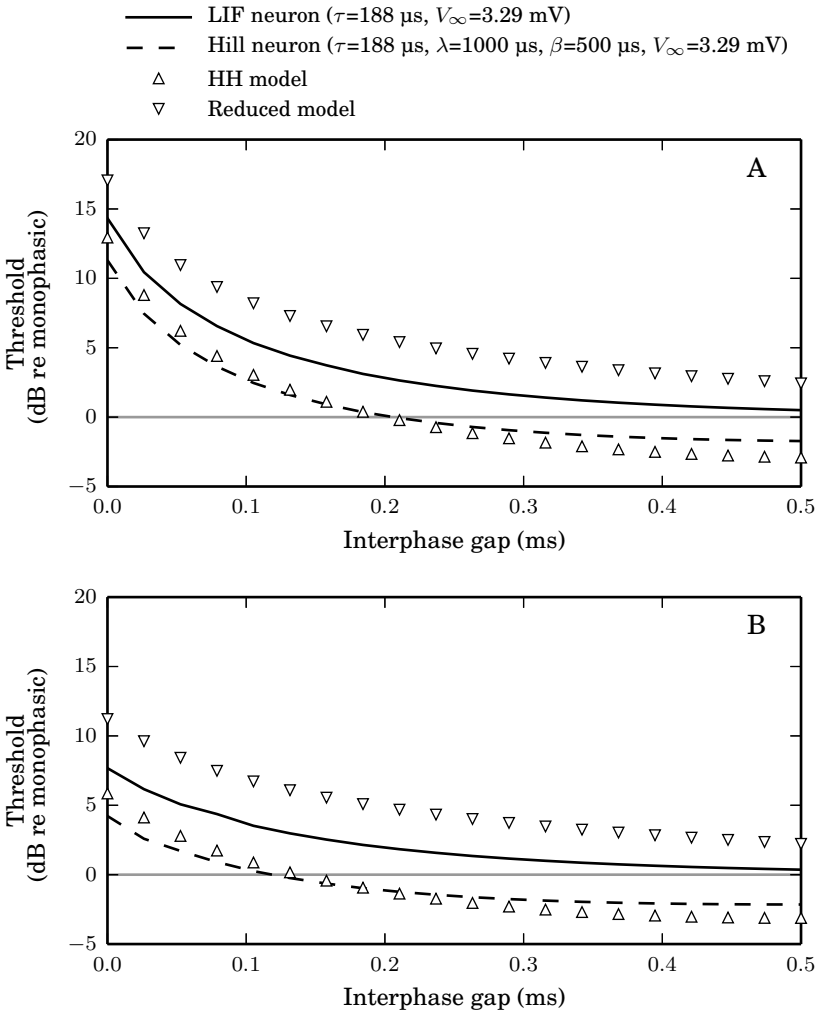

Figure 6.4: How the threshold of an AL-BP (**plot A**: 40 µs/phase duration; **plot B**: 100 µs/phase duration) depends on IPG (in the range of 0 to 500 µs) in the HH model (△), the reduced HH model (▽), the LIF neuron (**solid black line**), and the Hill model (**dashed black line**). The parameters of the models do not change between plots.

This section has shown that leaky integration combined with an accommodation process (i.e., as in the Hill model) is able to qualitatively reproduce how the threshold of an AL-BP depends on the pulse's phase duration and IPG, in particular, so as to reproduce the phenomenon of the AL-BP threshold falling below the monophasic threshold at an IPG of ∼200 µs. Extending the BLIF neuron so as to include an accommodative process should enable it to realistically respond to biphasic pulses of arbitrary shape and phase order. Demonstrating that an accommodative process is necessary for a phenomenological model to realistically respond to AL-BPs is a contribution that may have impact on existing phenomenological models that have been developed in the context of biphasic stimulation, but that do not have accommodative processes (e.g., Goldwyn et al., 2012; Hamacher, 2004).

6.2 Spike cancellation explains threshold when cathodic phase leads

In the BLIF neuron, there are two orthogonal sources of stochasticity. The random variable $\boldsymbol{\theta}$ provides the stochastic threshold that must be exceeded by V if excitation is to occur, and the random variable Y is the source of the temporal stochasticity of the action potential initiation period. When stimulated by a monophasic pulse, the probability of spiking is related only to the probability of the V variable exceeding a threshold, and is unrelated to the temporal stochasticity of the resulting spike that is due to Y. However, when stimulated by a near-threshold or suprathreshold CL-BP, the probability of the V variable exceeding threshold (which is almost exactly 1) has negligible effect on the probability of spiking, which is instead related to the probability of a spike being emitted prior to being cancelled by anodic current, which itself is related to Y, the delay between threshold crossing and spike emission.. The BLIF neuron thus predicts that excitability and temporal responsiveness are intrinsically interlinked in the case of cathodic-leading biphasic stimulation. To access the validity of this prediction, the firing outcomes of repeated trials of the stochastic HH model stimulated by a CL-BP were predicted on the basis of the time it took the phase point of a given trial to reach an arbitrary *benchmark state* (chosen as the time at which m first exceeds 0.085, a state that is achieved by all trials, including those wherein excitation does not occur). An input-output function was derived from these predictions (by means of maximum likelihood estimation of the parameters m and s of equation 2.12) and compared against the input-output function similarly derived from the actual

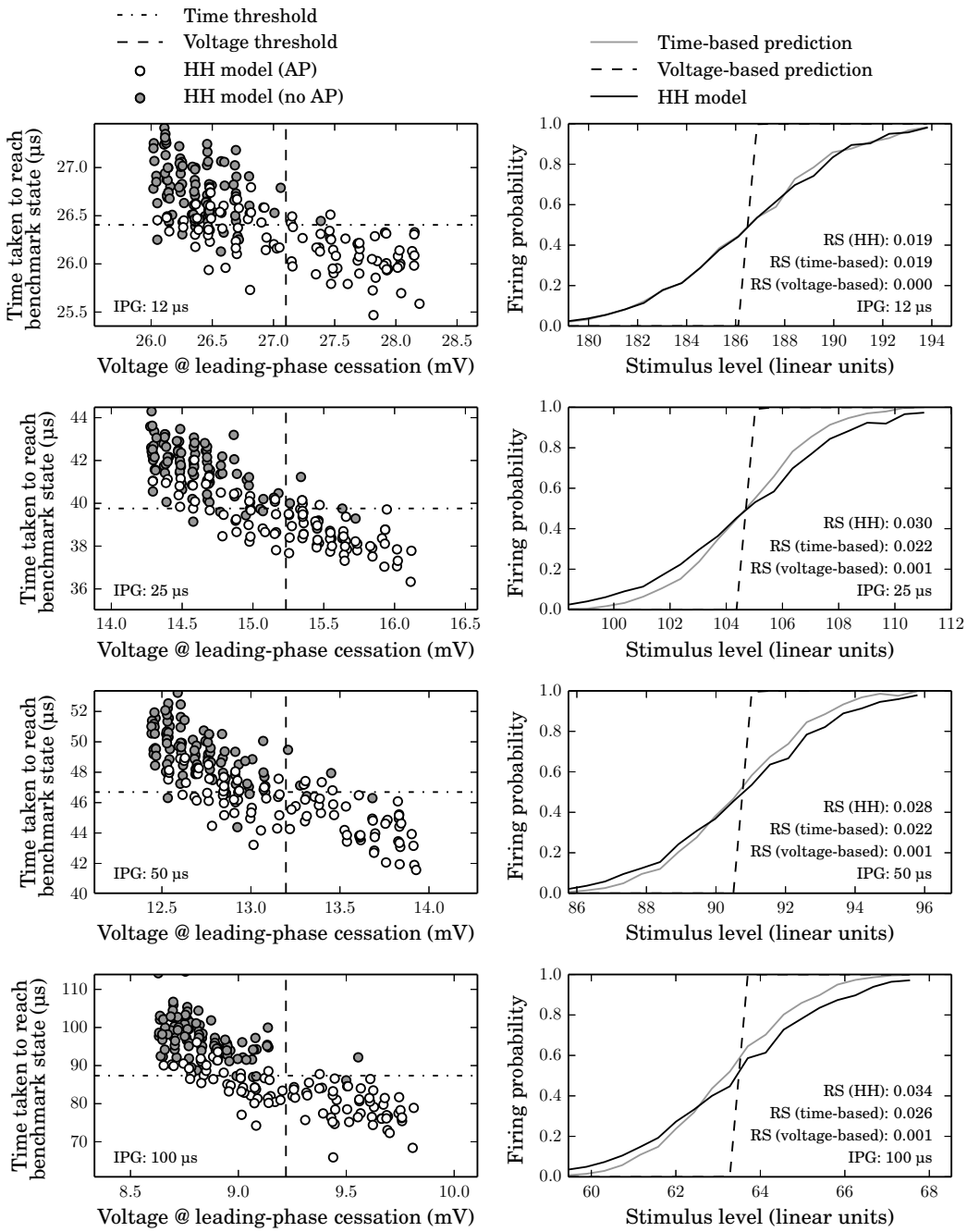

Figure 6.5: The firing outcome of a trial of the stochastic HH model is well predicted by the time it takes the model to reach an arbitrary, predefined, sub-threshold state (the *benchmark state*). The stochastic HH model was stimulated with a CL-BP (20 µs/phase duration; various IPGs) at various stimulus levels. For each trial, the time at which the model reached the benchmark state (*time-to-reach-benchmark-state*) was plotted (**left column**) against the membrane potential at the time of the leading phase's cessation (*voltage@leading-phase-cessation*). Each trial's firing outcome was predicted on the basis of its voltage@leading-phase-cessation (*voltage-based prediction*) and its time-to-reach-benchmark-state (*time-based prediction*). From these predictions and the actual firing outcomes (indicated by filled circles in the left column; **grey circles**: trials in which no action potential was elicited; **white circles**: trials in which an action potential *was* elicited), three input-output functions were derived and their RSs found (**right column**). This paradigm was repeated four times at different IPGs (0, 25, 50, and 100 µs; **rows**). The mean absolute difference in the RS derived from the voltage-based predictions and the actual firing outcomes was 0.027 (98% of the RS). The mean absolute difference in the RS derived from the time-based predictions and the actual firing outcomes was 0.005 (17% of the RS).

firing outcomes (Figure 6.5). The methodology was repeated at four different IPGs: 0, 25, 50, and 100 µs. At each IPG, the empirically-derived input-output function was closely approximated by the predicted input-output function, with the mean absolute difference between the two equal to 0.0055, or 20% of the mean empirical relative spread of 0.02775. These results are consistent with the theory of the BLIF neuron that the temporal responsiveness of the membrane affects whether a CL-BP will excite the membrane.

The time that it takes the phase point to reach the benchmark state is related to the voltage at the cessation of the leading phase of the CL-BP (Figure 6.6A). It seems reasonable to question, then, whether *time taken to reach benchmark state* is really the predictor variable, and whether *voltage at leading-phase cessation* would not better (or equally) predict the firing outcome. To providing supporting evidence that it is the *time*, and not the *voltage*, that is the predictor, input-output functions were derived from predictions made on the basis of the voltage at the leading phase's cessation (Figure 6.5, right column, dashed lines). In all cases, the voltage-derived input-output functions under-predicted the relative spread by an order of magnitude (with the average voltage-derived relative spread being 0.001, compared to the average empirically-derived relative spread of 0.02775).

The *time-threshold* is the time below which the *time to reach benchmark state* must be in order for a spike to be predicted in the methodology above. It is not an inherent property of the membrane, and varies with the IPG of the stimulus (as demonstrated in Figure 6.6A). In the BLIF neuron, the variable T_{Q_0} is the time before which a spike must be emitted in order for it not to be cancelled. Figure 6.6B shows that, when both the time-threshold and T_{Q_0} are normalised with respect to their values at an IPG of 500 µs, the time-threshold is well predicted by T_{Q_0}, suggesting that the BLIF neuron is able to capture and reproduce the way in which the excitability of the stochastic HH model is related to the temporal properties of excitation.

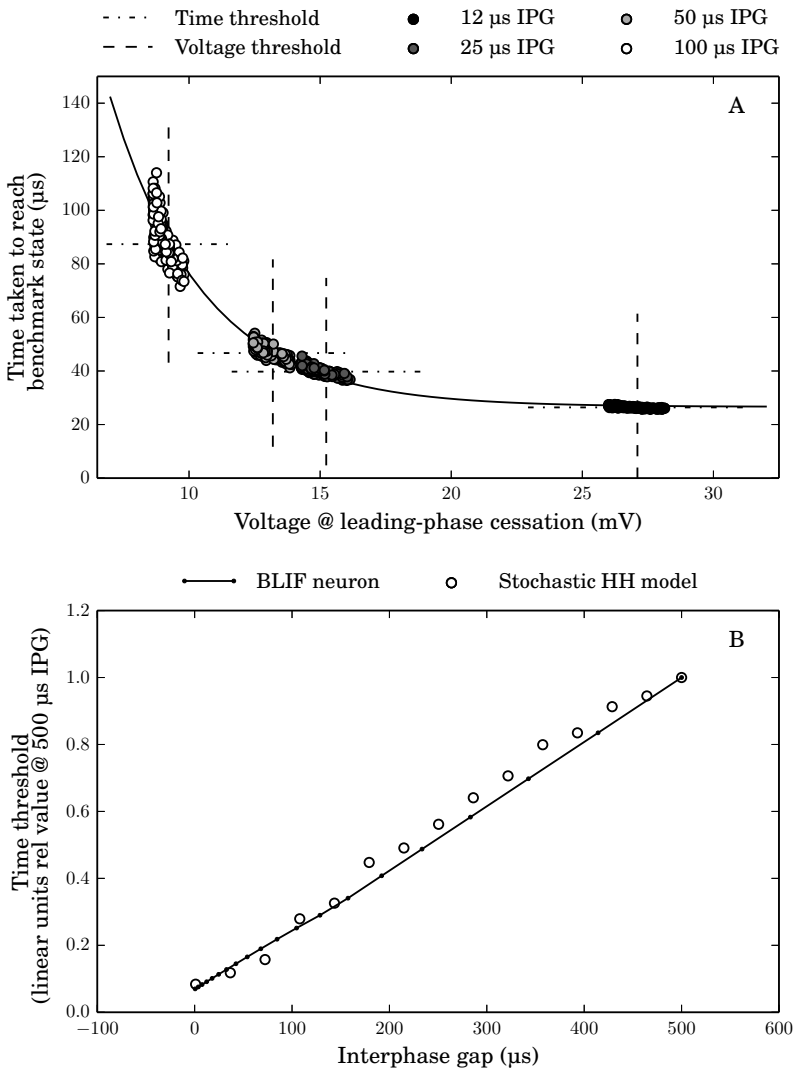

Figure 6.6: **Plot A** replots data (**filled circles**) from the left column of Figure 6.5 that relates time-to-reach-benchmark-state to voltage@leading-phase-cessation in a single plot. The data are well fit by a single exponential function of the form $\alpha \exp(-v/\kappa)+\beta$ (**solid line**). **Plot B** compares the time-threshold (see Figure 6.5) of the stochastic HH model against T_{Q_0}, the time before which a spike must be emitted in the BLIF neuron in order for it not to be cancelled. When both the time-threshold and T_{Q_0} are normalised with respect to their values at an IPG of 500 µs, the time-threshold is well predicted by T_{Q_0}.

6.3 Interactions between consecutive pulses

In an entirely passive membrane stimulated by a symmetric biphasic pulse, the charge delivered by the trailing phase removes the opposite-polarity charge delivered by the leading phase. As there is a delay between the two phases, some of the charge delivered by the leading phase leaks prior to the delivery of opposite-polarity charge by the trailing phase. Therefore, the trailing phase leaves a residue charge, and so if the trailing phase is hyperpolarising, then the membrane will be hyperpolarised following the delivery of the biphasic pulse, and vice-versa if the trailing phase is depolarising. Thus, in a train of AL-BPs, the interactions between pulses facilitate excitation, whereas in a train of CL-BPs, the interactions between pulses inhibit excitation. This mechanism has previously been proposed to explain thresholds in the SGCs (Miller et al., 1997; Eddington et al., 1994). The real membrane, however, is not passive, and so we may expect the active dynamics of not just the m dimension, but also the n and h dimensions, to affect how the membrane responds to a pulse train. To investigate the effect of these dimensions, the phase paths of the HH under two different stimulus conditions (cathodic-leading stimulation and anodic-leading stimulation) were projected to the (V, m) plane. In both conditions, the model was stimulated when at rest by a pair of biphasic pulses, each of 40 µs/phase duration and 0 µs IPG, separated by an interpulse interval of 500 µs. Both pulses were of an equal amplitude that was chosen to be the smallest amplitude at which an action potential was not generated. In the cathodic-leading condition, both pulses were CL-BPs, and in the anodic-leading condition, both pulses were AL-BPs. In the analysis below, the times t_1, t_2, and t_3, shall refer to the time of the first pulse's cessation, the second pulse's onset, and the second pulse's cessation, respectively.

Cathodic-leading biphasic stimulation

Let us consider first the case of the CL-BP-pair (Figure 6.7). The leading phase of the first pulse moves the phase point from its resting position at **a** to a higher value in the V dimension without a large effect in the m dimension. During the IPG, the phase point advances to higher values in the V and m dimensions. The trailing phase of the first pulse then moves the phase point to lower values in the V dimension. At the end of the first pulse (time t_1), the phase point is at the position marked by t_1. Throughout the pulse's delivery, the V-nullcline moved upwards, moving the resting node downwards and leftwards while simultaneously moving the saddle node upwards and rightwards (compare the resting V-nullcline, labelled *"V-n@ rest"*, with the V-

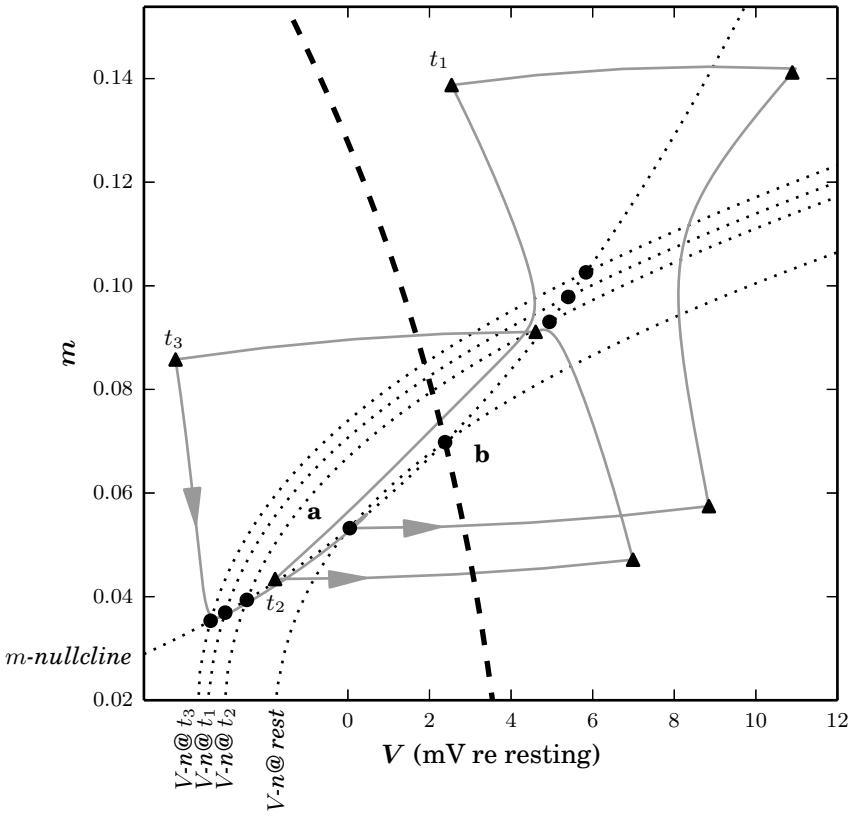

Figure 6.7: Phase path of the HH model stimulated by a pair of CL-BPs (40 µs/phase duration, 100 µs IPG) projected to the (V, m) phase plane (**grey line**). The second pulse is delivered 500 µs after the first, and both pulses are delivered at an equal level, chosen as the greatest level that does not result in excitation. Also plotted are the m-nullcline (**dotted line** labelled *"m-nullcline"*), the resting V-nullcline (**dotted lines** labelled *"V-n@ rest"*), the V-nullcline at times $t_{1..3}$ (**dotted lines** labelled *"V-n@ $t_{1..3}$"*; t_1 = 180 µs, t_2 = 230 µs, t_3 = 410 µs), the resting node (**a**), the saddle node (**b**), the locations of the phase point at the moments of each phase's onset/offset (**black triangles**), and the resting separatrix (**dashed line**). *At the end of the first CL-BP (labelled t_1), the system is close to excitation; at the end of the second CL-BP (labelled t_3), the system is far from excitation.*

nullcline at the time of the first pulse's cessation, labelled *"V-n@ t_1"*, and note the moving points of intersection between the V and m nullclines). The movement of the V-nullcline renders the model less excitable by moving the resting and saddle nodes away from one-another. It also increases the width of the well (the region enclosed by the nullclines; see Section 3.1.3), increasing the rate at which the phase point traverses the trajectory towards the resting node and away from the saddle node. By the time of the second pulse's onset at time t_2, the phase point is considerably downwards and leftwards of its initial resting position (**a**). Because of the advanced saddle node, the leading phase of the second pulse is insufficient to cause a self-sustained increase in V; after the phase's cessation, the phase point does advance to higher values in the m dimension, but only to lower values in the V dimension. Following the cessation of the second pulse, the phase point rapidly converges upon a point that is downwards and leftwards in comparison to the initial resting position (**a**). Over the course of 1 to 2 ms, the V-nullcline returns to its resting position and the phase point again converges upon the resting node at **a**.

The tangible qualitative feature of the analyses is that the second pulse was far less able to excite the model than the first pulse. It may thus be concluded that the interactions between consecutive CL-BPs inhibit excitation at the inter-pulse interval of 500 µs that was used here. If the second pulse were delivered sufficiently early during the downwards-leftwards sweep of the phase point from t_1, then the leading phase of the second pulse would restore the phase point to a position far beyond the saddle node in both the V and m dimensions, and so the interactions between pulses would facilitate excitation instead of inhibiting it; I have not investigated how short an inter-pulse interval would be necessary for this to occur.

To assess the validity of the hypothesis that the interactions between consecutive CL-BPs are inhibitory, the stochastic HH model was stimulated with a train of 5 CL-BPs delivered at a rate of 1,000 pulses per second (pps) and the cumulative spike count with respect to time was observed across 100 trials (Figure 6.8). All the pulses in the train have equal amplitude, phase duration (40 µs), and IPG (0 µs). Two different amplitudes were used, *individual threshold level* (L_1) and *compound threshold level* (L_2). The individual threshold is the level at which any of the individual pulses would evoke excitation with probability 0.5 when delivered in isolation. The compound threshold is the level at which the entire train evokes excitation (at any time) with probability 0.5. To avoid the confounding effects of refractoriness, once an action potential has been evoked in a given trial, the membrane potential is held at $+\infty$ for

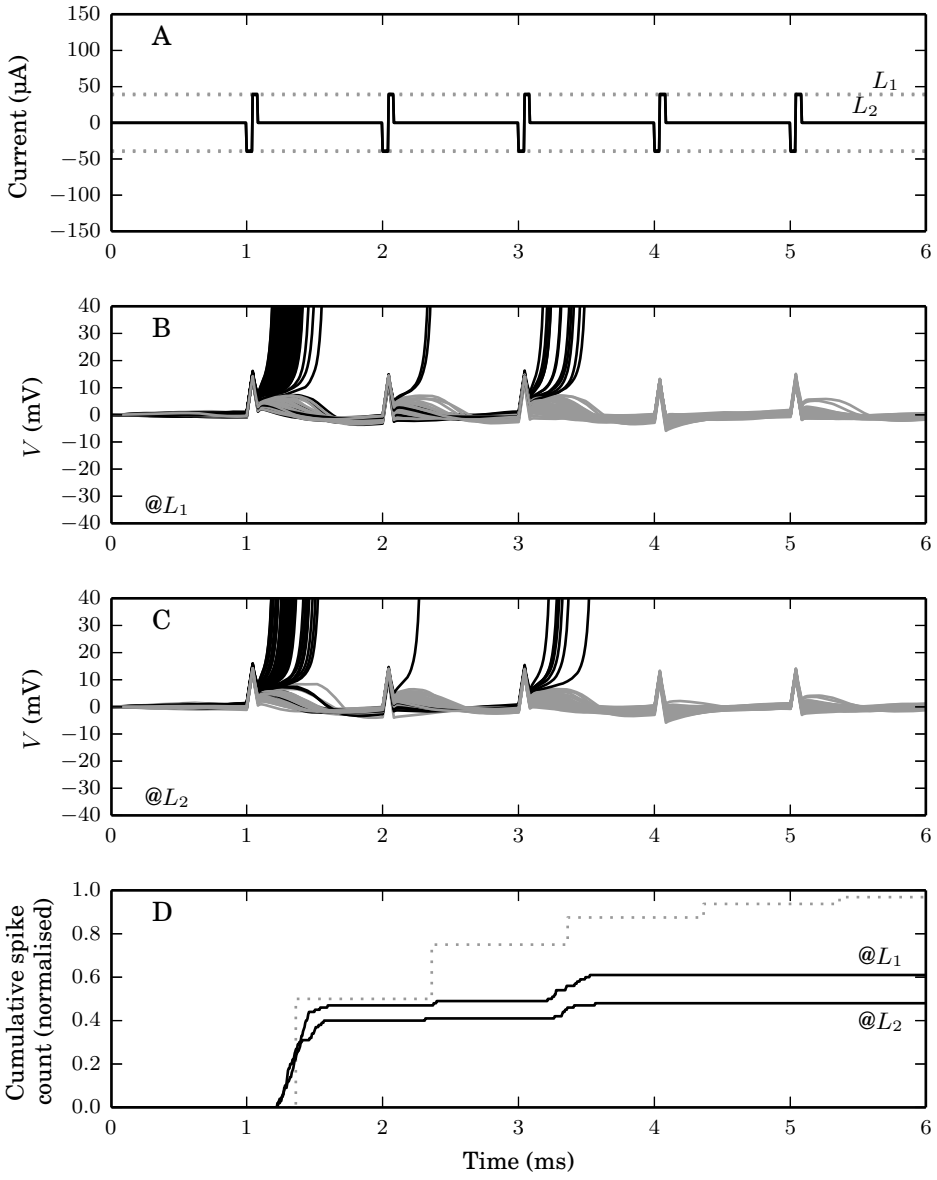

Figure 6.8: Responses of the HH neuron to trains of CL-BPs. The stimulus waveform (**black lines**, **plot A**) was delivered at two different levels, L_1 and L_2 (**grey dotted lines**, **plot A**; note, they are too closely-spaced to be distinguishable from one-another). L_1 is the level at which a single pulse from the train will evoke spiking with probability 0.5 if delivered in isolation. L_2 is the level at which the entire train will evoke spiking with probability 0.5. The membrane potential is plotted across multiple trials in **plot B** (stimulus level = L_1) and **plot C** (stimulus level = L_2). The cumulative spike count across multiple trials (normalised by the number of trials) is plotted (**plot D**) for both conditions (stimulus levels L_1 and L_2, corresponding to the upper and lower lines, respectively). Most spiking is in response to the first pulse. Temporal facilitation between pulses is weak.

the remainder of the trial, so that a given trial cannot contribute more than a single action potential. If there were no interactions between pulses, then when the train is delivered at individual threshold level, we would expect each pulse to excite 50% of the unexcited trials, as shown by the dotted line in plot D. By the end of the 5 pulses, we would expect 97% of the trials to have been excited. However, what we instead see is that the first pulse evokes excitation in 50% of the trials, but the subsequent pulses have almost no effect, with only ∼60% of the trials being excited by the train's cessation. This demonstrates that the interactions between the consecutive pulses cause each pulse (other than the first) to be less efficient in exciting the membrane than had it been delivered in isolation, consistent with the hypothesis from the above analysis.

Anodic-leading biphasic stimulation

Let us now consider the case of the AL-BP-pair (Figure 6.9). The leading phase of the first pulse moves the phase point from its resting position at **a** to a lower value in the V dimension, without a large effect in the m dimension. During the IPG, the phase point advances to lower values in m and higher values in V. The trailing phase of the first pulse then moves the phase point to higher values in V. At the time t_1 of the first pulse's cessation, the phase point is at the position marked by t_1. Throughout the pulse's delivery, the V-nullcline moves downwards (compare the V-nullcline at its resting position, labelled *"V-n@ rest*, to its position at time t_1, labelled *"V-n@* t_1*"*), causing the resting and saddle nodes to vanish: the only point at which the V- and m- nullclines intersect at the moment of the first pulse's cessation is at the excited node at very high values in the V and m dimensions (not shown). The phase point is thus attracted towards excitation after the first pulse's cessation, although the saddle node reappears at some point prior to the second pulse's onset, preventing excitation from being achieved (note that the V-nullcline at the time of the second pulse's onset, labelled *"V-n@* t_2*"*, intersects the m-nullcline, causing the reappearance of the resting and saddle nodes). At the time t_2 of the second pulse's onset, the phase point occupies a position just below and left of the saddle node (which has moved upwards and rightwards of its initial position at **b**). The second pulse's delivery affects the phase point in a similar way to the first, although, due to the movement of the V-nullclines, the phase point advances towards excitation less during the IPG of the second pulse than it did during the IPG of the first pulse. Upon cessation of the second pulse, the phase point is slightly advanced in both the V and m dimensions

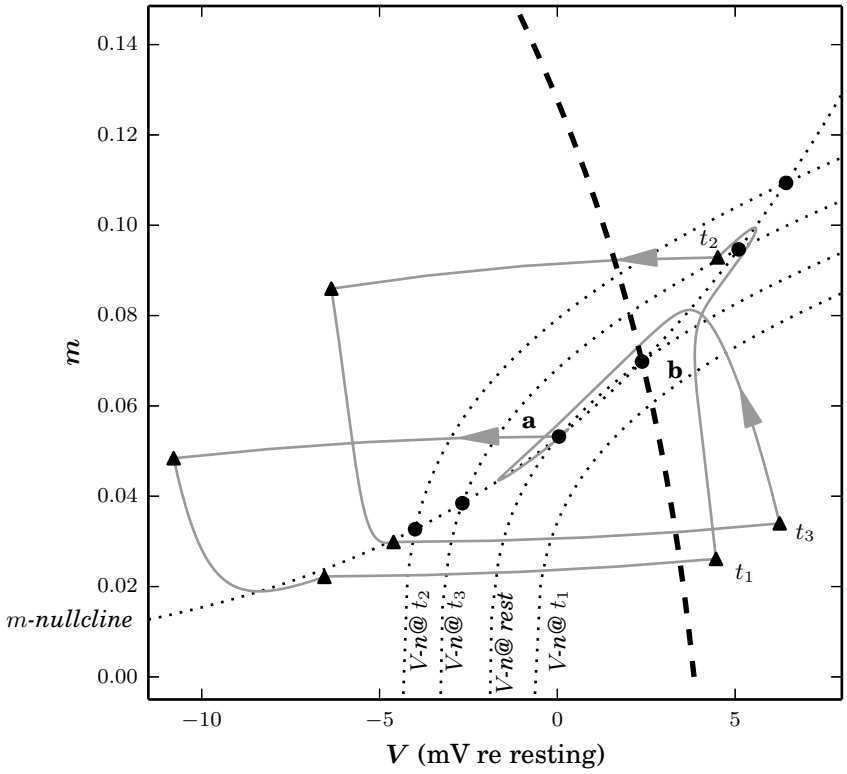

Figure 6.9: As in Figure 6.7, but with the two CL-BPs replaced by two AL-BPs of equal phase duration (40 µs/phase) and IPG (100 µs). *At the end of the first AL-BP (labelled t_1), the system is close to excitation; at the end of the second AL-BP (labelled t_3), the system is similarly close to excitation.*

compared to its position at the end of the first pulse. It is not clear from the projected phase paths whether the system is closer to excitation following the second pulse or the first, however it is clear that the system is qualitatively *close* to excitation following the cessation of both pulses. This may be compared to the case of cathodic-leading stimulation, wherein the system was almost excited by the first pulse, but following the second pulse, the system was clearly far from excitation.

To assess whether or not the stochastic HH model becomes more or less excitable following the delivery of an AL-BP, the methodology of Figure 6.8 was repeated using AL-BPs (Figure 6.10; all other parameters remain equal). In the case of individual threshold level stimulation, the delivery of the first pulse causes excitation in ∼52% of the trials, the third in ∼14% of the trials, and the fourth in ∼33%; the other pulses do not themselves cause excitation in a significant number of trials. Represented as percentages in terms of the number of trials unexcited by previous pulses, these figures become ∼52%, ∼29%, and 100%, respectively. If no interactions occurred between pulses, we would expect each pulse to evoke excitation in 50% of the trials unexcited by previous pulses. It thus seems that the first pulse inhibits the response to the second pulse, that the second pulse partially inhibits the response to the third, but that the third facilitates the response to the fourth. It would therefore seem like the interactions are more complex than a given AL-BP pulse simply inhibiting or facilitating subsequent pulses. These interactions may potentially be explained in terms of probability. If we suppose that each trial has a bias towards or against excitation, then those trials that are biased towards excitation shall most likely be excited by the first pulse, leaving mostly the trials biased against excitation for the second and subsequent pulses. The bias of a given trial changes with time, potentially explaining why the third pulse evoked excitation in more trials than the second pulse. Regardless of the mechanisms behind the interactions between AL-BPs, the fact excitation occurs in all 100 trials prior to the delivery of the fifth pulse indicates that the interactions between AL-BPs facilitate excitation, as the probability of this (100% excitation prior to the delivery of the fifth pulse in 100 trials) occurring by chance if there were no interactions between pulses is very small ($p = 0.0016$). This conclusion is consistent with the results of delivering both pulses at compound threshold level, where each pulse was individually unable to evoke excitation, yet the train of five pulses evoked excitation in ∼50% of the trials. Clearly, then, at this level, the individual pulses were in some way facilitating one another so as to achieve greater efficiency than would be possible individually.

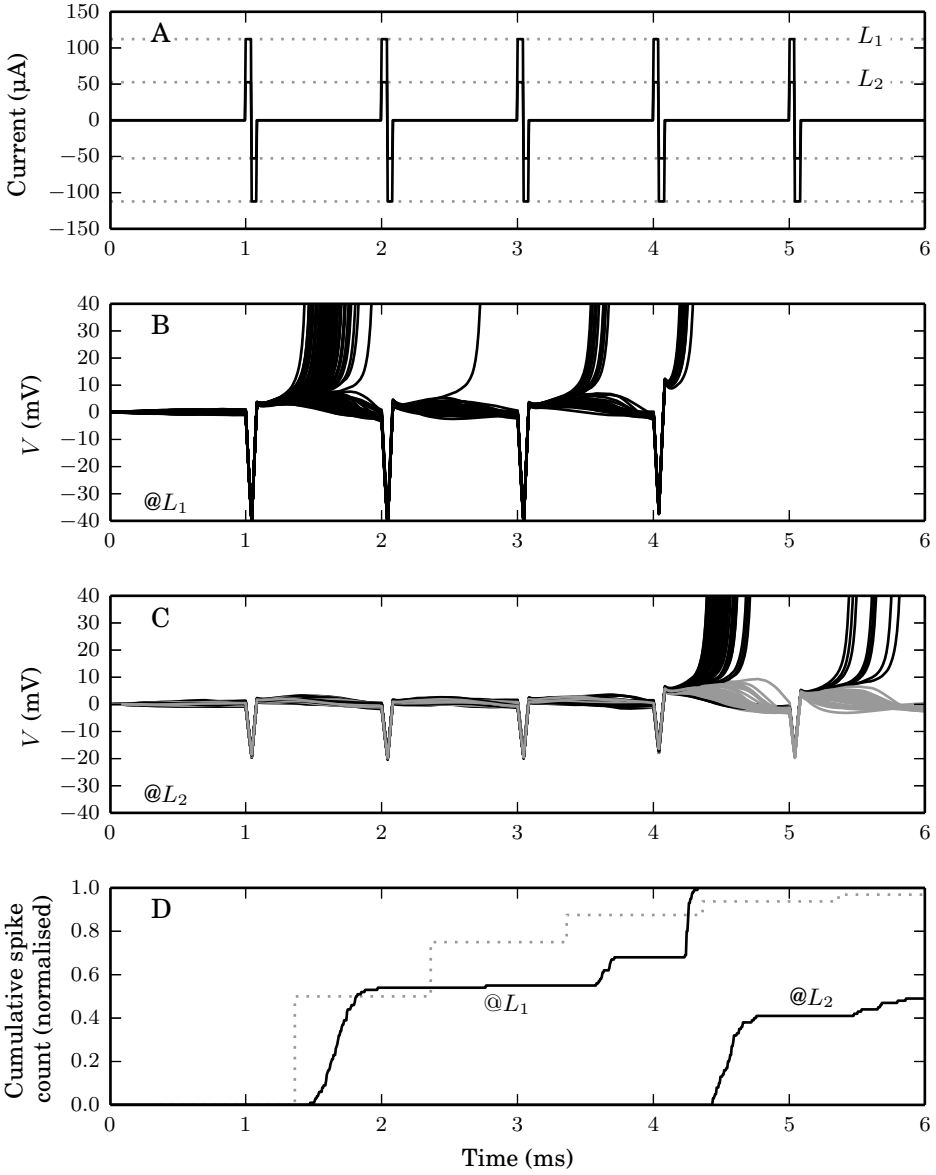

Figure 6.10: As in Figure 6.8, but the stimuli are trains of AL-BPs. The cumulative spike count of trials delivered at stimulus level L_1 (plot D, top line), shows that temporal facilitation occurs between pulses: the fourth pulse evokes spiking in 100% of the trials where spiking had not yet occurred; if there were no temporal facilitation then the fourth pulse would only evoke spiking in 50% of those trials. At level L_2, the first three pulses are subthreshold and almost all spiking is in response to the fourth pulse.

6.4 Discussion

This chapter has investigated how the responses of the HH model and its stochastic derivative are affected by the order in which the opposite polarity phases of a biphasic stimulus are delivered. Because the HH model has been widely accepted as a good model of the SGCs (Section 2.1.5), it is presumed that the SGCs shall be similarly affected by phase order, although this has not been demonstrated due to difficulties in comparing the results of this chapter against electrophysiological data.

The HH model (and its stochastic derivative) simulates a patch of membrane that is at equipotential. As such, the results of this chapter do not necessarily describe how the response of a whole neuron is affected by phase order (given that the neuron is *not* at equipotential), but instead describe how a single patch of membrane, or node or Ranvier (which is widely assumed to be at equipotential; e.g., see Ermentrout and Terman, 2010, chapter 6; Keener and Sneyd, 2010, chapter 6; Bressloff, 2013, chapter 2), is affected by phase order. The results of this chapter may therefore only be compared against electrophysiological data obtained from a membrane that is at equipotential, either by means of shorting the intracellular space (i.e., as done in *space-clamped* preparations), or by recording from only a single node of Ranvier. So far as I am aware, no space-clamp or single-node experiments have been conducted in SGCs due to practical difficulties arising from their small diameters, and so the results of this chapter cannot be directly compared against data from existing electrophysiological studies of SGCs.

A full biophysical model of the neuron, coupled with an electric field model of the cochlea, may potentially be used to circumvent the practical difficulties of obtaining the electrophysiological data that is necessary in order to verify the results of this chapter. The biophysical model of the neuron would allow the responses of a single node to be targeted, providing data against which the results of this chapter may be compared. The biophysical model itself must then be verified, but in this case, the responses of the model may be directly compared against the responses of SGCs.

Chapter 7

Discussion

In this thesis, I developed a novel phenomenological model of the electrical stimulation of the SGC, I investigated how monophasic and biphasic pulses excite the membrane in the HH model and its reduced and stochastic variants, and I developed novel methodologies in order to interpret and analyse the effects of the phase order of biphasic pulses. Further, in the cases where existing methodologies were applied (e.g., phase plane analysis), they were applied in contexts where they have not been previously (e.g., in understanding the effects of phase order in biphasic stimulation), and they have led to novel results (e.g., spike cancellation in the BLIF neuron). A main contribution of the thesis has been to investigate how anodic current may cancel an impending action potential in the HH model (referred to as *spike cancellation*), and to phenomenologically reproduce with the BLIF neuron how this affects the thresholds of CL-BPs.

7.1 Related work

7.1.1 Spike cancellation in the literature

The concept of spike cancellation has played a central role in this thesis, providing the underlying theory upon which the BLIF neuron was built, and motivating the analyses of chapters 3, 4, and 6. However, the concept of spike cancellation is not in itself novel, having previously been observed by van den Honert and Mortimer (1979), who described a *"vulnerable period"* of approximately 100 µs during which an impending action potential could be abolished by anodic stimulation. The vulnerable period has since been used in other electrophysiological studies to explain why biphasic pulses

are less efficient in exciting the neuron compared to monophasic pulses (Shepherd and Javel, 1999; Middlebrooks, 2004; Rubinstein et al., 2001; McKay and Henshall, 2003). In this section, I describe how the methodology and results of this thesis relate to those of previous studies that have also investigated spike cancellation.

The abolishing of the action potential

In their study, van den Honert and Mortimer offered an informal explanation of the vulnerable period, postulating that, following suprathreshold stimulation, a slow "regenerative process" (described as the opening of the sodium ion channels) is responsible for reversing the passive repolarisation of the membrane, maintaining a self-sustaining depolarisation (i.e., an action potential). They further say that under cathodic-leading biphasic stimulation, the anodic phase of the stimulus accelerates the passive repolarisation and abolishes the action potential. An "abolition threshold" was hypothesised to exist, defined as the current level required in order for a trailing anodic pulse to abolish the action potential evoked by a leading cathodic pulse of fixed amplitude. The dependence of the abolition threshold on stimulus parameters (namely, the current level of the cathodic pulse and the delay between the cathodic and anodic pulses) was investigated by means of the Frankenhaeuser and Huxley (1964) membrane equations. However, no theoretical explanation for the existence of the abolition threshold was given in terms of these equations. In this thesis, I have related the abolition threshold to the speed of the phase point (section 6.2), as well as the latency of the action potential (Chapter 5). I have also described the underlying cause of the vulnerable period in terms of the separatrix and the V and m dimensions of the HH model, instead of attributing it only to a "regenerative process" and "passive repolarisation". Further, I have quantified how the n and h variables of the HH model affect action potential abolition (by comparing the thresholds of CL-BPs in the reduced HH with those of the original HH model; section 6.1), and have described why they do not have a large effect on the qualitative dependency of a CL-BP's threshold on its IPG (section 3.3.2).

The activation time of the membrane

Rubinstein et al. (2001) published a related study that investigated the response of the membrane to CL-BPs, with the aim of relating biphasic thresholds to those of monophasic pulses. In the study, it is hypothesised that for a CL-BP to excite the membrane, it must drive the membrane above a threshold potential θ at least t_{act}

seconds prior to the pulse's cessation, where the θ is defined as

$$\theta = IR(1 - \exp(-\varphi/\tau)),$$

where I is the threshold level of a monophasic pulse of φ seconds duration, R is the membrane resistance, and τ is the membrane time constant. The study refers to t_{act} as the "activation time", and describes it as "the time required by the membrane to achieve an irreversible action potential trajectory prior to the phase reversal of the biphasic pulse." It takes values between ∼8 to ∼23 µs, depending on the membrane time constant, the phase duration of the CL-BP, the monophasic/biphasic threshold ratio, and, presumably the IPG, although the effects of the IPG were not investigated. The study relates the activation time to the vulnerable period of van den Honert and Mortimer.

While Rubinstein et al.'s concept of the activation time is related to the concept of spike cancellation in the BLIF neuron, the two are not equivalent. In particular, given that the activation time depends on the stimulus, it can not be incorporated into a phenomenological model as a parameter. By comparison, the spike cancellation of the BLIF neuron does not make any assumptions about the shape stimulus, and is defined in terms of constant parameters that do not depend on the stimulus. Further, the spike cancellation of the BLIF neuron *only* affects how the model responds to CL-BPs, having exactly no effect on how the model responds to AL-BPs. In stark comparison, Rubinstein et al. state that, regarding their analysis by means of the activation time, "there is no obvious reason why a similar analysis should not be applicable to anodal and anodal-first stimuli as long as latency shifts associated with level are properly interpreted." All of the results of this thesis point towards the membrane responding very differently to cathodic-leading and anodic-leading biphasic stimulation. It is clear that Rubinstein et al. were not aware of the disparities between cathodic-leading and anodic-leading biphasic stimulation that have been proposed by this thesis, suggesting that this thesis contributes substantially to our understanding of biphasic stimulation.

7.1.2 Use of phase plane analysis to understand excitation

In Chapters 3 and 4, I investigated how monophasic and biphasic pulses excite the membrane by analysing the (V, m)-projected phase paths of the HH model and its stochastic derivative. Previously, phase plane analysis has been used to analyse how cathodic monophasic pulses excite the membrane (Fitzhugh, 1960, 1961, 1969; Lecar

and Nossal, 1971). I have extended this methodology in the context of biphasic stimulation, and have produced novel results relating to the importance of phase order. Further, I use a novel methodology in interpreting the (V, m)-projected phase paths of the stochastic HH model to quantify how (or *when*) stochasticity affects the model's response (section 4.3.1), and demonstrate that this differs between cathodic-leading and anodic-leading biphasic stimulation. Further, while the fact that the saddle node of the HH model is not static when projected to the (V, m) plane has been noted previously by Fitzhugh (1969), I have illustrated its trajectory (section 3.3.2) and discussed throughout the thesis how it affects the responses of the model under stimulation by different pulse shapes.

7.1.3 The Rinzel reduction of the Hodgkin Huxley model

In Chapter 3, excitation was analysed from the point of view of the phase plane of the (V, m)-reduced HH model. This model holds the h and n variables of the HH model fixed at their resting values under the assumption that neither variable changes enough during the initial formation of the action potential to influence whether or not excitation occurs. The analyses of the chapter were motivated by a desire to find a biophysical interpretation of the spike cancellation strategy of the BLIF neuron in the context of cathodic-leading biphasic stimulation. In cathodic-leading biphasic stimulation, changes in h and n do not qualitatively change how the stimulus threshold level depends on IPG in the HH model (as evident by Figure 6.1B). However, in anodic-leading biphasic stimulation, changes in h and n do lead to a qualitative difference in behaviour: the biphasic threshold level in the HH model falls below the monophasic threshold level as the IPG is increased beyond ∼200 µs (40 µs/phase duration; see Figure 6.1A) due to the leading anodic phase inducing a decrease in h and n, rendering the membrane more excitable at the time of the trailing cathodic phase. Therefore, especially when analysing the response to anodic-leading biphasic stimulation, it would have been beneficial to use an alternative reduction of the HH model—one capable of reproducing the effects of changes in h and n, as well as V and m. One such model has been published by Rinzel (1985).

Rinzel's model reduces the four variables of the HH model to two variables, V and W. It does so by assuming that m is instantaneously affected by V (thereby removing m and replacing it with $m_\infty(V)$) and merging the h and n variables into a single variable, W, with

$$\frac{\mathrm{d}W}{\mathrm{d}t} = \frac{\phi(W_\infty(V) - W)}{\tau_W(V)},$$

where ϕ is the temperature correction factor of the HH model,

$$W_\infty(V) = S\frac{n_\infty(V) + S(1 - h_\infty(V))}{1 + S^2}$$
$$\tau_w(V) = 5\exp(-(V + 10)^2/55^2) + 1$$
$$S = \frac{1 - h_0}{n_0},$$

and h_0 and n_0 are the resting values of h and n in the HH model, respectively. The merging of h and n into a single variable was justified by noting that the (h, n)-projected phase point of the HH model follows an almost linear trajectory during an action potential (Fitzhugh, 1961), which Rinzel approximated by the line $h + Sn = 1$, with the constant S as previously defined, and so one variable (h or n) may be approximated given the other. The dynamics of V are then defined by making the substitutions

$$m \leftarrow m_\infty(V)$$
$$h \leftarrow 1 - W$$
$$n \leftarrow W/S$$

in (2.4), which described the dynamics of V in the HH model, resulting in

$$C\frac{\mathrm{d}V}{\mathrm{d}t} = I - \bar{g}_{\mathrm{Na}}m_\infty^3(V)(1 - W)(V - E_{\mathrm{Na}}) - \bar{g}_{\mathrm{K}}(W/S)^4(V - E_{\mathrm{K}}) - g_{\mathrm{L}}(V - E_{\mathrm{L}}). \quad (7.1)$$

The phase space of the Rinzel model is shown in Figure 7.1. The phase point is attracted in the W dimension to the W nullcline. When the phase point lies *below* the V nullcline, it is attracted rightwards in the V dimension, and when it lies *above*, it is attracted leftwards. The figure shows the trajectory of a *quasi-threshold*, which passes underneath the resting node from the left before sweeping upwards to closely adjoin the V nullcline. The quasi-threshold does not lead to a saddle node, but leads directly to the resting node, and so even if the phase point is placed *precisely* on the quasi-threshold, the system shall return to rest.[1] If the phase point lies below/rightwards of the quasi-threshold, then an action potential shall result, with the phase point first sweeping rightwards and then returning to rest via an anti-clockwise arc.

Like in the (V, m)-reduced HH model, an instantaneous injection of charge displaces

[1] Which is in contrast to in the (V, m)-reduce HH model, wherein placing the phase point on the separatrix results in the system reaching an unstable equilibrium at the saddle node, poised between becoming excited and returning to rest.

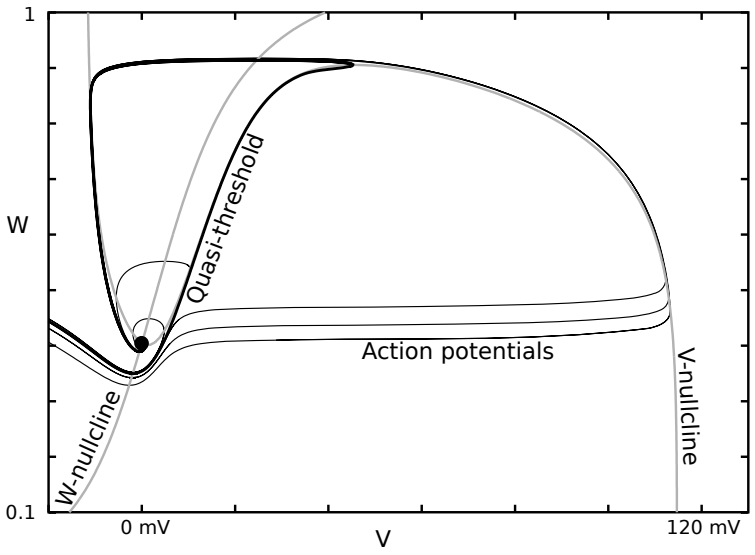

Figure 7.1: Phase plane of the Rinzel model, showing the stable resting node (**filled black circle**), the W and V nullclines (**bold grey lines**), the *quasi-threshold* (**bold black line**), and several example trajectories (**thin black lines**). All the plotted trajectories have an anti-clockwise direction. Numerical integration performed using the Runge-Kutta method with a time step of 10 µs.

the phase point horizontally in the (V, W) phase plane of the Rinzel model. The delivery of a charge-balanced CL-BP of infinitesimal duration per phase displaces the phase point first rightwards, due to the delivery of the leading cathodic phase, and then an equal amount leftwards, due to the delivery of the trailing anodic phase. During the interval between the two phases (the IPG), the phase point drifts, as determined by the dynamics of V and W. For an action potential to be evoked, this drift must move the phase point so far rightwards that it remains to the right of the quasi-threshold following the leftwards displacement of the trailing anodic phase.

If a CL-BP is delivered at such a level that the cathodic phase leaves the phase point exactly on the quasi-threshold, then the phase point shall traverse the quasi-threshold upwards and rightwards during the IPG. It then requires only an infinitesimal amount of trailing anodic charge to return the phase point to the left of the quasi-threshold, resulting in no action potential being emitted. This is similar to the case with the (V, m)-reduced HH model, in which the phase point would traverse the separatrix if

left upon it by the cathodic phase.[2] However, as the phase point advances further rightwards beyond the quasi-threshold (as occurs if the cathodic phase delivers ∼6 dB more charge than would be needed to displace the phase point from resting to quasi-threshold), its drift becomes increasingly rightwards (as evident from the example phase paths in Figure 7.1), with any upwards drift producing only negligible change in the distance of the phase point from the quasi-threshold. In such cases, the dynamics of W have negligible effect on whether or not an action potential will be initiated, and so need not be modelled when analysing only excitation. The time constant of m, however, increases with increasing V (up until $V = \sim 26$ mV), and so the approximation of m by $m_\infty(V)$, taken by the Rinzel model, becomes less accurate when the phase point is to the right of the quasi-threshold.

A charge-balanced CL-BP of short ($<\sim$200 µs) duration has a threshold level high enough that, when delivered at threshold level, the cathodic phase will displace the resting phase point well into the territory whereat changes in W have negligible effect on action potential initiation and m has a longer time constant. Further, at such short durations, the time constant of m is no longer negligible compared to the duration of the stimulus, and so accurately modelling the dynamics of m becomes more important, given that the different phases of the stimulus have very different effects on m. This suggests that the (V, m)-reduced model may offer insights not available with the Rinzel model when analysing excitation by short-duration CL-BPs. Conversely, though, the Rinzel model demonstrates that changes in n and h do affect excitability when the phase point lingers near the quasi-threshold during the IPG, as occurs during threshold-level stimulation by long-duration ($>\sim$200 µs) CL-BPs, due to their decreased thresholds.

The delivery of a charge-balanced AL-BP of infinitesimal duration per phase displaces the phase point of the Rinzel model first leftwards, due to the delivering of the leading anodic phase, and then an equal amount rightwards, due to the delivery of the trailing cathodic phase. During the IPG, the phase point drifts downwards and rightwards. Excitation may occur by either of two means: the leading anodic phase may displace the phase point to beneath the quasi-threshold (noting that the quasi-threshold forms a 'u'-like shape that contains the resting node; a leftwards displacement may cause the resting phase point to breach the 'u'), or the phase point may drift downwards/rightwards so far during the IPG that the delivery of the trailing

[2] Although, how the phase point departs from its quasi-threshold/separatrix traversal differs between models. In the (V, m)-reduced model, the phase point traverses the separatrix until it is deflected by the saddle node. In the Rinzel model, the quasi-threshold becomes increasingly more repulsive to the phase point the further upwards/rightwards it is traversed.

cathodic phase displaces the phase point beyond the quasi-threshold. In the former case, excitation occurs by means of anodic break, without the need for the cathodic phase at all—indeed, it is interesting to note that within a narrow range of stimulus levels, the delivery of the cathodic phase may *abolish* anodic break excitation by re-establishing the phase point within the 'u' of the quasi-threshold. In either case, the downwards motion of the phase point during the IPG has a large effect on whether or not an action potential is evoked, and so the Rinzel model proves very useful in analysing excitation by means of anodic-leading biphasic stimulation.

To conclude, Rinzel's reduction of the HH model provides an alternative framework with which to analyse excitation. It is very well suited to analysing excitation by means of anodic-leading biphasic stimulation, wherein changes in W have a strong influence on whether or not excitation occurs. It is potentially also useful in analysing excitation by means of long-duration cathodic-leading biphasic stimulation, wherein changes in W may also influence excitation, although to a lesser effect. However, it does not appear to be as well suited as the (V, m)-reduced HH model in analysing excitation by means of short-duration ($<\sim$200 µs) cathodic-leading biphasic stimulation, wherein changes in W have much less influence on excitation. It is without doubt that further analysis with the Rinzel model would compliment the analyses of this thesis, especially in understanding excitation by means of anodic-leading biphasic stimulation. However, given that the primary motivation of the analyses of this thesis has been to provide a biophysical interpretation of the spike cancellation of the BLIF neuron (noting that spike cancellation in the BLIF neuron occurs primarily under short-duration cathodic-leading biphasic stimulation), the choice of the (V, m)-reduced HH model seems justified.

7.2 Limitations of point models

The novel phenomenological model developed in this thesis, the BLIF neuron, is a point model, and as such, in common with all other point models, it only reproduces how a single node of Ranvier (or, equivalently, a single patch of membrane that is small enough to be at equipotential) responds to stimulation. However, in extracellular stimulation, the response of the neuron is not determined by a single node, but rather by the potentially large collection of nodes that are simultaneously stimulated (see section 2.2.3). This section discusses the caveats of applying the results of *any* point model (including the BLIF neuron) in the context of extracellular stimulation. Suggestions as to how these caveats may be addressed will be given in the next section.

Internodal stochastic independence

When stimulated by an electrode of a cochlear implant, a single SGC is simultaneously affected by the stimulus at its multiple nodes of Ranvier (see section 2.2.3). The SGC as a whole shall be excited if any of its individual nodes are excited. As the individual nodes are, at least to some extent, stochastically independent, the probability of *any* node being excited by a given stimulus is greater than the probability of a single, *given* node being excited by the same stimulus. Therefore, if a SGC is stimulated at a level that evokes an action potential with some probability p, then the probability of a given node initiating the action potential shall be less than p. If the distance between the electrode and axon is increased while simultaneously adjusting the stimulus level so as to continue to evoke an action potential with fixed probability p, then the probability of a given node initiating the action potential shall decrease due to more nodes being driven by the stimulus at larger electrode-axon distances. By these means, in a theoretical axon with a large number of nodes, the probability of a given node responding to a threshold-level stimulus may be made arbitrarily small. Even in a real axon with a finite number of nodes, the difference between the total firing probability and the per-nodal firing probability is considerable. In a biophysically-detailed model of a cat SGC stimulated by an electrode positioned 7 mm from it, the overall firing probability of the cell was 0.751, yet the greatest probability of a given node initiating the action potential was only 0.249 (Mino et al., 2004). Because firing probability is related to temporal variability, decreasing the probability of a given node initiating the action potential causes an increase in that node's temporal variability. In this way, the relation between the firing probability and the temporal variability of a SGC depend on the geometry of the cell in a way that cannot be reproduced by a point model. These results are due to Mino et al. (2004), who stimulated a stochastic HH model of the axon with a single cathodic pulse and varied the distance of the electrode from the axon while maintaining a fixed firing probability. They concluded that the increased temporal variability at increased electrode-axon distances was due to each individual node being driven to lower firing probabilities at greater electrode-axon distances as the stimulus recruited more nodes.

Changing latencies with increased nodal recruitment

The number of nodes that are excited by the stimulus depends on the stimulus level. At greater levels, current spread results in the stimulus being able to excite more central nodes (Woo et al., 2010; Rattay et al., 2001b). Action potentials evoked by

these nodes have fewer subsequent nodes through which to propagate, and as such, these action potentials have lower latencies. This results in discrete jumps in latency as the stimulus level is increased (Miller et al., 1999b, 2003; Javel et al., 1987; Javel, 1990). At the thresholds between these jumps, the latency distribution may have two or more peaks, with the most dramatic bimodal distributions occurring when the neighbouring nodes occur on opposing sides of the soma (Stypulkowski and van den Honert, 1984; Miller et al., 1999b).

Peak splitting

When the neuron is stimulated by a monophasic stimulus delivered via an extracellular electrode, the neuron is simultaneously depolarised and hyperpolarised at different points along its length. Because of the radically lower threshold of make excitation compared to break excitation (see Section 2.2.3), the action potential will normally only be initiated at a depolarised node. However, if the stimulus is a charge balanced pulse (e.g., a biphasic pulse) instead of a monophasic pulse, then every point along the neuron shall be depolarised by one of the pulse's phases, and so the action potential may potentially be initiated by any node. The specific node that initiates the action potential may vary stochastically between trials to the same stimulus, manifesting as multiple peaks in the distribution of spike timing due to the differing number of nodes through which the action potential must propagate prior to arrival at a more central site (Shepherd and Javel, 1999; Javel et al., 1987; Javel and Shepherd, 2000; van den Honert and Stypulkowski, 1987; Miller et al., 1999b). The relative contributions of the various peaks depend on the stimulus level; at higher levels, the earlier peak (corresponding to action potential initiation by more central nodes) shall dominate, where-as at lower levels, the later peaks shall dominate. This phenomenon has been termed *peak splitting* by Shepherd and Javel (1999).

Action potentials are always initiated by make-excitation

Chapters 3 and 4 demonstrated that a cathodic pulse excites the membrane in a very different way to an anodic pulse, illustrating the difference between make-excitation (in the case of the cathodic pulse) and break-excitation (in the case of the anodic pulse). However, in extracellular stimulation, an anodic pulse does not necessarily evoke an action potential via break-excitation, for make-excitation may also occur due to the pulse depolarising the neuron at the positions along where the activating function is negative (i.e., where the membrane is depolarised by anodic current; see

section 2.2.3). Indeed, it seems likely that break-excitation does not occur at all in extracellular stimulation because of its very high threshold (∼9.1 dB relative to make excitation, in the stochastic HH model). Data from a modelling study by Rattay et al. (2001a) supports this hypothesis. In the study, a biophysically-detailed model of the human cochlea was stimulated with anodic and cathodic monophasic pulses of equal duration. Changing the pulse polarity change the node that was responsible for initiating the action potential, suggesting that, regardless of the pulse's polarity, the action potential was initiated via the make-excitation at whichever node became most depolarised. That the node responsible for initiating the action potential is different in anodic and cathodic extracellular stimulation has also been reported in electrophysiological studies of the cat SGCs (Miller et al., 1998, 1999b). It has the effect of lowering the threshold of anodic stimulation by allowing the neuron to respond by make-excitation instead of break-excitation, which has a much higher threshold. This is reflected in Rattay et al.'s study, where the threshold of the anodic pulse was, averaged across distinct fibres, 0.082 dB *less* than the threshold of the cathodic pulse of equal duration.

Biphasic pulses

In extracellular stimulation, a biphasic pulse of either phase-order affects the neuron by hyperpolarising-and-then-depolarising the membrane at some points along its length, while simultaneously depolarising-and-then-hyperpolarising the membrane at other points. This is in contrast to in space-clamped conditions (i.e., where the membrane is at equipotential, as in the HH model or a point model), where a biphasic pulse *either* depolarises-and-then-hyperpolarises the membrane (in the case of a CL-BP), *or* hyperpolarises-and-then-depolarises the membrane (in the case of an AL-BP). The effect, then, of reversing the phase order of a biphasic pulse is different in space-clamped conditions and extracellular stimulation. In space-clamped conditions, reversing the phase order shall change the order in which the membrane was depolarised/hyperpolarised. In extracellular stimulation, reversing the phase order of the pulse *may* change the order in which the initiating node was depolarised/hyperpolarised, *or*, alternatively, it may change which node initiates the action potential (Coste and Pfingst, 1996; Parkins, 1989), so that the initiating node is depolarised/hyperpolarised in the same order regardless of the phase order of the stimulus. This may explain why the behaviour of the extracellularly-stimulated SGC appears to be relatively insensitive to phase order under biphasic stimulation (Shepherd and

Javel, 1999; Macherey et al., 2006), as the change in threshold due to a change in initiation node may be less than the change in threshold due to a change in depolarisation/hyperpolarisation order.

Neuron geometry and the extracellular field

How a neuron responds to extracellular stimulation is largely affected by its geometry and the electrical properties of the extracellular medium (Grill Jr, 1999; Rattay et al., 2001a; Loeb et al., 1983). Changing either the geometry of the neuron (for instance, to model the curvature of the SGCs as they exit the modulus of the cochlea), or the electrical field generated by the stimulating electrode (for instance, to model the effects that the different structures of the cochlea have on the generated field), may have a profound effect on the excitation pattern of the neuron (i.e., which nodes initiate the action potentials). From the previous discussions of this section, it is clear that changing which and how many nodes may potentially initiate action potentials shall change the probability of spiking, the temporal distribution of spiking, and how this distribution is affected by changes in the current level of the stimulus.

Concluding remarks

In the extracellular stimulation of a neuron, the geometry and morphology of the neuron interact with the electrical field generated by the stimulating electrode to produce a complex set of phenomena that cannot be reproduced by point models, including the BLIF neuron. Given that cochlear implants stimulate the SGCs by means of extracellular electrodes, this potentially limits the applicability of point models in reproducing the spiking activity of the SGCs in cochlear implant stimulation. Despite this, point models have been used extensively by previous studies to reproduce spiking activity in cochlear implant stimulation (e.g., Goldwyn et al., 2012; Bruce et al., 1999a,b,c; Chen and Zhang, 2007; Chen, 2012; Dynes, 1996; Motz and Rattay, 1986; Morse and Evans, 1999; Fredelake and Hohmann, 2012; Hamacher, 2004). The next section will suggest how a point model may be extended in order to reproduce the complexities of extracellular stimulation.

7.3 Alternatives to point models

The phenomena described in the previous section occur because, in extracellular stimulation, a stimulus may evoke an action potential at any one of many nodes, and the

effect of the stimulus on the membrane potential may vary between nodes, as described by the activating function. The varying effect of the stimulus on each node is typically reproduced by means of a biophysical model of the neuron coupled with an electric field model of the cochlea (e.g., Rattay et al., 2001b,a; Briaire and Frijns, 2000; Smit et al., 2010). However, these effects vary between subjects due to changes in cochlear morphology (Whiten, 2007), neural pathology (i.e., due to degeneration of the peripheral process, common in cochlear implant recipients; Hardie and Shepherd, 1999; Nadol Jr et al., 1989; Teoh et al., 2004; Micco and Richter, 2006; Whiten, 2007; Fayad and Linthicum, 2006), and electrode location (Kang et al., 2015; Briaire and Frijns, 2006; Shepherd et al., 1993; Whiten, 2007; Woo et al., 2010). Clearly, then, modelling *precisely* how the stimulus affects each node is overfitting the model to a particular subject. If the model is to facilitate the development of cochlear implant stimulation algorithms, then it should model only what is common across the majority of subjects, as reproducing effects which vary between subjects shall only lead to confusion in the interpretation of the model results. It is difficult to disentangle a biophysical model from the individual subjects from which it was morphological parametrised, and so to reproduce only the trends that are common among the majority of subjects, a phenomenological approach is well motivated. Such a phenomenological approach might simulate each node with an individual point model (such as the BLIF neuron), scaling the input to each by an amount related to the value of the activating function at the given node, and delaying the spiking output of each model to reproduce the delay incurred by the central-propagation of the action potential from the given node. The resulting model could be termed a *multipoint model*.

The methodology of linking two or more point models in a phenomenological model of the neuron has been well applied in the context of synaptic stimulation (Clopath et al., 2007; Kellems et al., 2010; Lánskỳ and Rodriguez, 1999b; Lánskỳ and Rospars, 1994; Lánskỳ and Rodriguez, 1999a; Rodriguez and Lánskỳ, 2000; Maršálek, 1999). The earliest example is the two-point model, proposed by Kohn (1989), where the passive properties of the dendrite are modelled separately to the spiking properties of the soma, and the two compartments linked via their membrane potentials. However, despite the prevalence of multipoint modelling in synaptic stimulation, multipoint modelling does not seem to have been applied in the context of extracellular electrical stimulation.[3]

[3] A recent exception to this is an unpublished study by Joshi et al. (2015), that feeds a stimulus signal and an inverted copy of the signal to two independent exponential integrate-and-fire neurons and sums their outputs.

7.4 Summary and future directions

The aim of this thesis has been to develop a phenomenological model capable of reproducing how SGCs responds to stimulation by a cochlear implant. The novel BLIF neuron (chapter 5) goes a long way towards accomplishing this: it reproduces the temporal distribution of spiking and how it is affected by stimulus parameters, and it reproduces how anodic current may raise the threshold of a cathodic pulse, even when delivered *after* the cathodic pulse, making it suitable for simulating responses to CL-BPs. However, the BLIF neuron does not form a complete model in itself, given that it does not recover following spiking or spike cancellation, and it does not reproduce the complexities of extracellular stimulation (discussed in section 7.2). A methodology by which to implement recovery following spiking and spike cancellation has already been proposed in Section 5.5.5, and similarly, a methodology by which a point model (such as the BLIF neuron) may be extended to reproduce the phenomena arising from extracellular stimulation has already been proposed in section 7.3. Thus, while this thesis has not presented a full phenomenological model of extracellular stimulation, it does outline how the BLIF neuron may be extended in order to achieve this goal.

As well as the contribution of the BLIF neuron itself, this thesis has contributed to the understanding of how different pulse shapes excite the membrane, particularly in the case of biphasic pulses. Chapters 3 and 4 provided novel qualitative descriptions of excitation under biphasic stimulation, making it very clear that the way by which excitation is achieved differs markedly between cathodic-leading and anodic-leading stimulation, consistent with the theory of the BLIF neuron. The effect of phase order on excitation was further analysed in chapter 6, which demonstrated quantitatively that the phase order of a biphasic stimulus affects its threshold level in the HH model (and its stochastic derivative). The chapter proposed that the thresholds may be explained by leaky integration and accommodation when the anodic phase is leading, and spike cancellation when the cathodic phase is leading. Analyses of the responses of the HH model (and its stochastic derivative) supported these theories. Finally, to demonstrate the importance of the different ways by which excitation occurs, Chapter 6 demonstrates that phase order affects how consecutive biphasic pulses interact with one another in the stochastic HH model. When the cathodic phase leads, it was shown that a leading pulse inhibits the membrane's response to a trailing pulse. When the anodic phase leads, it was shown that a leading pulse facilitates the membrane's response to a trailing pulse. These results are important in the context of cochlear

implants, which stimulate the SGCs by means of high-rate trains of biphasic pulses.

Bibliography

Abbas, P. J. and Brown, C. J. (1991). Electrically evoked auditory brainstem response: refractory properties and strength-duration functions. *Hearing Research*, 51(1):139–147.

Abbott, L. and Kepler, T. B. (1990). Model neurons: from Hodgkin-Huxley to Hopfield. In *Statistical Mechanics of Neural Networks*, pages 5–18. Springer-Verlag, Berlin Heidelberg, Germany.

Aidley, D. (1998). *The Physiology of Excitable Cells*. Cambridge University Press, Cambridge, UK.

Altman, K. and Plonsey, R. (1990). Analysis of excitable cell activation: relative effects of external electrical stimuli. *Medical and Biological Engineering and Computing*, 28(6):574–580.

Anderson, D. J., Rose, J. E., Hind, J. E., and Brugge, J. F. (1971). Temporal position of discharges in single auditory nerve fibers within the cycle of a sine-wave stimulus: frequency and intensity effects. *The Journal of the Acoustical Society of America*, 49(4B):1131–1139.

Ascher, U. M. and Petzold, L. R. (1998). *Computer methods for ordinary differential equations and differential-algebraic equations*, volume 61. SIAM, Philadelphia, USA.

Ashida, G. and Carr, C. E. (2011). Sound localization: Jeffress and beyond. *Current Opinion in Neurobiology*, 21(5):745–751.

Ashmore, J. (2008). Cochlear outer hair cell motility. *Physiological Reviews*, 88(1):173–210.

Bahmer, A. and Baumann, U. (2013). Effects of electrical pulse polarity shape on intra cochlear neural responses in humans: triphasic pulses with cathodic second phase. *Hearing Research*, 306:123–130.

Barr, R. C. and Plonsey, R. (1995). Threshold variability in fibers with field stimulation of excitable membranes. *IEEE Transactions on Biomedical Engineering*, 42(12):1185–1191.

Bergman, C. and Stampfli, R. (1966). Difference de permeabilite des fibres nerveuses myelinisees sensorielles et motrices a lion potassium. *Helvetica Physiologica et Pharmacologica Acta*, 24(4):247.

Bressloff, P. (2013). *Waves in Neural Media: From Single Neurons to Neural Fields*. Lecture Notes on Mathematical Modelling in the Life Sciences. Springer, New York, USA.

Briaire, J. J. and Frijns, J. H. (2000). Field patterns in a 3D tapered spiral model of the electrically stimulated cochlea. *Hearing Research*, 148(1):18–30.

Briaire, J. J. and Frijns, J. H. (2006). The consequences of neural degeneration regarding optimal cochlear implant position in scala tympani: a model approach. *Hearing Research*, 214(1):17–27.

Briggs, R. J., Tykocinski, M., Stidham, K., and Roberson, J. B. (2005). Cochleostomy site: implications for electrode placement and hearing preservation. *Acta Oto-Laryngologica*, 125(8):870–876.

Brown, A. M. and Hamann, M. (2014). Computational modeling of the effects of auditory nerve dysmyelination. *Frontiers in Neuroanatomy*, 8(73).

Bruce, I., Irlicht, L., White, M., O'Leary, S., Dynes, S., Javel, E., and Clark, G. (1999a). A stochastic model of the electrically stimulated auditory nerve: Pulse-train response. *IEEE Transactions on Biomedical Engineering*, 46(6):630–637.

Bruce, I., White, M., Irlicht, L., O'Leary, S., Dynes, S., Javel, E., and Clark, G. (1999b). A stochastic model of the electrically stimulated auditory nerve: single-pulse response. *IEEE Transactions on Biomedical Engineering*, 46(6):617–629.

Bruce, I. C. (2007). Implementation issues in approximate methods for stochastic Hodgkin-Huxley models. *Annals of Biomedical Engineering*, 35(2):315–318.

Bruce, I. C. (2009). Evaluation of stochastic differential equation approximation of ion channel gating models. *Annals of Biomedical Engineering*, 37(4):824–838.

Bruce, I. C., White, M. W., Irlicht, L. S., Leary, S. J., and Clark, G. M. (1999c). The effects of stochastic neural activity in a model predicting intensity perception

with cochlear implants: low-rate stimulation. *IEEE Transactions on Biomedical Engineering*, 46(12):1393–1404.

Brummer, S. and Turner, M. (1977). Electrochemical considerations for safe electrical stimulation of the nervous system with platinum electrodes. *IEEE Transactions on Biomedical Engineering*, (1):59–63.

Butikofer, R. and Lawrence, P. D. (1978). Electrocutaneous nerve stimulation–I: Model and experiment. *IEEE Transactions on Biomedical Engineering*, (6):526–531.

Calvin, W. H. and Stevens, C. F. (1968). Synaptic noise and other sources of randomness in motoneuron interspike intervals. *Journal of Neurophysiology*, 31(4):574–587.

Cappaert, N. L., Ramekers, D., Martens, H. C., and Wadman, W. J. (2013). Efficacy of a new charge-balanced biphasic electrical stimulus in the isolated sciatic nerve and the hippocampal slice. *International Journal of Neural Systems*, 23(01).

Carlyon, R., Van Wieringen, A., Deeks, J., Long, C., Lyzenga, J., and Wouters, J. (2005). Effect of inter-phase gap on the sensitivity of cochlear implant users to electrical stimulation. *Hearing Research*, 205(1-2):210–224.

Cartee, L. (2000). Evaluation of a model of the cochlear neural membrane. II: Comparison of model and physiological measures of membrane properties measured in response to intrameatal electrical stimulation. *Hearing Research*, 146(1-2):153–166.

Cartee, L., van den Honert, C., Finley, C., and Miller, R. (2000). Evaluation of a model of the cochlear neural membrane. I. Physiological measurement of membrane characteristics in response to intrameatal electrical stimulation. *Hearing Research*, 146(1-2):143–152.

Cartee, L. A., Miller, C. A., and van den Honert, C. (2006). Spiral ganglion cell site of excitation I: comparison of scala tympani and intrameatal electrode responses. *Hearing Research*, 215(1):10–21.

Casado, J. M. (2003). Synchronization of two Hodgkin-Huxley neurons due to internal noise. *Physics Letters A*, 310(5):400–406.

Chen, F. and Zhang, Y. (2007). An integrate-and-fire-based auditory nerve model and its response to high-rate pulse train. *Neurocomputing*, 70(4):1051–1055.

Chen, F. and Zhang, Y.-t. (2006). Loudness normalization for cochlear implant using pulse-rate modulation to convey mandarin tonal information: a model-based study.

In *Engineering in Medicine and Biology Society, 2006. EMBS'06. 28th Annual International Conference of the IEEE*, pages 1236–1239. IEEE.

Chen, X. (2012). *Pulsatile electrical stimulation of auditory nerve fibres: a modelling approach*. PhD thesis, University of Warwick, UK.

Chiu, S., Ritchie, J., Rogart, R., and Stagg, D. (1979). A quantitative description of membrane currents in rabbit myelinated nerve. *The Journal of Physiology*, 292(1):149–166.

Chow, C. C. and White, J. A. (1996). Spontaneous action potentials due to channel fluctuations. *Biophysical Journal*, 71(6):3013.

Clay, J. R. and DeFelice, L. J. (1983). Relationship between membrane excitability and single channel open-close kinetics. *Biophysical Journal*, 42(2):151.

Clopath, C., Jolivet, R., Rauch, A., Lüscher, H., and Gerstner, W. (2007). Predicting neuronal activity with simple models of the threshold type: Adaptive exponential integrate-and-fire model with two compartments. *Neurocomputing*, 70(10):1668–1673.

Cohen, L. T. (2009a). Practical model description of peripheral neural excitation in cochlear implant recipients: 1. Growth of loudness and ECAP amplitude with current. *Hearing Research*, 247(2):87–99.

Cohen, L. T. (2009b). Practical model description of peripheral neural excitation in cochlear implant recipients: 2. Spread of the effective stimulation field, from ECAP and FEA. *Hearing Research*, 247(2):100–111.

Cohen, L. T. (2009c). Practical model description of peripheral neural excitation in cochlear implant recipients: 3. ECAP during bursts and loudness as function of burst duration. *Hearing Research*, 247(2):112–121.

Cohen, L. T. (2009d). Practical model description of peripheral neural excitation in cochlear implant recipients: 4. Model development at low pulse rates: General model and application to individuals. *Hearing Research*, 248(1):15–30.

Cohen, L. T. (2009e). Practical model description of peripheral neural excitation in cochlear implant recipients: 5. Refractory recovery and facilitation. *Hearing Research*, 248(1):1–14.

Colombo, J. and Parkins, C. (1987). A model of electrical excitation of the mammalian auditory-nerve neuron. *Hearing Research*, 31(3):287–311.

Cooley, J. and Dodge Jr, F. (1966). Digital computer solutions for excitation and propagation of the nerve impulse. *Biophysical Journal*, 6(5):583–599.

Coste, R. L. and Pfingst, B. E. (1996). Stimulus features affecting psychophysical detection thresholds for electrical stimulation of the cochlea. III. Pulse polarity. *The Journal of the Acoustical Society of America*, 99(5):3099–3108.

Cotterill, R. (2003). *Biophysics: An Introduction*. John Wiley & Sons, Chichester, England.

Cudmore, R. H., Fronzaroli-Molinieres, L., Giraud, P., and Debanne, D. (2010). Spike-time precision and network synchrony are controlled by the homeostatic regulation of the d-type potassium current. *The Journal of Neuroscience*, 30(38):12885–12895.

Daley, D. and Vere-Jones, D. (2003). *An Introduction to the Theory of Point Processes, Volume I: Elementary Theory and Methods of Probability and its Applications*. Springer-Verlag, New York, USA.

Dayan, P. and Abbott, L. L. (2001). *Theoretical Neuroscience: Computational and Mathematical Modeling of Neural Systems*. MIT Press, Cambridge, MA, USA.

De Vries, G. and Sherman, A. (2000). Channel sharing in pancreatic β-cells revisited: Enhancement of emergent bursting by noise. *Journal of Theoretical Biology*, 207(4):513–530.

Dean, D. and Lawrence, P. D. (1983). Application of phase analysis of the frankenhaeuser-Huxley equations to determine threshold stimulus amplitudes. *IEEE Transactions on Biomedical Engineering*, (12):810–818.

Dean, D. and Lawrence, P. D. (1985). Optimization of neural stimuli based upon a variable threshold potential. *IEEE Transactions on Biomedical Engineering*, (1):8–14.

DeFelice, L. J. and Isaac, A. (1993). Chaotic states in a random world: relationship between the nonlinear differential equations of excitability and the stochastic properties of ion channels. *Journal of Statistical Physics*, 70(1-2):339–354.

Dietz, M., Marquardt, T., Salminen, N. H., and McAlpine, D. (2013). Emphasis of spatial cues in the temporal fine structure during the rising segments of amplitude-modulated sounds. *Proceedings of the National Academy of Sciences*, 110(37):15151–15156.

Dodla, R., Svirskis, G., and Rinzel, J. (2006). Well-timed, brief inhibition can promote spiking: postinhibitory facilitation. *Journal of Neurophysiology*, 95(4):2664–2677.

Drennan, W. R., Won, J. H., Dasika, V. K., and Rubinstein, J. T. (2007). Effects of temporal fine structure on the lateralization of speech and on speech understanding in noise. *Journal of the Association for Research in Otolaryngology*, 8(3):373–383.

Dynes, S. (1996). *Discharge characteristics of auditory nerve fibers for pulsatile electrical stimuli*. PhD thesis, Massachusetts Institute of Technology, MA, USA.

Eddington, D. K., Tierney, J., Noel, V., Hermann, B., Whearty, M., and Finley, C. (1994). Speech processors for auditory prostheses. *Eighth quarterly progress report, NIH contract*.

Ermentrout, G. and Terman, D. (2010). *Mathematical Foundations of Neuroscience*. Interdisciplinary Applied Mathematics. Springer, New York, USA.

Estep, D. (2006). *Practical Analysis in One Variable*. Undergraduate Texts in Mathematics. Springer, New York, USA.

Faisal, A., Selen, L., and Wolpert, D. (2008). Noise in the nervous system. *Nature Reviews Neuroscience*, 9(4):292–303.

Faisal, A. A. and Laughlin, S. B. (2007). Stochastic simulations on the reliability of action potential propagation in thin axons. *PLoS Comput Biol*, 3(5):e79.

Favre, E. and Pelizzone, M. (1993). Channel interactions in patients using the ineraid multichannel cochlear implant. *Hearing Research*, 66(2):150–156.

Fay, R. R. and Popper, A. N. (2005). Introduction to sound source localization. In *Sound Source Localization*, pages 1–5. Springer-Verlag, New York, USA.

Fayad, J. N. and Linthicum, F. H. (2006). Multichannel cochlear implants: relation of histopathology to performance. *The Laryngoscope*, 116(8):1310–1320.

Fearn, R. and Wolfe, J. (2000). The relative importance of rate and place: experiments using pitch scaling techniques with cochlear implantees. *Annals of Otology, Rhinology and Laryngology*, 109(12):51–53.

Ferguson, A., Sweeney, J., Durand, D., and Mortimer, J. (1987). Finite difference modelling of nerve cuff electric fields. In *Proceedings of the 9th Annual Conference of the Engineering in Medicine and Biological Society*, volume 3, pages 1579–1580.

Finke, C., Vollmer, J., Postnova, S., and Braun, H. A. (2008). Propagation effects of current and conductance noise in a model neuron with subthreshold oscillations. *Mathematical Biosciences*, 214(1):109–121.

Fitzhugh, R. (1960). Thresholds and plateaus in the Hodgkin-Huxley nerve equations. *The Journal of General Physiology*, 43(5):867–896.

Fitzhugh, R. (1961). Impulses and physiological states in theoretical models of nerve membrane. *Biophysical Journal*, 1(6):445–466.

Fitzhugh, R. (1969). *Mathematical models of excitation and propagation in nerve*. McGraw-Hill, New York, USA.

Fox, R. F. (1997). Stochastic versions of the Hodgkin-Huxley equations. *Biophysical Journal*, 72(5):2068–2074.

Fox, R. F. and Lu, Y.-n. (1994). Emergent collective behavior in large numbers of globally coupled independently stochastic ion channels. *Physical Review E*, 49(4):3421.

Frankenhaeuser, B. and Huxley, A. (1964). The action potential in the myelinated nerve fibre of Xenopus laevis as computed on the basis of voltage clamp data. *The Journal of Physiology*, 171(2):302–315.

Frankenhaeuser, B. and Vallbo, Å. (1965). Accommodation in myelinated nerve fibres of Xenopus laevis as computed on the basis of voltage clamp data. *Acta Physiologica Scandinavica*, 63(1-2):1–20.

Fredelake, S. and Hohmann, V. (2012). Factors affecting predicted speech intelligibility with cochlear implants in an auditory model for electrical stimulation. *Hearing Research*, 287(1):76–90.

Fretz, R. J. and Fravel, R. P. (1985). Design and function: a physical and electrical description of the 3M House cochlear implant system. *Ear and Hearing*, 6(3):14S–19S.

Fuchs, P. A., Glowatzki, E., and Moser, T. (2003). The afferent synapse of cochlear hair cells. *Current Opinion in Neurobiology*, 13(4):452–458.

Game, C., Thomson, D., Gibson, W., and Pauka, C. (1989). Polarity order of biphasic square pulse electric current stimulation of human cochlear nerve: observations with transtympanic electrodes. *Journal of the Neurological Sciences*, 90(3):291–298.

Gelfand, S. A. (2009). *Essentials of Audiology*. Thieme, New York, USA.

Gerstner, W. (1991). Associative memory in a network of 'biological' neurons. In *Advances in Neural Information Processing Systems*, volume 3, pages 84–90. Morgan Kaufmann, San Mateo.

Gerstner, W. (1995). Time structure of the activity in neural network models. *Physical Review E*, 51(1):738.

Gerstner, W., Kistler, W. M., Naud, R., and Paninski, L. (2014). *Neuronal Dynamics: From Single Neurons to Networks and Models of Cognition*. Cambridge University Press, Cambridge, UK.

Gerstner, W. and van Hemmen, J. L. (1992). Associative memory in a network of 'spiking' neurons. *Network: Computation in Neural Systems*, 3(2):139–164.

Gerwinn, S., Macke, J. H., and Bethge, M. (2010). Bayesian inference for generalized linear models for spiking neurons. *Frontiers in Computational Neuroscience*, 4(12). DOI: 10.3389/fncom.2010.00012.

Girvin, J. P., Marks, L. E., Antunes, J. L., Quest, D. O., OKeefe, M. D., Ning, P., and Dobelle, W. H. (1982). Electrocutaneous stimulation I. The effects of stimulus parameters on absolute threshold. *Perception & Psychophysics*, 32(6):524–528.

Goldwyn, J., Rubinstein, J., and Shea-Brown, E. (2012). A point process framework for modeling electrical stimulation of the auditory nerve. *Journal of Neurophysiology*, 108(5):1430–1452.

Goldwyn, J. H. and Shea-Brown, E. (2011). The what and where of adding channel noise to the Hodgkin-Huxley equations. *PLoS Computational Biology*, 7(11):e1002247.

Gorman, P. H. and Mortimer, J. T. (1983). The effect of stimulus parameters on the recruitment characteristics of direct nerve stimulation. *IEEE Transactions on Biomedical Engineering*, (7):407–414.

Greenwood, D. D. (1990). A cochlear frequency-position function for several species—29 years later. *The Journal of the Acoustical Society of America*, 87(6):2592–2605.

Grill Jr, W. M. (1999). Modeling the effects of electric fields on nerve fibers: influence of tissue electrical properties. *IEEE Transactions on Biomedical Engineering*, 46(8):918–928.

Grothe, B., Pecka, M., and McAlpine, D. (2010). Mechanisms of sound localization in mammals. *Physiological Reviews*, 90(3):983–1012.

Grumet, A. E. (1999). *Electric stimulation parameters for an epi-retinal prosthesis*. PhD thesis, Massachusetts Institute of Technology, MA, USA.

Hamacher, V. (2004). *Signalverarbeitungsmodelle des elektrisch stimulierten Gehörs*. Mainz Verlag, Germany.

Hanekom, T. (2001). Three-dimensional spiraling finite element model of the electrically stimulated cochlea. *Ear and Hearing*, 22(4):300–315.

Hardie, N. A. and Shepherd, R. K. (1999). Sensorineural hearing loss during development: morphological and physiological response of the cochlea and auditory brainstem. *Hearing Research*, 128(1):147–165.

Harrison, J. M. and Howe, M. E. (1974). Anatomy of the afferent auditory nervous system of mammals. In Keidel, W. D. and Neff, W. D., editors, *Auditory System: Anatomy Physiology (Ear)*, pages 283–336. Springer, Berlin, Heidelberg, Germany.

Hartmann, R., Topp, G., and Klinke, R. (1984). Discharge patterns of cat primary auditory fibers with electrical stimulation of the cochlea. *Hearing Research*, 13(1):47–62.

Hastie, T. and Tibshirani, R. (1987). Generalized additive models: some applications. *Journal of the American Statistical Association*, 82(398):371–386.

Hastie, T. J. and Tibshirani, R. J. (1990). *Generalized Additive Models*, volume 43. CRC Press, Boca Raton, Florida, USA.

Higham, D. J. (2001). An algorithmic introduction to numerical simulation of stochastic differential equations. *SIAM Review*, 43(3):525–546.

Hill, A. (1936a). Excitation and accommodation in nerve. *Proceedings of the Royal Society of London. Series B, Biological Sciences*, 119(814):305–355.

Hill, A. (1936b). The strength-duration relation for electric excitation of medullated nerve. *Proceedings of the Royal Society of London. Series B, Biological Sciences*, 119(815):440–453.

Hille, B. and Catterall, W. (2012). Electrical excitability and ion channels. In Siegel, G., Agranoff, R., and Molinoff, P., editors, *Basic Neurochemistry: Molecular, Cellular and Medical Aspects*, pages 63–80. Raven Press, New York, USA.

Hodgkin, A. and Huxley, A. (1952). A quantitative description of membrane current and its application to conduction and excitation in nerve. *Bulletin of Mathematical Biology*, 52(1):25–71.

Hofmann, L., Ebert, M., Tass, P. A., and Hauptmann, C. (2011). Modified pulse shapes for effective neural stimulation. *Frontiers in Neuroengineering*, 4(9). DOI: 10.3389/fneng.2011.00009.

Hong, R., Rubinstein, J., Wehner, D., and Horn, D. (2003). Dynamic range enhancement for cochlear implants. *Otology & Neurotology*, 24(4):590.

Huang, Y., Rüdiger, S., and Shuai, J. (2013). Langevin approach for stochastic Hodgkin-Huxley dynamics with discretization of channel open fraction. *Physics Letters A*, 377(44):3223–3227.

Huber, M. T. and Braun, H. A. (2007). Conductance versus current noise in a neuronal model for noisy subthreshold oscillations and related spike generation. *Biosystems*, 89(1):38–43.

Hudspeth, A. (2008). Making an effort to listen: mechanical amplification in the ear. *Neuron*, 59(4):530–545.

Imennov, N. and Rubinstein, J. (2009). Stochastic population model for electrical stimulation of the auditory nerve. *IEEE Transactions on Biomedical Engineering*, 56(10):2493–2501.

Izhikevich, E. M. (2007). *Dynamical Systems in Neuroscience*. MIT Press, Cambridge, MA, USA.

Jack, J. J. B., Noble, D., and Tsien, R. W. (1975). *Electric Current Flow in Excitable Cells*. Clarendon Press, Oxford, UK.

Javel, E. (1990). Acoustic and electrical encoding of temporal information. In Miller, J. M. and Spelman, F. A., editors, *Cochlear Implants: Models of the Electrically Stimulated Ear*, pages 247–295. Springer-Verlag, New York, USA.

Javel, E. and Shepherd, R. (2000). Electrical stimulation of the auditory nerve: III. Response initiation sites and temporal fine structure. *Hearing Research*, 140(1-2):45–76.

Javel, E., Tong, Y., Shepherd, R., and Clark, G. (1987). Responses of cat auditory nerve fibers to biphasic electrical current pulses. *Annals of Otology, Rhinology and Laryngology*, 96(128):26–30.

Johnson, D. H. (1980). The relationship between spike rate and synchrony in responses of auditory-nerve fibers to single tones. *The Journal of the Acoustical Society of America*, 68(4):1115–1122.

Jolivet, R., Lewis, T. J., and Gerstner, W. (2004). Generalized integrate-and-fire models of neuronal activity approximate spike trains of a detailed model to a high degree of accuracy. *Journal of Neurophysiology*, 92(2):959–976.

Jolivet, R., Rauch, A., Lüscher, H.-R., and Gerstner, W. (2006). Predicting spike timing of neocortical pyramidal neurons by simple threshold models. *Journal of Computational Neuroscience*, 21(1):35–49.

Joris, P. and Yin, T. C. (2007). A matter of time: internal delays in binaural processing. *Trends in Neurosciences*, 30(2):70–78.

Joris, P. X. and Verschooten, E. (2013). On the limit of neural phase locking to fine structure in humans. In Moore, J. B. C., Patterson, D. R., Winter, M. I., Carlyon, P. R., and Gockel, E. H., editors, *Basic Aspects of Hearing: Physiology and Perception*, pages 101–108. Springer-Verlag, New York, USA.

Joshi, S., Dau, T., and Epp, B. (2015). A model of auditory nerve responses to electrical stimulation. *38th Mid-Winter Meeting of the Association for Research in Otolaryngology*. Baltimore, Maryland, USA.

Kang, S., Chwodhury, T., Moon, I. J., Hong, S. H., Yang, H., Won, J. H., and Woo, J. (2015). Effects of electrode position on spatio-temporal auditory nerve fiber responses: A 3D computational model study. *Computational and Mathematical Methods in Medicine*, 2015:934382.

Keener, J. and Sneyd, J. (2010). *Mathematical Physiology: I: Cellular Physiology*, volume 1. Springer-Verlag, New York, USA.

Kellems, A. R., Chaturantabut, S., Sorensen, D. C., and Cox, S. J. (2010). Morphologically accurate reduced order modeling of spiking neurons. *Journal of Computational Neuroscience*, 28(3):477–494.

Kistler, W. M., Gerstner, W., and van Hemmen, J. L. (1997). Reduction of the Hodgkin-Huxley equations to a single-variable threshold model. *Neural Computation*, 9(5):1015–1045.

Kohn, A. F. (1989). Dendritic transformation of random synaptic inputs as measured from a neuron's spike train-modelling and simulation. *IEEE Transactions on Biomedical Engineering*, 36(1):44–54.

Kong, Y.-Y. and Carlyon, R. P. (2010). Temporal pitch perception at high rates in cochlear implants. *The Journal of the Acoustical Society of America*, 127(5):3114–3123.

Kong, Y.-Y., Deeks, J. M., Axon, P. R., and Carlyon, R. P. (2009). Limits of temporal pitch in cochlear implants. *The Journal of the Acoustical Society of America*, 125(3):1649–1657.

Koyama, S., Eden, U. T., Brown, E. N., and Kass, R. E. (2010). Bayesian decoding of neural spike trains. *Annals of the Institute of Statistical Mathematics*, 62(1):37–59.

Koyama, S. and Kass, R. E. (2008). Spike train probability models for stimulus-driven leaky integrate-and-fire neurons. *Neural Computation*, 20(7):1776–1795.

Laback, B., Majdak, P., and Baumgartner, W.-D. (2005). Interaural time differences in temporal fine structure, onset, and offset in bilateral electrical hearing. *Perception*, 416:87–90.

Lánskỳ, P. and Rodriguez, R. (1999a). The spatial properties of a model neuron increase its coding range. *Biological Cybernetics*, 81(2):161–167.

Lánskỳ, P. and Rodriguez, R. (1999b). Two-compartment stochastic model of a neuron. *Physica D: Nonlinear Phenomena*, 132(1):267–286.

Lánskỳ, P. and Rospars, J.-P. (1994). Stochastic model of intensity coding in olfactory neurons. In Pribram, K., editor, *Origins: Brain and Self Organization*, pages 268–285. Lawrence Erlbaum Associates, Hillsdale, New Jersey, USA.

Lapicque, L. (1907). Recherches quantitatives sur lexcitation électrique des nerfs traitée comme une polarisation. *Journal de Physiologie et de Pathologie Gnrale*, 9(1):620–635.

Lecar, H. and Nossal, R. (1971). Theory of threshold fluctuations in nerves: I. Relationships between electrical noise and fluctuations in axon firing. *Biophysical Journal*, 11(12):1048–1067.

Levitan, I. B., Kaczmarek, L. K., et al. (2015). *The Neuron: Cell and Molecular Biology*. Oxford University Press, Oxford, UK.

Litvak, L. (2002). *Towards a better speech processor for cochlear implants: Auditory-nerve responses to high-rate electric pulse trains*. PhD thesis, Massachusetts Institute of Technology, MA, USA.

Litvak, L., Delgutte, B., and Eddington, D. (2003a). Improved neural representation of vowels in electric stimulation using desynchronizing pulse trains. *The Journal of the Acoustical Society of America*, 114:2099.

Litvak, L., Delgutte, B., and Eddington, D. (2003b). Improved temporal coding of sinusoids in electric stimulation of the auditory nerve using desynchronizing pulse trains. *The Journal of the Acoustical Society of America*, 114:2079.

Litvak, L., Smith, Z., Delgutte, B., and Eddington, D. (2003c). Desynchronization of electrically evoked auditory-nerve activity by high-frequency pulse trains of long duration. *The Journal of the Acoustical Society of America*, 114:2066.

Loeb, G. E., White, M. W., and Jenkins, W. M. (1983). Biophysical considerations in electrical stimulation of the auditory nervous system. *Annals of the New York Academy of Sciences*, 405(1):123–136.

Loizou, P. C. (1998). Mimicking the human ear. *IEEE Signal Processing Magazine*, 15(5):101–130.

Macherey, O., Carlyon, R., Van Wieringen, A., and Wouters, J. (2007). A dual-process integrator-resonator model of the electrically stimulated human auditory nerve. *Journal of the Association for Research in Otolaryngology*, 8(1):84–104.

Macherey, O., Carlyon, R. P., Van Wieringen, A., Deeks, J. M., and Wouters, J. (2008). Higher sensitivity of human auditory nerve fibers to positive electrical currents. *Journal of the Association for Research in Otolaryngology*, 9(2):241–251.

Macherey, O., Deeks, J. M., and Carlyon, R. P. (2011). Extending the limits of place and temporal pitch perception in cochlear implant users. *Journal of the Association for Research in Otolaryngology*, 12(2):233–251.

Macherey, O., Van Wieringen, A., Carlyon, R. P., Deeks, J. M., and Wouters, J. (2006). Asymmetric pulses in cochlear implants: effects of pulse shape, polarity, and rate. *Journal of the Association for Research in Otolaryngology*, 7(3):253–266.

Majdak, P., Laback, B., and Baumgartner, W.-D. (2006). Effects of interaural time differences in fine structure and envelope on lateral discrimination in electric hearinga). *The Journal of the Acoustical Society of America*, 120(4):2190–2201.

Maršálek, P. (1999). *Biophysical models of neurons*. PhD thesis, Charles University Prague, Faculty of Mathematics and Physics, Prague, Czech Republic.

Matsuoka, A., Rubinstein, J., Abbas, P., and Miller, C. (2001). The effects of interpulse interval on stochastic properties of electrical stimulation: models and measurements. *IEEE Transactions on Biomedical Engineering*, 48(4):416–424.

Matthews, G. (1978). Strength-duration properties of single units driven by electrical stimulation of the lateral hypothalamus in rats. *Brain Research Bulletin*, 3(2):171–174.

McAlpine, D. and Grothe, B. (2003). Sound localization and delay lines-do mammals fit the model? *Trends in Neurosciences*, 26(7):347–350.

McCullagh, P. and Nelder, J. A. (1989). *Generalized Linear Models*, volume 37. Chapman and Hall, London, UK.

McKay, C. M. and Henshall, K. R. (2003). The perceptual effects of interphase gap duration in cochlear implant stimulation. *Hearing Research*, 181(1):94–99.

McNeal, D. (1976). Analysis of a model for excitation of myelinated nerve. *IEEE Transactions on Biomedical Engineering*, (4):329–337.

Meier, J. H., Rotten, W., Zoutman, A. E., Boom, H. B., and Bergveld, P. (1992). Simulation of multipolar fiber selective neural stimulation using intrafascicular electrodes. *IEEE Transactions on Biomedical Engineering*, 39(2):122–134.

Mensi, S., Naud, R., and Gerstner, W. (2011). From stochastic nonlinear integrate-and-fire to generalized linear models. *Advances in Neural Information Processing Systems*, 24:1377–1385.

Micco, A. G. and Richter, C.-P. (2006). Tissue resistivities determine the current flow in the cochlea. *Current Opinion in Otolaryngology & Head and Neck Surgery*, 14(5):352–355.

Middlebrooks, J. (2004). Effects of cochlear-implant pulse rate and inter-channel timing on channel interactions and thresholds. *The Journal of the Acoustical Society of America*, 116(1):452–468.

Mihalas, S. and Niebur, E. (2009). A generalized linear integrate-and-fire neural model produces diverse spiking behaviors. *Neural Computation*, 21(3):704–718.

Miller, A., Smith, D., and Pfingst, B. (1999a). Across-species comparisons of psychophysical detection thresholds for electrical stimulation of the cochlea: II. Strength-duration functions for single, biphasic pulses. *Hearing Research*, 135(1):47–55.

Miller, A. L., Morris, D. J., and Pfingst, B. E. (1997). Interactions between pulse separation and pulse polarity order in cochlear implants. *Hearing Research*, 109(1):21–33.

Miller, C., Abbas, P., and Robinson, B. (2001a). Response properties of the refractory auditory nerve fiber. *Journal of the Association for Research in Otolaryngology*, 2(3):216–232.

Miller, C., Abbas, P., Robinson, B., Rubinstein, J., and Matsuoka, A. (1999b). Electrically evoked single-fibre action potentials from cat: responses to monopolar, monophasic stimulation. *Hearing Research*, 130(1-2):197–218.

Miller, C., Abbas, P., and Rubinstein, J. (1999c). An empirically based model of the electrically evoked compound action potential. *Hearing Research*, 135(1-2):1–18.

Miller, C., Abbas, P., Rubinstein, J., Robinson, B., Matsuoka, A., and Woodworth, G. (1998). Electrically evoked compound action potentials of guinea pig and cat: responses to monopolar, monophasic stimulation. *Hearing Research*, 119(1-2):142–154.

Miller, C., Robinson, B., Rubinstein, J., Abbas, P., and Runge-Samuelson, C. (2001b). Auditory nerve responses to monophasic and biphasic electric stimuli. *Hearing Research*, 151(1-2):79–94.

Miller, C. A., Abbas, P. J., Nourski, K. V., Hu, N., and Robinson, B. K. (2003). Electrode configuration influences action potential initiation site and ensemble stochastic response properties. *Hearing Research*, 175(1):200–214.

Miller, M. I. and Mark, K. E. (1992). A statistical study of cochlear nerve discharge patterns in response to complex speech stimuli. *The Journal of the Acoustical Society of America*, 92(1):202–209.

Mino, H. and Rubinstein, J. (2006). Effects of neural refractoriness on spatio-temporal variability in spike initiations with electrical stimulation. *IEEE Transactions on Neural Systems and Rehabilitation Engineering*, 14(3):273–280.

Mino, H., Rubinstein, J., Miller, C., and Abbas, P. (2004). Effects of electrode-to-fiber distance on temporal neural response with electrical stimulation. *IEEE Transactions on Biomedical Engineering*, 51(1):13–20.

Mino, H., Rubinstein, J. T., and White, J. A. (2002). Comparison of algorithms for the simulation of action potentials with stochastic sodium channels. *Annals of Biomedical Engineering*, 30(4):578–587.

Mogyoros, I., Kiernan, M. C., and Burke, D. (1996). Strength-duration properties of human peripheral nerve. *Brain*, 119(2):439–448.

Moon, A. K., Zwolan, T. A., and Pfingst, B. E. (1993). Effects of phase duration on detection of electrical stimulation of the human cochlea. *Hearing Research*, 67(1):166–178.

Moore, B. C. (2012). *An Introduction to the Psychology of Hearing*. Emerald Group Publishing Limited, Bingley, UK.

Moore, B. C. (2014). *Auditory Processing of Temporal Fine Structure: Effects of Age and Hearing Loss*. World Scientific Publishing, Singapore.

Morse, R. P. and Evans, E. F. (1996). Enhancement of vowel coding for cochlear implants by addition of noise. *Nature Medicine*, 2(8):928–932.

Morse, R. P. and Evans, E. F. (1999). Additive noise can enhance temporal coding in a computational model of analogue cochlear implant stimulation. *Hearing Research*, 133(1):107–119.

Motz, H. and Rattay, F. (1986). A study of the application of the Hodgkin-Huxley and the Frankenhaeuser-Huxley model for electrostimulation of the acoustic nerve. *Neuroscience*, 18(3):699–712.

Nadol Jr, J., Young, Y., and Glynn, R. (1989). Survival of spiral ganglion cells in profound sensorineural hearing loss: implications for cochlear implantation. *The Annals of Otology, Rhinology, and Laryngology*, 98(6):411–416.

Naud, R. and Gerstner, W. (2012). The performance (and limits) of simple neuron models: Generalizations of the leaky integrate-and-fire model. In Le Novere, N., editor, *Computational Systems Neurobiology*, pages 163–192. Springer-Verlag, New York, USA.

Negm, M. H. and Bruce, I. C. (2008). Effects of I_h and I_{KLT} on the response of the auditory nerve to electrical stimulation in a stochastic Hodgkin-Huxley model. In *Engineering in Medicine and Biology Society, 2008. Proceedings of the 30th Annual International Conference of the IEEE*, pages 5539–5542. DOI: 10.1109/iembs.2008.4650469.

Nelder, J. and Wedderburn, R. (1972). Generalized linear models. *Journal of the Royal Statistical Society. Series A (General)*, 135:370–384.

Nie, K., Stickney, G., and Zeng, F.-G. (2005). Encoding frequency modulation to improve cochlear implant performance in noise. *IEEE Transactions on Biomedical Engineering*, 52(1):64–73.

Noble, D. and Stein, R. (1966). The threshold conditions for initiation of action potentials by excitable cells. *The Journal of Physiology*, 187(1):129–162.

O'Gorman, D., Brughera, A., and Colburn, S. (2013). Does neural shunting limit temporal coding by the auditory nerve at high pulse rates? In *2013 Conference in Implantable Auditory Prostheses, California*. Poster.

O'Gorman, D., White, J., and Shera, C. (2009). Dynamical instability determines the effect of ongoing noise on neural firing. *Journal of the Association for Research in Otolaryngology*, 10(2):251–267.

Ooyama, H. and Wright, E. B. (1961). Anode break excitation on single Ranvier node of frog nerve. *American Journal of Physiology-Legacy Content*, 200(2):209–218.

Ozer, M. and Ekmekci, N. H. (2005). Effect of channel noise on the time-course of recovery from inactivation of sodium channels. *Physics Letters A*, 338(2):150–154.

Palmer, A. and Russell, I. (1986). Phase-locking in the cochlear nerve of the guinea-pig and its relation of the receptor potential of inner hair-cells. *Hearing Research*, 24(1):1–15.

Paninski, L., Pillow, J. W., and Simoncelli, E. P. (2004). Maximum likelihood estimation of a stochastic integrate-and-fire neural encoding model. *Neural Computation*, 16(12):2533–2561.

Panizza, M., Nilsson, J., Roth, B. J., Rothwell, J., and Hallett, M. (1994). The time constants of motor and sensory peripheral nerve fibers measured with the method of latent addition. *Electroencephalography and Clinical Neurophysiology*, 93(2):147–154.

Parkins, C. (1989). Temporal response patterns of auditory nerve fibers to electrical stimulation in deafened squirrel monkeys. *Hearing Research*, 41(2):137–168.

Parkins, C. and Colombo, J. (1987). Auditory-nerve single-neuron thresholds to electrical stimulation from scala tympani electrodes. *Hearing Research*, 31(3):267–285.

Patton, K. T. and Thibodeau, G. A. (2016). *Anatomy & Physiology*. Elsevier Health Sciences, Philadelphia, USA.

Pfingst, B. E., De Haan, D. R., and Holloway, L. A. (1991). Stimulus features affecting psychophysical detection thresholds for electrical stimulation of the cochlea. I: phase duration and stimulus duration. *The Journal of the Acoustical Society of America*, 90(4):1857–1866.

Pickles, J. O. (2012). *An Introduction to the Physiology of Hearing*. Emerald Group Publishing Limited, Bingley, UK.

Plack, C. J. and Oxenham, A. J. (2005a). Overview: The present and future of pitch. In Plack, C. J., Oxenham, A. J., Fay, R. R., and Popper, A. N., editors, *Pitch*, pages 1–6. Springer-Verlag, New York, USA.

Plack, C. J. and Oxenham, A. J. (2005b). The psychophysics of pitch. In Plack, C. J., Oxenham, A. J., Fay, R. R., and Popper, A. N., editors, *Pitch*, pages 7–55. Springer-Verlag, New York, USA.

Plesser, H. E. and Gerstner, W. (2000). Noise in integrate-and-fire neurons: From stochastic input to escape rates. *Neural Computation*, 12(2):367–384.

Plonsey, R. and Barr, R. C. (1995). Electric field stimulation of excitable tissue. *IEEE Transactions on Biomedical Engineering*, 42(4):329–336.

Plonsey, R. and Barr, R. C. (2000). *Bioelectricity: A Quantitative Approach*, chapter Electrical stimulation of excitable tissue, pages 179–216. Springer-Verlag, New York, USA.

Plourde, E., Delgutte, B., and Brown, E. (2011). A point process model for auditory neurons considering both their intrinsic dynamics and the spectro-temporal properties of an extrinsic signal. *IEEE Transactions on Biomedical Engineering*, 58(6):1507–1510.

Potrusil, T., Wenger, C., Glueckert, R., Schrott-Fischer, A., and Rattay, F. (2012). Morphometric classification and spatial organization of spiral ganglion neurons in

the human cochlea: consequences for single fiber response to electrical stimulation. *Neuroscience*, 214:120–135.

Prado-Guitierrez, P., Fewster, L. M., Heasman, J. M., McKay, C. M., and Shepherd, R. K. (2006). Effect of interphase gap and pulse duration on electrically evoked potentials is correlated with auditory nerve survival. *Hearing Research*, 215(1):47–55.

Quarteroni, A., Sacco, R., and Saleri, F. (2010). *Numerical Mathematics*, volume 37. Springer-Verlag, Berlin, Heidelberg, Germany.

Rabbitt, R. and Holmes, M. (1988). Three-dimensional acoustic waves in the ear canal and their interaction with the tympanic membrane. *The Journal of the Acoustical Society of America*, 83(3):1064–1080.

Ramekers, D., Versnel, H., Strahl, S. B., Smeets, E. M., Klis, S. F., and Grolman, W. (2014). Auditory-nerve responses to varied inter-phase gap and phase duration of the electric pulse stimulus as predictors for neuronal degeneration. *Journal of the Association for Research in Otolaryngology*, 15(2):187–202.

Ranck Jr, J. B. (1975). Which elements are excited in electrical stimulation of mammalian central nervous system: a review. *Brain Research*, 98(3):417–440.

Rangayyan, R. M. (2015). *Biomedical Signal Analysis*, volume 33. John Wiley & Sons, Chichester, England.

Rattay, F. (1986). Analysis of models for external stimulation of axons. *IEEE Transactions on Biomedical Engineering*, (10):974–977.

Rattay, F. (1987). Ways to approximate current-distance relations for electrically stimulated fibers. *Journal of Theoretical Biology*, 125(3):339–349.

Rattay, F. (1988). Modeling the excitation of fibers under surface electrodes. *IEEE Transactions on Biomedical Engineering*, 35(3):199–202.

Rattay, F. (1989). Analysis of models for extracellular fiber stimulation. *IEEE Transactions on Biomedical Engineering*, 36(7):676–682.

Rattay, F. (1990). *Electrical Nerve Stimulation: Theory, Experiments and Applications*. Springer-Verlag, Wien, Austria.

Rattay, F. (1998). Analysis of the electrical excitation of CNS neurons. *IEEE Transactions on Biomedical Engineering*, 45(6):766–772.

Rattay, F. (1999). The basic mechanism for the electrical stimulation of the nervous system. *Neuroscience*, 89(2):335–346.

Rattay, F. and Aberham, M. (1993). Modeling axon membranes for functional electrical stimulation. *IEEE Transactions on Biomedical Engineering*, 40(12):1201–1209.

Rattay, F., Leao, R. N., and Felix, H. (2001a). A model of the electrically excited human cochlear neuron. II. influence of the three-dimensional cochlear structure on neural excitability. *Hearing Research*, 153(1):64–79.

Rattay, F., Lutter, P., and Felix, H. (2001b). A model of the electrically excited human cochlear neuron: I. contribution of neural substructures to the generation and propagation of spikes. *Hearing Research*, 153(1):43–63.

Rattay, F., Paredes, L., and Leao, R. (2012). Strength-duration relationship for intra-versus extracellular stimulation with microelectrodes. *Neuroscience*, 214:1–13.

Reilly, J., Freeman, V., and Larkin, W. (1985). Sensory effects of transient electrical stimulation-evaluation with a neuroelectric model. *IEEE Transactions on Biomedical Engineering*, 32(12):1001–1011.

Rinzel, J. (1985). Excitation dynamics: insights from simplified membrane models. *Federation Proceedings*, 44(15):2944–2946.

Robert, M. E. (2006). Integrate-and-fire model for electrically stimulated nerve cell. *IEEE Transactions on Biomedical Engineering*, 53(4):756–758.

Robles, L. and Ruggero, M. A. (2001). Mechanics of the mammalian cochlea. *Physiological Reviews*, 81(3):1305–1352.

Rodriguez, R. and Lánskỳ, P. (2000). A simple stochastic model of spatially complex neurons. *Biosystems*, 58(1):49–58.

Rosen, S. (1992). Temporal information in speech: acoustic, auditory and linguistic aspects. *Philosophical Transactions of the Royal Society B: Biological Sciences*, 336(1278):367–373.

Rowat, P. (2007). Interspike interval statistics in the stochastic Hodgkin-Huxley model: Coexistence of gamma frequency bursts and highly irregular firing. *Neural Computation*, 19(5):1215–1250.

Rowat, P. F. and Elson, R. C. (2004). State-dependent effects of Na channel noise on neuronal burst generation. *Journal of Computational Neuroscience*, 16(2):87–112.

Rubinstein, J. (1993). Axon termination conditions for electrical stimulation. *IEEE Transactions on Biomedical Engineering*, 40(7):654–663.

Rubinstein, J. (1995). Threshold fluctuations in an n sodium channel model of the node of Ranvier. *Biophysical Journal*, 68(3):779–785.

Rubinstein, J., Miller, C., Mino, H., and Abbas, P. (2001). Analysis of monophasic and biphasic electrical stimulation of nerve. *IEEE Transactions on Biomedical Engineering*, 48(10):1065–1070.

Rubinstein, J. and Spelman, F. (1988). Analytical theory for extracellular electrical stimulation of nerve with focal electrodes. I. passive unmyelinated axon. *Biophysical Journal*, 54(6):975–981.

Rubinstein, J., Wilson, B., Finley, C., and Abbas, P. (1999). Pseudospontaneous activity: stochastic independence of auditory nerve fibers with electrical stimulation. *Hearing Research*, 127(1-2):108–118.

Rubinstein, J. T. (2004). How cochlear implants encode speech. *Current Opinion in Otolaryngology & Head and Neck Surgery*, 12(5):444–448.

Saarinen, A., Linne, M.-L., and Yli-Harja, O. (2008). Stochastic differential equation model for cerebellar granule cell excitability. *PLoS Computational Biology*, 4(2):e1000004.

Sato, D., Xie, L.-H., Nguyen, T. P., Weiss, J. N., and Qu, Z. (2010). Irregularly appearing early afterdepolarizations in cardiac myocytes: random fluctuations or dynamical chaos? *Biophysical Journal*, 99(3):765–773.

Schiff, S. J. (2012). *Neural Control Engineering: the Emerging Intersection Between Control Theory and Neuroscience*. MIT Press, Cambridge, MA, USA.

Schmid, G., Goychuk, I., and Hänggi, P. (2001). Stochastic resonance as a collective property of ion channel assemblies. *Europhysics Letters*, 56(1):22.

Schwarz, J. R. and Eikhof, G. (1987). Na currents and action potentials in rat myelinated nerve fibres at 20 and 37 c. *Pflügers Archiv*, 409(6):569–577.

Shannon, R. (1993). Psychophysics. In Tyler, R., editor, *Cochlear implants: Audiological foundations*, pages 357–388. Singular Publishing Group, San Diego, CA.

Shannon, R. V. (1983). Multichannel electrical stimulation of the auditory nerve in man. I. basic psychophysics. *Hearing Research*, 11(2):157–189.

Shepherd, R., Hardie, N., and Baxi, J. (2001). Electrical stimulation of the auditory nerve: single neuron strength-duration functions in deafened animals. *Annals of Biomedical Engineering*, 29(3):195–201.

Shepherd, R., Hatsushika, S., and Clark, G. M. (1993). Electrical stimulation of the auditory nerve: the effect of electrode position on neural excitation. *Hearing Research*, 66(1):108–120.

Shepherd, R. and Javel, E. (1999). Electrical stimulation of the auditory nerve: II. effect of stimulus waveshape on single fibre response properties. *Hearing Research*, 130(1-2):171–188.

Shuai, J. and Jung, P. (2002). Optimal intracellular calcium signaling. *Physical Review Letters*, 88(6):068102.

Skaugen, E. and Walløe, L. (1979). Firing behaviour in a stochastic nerve membrane model based upon the HodgkinHuxley equations. *Acta Physiologica Scandinavica*, 107(4):343–363.

Smit, J., Hanekom, T., and Hanekom, J. (2008). Predicting action potential characteristics of human auditory nerve fibres through modification of the Hodgkin-Huxley equations. *South African Journal of Science*, 104(7-8):284–292.

Smit, J. E., Hanekom, T., Van Wieringen, A., Wouters, J., and Hanekom, J. J. (2010). Threshold predictions of different pulse shapes using a human auditory nerve fibre model containing persistent sodium and slow potassium currents. *Hearing Research*, 269(1):12–22.

Smith, D. W. and Finley, C. C. (1997). Effects of electrode configuration on psychophysical strength-duration functions for single biphasic electrical stimuli in cats. *The Journal of the Acoustical Society of America*, 102:2228–2237.

Smith, Z. M., Delgutte, B., and Oxenham, A. J. (2002). Chimaeric sounds reveal dichotomies in auditory perception. *Nature*, 416(6876):87–90.

Spoendlin, H. (1970). *Frequency Analysis and Periodicity Detection in Hearing*, chapter Structural basis of peripheral frequency analysis, pages 2–36. Sijthoff, Leiden.

Spoendlin, H. (1985). Anatomy of cochlear innervation. *American Journal of Otolaryngology*, 6(6):453–467.

Sterratt, D., Graham, B., Gillies, A., and Willshaw, D. (2011). *Principles of Computational Modelling in Neuroscience*. Cambridge University Press, Cambridge, UK.

Stinson, M. R. (1985). The spatial distribution of sound pressure within scaled replicas of the human ear canal. *The Journal of the Acoustical Society of America*, 78(5):1596–1602.

Stocks, N. G., Allingham, D., and Morse, R. (2002). The application of suprathreshold stochastic resonance to cochlear implant coding. *Fluctuation and Noise Letters*, 2(03):L169–L181.

Stypulkowski, P. and van den Honert, C. (1984). Physiological properties of the electrically stimulated auditory nerve. I. compound action potential recordings. *Hearing Research*, 14(3):205–223.

Tasaki, I. (1956). Initiation and abolition of the action potential of a single node of Ranvier. *The Journal of General Physiology*, 39(3):377–395.

Teoh, S. W., Pisoni, D. B., and Miyamoto, R. T. (2004). Cochlear implantation in adults with prelingual deafness. part II. underlying constraints that affect audiological outcomes. *The Laryngoscope*, 114(10):1714–1719.

Tong, Y. and Clark, G. M. (1985). Absolute identification of electric pulse rates and electrode positions by cochlear implant patients. *The Journal of the Acoustical Society of America*, 77(5):1881–1888.

Townshend, B., Cotter, N., Van Compernolle, D., and White, R. (1987). Pitch perception by cochlear implant subjects. *The Journal of the Acoustical Society of America*, 82(1):106–115.

Truccolo, W., Eden, U. T., Fellows, M. R., Donoghue, J. P., and Brown, E. N. (2005). A point process framework for relating neural spiking activity to spiking history, neural ensemble, and extrinsic covariate effects. *Journal of Neurophysiology*, 93(2):1074–1089.

Tuckwell, H. C. (1988). *Introduction to Theoretical Neurobiology: Volume 1, Linear Cable Theory and Dendritic Structure*. Cambridge University Press, Cambridge, UK.

Tyler, R. S. (1988). Open-set word recognition with the 3m/vienna single-channel cochlear implant. *Archives of Otolaryngology-Head & Neck Surgery*, 114(10):1123–1126.

Undurraga, J. A., Carlyon, R. P., Wouters, J., and Van Wieringen, A. (2013). The polarity sensitivity of the electrically stimulated human auditory nerve measured at the level of the brainstem. *Journal of the Association for Research in Otolaryngology*, 14(3):359–377.

Vallbo, A. (1964). Accommodation related to inactivation of the sodium permeability in single myelinated nerve fibres from Xenopus laevis. *Acta Physiologica Scandinavica*, 61:429–444.

van den Honert, C. and Mortimer, J. (1979). The response of the myelinated nerve fiber to short duration biphasic stimulating currents. *Annals of Biomedical Engineering*, 7(2):117–125.

van den Honert, C. and Stypulkowski, P. (1984). Physiological properties of the electrically stimulated auditory nerve. II. single fiber recordings. *Hearing Research*, 14(3):225–243.

van den Honert, C. and Stypulkowski, P. (1987). Temporal response patterns of single auditory nerve fibers elicited by periodic electrical stimuli. *Hearing Research*, 29(2):207–222.

Van Wieringen, A., Macherey, O., Carlyon, R. P., Deeks, J. M., and Wouters, J. (2008). Alternative pulse shapes in electrical hearing. *Hearing Research*, 242(1):154–163.

Verveen, A. (1960). On the fluctuation of threshold of the nerve fibre. In Tower, D. and Schade, J., editors, *Structure and Function of the Cerebral Cortex*, pages 282–288. Elsevier, Amsterdam, Netherlands.

Verveen, A. (1961). *Fluctuation in Excitability*. Drukkerij Holland N.V., Amsterdam, Netherlands.

Wang, M., Hou, Z., and Xin, H. (2004). Double-system-size resonance for spiking activity of coupled Hodgkin-Huxley neurons. *ChemPhysChem*, 5(10):1602–1605.

Warman, E., Grill, W., Durand, D., and Mortimer, J. (1991). A new formulation of the activating function for estimation of neural excitation thresholds. *Engineering in Medicine and Biology Society, Proceedings of the Annual International Conference of the IEEE*, 13(2):916–917.

Warman, E. N., Grill, W. M., and Durand, D. (1992). Modeling the effects of electric fields on nerve fibers: determination of excitation thresholds. *IEEE Transactions on Biomedical Engineering*, 39(12):1244–1254.

Weitz, A., Behrend, M., Humayun, M., Chow, R., and Weiland, J. (2011). Interphase gap decreases electrical stimulation threshold of retinal ganglion cells. *Engineering in Medicine and Biology Society, Proceedings of the Annual International Conference of the IEEE*, 2011:6725–6728.

Weitz, A. C., Behrend, M. R., Ahuja, A. K., Christopher, P., Wei, J., Wuyyuru, V., Patel, U., Greenberg, R. J., Humayun, M. S., Chow, R. H., et al. (2014). Interphase gap as a means to reduce electrical stimulation thresholds for epiretinal prostheses. *Journal of Neural Engineering*, 11(1):016007.

White, J. A., Klink, R., Alonso, A., and Kay, A. R. (1998). Noise from voltage-gated ion channels may influence neuronal dynamics in the entorhinal cortex. *Journal of Neurophysiology*, 80(1):262–269.

White, M. W., Merzenich, M. M., and Gardi, J. N. (1984). Multichannel cochlear implants: Channel interactions and processor design. *Archives of Otolaryngology—Head & Neck Surgery*, 110(8):493–501.

Whiten, D. M. (2007). *Electro-Anatomical Models of the Cochlear Implant*. PhD thesis, Massachusetts Institute of Technology, MA, USA.

Wightman, F. L. and Kistler, D. J. (1992). The dominant role of low-frequency interaural time differences in sound localization. *The Journal of the Acoustical Society of America*, 91(3):1648–1661.

Wilson, B., Lawson, D., Zerbi, M., and Finley, C. (1992). Speech processors for auditory prostheses. *Twelfth quarterly progress report, NIH project N01-DC-9-2401*.

Wilson, B. S. (2013). Toward better representations of sound with cochlear implants. *Nature Medicine*, 19(10):1245–1248.

Wilson, B. S. (2015). Getting a decent (but sparse) signal to the brain for users of cochlear implants. *Hearing Research*, 322:24–38.

Wilson, B. S., Finley, C. C., Lawson, D. T., Wolford, R. D., Eddington, D. K., and Rabinowitz, W. M. (1991). Better speech recognition with cochlear implants. *Nature*, 352(6332):236–238.

Woo, J., Miller, C. A., and Abbas, P. J. (2009). Biophysical model of an auditory nerve fiber with a novel adaptation component. *IEEE Transactions on Biomedical Engineering*, 56(9):2177–2180.

Woo, J., Miller, C. A., and Abbas, P. J. (2010). The dependence of auditory nerve rate adaptation on electric stimulus parameters, electrode position, and fiber diameter: a computer model study. *Journal of the Association for Research in Otolaryngology*, 11(2):283–296.

Wright, A., Davis, A., Bredberg, G., Ulehlova, L., and Spencer, H. (1986). Hair cell distributions in the normal human cochlea. *Acta Oto-Laryngologica. Supplementum*, 444:1–48.

Wysocki, J. and Skarzyński, H. (1997). Cochleostomy during the intracochlear implantation. anatomical conditions in children and adults. *Otolaryngologia Polska. The Polish Otolaryngology*, 52(6):689–694.

Zeng, F.-G., Nie, K., Stickney, G. S., Kong, Y.-Y., Vongphoe, M., Bhargave, A., Wei, C., and Cao, K. (2005). Speech recognition with amplitude and frequency modulations. *Proceedings of the National Academy of Sciences of the United States of America*, 102(7):2293–2298.

Zwislocki, J. and Feldman, R. (1956). Just noticeable differences in dichotic phase. *The Journal of the Acoustical Society of America*, 28(5):860–864.